

Diss. ETH No. 15714

**Cavitand-, Fullerene-, and Porphyrin-
containing *Langmuir* Films: Preparation of
Mechanically and Optically Active Monolayers**

A dissertation submitted to the
SWISS FEDERAL INSTITUTE OF TECHNOLOGY ZÜRICH

For the degree of
Doctor of Natural Sciences

Presented by

Federica Marotti

Dottore in Chimica
Università “La Sapienza” di Roma, Italy
born May 21, 1972 in Rome, Italy

Accepted on the recommendation of
Prof. Dr. François Diederich, examiner
Dr. Carlo Thilgen, co-examiner
Prof. Dr. Peter Walde, co-examiner
Dr. Jean-Louis Gallani, co-examiner

Zürich 2004

Ai miei genitori

“Cogito, ergo sum!”

René Descartes

Aknowledgements

I would like to thank *Prof. Dr. François Diederich* for giving me the opportunity to work on such an interesting and challenging project, and also for his guidance as well as for his encouragement during my PhD Thesis. I greatly appreciated his enthusiasm as well as the freedom I had in the execution of the project.

I sincerely thank *Dr. Carlo Thilgen* for accepting the co-examination of my Thesis and for his rigorous and critical comments while proof-reading this manuscript. Thank you very much; I know that it was hard time for you!

I am thankful to *Dr. Jean-Louis Gallani* for accepting the co-examination of my Thesis and for helpful suggestions about the Langmuir and Langmuir-Blodgett technique.

Also, I would like to thank *Prof. Peter Walde* for being my co-examiner.

I would like to thank *Becky Hof*, and *Dr. Davide Bonifazi* for their critical proof-reading of this manuscript.

I am grateful to *Irma Näf* for all very accurate help with administrative problems.

I want to thank all the members of the ETH staff for the valuable services they provided. In particular, Rolf Häfliger for the rapidity in performing HR-MALDI mass analyses.

I thank all the members of the *Diederich's* group for their friendship and for creating a very pleasant working environment.

Merçi à *Dr. David Carcache* (il mio toro preferito), it was a really pleasure to know you and to share with you nice moments in- and out- the lab.

With you, *Markus Frei and Kaspar Schärer* I shared a really great time and I really enjoyed our “special” conversation; *Tobias Welti* for his prompt help in solving my problems with the computers; *Henry Dube* for his help with Mopac and for his guidance in cleaning the rotavap!

Dr. Olivier Enger, Dr. Nils F. Utesch, Dr. Nicolle Moonen, Dr. Severin Odermatt, Markus Frei, Romain Siegrist, Marine Guillot, Dr. Fraser Hof, Becky and Sophie Hof, Christine Crane, Vito Convertino, Dr. Nikos Chronakis, Dr. Jacob Olsen, Dr. Frieder Mitzel, Dr. Delphine Felder, Dr. Peter Manini, Dr. Davide Bonifazi, Carmen Atienza, and Lorenzo Alonso, I could never forget the nice time we had together in the chemistry building, or outside of the ETH. You all made my life in Zürich a real pleasure!

I am grateful to *Christine Crane, Vito Convertino*, and *Dr. Raffaella Faraoni* for their friendship, I will keep you in my heart.

I would like to thank a very special person *Dr. Nikos Chronakis*, you always supported me with your suggestions and your encouragement. I am really glad to have found a very good friendship.

Un grazie immenso al *Dr. Peter Manini* per la sua grande amicizia e disponibilità e per aver sopportato tutti i miei nervosismi. Porterò sempre con me ogni istante passato insieme.

Un ringraziamento speciale va al *Dr. Davide Bonifazi*: hai avuto un grosso peso in questa tesi di dottorato. Grazie per le interessanti discussioni e per gli innumerevoli spunti che mi hai dato. È stato divertente e anche un po' doloroso dividere l'ufficio con te; chissà se zio Bruno è dello stesso parere?

Grazie, grazie, grazie a *Giulio Casi* per la tua amicizia e per le tue deliziose cenate; *Rudi Fasan* (siamo gemelli!!!!) che con il tuo sorriso (.....i tuoi bei dentoni) e buon umore hai rischiarato le giornate un po' più scure; *Dr. Silvia Rasi* per essermi stata amorevolmente vicino quando non era poi tanto facile farlo; *Dr. Salvatore Chessari* per

le interessanti analisi sulla vita: è stato un vero piacere condividere con te la mia esperienza zurighese, sono molto contenta di averti conosciuto!

E non posso non dire GRAZIE alle mie due piú care amiche *Dr. Paola Luci* e *Dr. Francesca Vitali*. Vi ringrazio per i bellissimi e significativi momenti che abbiamo trascorso e continueremo a trascorrere insieme. Mi avete incoraggiato e supportato (e anche sopportato) nei momenti belli cosí come in quelli brutti con un amore incondizionato di cui solo una grandissima amicizia è capace. Vi adoro!!!

E infine un grazie di cuore va a mio padre e mia madre che mi hanno insegnato ad amare la vita ed ad accettare e fronteggiare con un sorriso le difficoltà, senza mai demordere. Grazie per avermi sostenuto, senza perdere mai la fiducia in me, e per avermi amato senza chiedere nulla in cambio.

Publications and Presentations

Publications

M. Frei, F. Marotti, F. Diederich, *Chem. Commun.* **2004**, 1362-1363. *Zn^{II}-Induced Conformational Control of Amphiphilic Cavitands in Langmuir Monolayers.*

F. Marotti, D. Bonifazi, R. Gehrig, , R. Paulini, J.-L. Gallani, F. Diederich, manuscript in preparation. *Fullerene- and Porphyrin-appendend Crown Ethers: Synthesis and Preparation of Stable Langmuir and Langmuir–Blodgett Films.*

Poster Presentations

M. Frei, F. Marotti, F. Diederich, “*NMR and Langmuir Investigations of Conformational Switching of Amphiphilic Grippers*”, Kick off-Meeting for the 2nd phase of the National Research Program, Bern, Switzerland, July **2003**.

Table of Contents

| | |
|--|-----------|
| <i>Abbreviations</i> | i |
| <i>Abstract</i> | v |
| <i>Riassunto</i> | xi |
| 1 Introduction | 1 |
| 1.1 Organic Thin Films | 1 |
| 1.2 General Account of Self-Assembly | 2 |
| 1.2.1 Self-Assembled Monolayers (SAMs) | 3 |
| 1.2.1.1 Self-Assembled Monolayers of Cavitands | 5 |
| 1.2.1.2 Self-Assembled Fullerene Monolayers of Fullerene and of Fullerene Derivatives | 8 |
| 1.2.1.3 Self-Assembled Porphyrin Monolayers | 11 |
| 1.3 Langmuir and Langmuir-Blodgett Films | 15 |
| 1.3.1 The History of <i>Langmuir</i> and <i>Langmuir-Blodgett</i> Films | 15 |
| 1.3.2 <i>Langmuir</i> Monolayer Technique | 17 |
| 1.3.3 Film Deposition: <i>Langmuir-Blodgett</i> Technique | 21 |
| 1.3.4 Characterization and Properties of Monolayers | 24 |
| 1.3.4.1 <i>Brewster</i> Angle Microscopy (BAM) | 24 |
| 1.3.4.2 Grazing Incidence X-ray Diffraction | 29 |
| 2 Langmuir Investigations into the Vase-Kite Conformational Control of Amphiphilic Molecular Grippers | 33 |
| 2.1 Introduction | 35 |
| 2.2 Langmuir Monolayers of Amphiphilic Calix[4]arene- and Resorcin[4]arene-Based Cavitands | 39 |
| 2.3 Vase-to-Kite Conversion at the Air-Water Interface | 46 |
| 2.3.1 pH-Induced Conformational Conversion at the Air-Water Interface | 46 |
| 2.3.2 <i>Langmuir</i> Films of Resorcin[4]arene Cavitand 11 on Various Ion-Containing Subphases | 48 |

| | | |
|------------|---|------------|
| 2.3.3 | Zn(II)-induced Conformational Control of Amphiphilic Cavitand 11 | 52 |
| 2.4 | Conformational Transitions of <i>Langmuir</i> Monolayers of Resorcin[4]arene-Based Cavitands bearing Polyethylene Glycol Chains at the Lower Rim | 55 |
| 2.5 | <i>Langmuir</i> Monolayers of Cavitands with Alkyl Chains at the Lower Rim | 59 |
| 2.6 | Conclusion | 60 |
| 3 | Fullerene-Ionophore Conjugates: Formation of Complexes with Metal Cations at the Air-Water Interface | 63 |
| 3.1 | Introduction | 64 |
| 3.1.1 | The Structure of [60]Fullerene | 64 |
| 3.1.2 | Electrochemical Properties of C ₆₀ | 66 |
| 3.1.3 | Spectroscopic Properties | 67 |
| 3.2 | Fullerene- and Crown Ether-containing <i>Langmuir</i> Films | 67 |
| 3.2.1 | Thin Film Fullerene-Based Materials | 67 |
| 3.2.2 | <i>Langmuir</i> Monolayers Containing Macrocyclic Ionophores | 73 |
| 3.3 | <i>Langmuir</i> Monolayers of Fullerene-Ionophore Conjugates 35 and 36 | 76 |
| 3.3.1 | <i>Langmuir</i> Monolayers of 35 and 36 on Pure Water and on 1M aq. LiCl, CaCl ₂ , NaCl, KCl, and CsCl as Subphases | 77 |
| 3.4 | Conclusion | 85 |
| 4 | <i>Langmuir–Blodgett</i> Multilayers of Porphyrin- and [60]Fullerene-Containing Derivatives: Spectroscopic Investigations | 87 |
| 4.1 | General account of Porphyrins | 88 |
| 4.2 | Thin Film of Porphyrin Derivatives | 90 |
| 4.3 | <i>Langmuir–Blodgett</i> Investigations of Porphyrin Derivatives | 94 |
| 4.3.1 | Porphyrin-Crown Ether Derivative 42 : <i>Langmuir</i> and <i>Langmuir–Blodgett</i> Films | 94 |
| 4.3.2 | Porphyrin-Crown Ether Derivative 43 : <i>Langmuir</i> and <i>Langmuir–Blodgett</i> Films | 101 |
| 4.3.2 | Porphyrin-Crown Ether-Fullerene Conjugate 44 : <i>Langmuir</i> and <i>Langmuir–Blodgett</i> Films | 106 |
| 4.4 | Conclusion | 110 |

| | | |
|------------|---|------------|
| 5 | Towards Novel Fullerene-porphyrin Architectures: Attempted Synthesis of Fullerene-sandwiching Macrocyclic Bis(Metallo Porphyrin) and Porphyrin-Crown Ether | 113 |
| 5.1 | Attempted Preparation of Porphyrin-containing Macrocycles | 116 |
| 5.1.1 | Synthesis of Porphyrin 48 | 116 |
| 5.1.2 | Toward the Synthesis of Macrocyclic Bis (Metallo Porphyrin) 58 | 117 |
| 5.1.3 | Toward the Synthesis of Macrocyclic Porphyrin-Crown Ether 61 | 118 |
| 5.2 | Conclusion | 122 |
| 6 | Experimental Part | 123 |
| 6.1 | General Instrumentation | 123 |
| 6.1.1 | Materials | 123 |
| 6.1.2 | Experimental Procedures | 124 |
| 6.2 | <i>Langmuir and Langmuir–Blodgett Films</i> | 132 |
| 6.2.1 | General Instrumentation | 132 |
| 6.2.2 | Experimental Procedures | 133 |
| 7 | Literature | 143 |

Abbreviations

| | |
|---------------------|---|
| Å | Angstrom (1 Å = 10 ⁻¹⁰ m) |
| <i>A</i> | area per molecule (Å ²) |
| AFM | atomic force microscopy |
| aq. | aqueous |
| 5'-AMP ⁻ | 5-adenosine monophosphate |
| BAC | 5,11,17,23-tetra-tert-butyl-25,27-bis(2-aminoethoxy)-21,28-dihydroxycalix[4]arene |
| BAM | <i>Brewster</i> angle microscope |
| B.p. | boiling point |
| <i>c</i> | concentration |
| <i>ca.</i> | <i>circa</i> |
| cal | calorie (1 cal = 4.814 J) |
| calc. | calculated |
| CAV | cavitand |
| °C | degree centigrade (0 °C = 273.15 K) |
| CCD | charge coupled device |
| cm | centimeter |
| conc. | concentrated |
| CT | charge-transfer |
| δ | chemical shift (NMR) |
| <i>d</i> | thickness |
| DCC | <i>N,N'</i> -dicyclohexylcarbodiimide |
| dL | deciliter |
| DMAP | <i>N,N</i> -dimethylaminopyridine |
| DMF | <i>N,N</i> -dimethylformamide |
| DNA | deoxyribonucleic acid |
| dppp | 1,3-bis(diphenylphosphino)propane |
| ε | extinction coefficient |
| <i>E</i> | energy |

Abbreviations

| | |
|----------------------|--|
| $E_{1/2}$ | half-wave potential |
| <i>e.g.</i> | <i>exempli gratia</i> (latin) – for example |
| ET | electron transfer |
| eV | electronvolt, 1 eV = 96.485 kJ mol ⁻¹ |
| Fc | ferrocene |
| Fc ⁺ | ferricinium |
| g | gram |
| γ | surface tension |
| 5'-GMP ²⁻ | 5-guanosine monophosphate |
| GOX | glucose oxidase |
| h | hour |
| HMO | <i>Hückel</i> molecular orbital |
| HOMO | highest occupied molecular orbital |
| <i>i.e.</i> | <i>id est</i> (latin) – that is to say |
| IPR | isolated pentagon rule |
| IR | infrared spectroscopy |
| ITO | indium-tin-oxide |
| J | joule |
| J | coupling constant (NMR) |
| K | <i>Kelvin</i> |
| Kcal | kilocalorie |
| λ | wavelength |
| λ_{\max} | longest wavelength maxima (UV-VIS) |
| L | liter |
| LC | liquid-condensed |
| LE | liquid-expanded |
| LB | <i>Langmuir-Blodgett</i> |
| LUMO | lowest unoccupied molecular orbital |
| m | meter |
| m | medium (IR), multiplet (NMR) |
| M | molarity (moles L ⁻¹) |
| M | metal |
| MALDI-TOF | matrix-assisted laser-desorption-ionization time-of-flight |

| | |
|------------------|---|
| Me | methyl |
| mg | milligram |
| mL | milliliter |
| mm | millimeter |
| mM | millimolar |
| mN | milliNewton |
| MΩ | megaohm |
| mol | mole |
| M.p. | melting point |
| MU | 11-mercaptoundecanol |
| MV ²⁺ | methyl viologen dication |
| MV ^{+•} | methyl viologen radical cation |
| mV | millivolt |
| M_W | molecular weight |
| μL | microliter |
| n | refractive index |
| N_A | <i>Avogadro's</i> number |
| nm | nanometer |
| NMR | nuclear magnetic resonance |
| ODA | <i>n</i> -octadecylamine |
| OSWV | <i>Osteryoung</i> square wave voltammetry |
| π | surface pressure (mN m ⁻¹) |
| π_c | collapse pressure (mN m ⁻¹) |
| P | porphyrin |
| P3DT | poly(3-dodecyl thiophene) |
| PEG 1000 | polyethylene glycol 1000 |
| PM3 | parameter model 3 |
| ppm | parts per million |
| PVNK | poly(<i>N</i> -vinyl carbazole) |
| q | quartet (NMR) |
| QCM | quartz crystal microbalance |
| RNA | ribonucleic acid |
| r.t. | room temperature |

Abbreviations

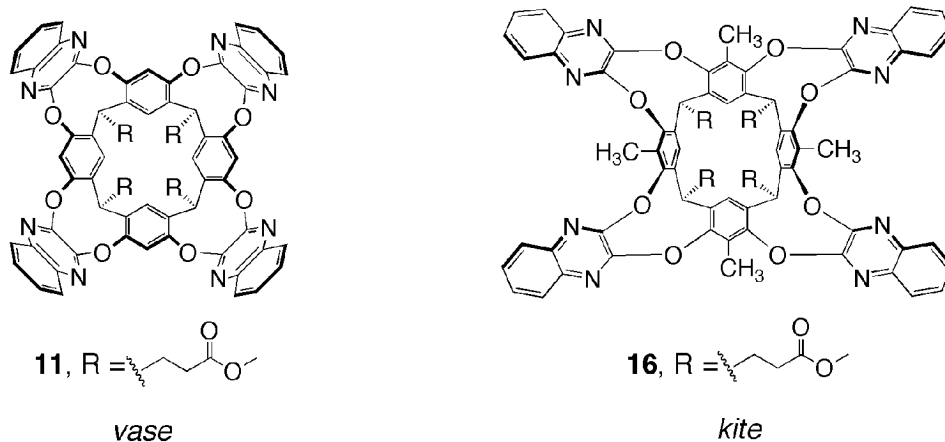
| | |
|------------|---|
| SA | stearic acid |
| SAM | self-assembly monolayer |
| SC-ISE | solid-contacted ion-selective electrode |
| STM | scanning tunneling microscopy |
| θ | angle of incidence |
| θ_A | wettability |
| θ_B | <i>Brewster</i> angle |
| Γ | surface coverage |
| t | triplet |
| TFA | trifluoroacetic acid |
| THF | tetrahydrofuran |
| TLC | thin layer chromatography |
| TR | transfer ratio |
| TMV | tobacco mosaic virus |
| UV | ultra-violet |
| V | volume |
| V | volt |
| VIS | visible |
| vs. | <i>versus</i> (latin) – against |
| VT | variable temperature |
| w | weak (IR) |

Abstract

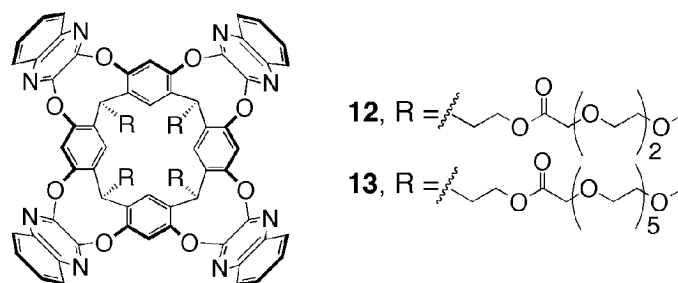
The *Langmuir* technique is one of the most common methods for preparing two-dimensional molecular assemblies. In this method, a solution of an amphiphilic compound in a low-boiling solvent, usually immiscible with water, is spread on a water subphase. After the solvent has evaporated, the amphiphilic molecules form a monolayer in which their hydrophilic heads interact with the water subphase and the hydrophobic tails are directed away from it. Compression of the monolayer on the water subphase leads to a reduction of the area available per molecule (A), thus causing an increase in surface pressure (π). The resulting π - A isotherm (surface pressure as a function of the molecular area at constant temperature) provides information on the molecular packing within the monolayer, the orientation of the headgroups, the molecular area requirement, and possible interactions with molecules or ions dissolved in the aqueous subphase. The monolayer formed at the air-water interface can be transferred onto a solid support (*Langmuir-Blodgett* deposition). Due to the ease in assembling amphiphiles into a variety of thin films with defined composition, structure, and thickness, the *Langmuir* and *Langmuir-Blodgett* (LB) techniques have allowed the development of novel functional materials by many scientists.

In the first part of *Chapter 1*, the reader is introduced to the concept of self-assembly along with its applications in the fields of self-assembled monolayers (SAMs) and molecular recognition. This section is concluded with a description of significant examples of self-assembled monolayers comprising resorcin[4]arene-based cavitands, fullerenes, and porphyrins. The second part of *Chapter 1* consists of a comprehensive description of the *Langmuir* and *Langmuir-Blodgett* techniques as well as of *Brewster* angle microscopy (BAM) as one of the most common methods to analyze the morphology of the *Langmuir* films formed at the air-water interface.

The discussion of the research carried out in the context of the present thesis starts with *Chapter 2*. After an introductory general account on the resorcin[4]arene-based cavitands, their conformational properties are discussed along with the discovery of pH-promoted *vase-kite* switching which we investigated at the air-water interface. Amphiphilic cavitand **11** and velcrand **16** which, at room temperature, prefer the *vase* and *kite* conformation, respectively, were spread on water to demonstrate that the *Langmuir* technique allows a distinction between the two geometries at the air-water interface.

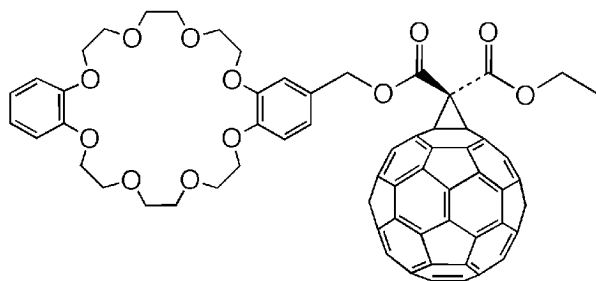
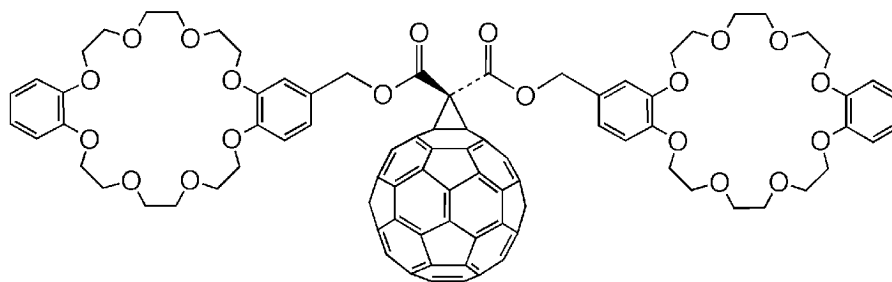


The molecular area requirement obtained by extrapolating the linear part of the π - A isotherm of cavitand **11** is 125 \AA^2 which well reproduces the theoretical value expected for the *vase* conformation (120 \AA^2). In case of cavitand **16**, the obtained value is 140 \AA^2 , about half of the area calculated for the *kite* conformation (290 \AA^2). This value suggests that **16** undergoes dimerization, leading to the formation of velcralexes at the air-water interface. The conformational switching was investigated by spreading cavitand **11** on a water subphase containing trifluoroacetic acid (TFA). Evidence for successful conformational control was obtained by variations in the limiting molecular area which increases (from 125 \AA^2 to 223 \AA^2) by increasing the concentration of TFA in the aqueous subphase. The spreading behavior of **11** was further investigated after addition of $\text{Zn}(\text{OAc})_2$ to the water subphase which led to the discovery of a new Zn(II)-promoted conformational switching. Molecular modeling calculation and $^1\text{H-NMR}$ spectroscopic investigations supported the formation of a stoichiometric *kite*-cavitand $\cdot 2 \text{ Zn}(\text{II})$ complex with each metal ion coordinating to two neighboring quinoxaline nitrogen atoms. The last part of *Chapter 2* describes investigations on the influence of the length of the polyethylene glycol chain on the monolayer packing of cavitands **12** and **13**.



In particular, cavitand **13** with five glycol units in each of the four hydrophilic “legs”, required a larger area per molecule at low pressure than cavitand **12**, having only two such units per “leg”. The different acyl groups also explain the behavior of monolayers in experiments with high concentrations: No phase transition was observed with cavitand **12**, at high concentration, whereas in the case of cavitand **13**, two transitions were detected. Five glycolic units better approximate the limit case of PEG2000+ (notation referred to a PEG polymer derivatized with a hydrophobic headgroup), the *Langmuir* films of which display both transitions.

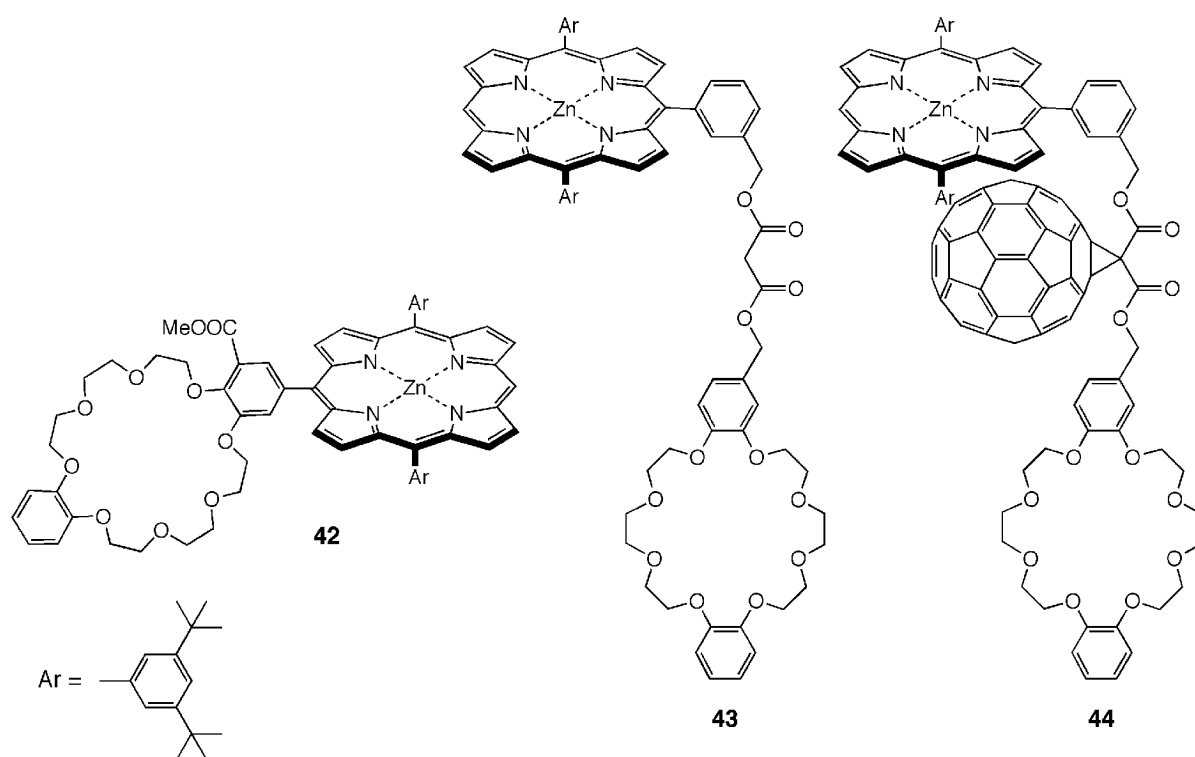
Chapter 3 starts with a general account of buckminsterfullerene and its main electronic and spectroscopic properties along with its incorporation into *Langmuir* monolayers. The second part of this *Chapter* is an investigation of the spreading behavior of fullerene-ionophore conjugates **35** and **36** on pure water and on aqueous subphases containing the metal ions Li^+ , Na^+ , K^+ , Cs^+ , and Ca^{2+} .

**35****36**

The presence of the dibenzo [24]crown-8 ether unit(s) in **35** and **36** leads to an improvement of the spreading behavior as compared to pristine C_{60} (60 \AA^2 (**35**) and 75 \AA^2 (**36**)). The areas per molecule are larger than in the case of unmodified buckminsterfullerene, even though they are still smaller than the theoretical value expected for the carbon cage (86 \AA^2). The limiting molecular areas increase on subphases containing alkali metal chlorides or

CaCl_2 , particularly in the cases of KCl and CsCl , due to the complexation of the cations by the crown ether moieties. The binding event leads to a conformational change of the crown ether, which adopts a more extended conformation and becomes more hydrophilic which provides a better anchoring on the subphase. The larger variation of the area per molecule observed upon addition of Cs^+ ions is due to the greater stability of the corresponding complex ($\log K = 3.78$ in MeOH).

In collaboration with *Dr. Jean-Louis Gallani (CNRS, Strasbourg)*, the spreading behavior of porphyrin-(dibenzo[24]crown-8) conjugates **42** and **43**, and of porphyrin-[60]fullerene-(dibenzo[24]crown-8) conjugate **44** was investigated in detailed *Langmuir* studies performed in order to investigate their spreading behavior (*Chapter 4*).



The three porphyrin derivatives show different behavior within the monolayers. In particular, conjugates **42** and **44** form more rigid monolayers than **43** and their spreading behavior is strongly affected by the presence of K^+ and Cs^+ ions in the water subphase. In the case of compound **42**, the isotherms show a phase transition corresponding to an orientational change of the porphyrin during the compression. At low pressure, the porphyrin unit of **42** lies horizontal on the water subphase and its area requirement becomes predominant when compared to the crown ether moiety. Under compression, the molecules

approach each other and the porphyrin-porphyrin stacking causes the tetrapyrrolic system to change orientation from parallel to normal with respect to the water surface. At higher pressure, the molecular area of the crown ether predominates and the complexation of metal ions becomes more important than in the case of derivative **43**. In fact, in conjugate **43**, the porphyrin does not dramatically change orientation and it stays nearly horizontal during the entire compression of the monolayer. It should be mentioned that the area occupied by a horizontal porphyrin ring is larger than the area of the crown ether both in the absence and in the presence of an alkali metal ion. Moreover, a flexible linker such as the malonate unit between the hydrophobic and the hydrophilic part of **43**, gives more degrees of freedom to the molecule and, consequently, the corresponding monolayers are less rigid than those of derivative **42**. The UV-VIS absorption spectra of LB multilayers of derivatives **42** show significant red-shifts of the *Soret* and *Q*-bands, confirming extensive porphyrin-porphyrin stacking. Conjugate **44** shows a strong influence of alkali ions in the water subphase on its spreading behavior, even if the porphyrin is locked atop the fullerene in horizontal, tangential position. The different behavior of **44** and **43** may be related to the fact that the fullerene moiety increases the hydrophobic character of the molecule. Therefore, the complexation of alkali metal ions by the crown ether moiety becomes important to reestablish a better balance between the hydrophobic and the hydrophilic part of **44**, thus leading to a better anchoring of the molecule on the aqueous subphase. An even more pronounced red-shift of the *Soret* and *Q*-bands was observed for conjugate **44** compared to **43** as consequence of the well-known attractive interactions between the fullerene moiety and the porphyrin. In accord with the low transfer ratios and the poor quality of the LB multilayers, the absorption intensity for all derivatives decreases with increasing numbers of depositions, showing that previously deposited molecules are lost in subsequent dipping cycles. Upon depositing further layers, no additional red-shifting of the *Soret* band was observed, suggesting that the exciton interactions are a consequence of intermolecular interactions occurring within the layers rather than between the layers.

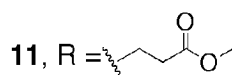
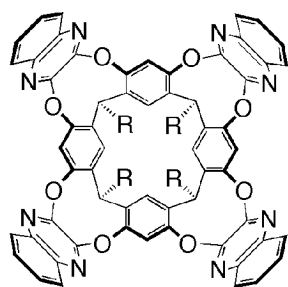
The last part of this thesis, *Chapter 5*, consists of a comprehensive descriptions of the attempts toward the synthesis of the [60]fullerene-sandwiching macrocyclic bis(metallo porphyrin) and porphyrin-crown ether.

Riassunto

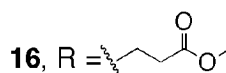
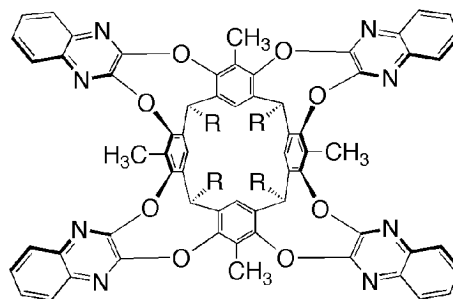
La tecnica *Langmuir* è uno dei metodi piú conosciuti per preparare aggregati molecolari bidimensionali. Nel suo *modus operandi*, una molecola anfifila sciolta in un solvente volatile e immiscibile con l'acqua è distribuita su una superficie acquosa. Dopo l'evaporazione del solvente, le molecole anfifile formano un film nel quale la loro parte idrofila interagisce con l'acqua e la testa idrofoba si dispone lontano dalla superficie acquosa. Una barriera mobile comprime lo strato di molecole provocando una riduzione dell'area molecolare disponibile (A) e un conseguente aumento della tensione superficiale (π). La curva della pressione in funzione della variazione dell'area per molecola è ricca di informazioni riguardanti la capacità delle molecole di impacchettarsi all'interno dello strato, la loro orientazione, la loro area e infine, le possibili interazioni con eventuali molecole o ioni dissolti nella fase acquosa. Il *Langmuir* film può essere trasferito dalla fase acquosa su un supporto solido (deposizione *Langmuir-Blodgett*). Grazie alla possibilità di formare film sottili caratterizzati da un elevato ordine, una controllata struttura e spessore, le due tecniche di *Langmuir* e *Langmuir-Blodgett* (LB) hanno attratto l'attenzione di un elevato numero di scienziati interessati allo sviluppo di nuovi materiali organici.

Nella prima parte del *Capitolo 1*, al lettore vengono presentati i concetti dell'aggregazione spontanea, e la loro applicazione nel campo del riconoscimento molecolare. Questo paragrafo si conclude con la descrizione di selezionati modelli di aggregati spontanei, costituiti da cavitandi, fullereni e porfirine. La seconda parte del *Capitolo 1* consiste in una approfondita descrizione di ambedue le tecniche di *Langmuir* e *Langmuir-Blodgett* e della microscopia dell'angolo di *Brewster*, considerata uno dei piú comuni metodi di analisi della morfologia degli strati molecolari formati all'interfaccia aria-acqua.

Il presente lavoro di ricerca inizia con il *Capitolo 2* che contiene, nella sua prima parte, una breve descrizione delle caratteristiche strutturali e delle proprietà chimiche di un gruppo di molecole denominate cavitandi. La scoperta di un equilibrio tra una conformazione chiusa (*vase*) rassomigliante ad un vaso e una aperta (*kite*) che ricorda un aquilone e della possibilità di regolare l'equilibrio attraverso variazioni di pH, ha suggerito lo studio del cambio conformazionale all'interfaccia aria-acqua. Quindi, due cavitandi anfifili **11** e **16**, i quali adagiano rispettivamente nella conformazione a vaso e ad aquilone, sono stati distribuiti sulla superficie dell'acqua con lo scopo di dimostrare che la tecnica *Langmuir* permette una distinzione delle due conformazioni.

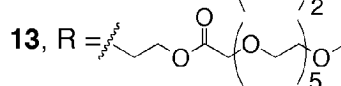
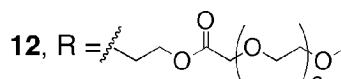


vase



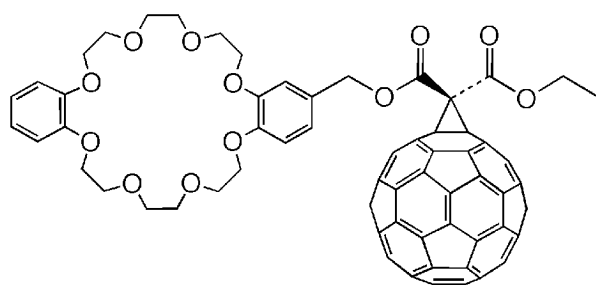
kite

L'area molecolare ottenuta dall'estrapolazione della parte lineare dell'isoterma π - A , è 125 \AA^2 per il cavitando **11**, la quale concorda perfettamente con il valore teorico corrispondente alla conformazione a vaso (120 \AA^2). Per il cavitando **16**, invece, il valore trovato di 140 \AA^2 che è circa la metà del valore predetto per la conformazione ad aquilone (290 \AA^2), suggerisce che la molecola è aggregata in dimeri, denominati velcraplessi. Alla luce di questi risultati, l'equilibrio conformazionale è stato studiato distribuendo il cavitando **11** sulla fase acquosa contenente acido trifluoro acetico (TFA). Il cambio di conformazione da vaso ad aquilone è stato evidenziato dalla variazione dell'area molecolare che aumenta (da 125 \AA^2 a 223 \AA^2) in seguito ad un aumento di acidità dell'acqua. L'ulteriore analisi dell'equilibrio conformazionale del cavitando **11**, su una fase acquosa contenente $\text{Zn}(\text{OAc})_2$, ha portato a scoprire che lo ione $\text{Zn}(\text{II})$ favorisce il cambio conformazionale dalla forma vaso alla forma aquilone. Studi spettroscopici ($^1\text{H-NMR}$) hanno confermato la formazione di un complesso 1 : 2 tra l'aquilone e lo ione $\text{Zn}(\text{II})$ nel quale il metallo coordina una coppia di atomi di azoto adiacenti. L'ultima parte del *Capitolo 2* presenta lo studio dell'influenza della lunghezza della catena di glicole polietilenico sul film molecolare formato dai cavitandi **12** e **13**.

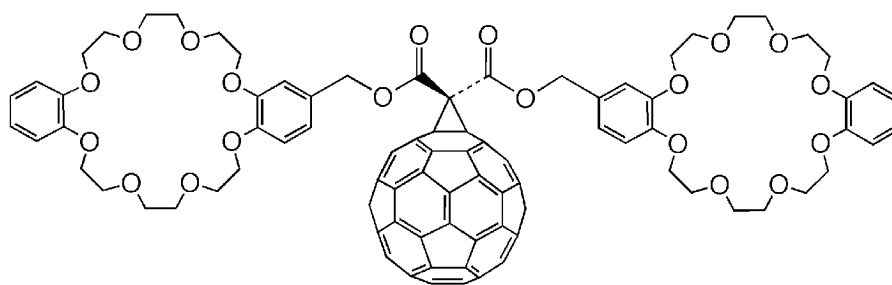


In particolare il cavitando **13**, contenente gruppi idrofili costituiti da cinque unità di glicole polietilenico, occupa a piccole tensioni superficiali, un'area molecolare più grande del cavitando **12** che ha solo due unità di glicole polietilenico. La differente lunghezza delle catene idrofile, spiega anche il comportamento dello strato molecolare ad elevate concentrazioni: l'isoterma del cavitando **12** non presenta nessuna transizione a più elevate concentrazioni, mentre l'isoterma del cavitando **13** presenta due transizioni a basse ed alte concentrazioni. Evidentemente catene con cinque unità di glicole polietilenico approssimano meglio sistemi tipo il PEG2000, per il quale entrambe le transizioni sono evidenti.

Il *Capitolo 3* inizia con un'introduzione sul fullerene, le sue principali proprietà elettroniche e spettroscopiche e la sua inclusione in strati molecolari di tipo *Langmuir*. La seconda parte di questo capitolo presenta, invece, uno studio sistematico del carattere anfifilo di due molecole **35** e **36**, costituite dal fullerene coniugato con uno ionoforo, sulla fase acquosa nella quale sono solubilizzati diversi ioni, come Li^+ , Na^+ , K^+ , Cs^+ e Ca^{2+}



35

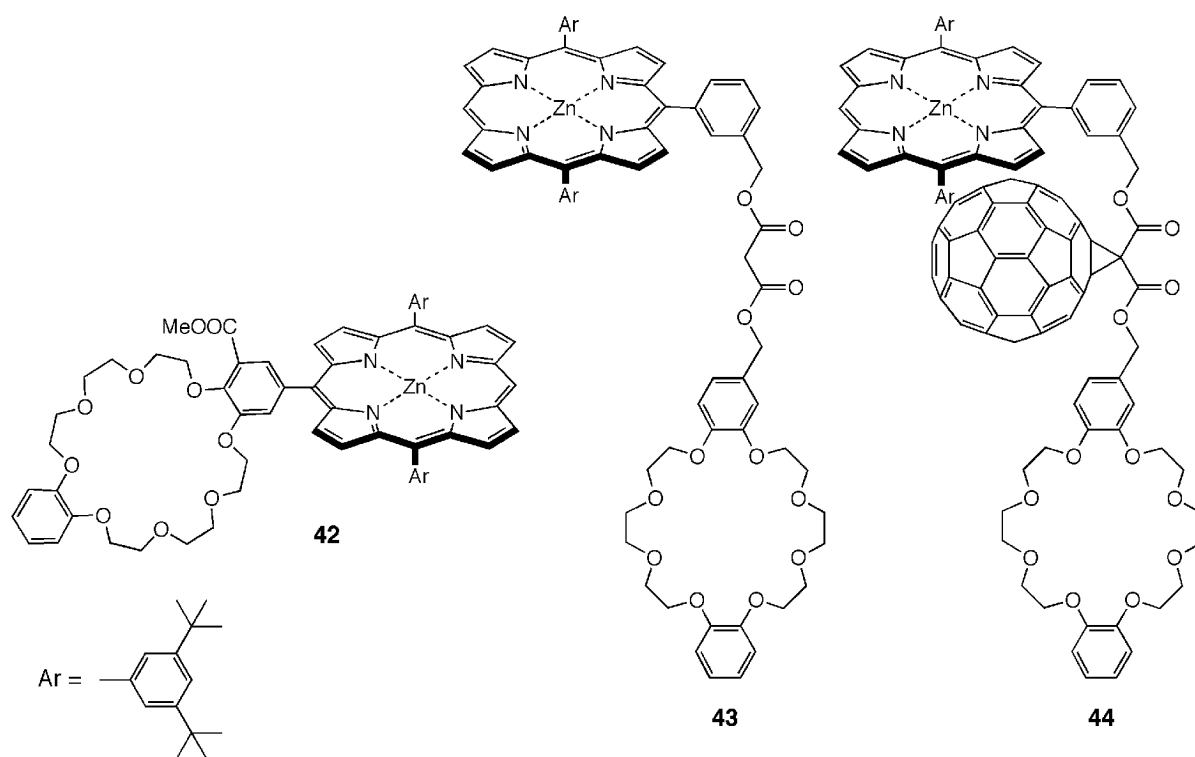


36

La presenza dell'etere corona in entrambi i derivati del fullerene **35** e **36** influenza fortemente le loro caratteristiche anfifile rispetto al fullerene puro. Infatti, l'area molecolare aumenta per entrambi i derivati (60 \AA^2 (**35**) and 75 \AA^2 (**36**)) rispetto al puro C_{60} , sebbene sia ancora piccola rispetto al valore teorico della sfera del fullerene (86 \AA^2). L'area per molecola aumenta sensibilmente nel caso di KCl and CsCl solubilizzati nella fase acquosa, grazie alla

formazione di un complesso tra i due ioni e l'etere corona. Questa complessazione favorisce un cambio conformazionale della corona dell'etere, il quale adotta una piú estesa conformazione e diventa piú idrofilo, ancorando meglio la molecola alla superficie acquosa. La maggiore variazione dell'area molecolare osservata nel caso dello ione Cs^+ è legata alla maggiore stabilità del suo complesso ($\log K = 3.78$ in MeOH).

In collaborazione con il *Dr. Jean-Louis Gallani (CNRS, Strasbourg)* sono stati dettagliatamente studiati gli strati molecolari formati da porfirine-etere corona coniugati **42** e **43** e porfirina-etere corona-fullerene coniugato **44** all'interfaccia aria-acqua con lo scopo di analizzare le loro caratteristiche anfifile.



Tutti e tre i derivati delle porfirine mostrano un diverso comportamento all'interno dello strato molecolare. In particolare, i derivati **42** e **44** formano film piú rigidi rispetto al derivato **43** e il loro carattere anfifilo è fortemente influenzato dalla presenza degli ioni K^+ e Cs^+ nella fase acquosa. Nel caso del composto **42**, le isoterme mostrano una fase di transizione correlata alla diversa orientazione dell'anello porfirinico. Per il derivato **42**, a basse pressioni, la porfirina si dispone parallela alla superficie dell'acqua e la sua area molecolare risulta predominare sull'area occupata dall'etere corona. In seguito alla compressione, l'anello della porfirina cambia la sua orientazione da orizzontale a verticale.

Ad alte pressioni l'area molecolare dell'etere corona risulta predominante e la complessazione con gli ioni alcalini diventa piú significativa rispetto al derivato **43**. Infatti in **43**, la porfirina non cambia drammaticamente la sua orientazione e rimane circa orizzontale durante tutta la compressione del film molecolare. Deve essere menzionato che l'area occupata da una porfirina disposta orizzontale è piú grande dell'area dell'etere corona, in assenza e presenza di metallic alcalini. La presenza del malonato come ponte tra le parti idrofoba e idrofila conferisce piú gradi di libertà alla molecola con conseguente formazione di film molecolari meno rigidi, rispetto al derivato **42**. Gli spettri di assorbimento della molecola **42**, mostrano uno spostamento verso il rosso, della banda di *Soret* e delle bande *Q*, confermando un forte *stacking* tra gli anelli porfirinici. Il composto **44** mostra una forte influenza degli ioni alcalini sulle sue caratteristiche anfifile, anche se la porfirina è bloccata dal fullerene in posizione orizzontale. Il diverso comportamento dei composti **44** e **43** può essere legato alla presenza del fullerene che aumenta il carattere idrofobo della molecola. Quindi la complessazione con metalli alcalini diventa importante per ristabilire un migliore bilanciamento tra la parte idrofoba e idrofila di **44**. Lo spettro di assorbimento del derivato **44** mostra uno spostato verso il rosso delle bande *Q* e di *Soret* piú evidente del composto **44**, a causa di un aggiuntiva interazione fra l'anello porfirinico e il fullerene. In accordo con il basso indice di trasferimento e di conseguenza la bassa qualità dei multistrati molecolari (*LB multilayers*), l'intensità di assorbimento per tutti e tre i derivati della porfirina diminuisce all'aumentare del numero di strati, mostrando che le molecole precedentemente depositate sono perse nei diversi cicli di deposizione. Dal momento che lo spostamento delle bande *Q* e di *Soret* è indipendente dal numero di strati depositati, possiamo ipotizzare che le interazioni intermolecolari avvengano all'interno dello stesso strato piuttosto che tra strati contigui.

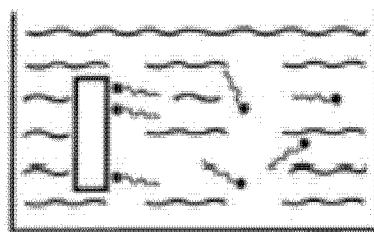
L'ultima parte di questo lavoro di tesi, *il Capitolo 5*, consiste nella descrizione dei tentativi fatti per sintetizzare due molecole nelle quali il fullerene è incapsulato tra due porfirine e tra una porfirina e un etere corona.

1 Introduction

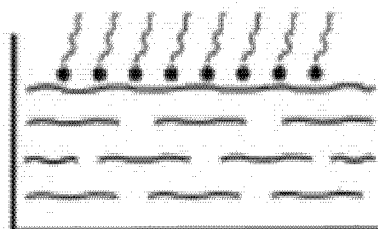
1.1 Organic Thin Films

Recently organic thin films have attracted considerable attention for the possibility of transferring the optical, electronic, optoelectronic, and chemical properties of the adsorbed molecules to a liquid or solid surface. *Figure 1.1* is a schematic representation of the main techniques for the preparation of thin films. The distinguishing feature of these methods is self-organization; the molecules or ions adjust their own positions to reach a thermodynamic minimum.

1. Self-Assembled Monolayers



2. *Langmuir* Films of amphiphilic molecules at liquid/air interface



3. *Langmuir-Blodgett* Films of *Langmuir* films transferred onto solid support

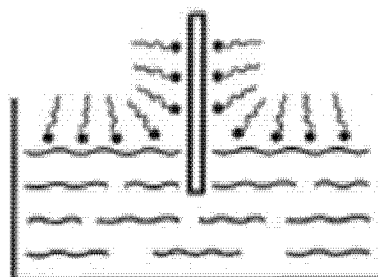


Figure 1.1 Overview of various preparation routes of crystalline organic thin films as reported by Schreiber [1].

1. Self-Assembled monolayers (SAMs) consist of two-dimensional films formed by the spontaneous adsorption of molecules onto a surface [1-3].
2. *Langmuir* films consist of amphiphilic molecules spread at a liquid/gas interface such as a water/air boundary [2].
3. *Langmuir-Blodgett* (LB) films are prepared by transferring *Langmuir* films to a solid substrate [2].

Because this thesis deals with the preparation of *Langmuir* and *Langmuir-Blodgett* monolayers, the following Sections give an overview of self-assembly including SAMs as well as *Langmuir* and LB films.

1.2 General Account of Self-Assembly

Self-assembly may be defined as the spontaneous formation of complex defined structures from pre-designed building blocks. In biology, particularly important examples of self-assembly are: The formation of the double-stranded DNA [4] by association of two complementary chains of DNA, the formation of the hemoglobin by self-association of four subunits, and the formation of cellular membranes from phospholipids self-assembled in bilayers [4]. The concept of self-assembly originated with studies on the tobacco mosaic virus (TMV) and the enzyme ribonuclease. TMV is a virus consisting of a single type of protein arranged in a helical fashion and encapsulating the viral RNA (*Figure 1.2*) [3, 5], carrier of the genetic information.

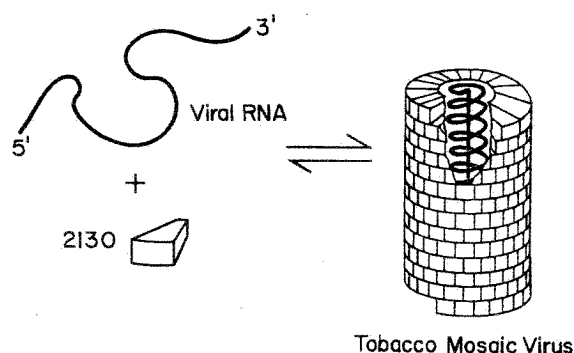


Figure 1.2 Self-assembly of the tobacco mosaic virus (TMV) as reported by *Lindsey* [3]. The protein subunits predetermine the helical shape. All information for assembly is contained within the constituting components.

The virus is composed of 2130 identical protein subunits, each with 158 amino acid residues, that form the viral protein coat around a single stretch of RNA. Experiments by *Fraenkel-Conrat* and *Williams* [6] demonstrated the TMV could be dissociated into its component parts and reassembled in vitro to reform the infectious virus particle. All the information necessary to faithfully assemble the virus is built into the constituent parts, which associate spontaneously with high specificity, control, and efficiency. In general, biological self-assembly occurs under thermodynamic control allowing error checking¹ and high fidelity and under the principle of positive cooperativity².

Self-assembling motifs are not restricted to biology. Molecular crystals are self-organizing structures. Micelles and bilayers composed of detergents and lipids display a rich variety of self-organizing behaviors. Molecular recognition and supramolecular chemistry are active fields of research concerned with noncovalent self-assembly, such as self-assembled monolayers [7-9].

1.2.1 Self-Assembled Monolayers (SAMs)

Self-assembled monolayers (SAMs) are ordered molecular assemblies that form spontaneously by chemisorption of functionalized molecules with a specific affinity of their headgroups for the substrate [2]. They represent the most common class of non-biological systems involving self-assembly. They are robust, relatively stable, and capable of providing versatility, at both the molecular and the bulk levels. They offer a vehicle for investigating specific interactions at interfaces, and stability of two-dimensional structures.

The constituting self-assembling surfactant molecules consist of three parts (*Figure 1.3*): The first part is the headgroup. It causes the exothermic process of chemisorption on the surface of the substrate. The energies associated with the process are on the order of tens of kcal/mol (*e.g.* 40-45 kcal/mol for thiolates on gold). The second part is the alkyl chain. It is responsible for the intermolecular distance, the molecular orientation, and the degree of order in the film. The energies associated with the *van der Waals* interaction between alkyl chains are on the order of 10 kcal/mol (*e.g.* 14 kcal/mol for octanethiol [10]). The third part is a tail group that constitutes the outer surface of the film. The principal driving force for the formation of these films is a specific interaction between the headgroup and the substrate

¹ Malformed or defective subunits are excluded since they don't have the required set of bonding sites for the self-assembly.

² The monomeric building blocks self-assemble to give the final aggregate but not intermediate structures.

surface. Provided these interactions are strong, SAMs form stable films. Depending on the structure of the molecules, these films can be disordered or well-packed (*Figure 1.3*). The degree of order in monolayers is a product of many factors, including geometric aspects, electrostatic, and dipole-dipole interactions within the monolayers.

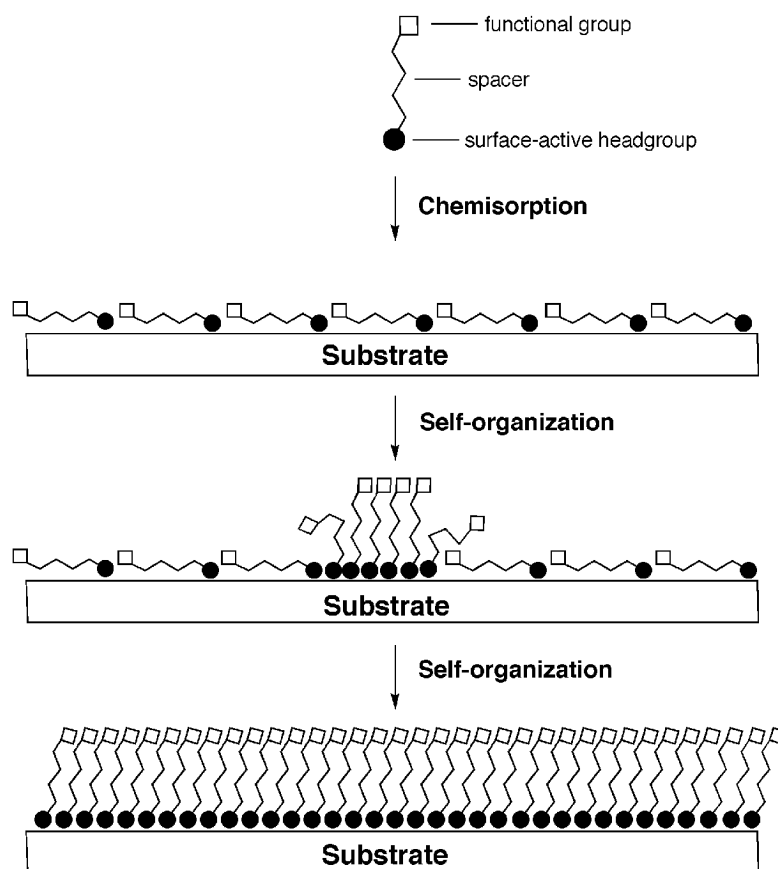


Figure 1.3 Schematic illustration of the formation of SAMs of surfactant molecules on a solid surface.

The most widely studied systems have been SAMs formed by chemisorption of alkanethiols on gold. In 1983, *Nuzzo* and *Allara* [9] showed that dialkyl disulfides (RS-SR) form close-packed and well-ordered monolayers due to strong Au-S bonds between sulfur atoms and gold (~ 44 kcal/mol) [11]. This experimental finding, together with the considerations that gold is an inert metal, and does not form stable superficial oxide layers, opened new and interesting possibilities from an application point of view. Thin films containing functional molecules are of high interest, owing to the possibility of transferring the properties of the adsorbed molecules to a solid or liquid surface. In this context, some selected examples of

SAMs containing functional molecules such as resorcin[4]arenes, fullerenes, and porphyrins are described.

1.2.1.1 Self-Assembled Monolayers of Cavitands

Over the last two decades, different synthetic receptors for the binding and recognition of neutral molecules were prepared. Among these, cavitands are a class of very interesting and versatile molecular receptors. The complexation properties of cavitands were extensively studied in the solid state [12, 13], in solution [14-16], and in the gas phase [17-19]. Nevertheless, there are relatively few examples that describe the transfer of self-assembled monolayers from the solution [20-22] phase to surfaces. *Dalcanale* and coworkers reported self-assembly of coordination cages **3** and **4** from cavitand molecules **1** and **2** with $[\text{Pd}(\text{dppp})(\text{CF}_3\text{SO}_3)_2]^3$ both in solution and immobilized on gold surface (*Figure 1.4*).

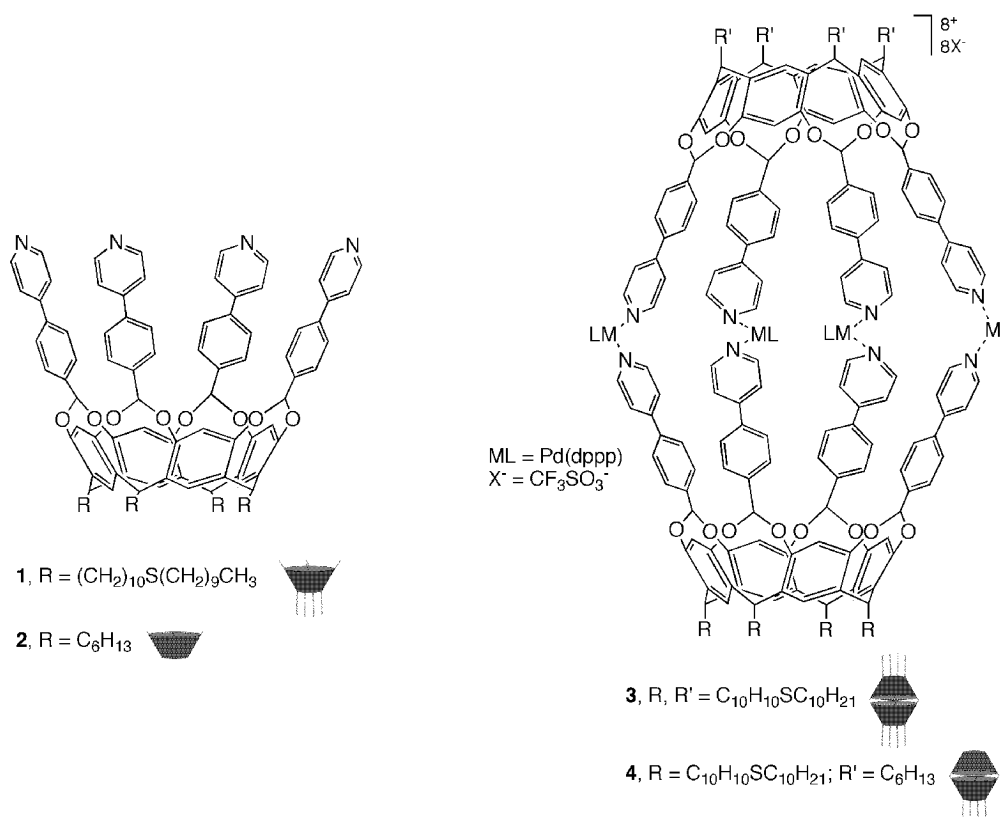


Figure 1.4 Molecular structures of cavitands **1** and **2** and, self-assembled cages **3** and **4**, as reported by *Dalcanale et al.* [23].

³ dppp = 1,3-bis(diphenylphosphino)propane

Figure 1.5 shows two different approaches for the formation of SAMs on Au(111), the first leading to homo-assembled, the second to hetero-assembled cages. The approach is the direct incorporation of homo-“dimer” **3** (Figure 1.4), preformed in acetone, into the SAM of 11-mercaptoundecanol (MU) on gold. After extensive rinsing, the sample surface was analyzed by atomic force microscopy (AFM) to measure the height of **3** (5.27 nm), as schematically described in Figure 1.5 a. The second approach is the incorporation of hetero-“dimer” **4** (Figure 1.4) starting by insertion of cavitand **1** (Figure 1.4) into the MU SAM (Figure 1.5 b) followed by cage self-assembly with the cavitand **2** (Figure 1.5 c). After extensive rinsing, the monolayers were analyzed by AFM. The observed heights of cavitand **1** (1.87 nm) and cage **4** (3.96 nm) are consistent with the dimensions obtained by X-ray analysis.

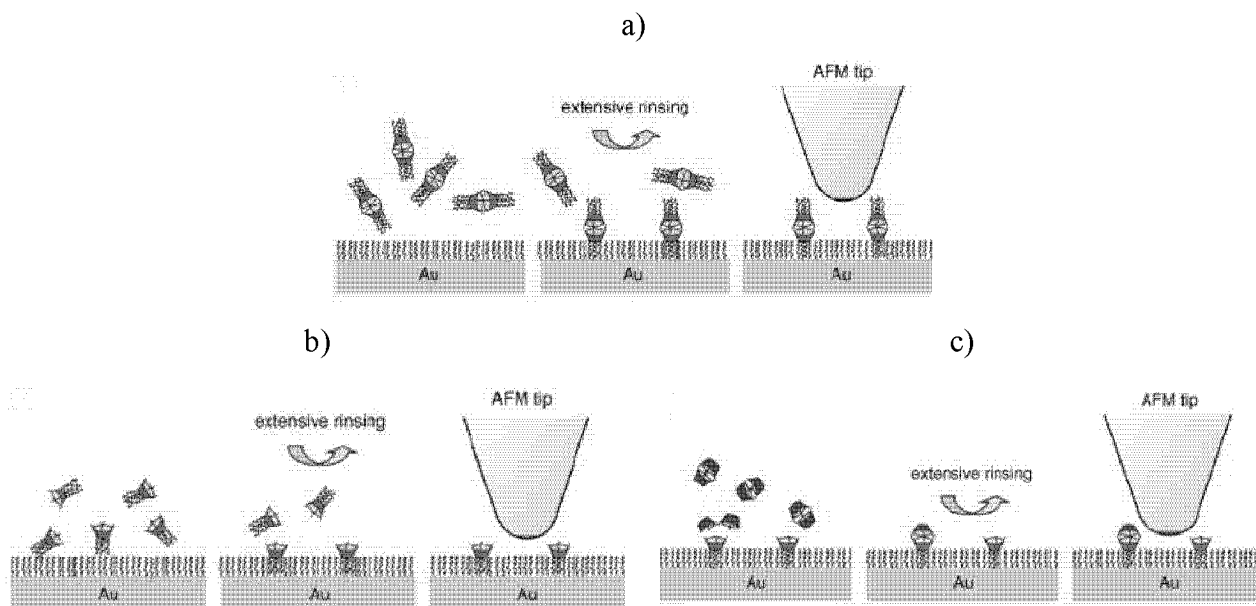


Figure 1.5 Schematic representation of the insertion of a) homo-“dimeric” cages **3** and b) hetero-“dimeric” cages **4** in a MU SAM, as reported by *Dalcanale* and co-workers [23].

The reversibility of the above-described metal-directed self-assembly can be exploited to reversibly encapsulate guests in the surface-confined cages. Also, the formation of hetero-“dimeric” cages from cavitands with different substituents at the lower rim and cavities of different molecular dimensions in the upper part allows for new applications in the preparation of nanoscale electronic devices. Cavitands with cavities of various sizes can be used as chemical sensors. Schematically, a chemical sensor consists of both a sensing

material, interacting with the species present in the environment, and a transducer which converts the chemical informations into measurable data [24]. *Dalcanale* and co-workers studied the formation of SAMs on gold with cavitand **5** (Figure 1.6) carrying four dialkyl sulfide chains as a model system.

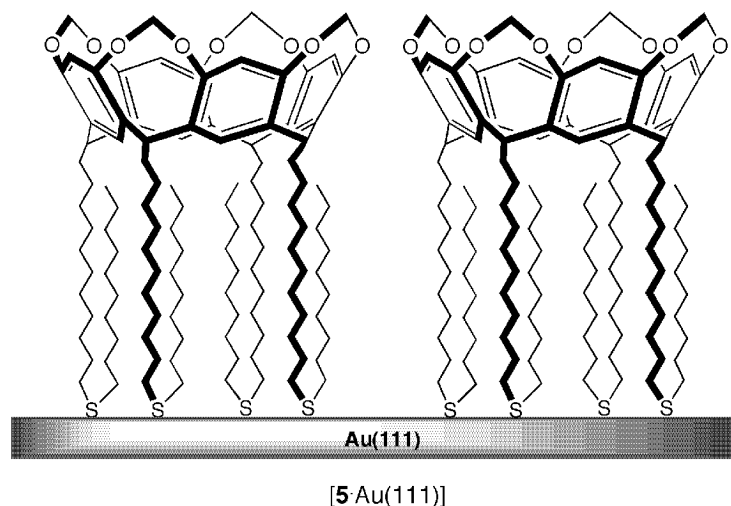


Figure 1.6 SAM of MeCav-thioether **5** reported by *Dalcanale* and coworkers [25].

They observed the response of cavitand **5** to different analytes by exposing the SAM to a range of vapor concentrations between 0 and 2000 ppm. Cavitand **5** showed good selectivity for three analytes, namely acetonitrile, nitromethane, and perchloroethylene as opposed to *n*-hexane, benzene, and toluene. In the case of *n*-hexane, the insignificant response of the sensor is related to *van der Waals* interactions between the alkyl tails of the cavitand and *n*-hexane which may be preferred over interactions with the cavities [25]. The low affinity for benzene molecules is presumably due to their inability to form host-guest complexes within the small cavities. Recently, it was observed that aromatic vapors can be selectively complexed with cavitands that have deeper cavities [26]. In particular, the same authors observed that SAMs of a quinoxaline-bridged cavitand with its 8.3 Å deep cavity and its closed *vase* conformation preferentially responds to aromatic vapors. Apart from the possibility to change the dimension of the cavity, the conformation of the cavity can also be switched between *vase* and *kite* forms (see Chapter 2), as studied extensively by *Cram et al.* [27]. *Diederich* and co-workers investigated the potential of this system as molecular gripper for the manipulation of single molecules. The cavitand in the *vase* conformation should be able to capture a molecule and hold it during translocation, releasing it upon changing to the *kite* conformation. The authors prepared self-assembled monolayers of resorcinarene-based

cavitand **6** (Figure 1.7) on gold. These monolayers showed a lower wettability⁴ ($\theta_a(\text{H}_2\text{O}) = 97^\circ$) than those observed for simple alkanethiols terminated with methyl groups ($\theta_a(\text{H}_2\text{O}) = 111\text{--}114^\circ$ [29]), because of the more hydrophilic character of the exposed cavitand moieties (Figure 1.7).

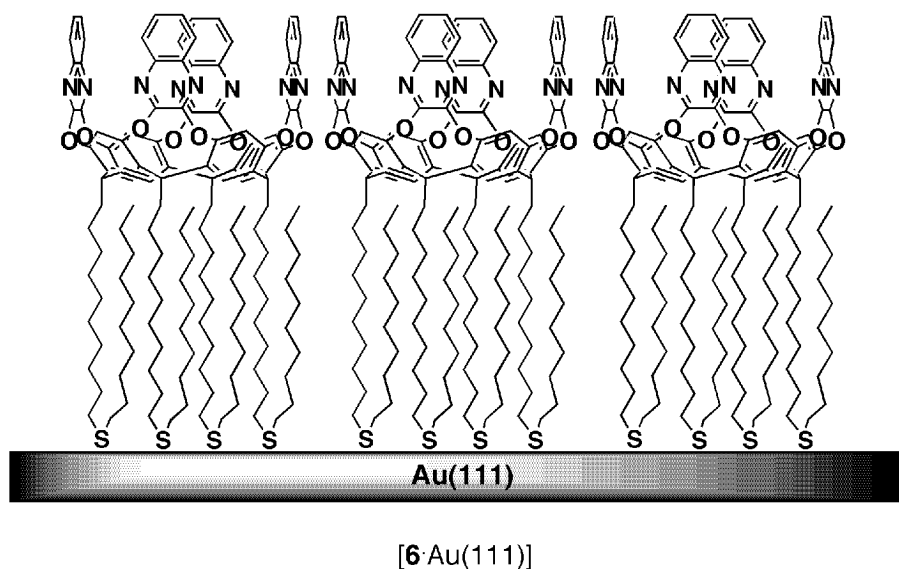


Figure 1.7 Schematic representation of a SAM of resorcinarene-based cavitand **6** in the *vase* conformation.

The characterization of this monolayer by scanning tunneling microscopy (STM) showed a well-ordered monolayer and suggested that the cavitand is present in the *vase* conformation [30].

1.2.1.2 Self-Assembled Monolayers of Fullerenes and of Fullerene Derivatives

Self-assembled monolayers of C_{60} and its derivatives have become a field of intensive investigations [31–34] because of the interesting optical and electrochemical behavior of the carbon sphere [33, 35–40]. *Diederich, Pretsch*, and co-workers prepared a gold electrode

⁴ The wetting contact angle or wettability (θ) is measured by placing a small drop of a liquid (water or hexadecane) on the horizontal substrate and measuring the angle subtended by the edge of the drop and the substrate. Depending on the polarity of the surface and the liquid, the droplet may spread on the horizontal substrate assuming different shapes and consequently different contact angles which provide information about the polarity of the outer surface of the SAM (static experiment), as well as the packing of the monolayer (dynamic experiment). $\theta_a(\text{H}_2\text{O})$ is the contact angle formed by a drop of water on the horizontal substrate [2, 28].

modified with redox-active SAM of a fullerene-alkanethiol conjugate **7** [41] (*Figure 1.8*). This work resulted in the fabrication of a solid-contacted ion-selective electrode (SC-ISEs) [42, 43].

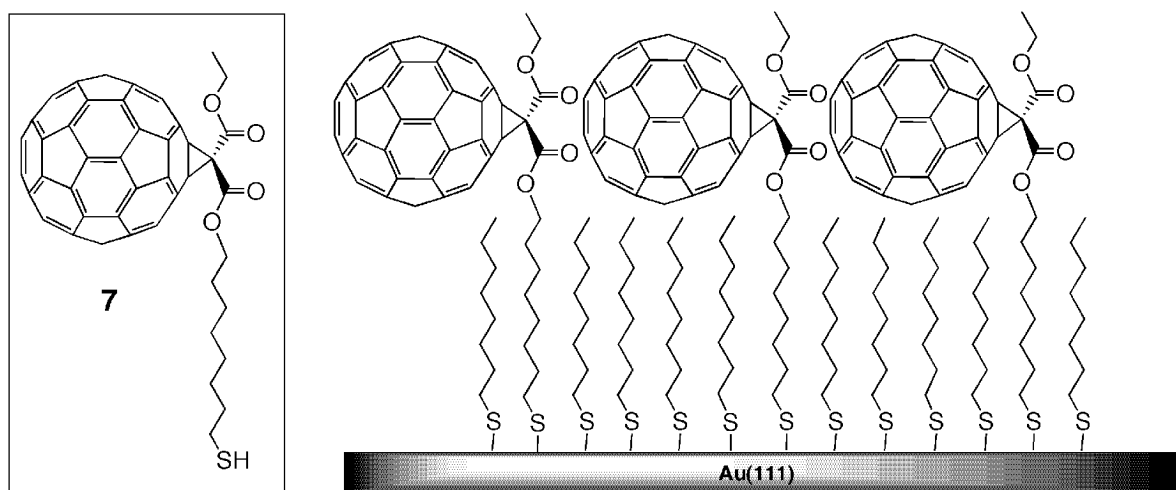


Figure 1.8 Schematic representation of mixed SAMs of C₆₀-derivative **7** and *n*-octanethiol on gold, as reported by *Diederich, Pretsch, et al.* [41-43].

The monolayer was characterized by cyclic voltammetry, ellipsometry, contact angle, and IR measurements. Since C₆₀ represents a bulky tail group, no dense packing of the molecule in the aliphatic regions of the SAM structure can be expected. Then, to increase the stability and the structural order of the SAM formed by **7**, a mixed monolayer obtained through incorporation of *n*-octanethiol molecules in the pre-formed SAM (*Figure 1.8*) was formed. Contact angle measurements and cyclic voltammetry with the mixed monolayer indicated that *n*-octanethiol molecules not only filled the uncovered hydrophilic Au surface, leading to an enhancement of the packing density, but also replaced in part the electroactive components. The surface coverage in **7** was reduced from $3.9 \times 10^{-10} \text{ mol cm}^{-2}$ (homogeneous SAM) to $0.8 \times 10^{-10} \text{ mol cm}^{-2}$ (mixed monolayer). This reduction had, however, no effect on the response of the SC-ISEs [43]. Cyclic voltammetry measurements exhibited a reversible one-electron reduction wave ($E_{1/2} = -680 \text{ mV vs. Ag/AgCl}$) which was ascribed to the first fullerene-centered reduction, corresponding to the reported values for SAMs of C₆₀ on gold [33, 44, 45]. The second reduction was not observed, probably due to a retro-Bingel reaction which results in the removal of the fullerene from the surface of the electrode. However, when the system is more stable electrochemically than fullerene

derivative **7**, the second reduction wave is not as noticeable when the monolayer fully covers the electrode surface. *Mirkin et al.* reported that the coverage-dependent electrochemical responses of the fullerene-derived thiol are attributed to the relative amounts of free volume available within the film [34]. When the monolayer undergoes sequential reductions, only the portion that can incorporate charge-compensating ions will be electrochemically active. As to the second reduction, the space available to counterions is generally reduced significantly after the first reduction, thus leading to a reduction of the current. Consequently, the presence of bulky groups in SAMs should favor the formation of interstitial holes within the monolayer and lead to sufficient free space for charge-compensating ions in electrochemical experiments. According to these experimental findings, *Fox* and co-workers [46] prepared a self-assembled monolayer of fullerene derivative **8** (Figure 1.9).

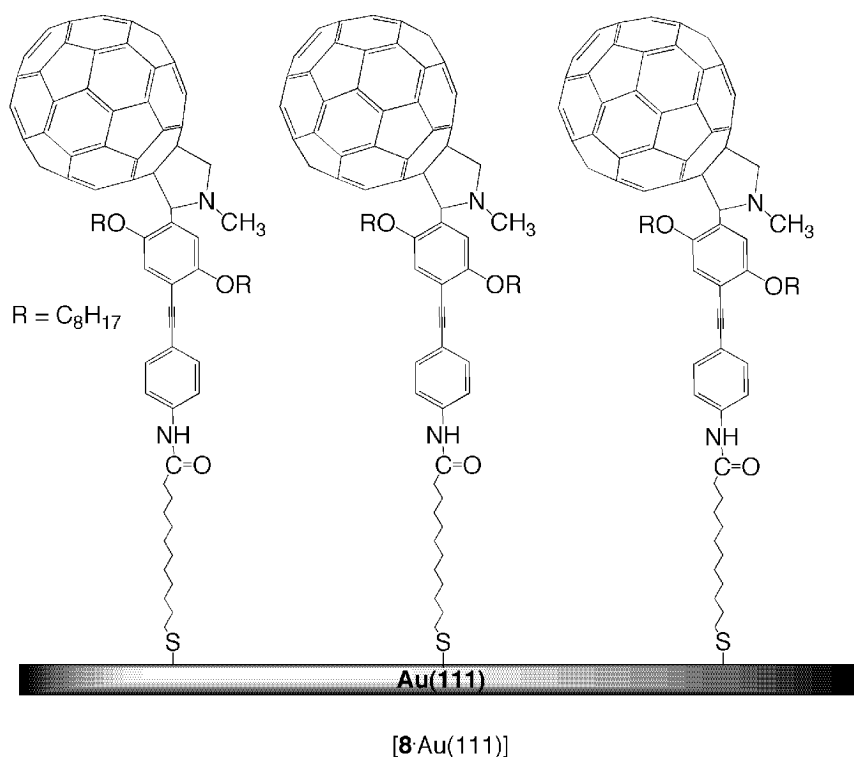


Figure 1.9 SAM of C₆₀-derivative **8** bearing a thiol binding group suitable for adsorption on Au(111), as reported by *Fox et al.* [46].

The presence of alkoxy chains on the aromatic rings produced a low-density monolayer as suggested by the measured surface coverage ($\Gamma \sim 0.991 \times 10^{-10}$ mol cm⁻²). Consequently, there is sufficient free space within the monolayer to incorporate enough charge-

compensating ions to satisfy the requirements for fullerene dianion formation upon electrochemical reduction of the film. Cyclic voltammetric measurements showed two well-resolved reversible peaks ($E^0_1 = -0.65$ V, $E^0_2 = -1.04$ V; vs. Ag/AgCl) for the first and second fullerene-centered one-electron reductions [46]. Alternatively, a molecular recognition event has been used to prepare a self-assembled fullerene-containing monolayer on Au(111).

Echegoyen and co-workers reported the first example of a monolayer of a crown ether-fullerene conjugate by taking advantage of the ammonium ion-crown ether interaction (*Figure 1.10*) [47]. The applied strategy involves the formation of a thiolated SAM terminating in ammonium groups, followed by secondary self-assembly of a monolayer of a fullerene-derived crown ether which is driven by the complexation of the latter by the ammonium ions [48]. This specific interaction was confirmed by desorption experiments that showed the fully reversible nature of the self-assembly process. The determination of the surface coverage, was determined by *Osteryoung* square wave voltammetry (OSWV) to 1.4×10^{-10} mol cm $^{-2}$ which is close to the experimental value for well packed monolayers of C $_{60}$ ($\sim 1.9 \times 10^{-10}$ mol cm $^{-2}$) [49].

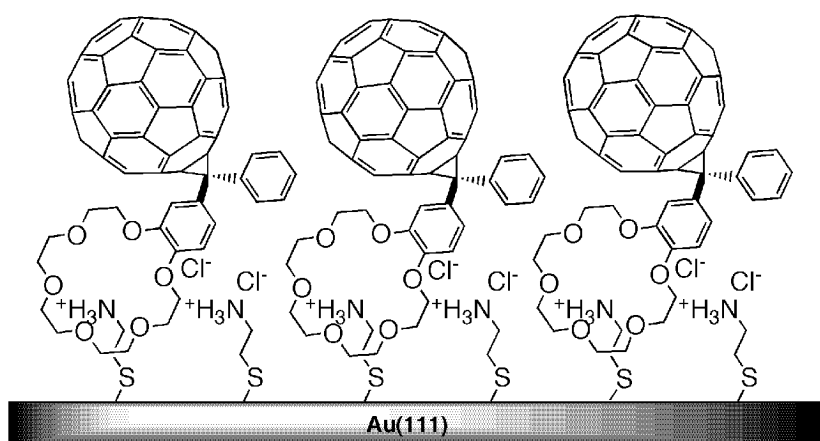


Figure 1.10 Schematic representation of SAMs of a crown ether-fullerene conjugate as reported by *Echegoyen et al.* [47].

1.2.1.3 Self-Assembled Porphyrin Monolayers

Construction of a very efficient system for artificial photosynthesis is one of the most important goals in the field of modern functional materials. In this context, the covalent derivatization of SAMs by attachment of functional molecules has been pursued to construct well-organized molecular assemblies containing photo- and electroactive units on gold surfaces. A variety of examples using ferrocenes [50, 51], azobenzenes [52, 53], porphyrins

[54-56], and fullerenes [33, 57-59] have been published. *Uosaki* and co-workers very efficiently generated a photocurrent induced by visible light at a gold electrode modified by a SAM depicted in *Figure 1.11*.

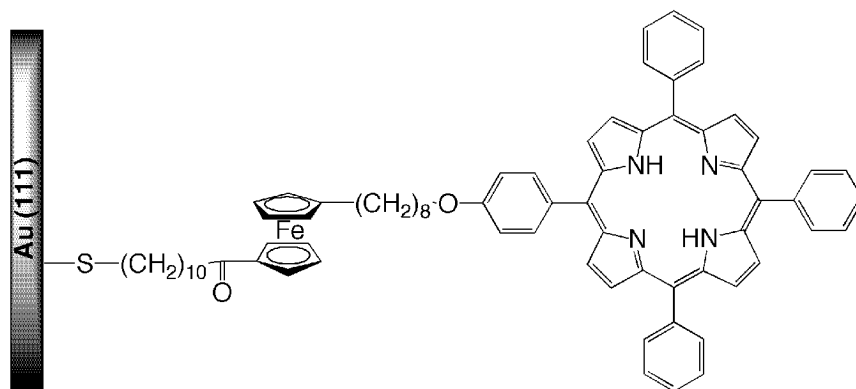


Figure 1.11 SAM of porphyrin derivative PC₈FcC₁₁SH.

The attached functional molecule includes porphyrin, ferrocene, and thiol units as photoactive, electron-transporting/relaying, and surface-binding groups, respectively (*Figure 1.11*) [60]. According to the underlying idea, *Uosaki et al.* prepared a SAM with a photoactive (S) and an electron-relay group (R) attached to a metal electrode (M). This system is a good candidate to mimic the photosynthesis of natural systems when immersed in a solution containing an electron acceptor (A), such as methyl viologen (MV), the redox potential of which is much more negative than that of the relay (*Figure 1.12*). Since the electrode potential is more negative than the redox potential of the ferrocene moiety, the photoexcited electron of the porphyrin was transferred to the electron acceptor, the methyl viologen dication (MV²⁺) which was reduced to the radical cation MV^{+•}. Then, the electron transfer from the electrode to the vacant HOMO of the porphyrin took place via the ferrocene group (*Figure 1.12*). The reverse electron transfer from the excited porphyrin to the gold electrode was prevented because of the large distance between the two moieties [60].

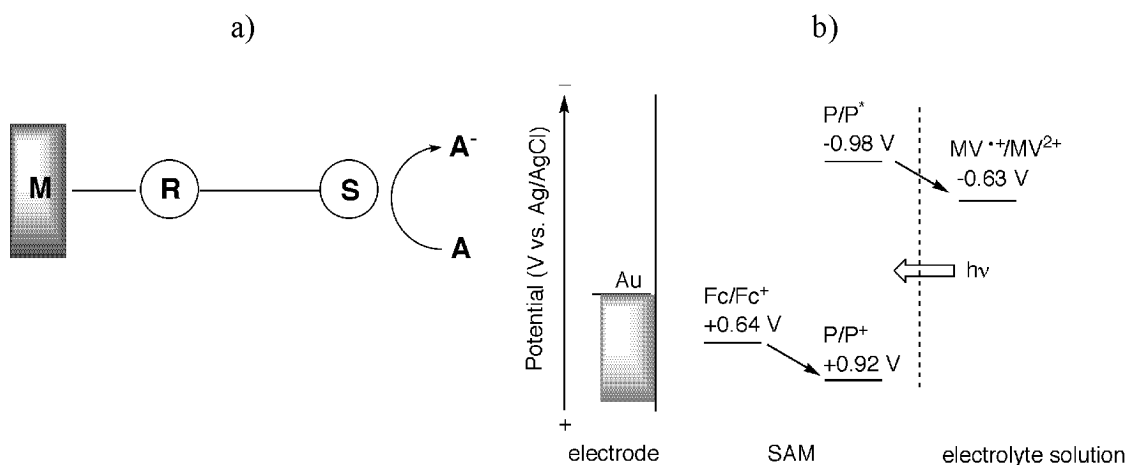


Figure 1.12 a) SAM containing a photoactive (S), an electron relay (R), and an electrolyte solution containing an electron acceptor (A). b) Energy diagram for the $\text{PC}_8\text{FcC}_{11}\text{SH}$ -modified gold electrode. Fc, Fc^+ , P, P^+ , and P^* are ferrocene, ferricinium cation, porphyrin, oxidized state of porphyrin, and excited state of porphyrin, respectively, as reported by *Uosaki et al.* [60].

In the area of chemical sensors, porphyrins represent very attractive molecules [61, 62]. They are able to reversibly bind a large number of chemical compounds, thus mimicking some biological activity, *e.g.* that of hemoglobin [63]. Porphyrins are stable compounds that can coordinate to different metals, allowing the preparation of a wide range of sensors with different selectivities. In this context, *Paollesse et al.* prepared a SAM of mercaptoporphyrins **9** and **10** (*Figure 1.13*) for quartz crystal microbalance (QCM) chemical sensors⁵ [65]. They observed that the two porphyrins showed different orientations in the SAM, depending on the number of sulfide groups at the peripheral positions of the macrocycles (*Figure 1.13*). Porphyrin **9** with one SH group is oriented perpendicular to the gold surface, an orientation which is assisted by possible π - π interactions between macrocycles [54]. Porphyrin **10** with four SH groups is oriented parallel to the gold surface [66].

⁵ The quartz crystal microbalance sensor is based on interaction between analyte and thin organic layers coated on the surface of quartz crystal. The resulting mass changes on the sensor surface produce variation in the fundamental frequency of the oscillating quartz disc [24, 64].

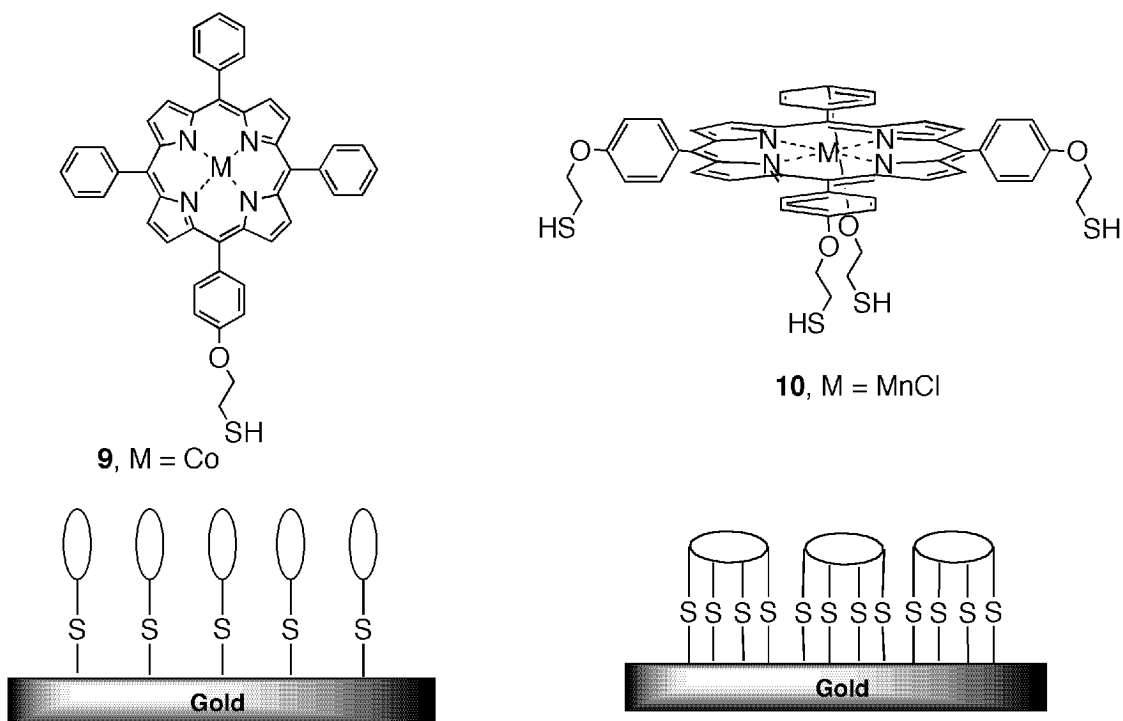


Figure 1.13 Structures of mercaptoporphyrins **9** and **10**, and their orientation in self-assembled monolayers on gold.

Because of these distinct porphyrin arrangements, **9** and **10** showed different selectivities toward analytes such as ethanol, triethylamine, and ethylenediamine. In case of ethanol and triethylamine, the QCM frequency response to the analyte is approximately two times higher with porphyrin **10** as compared to **9** because the orientation of **10** inhibits all π - π interactions, thus allowing a stronger binding of the analytes. On the other hand, the orientation of **10** hampers the binding of bidentate ligands such as ethylenediamine, showing a lower sensitivity (factor ~ 1.8) than **9** for this analyte.

In the context of chemical sensors, *Cahen et al.* [67] reported a new type of electronic sensor able to detect NO at concentrations down to $1 \mu\text{M}$ in physiological solution ($\text{pH} = 7.4$) at room temperature. This device is constituted of hemin molecules self-assembled together with benzoic acid on a GaAs surface to which they are attached through two carboxylate groups (*Figure 1.14*). Due to the presence of only two binding groups, the iron-porphyrins are oriented perpendicular to the surface. The sensor MOCSER (molecular controlled semiconductor resistor) consists of a transducer (GaAs/Al,Ga)As, a conducting n-GaAs layer, and an ultra-thin insulating layer covering the conducting layer [68]. The 1 : 1 mixed monolayer (hemin/benzoic acid) is adsorbed on the surface of n-GaAs substrate.

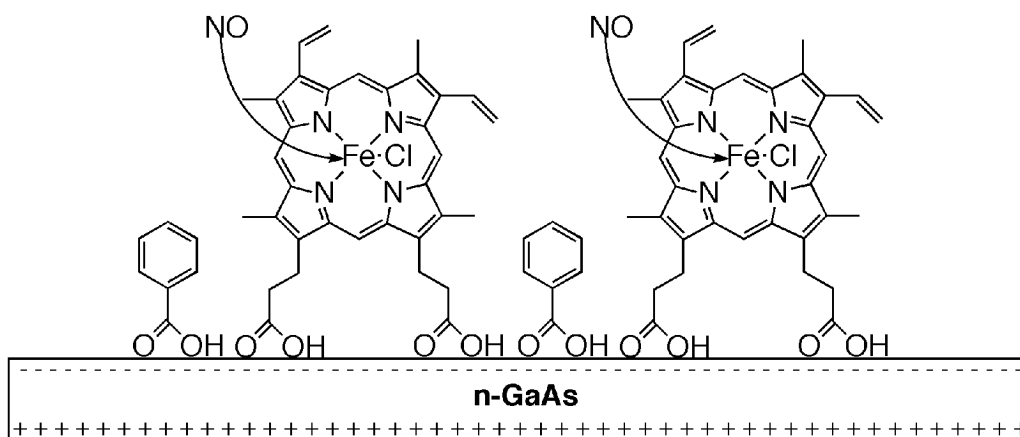


Figure 1.14 Binding of NO to a layer of hemin/benzoic acid molecules on n-GaAs surface, as reported by Cahen *et al.* [67].

This sensor works in a such way that when molecules or ions of the analyte bind the receptor sites of the molecules, the current through the device changes. In particular, upon injection of the NO-releasing solution the current rapidly increases and saturates in less than about 10 min. The device with a pure hemin monolayer adsorbed, also responds to NO, but the signal is smaller than with 1 : 1 mixed monolayer. This indicates that addition of benzoic acid spacers enhances the NO binding rate to the hemin, probably because they prevent the porphyrin-porphyrin interactions [69].

1.3 *Langmuir* and *Langmuir–Blodgett* Films

1.3.1 The History of *Langmuir* and *Langmuir–Blodgett* Films

Historically the study of monomolecular films began in the eighteenth century with an astute observation of *Benjamin Franklin*, an American politician, during his visit to England [70] where he carried out simple experiments spreading a small quantity of oil on a pond in Clapham [71]. Later on, Rayleigh estimated that the films of oil were between 10 and 20 Å thick, very close to the thickness of monomolecular film of fatty acids.

Extract of a Letter to Doctor BROWNRIEGG. from
Doctor FRANKLIN.

London, Nov. 7, 1773.

At length being at CLAPHAM where there is, on the common, a large pond, which I observed to be one day very rough with the wind, I fetched out a cruet of oil, and dropt a little of it on the water. I saw it spread itself with surprizing swiftness upon the surface; but the effect of smoothing the waves was not produced; for I had applied it first on the leeward side of the pond, where the waves were largest, and the wind drove my oil back upon the shore. I then went to the windward side, where they began to form; and there the oil, though not more than a tea spoonful, produced an instant calm over a space several yards square, which spread amazingly, and extended itself gradually till it reached the lee side, making all that quarter of the pond, perhaps half an acre, as smooth as a looking-glass.

In these experiments, one circumstance struck me with particular surprize. This was the sudden, wide, and forcible spreading of a drop of oil on the face of the water, which I do not know that any body has hitherto considered. If a drop of oil is put on a polished marble table, or on a looking-glass that lies horizontally; the drop remains in its place, spreading very little. But when put on water it spreads instantly many feet round, becoming so thin as to produce the prismatic colours, for a considerable space, and beyond them so much thinner as to be invisible, except in its effect of smoothing the waves at a much greater distance. It seems as if a mutual repulsion between its particles took place as soon as it touched the water, and a repulsion so strong as to act on other bodies swimming on the surface, as straws, leaves, chips, &c. forcing them to recede every way from the drop, as from a center, leaving a large clear space. The quantity of this force, and the distance to which it will operate, I have not yet ascertained; but I think it a curious enquiry, and I wish to understand whence it arises.

Figure 1.15 Part of Benjamin Franklin's original paper [71].

Modern investigations of molecular films began with the experiments of *Agnes Pockels*. By the time she wrote a famous letter to *Lord Rayleigh* [72], she had invented many of the techniques which are now standard "tools of the trade". She described her design of a rectangular water basin filled with water to the brim, with a strip of metal (tin) laid across it, just in contact with the water. Thus, by moving the strip, she could vary the area of the water surface. In this way she studied the variation in the surface tension of an oil-contaminated water surface [72]. Finally, in 1917, *Irving Langmuir* developed a number of new techniques including the surface film balance. In this device, a movable float separates a clean water surface from the area covered by a thin film; the deflection of the float provides a direct measure of the forces involved [73-75]. A schematic diagram of the *Langmuir's* surface film balance is shown in *Figure 1.16* [74].

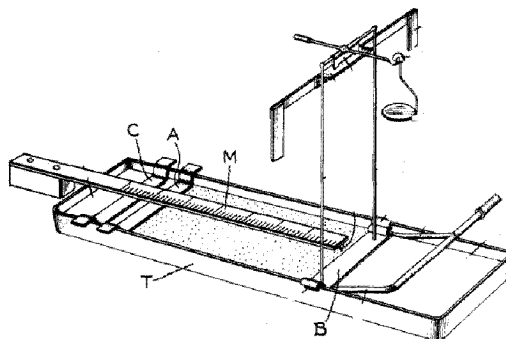


Figure 1.16 *Langmuir's* original film balance [74]. A, B, and C are paper strips; M is a meter stick, and T is the trough.

Langmuir confirmed that films of fatty acids on water have the thickness of a single molecule (monolayer) and he also concluded that these molecules are orientated with their polar functional groups immersed in the water surface and the long non-polar hydrocarbon chain directed nearly perpendicularly to the water subphase [74]. *Langmuir* studied the properties of monolayers of a long-chain carboxylic acid at the air-water interface and observed that the surface density of these molecules is independent of the length of the fatty acid chain. In 1919, *Blodgett*, under *Langmuir*'s guidance, succeeded in producing the first multilayer films on a solid support [76-78], which are now referred to as *Langmuir-Blodgett* (LB) films. These films are distinct from *Langmuir* films, a term reserved for a floating monolayer. After this brief historical introduction, the *Langmuir* and *Langmuir-Blodgett* techniques, together with analytical methods used to characterize organic thin films, are discussed in the following *Sections*.

1.3.2 *Langmuir* Monolayer Technique

Certain organic molecules will orient themselves at the interface between a gaseous and a liquid phase in such a way as to minimize their free energy [79-81]. The resulting film is one molecule in thickness and it is commonly called a monomolecular layer or simply a monolayer. Most monolayer materials are applied to the water surface by first dissolving them in suitable solvent. This solvent should be capable of dispersing the molecules of the film-forming material at the air-water interface and then evaporating completely to avoid film contamination. Usually the spreading solvents should be volatile, immiscible with water, and have a boiling point ranging between 40 and 80 °C. When the solution is applied to the water surface, spreading takes place until the surface pressure has risen to an equilibrium value. This equilibrium spreading pressure corresponds to the spontaneously generated pressure when the bulk solid is placed in contact with the water surface. A comparison may be drawn with the vapor pressure of a bulk solid. An equilibrium vapor pressure exists for the solid in presence of its vapor. If this vapor pressure is exceeded, *i.e.* the vapor becomes supersaturated, deposition onto the solid surface will occur. Analogously, if the surface pressure is greater than the equilibrium spreading pressure, small droplets or lenses will form on the water subphase. The quantity of amphiphile that needs to be spread on the water subphase to form a stable, fully covered monolayer is given by equation 1.1:

$$c = (A_m \times M_w) / V \times A_0 \times N_A \quad (1.1)$$

where c is the concentration of the spreading solution (g mL^{-1}), A_m the theoretical molecular area (nm^2), M_w the molecular weight (g/mol), V the volume of the spreading solution (mL), A_0 the area of the *Langmuir* trough occupied by water (nm^2), and N_A *Avogadro's* number (mol^{-1}).

In a typical *Langmuir* experiment, a dilute solution of an amphiphilic molecule such as stearic acid in a volatile solvent is spread drop by drop on the water subphase. The monolayer spreads spontaneously over the clean water surface to cover the available area of the trough. One or more movable teflon barriers placed across the trough serve to vary the area of the monolayer. As the solvent evaporates, a monolayer is formed as dictated by the amphiphilic nature of the molecules. In case of stearic acid, the headgroups ($-\text{CO}_2\text{H}$) are immersed in the water and the tail groups ($\text{C}_{17}\text{H}_{35}$) remain outside. When the distance between the stearic acid molecules is large, their intermolecular interactions are small and the monolayer has relatively little effect on the surface tension of the water. When the compression of the monolayer by the barrier system starts, the molecules of the amphiphile begin to repulse each other. This two-dimensional analog of the pressure of a gas is called surface pressure π and is given by equation 1.2,

$$\pi = \gamma_0 - \gamma \quad (1.2)$$

where γ_0 is the surface tension of the pure liquid and γ the surface tension of the film-covered surface. The most common method to monitor the variation of the surface pressure is the *Wilhelmy* balance technique which consists of a thin plate, usually glass, quartz, mica, or platinum, suspended in such a way as to cross the gas/liquid interface. The forces acting on the plate are related to gravity and surface tension. The spreading of amphiphiles on the water subphase affects the surface tension and, consequently, the force acting on the plate. The resulting variations are recorded as a plot of surface pressure vs. water surface area available per molecule. Since the measurements are usually carried out at constant temperature, the resulting plot is known as *pressure–area* isotherm. The isotherm is recorded by compressing the molecules at the air-water interface until a close-packed monolayer is reached (*Figure 1.17*).



Figure 1.17 Monolayer of stearic acid on a water surface: a) expanded, b) partly compressed, and c) close-packed.

The shape of the isotherm is characteristic of the molecule forming the film and, hence, it provides a two-dimensional “fingerprint”. It can provide valuable information on the stability of the monolayer at the water-air interface, the reorientation of molecules in the two-dimensional system, phase transitions, and conformational transformations. The *pressure–area* isotherm usually consists of three distinct regions [82] shown in Figure 1.18 as G, L, and S. In the low pressure region (G) the molecules behave as a two-dimensional gas; they are far enough apart on the water surface to undergo only weak interactions with their neighbors (Figure 1.17 a).

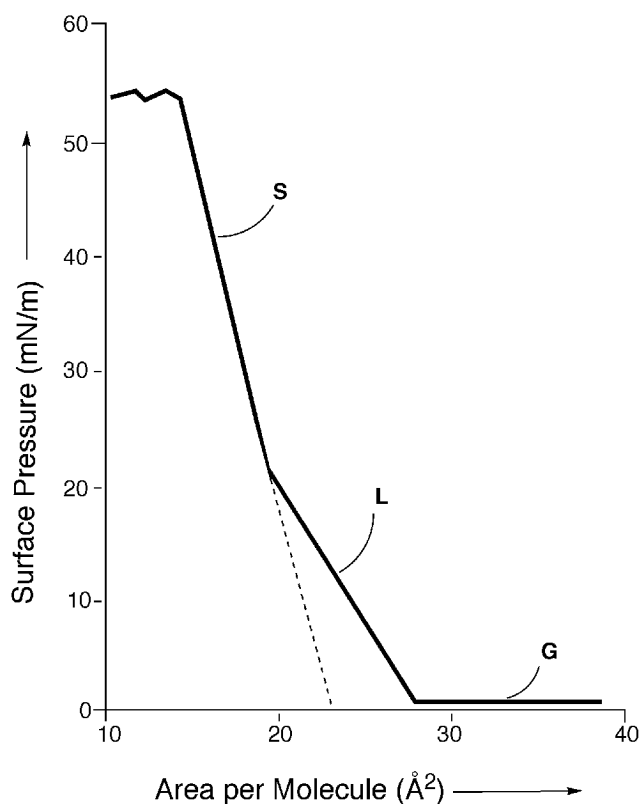


Figure 1.18 Surface pressure (π) vs. area per molecule (\AA^2) for stearic acid as reported by Miñones *et al.* [83]. G = gas phase, L = liquid phase, and S = solid phase.

For an ideal two-dimensional gaseous phase, the molecules should have negligible size compared to the interface area and, thus, should obey equation 1.3 for an ideal two-dimensional gas:

$$\pi A = kT \quad (1.3)$$

where π is the surface pressure (mN m^{-1}), A the area per molecule (nm^2), k is a constant of the gas ($8.3143 \text{ J mol}^{-1} \text{ K}^{-1}$), and T is the temperature (K).

As the surface area of the monolayer is reduced from its initial value, there is a gradual increase of surface pressure which corresponds to a phase transition. In the “liquid” state (L), generally called *expanded* monolayer phase, the hydrocarbon chains, which were originally distributed near the water subphase (*Figure 1.17 a*), are lifting away (*Figure 1.17 b*), assuming a more regular orientation with their polar groups in contact with the subphase. In the expanded phase, the area per molecule varies considerably with the surface pressure. There is no apparent relation between the observed molecular area and the dimensions of the constituent molecules. As the molecular area is progressively reduced, the intermolecular distance between the molecules decreases, leading to an increase in surface pressure, and condensed phases may appear. The inflection point observed at $\sim 20 \text{ mN m}^{-1}$ for stearic acid (see isotherm in *Figure 1.18*) represents the transition to an ordered solid-like arrangement of the two-dimensional array of molecules. In this condensed monolayer state (S), the molecules are closely packed and oriented with the hydrocarbon chains pointing away from the water surface (*Figure 1.17 c*). If this portion of the isotherm is extrapolated to zero surface pressure (dotted line in *Figure 1.18*), the intercept gives the area per molecule that would be expected for the hypothetical state of a close-packed layer at zero surface pressure. This value of $\sim 22 \text{ \AA}$ (*n*-alkanoic acid) [83-85] is close to that occupied by a stearic acid molecule in a single crystal, thus confirming the interpretation of a compact film as two-dimensional solid. The monolayer can be further compressed to values that are considerably higher than the equilibrium spreading pressure. The surface pressure continues to increase with decreasing surface area until a maximum is reached and the area of the monolayer decreases if the pressure is kept constant, or the pressure drops if the film is held at constant area. This point is referred to as *collapse*. The collapse pressure π_c is reached when the film irretrievably loses its monomolecular form. The forces exerted on the monolayer become too

strong for confinement in two dimensions, and molecules are ejected out of the monolayer, as illustrated in *Figure 1.19*.

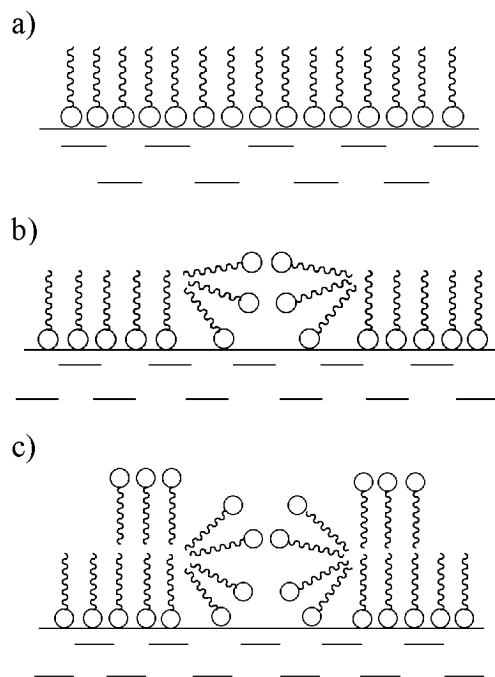


Figure 1.19 Schematic representation of the monolayer at: a) $\pi < \pi_c$, b) $\pi = \pi_c$, and c) $\pi > \pi_c$. π = surface pressure and π_c = collapse pressure.

In case of stearic acid the collapse of the monolayer is due to the formation of disordered multilayers (*Figure 1.19 c*) [86-88].

1.3.3 Film Deposition: *Langmuir–Blodgett* Technique

The *Langmuir–Blodgett* (LB) technique, first introduced by *Langmuir* and extensively applied by *Blodgett* [76, 78, 89, 90], involves the vertical movement of a solid support (glass, quartz, silicon) through the monolayer/air interface (*Figure 1.20*) [91, 92]. The surface pressure value that gives best *Langmuir–Blodgett* depositions depends on the nature of the monolayer. In general, organic thin films are transferred at the surface pressure corresponding to the “solid” phase, *i.e.* 20-40 mN m⁻¹ in the case of fatty acids. As the film is removed from the water surface, the surface pressure decreases, due to the smaller number of molecules remaining at the air-water interface.

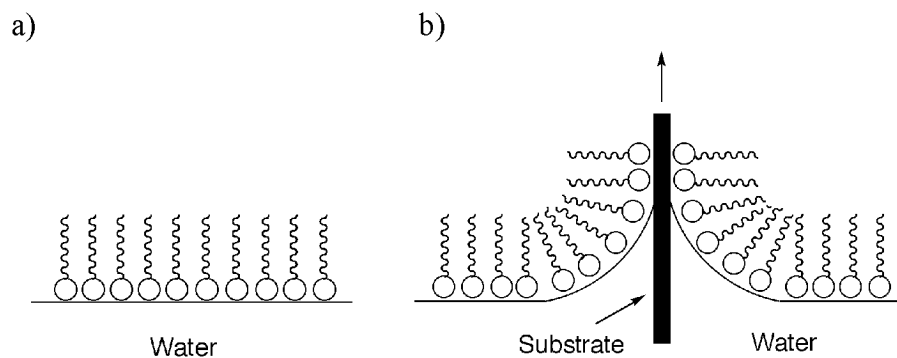


Figure 1.20 Schematic representation of the *Langmuir–Blodgett* technique. a) Firstly, a *Langmuir* film is formed at the air-water interphase, and b) secondly a solid substrate is passed through the interface to form a LB film on its surface [93].

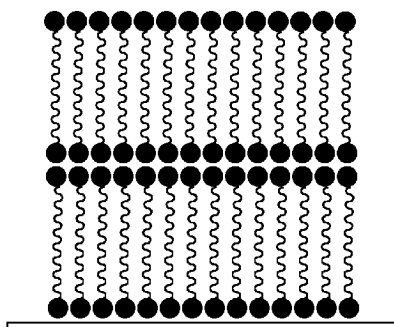
Because the transfer process and the quality of LB films are dependent on the surface pressure applied during the deposition, the pressure is maintained constant by moving the barrier to reduce the area available to the amphiphiles [93, 94]. The rate at which a slide can be withdrawn from the water phase depends partly on the rate at which the liquid film drains off the monolayer/slide interface and partly on dynamic properties of the monolayer on the water subphase. A highly viscous monolayer will be unable to adjust itself to maintain a homogeneous film close to a rapidly moving substrate, leading to unsatisfactory deposition [95, 96]. The deposition of the monolayer can occur during emersion from or immersion into the water surface of the slide, depending on the hydrophilic or hydrophobic character of the solid support. If the used slide has a hydrophilic surface, the transfer of the monolayer will occur during the emersion. Then, the hydrophilic headgroups are turned toward the hydrophilic surface of the slide, leading to a hydrophobic surface of the LB film. On the other hand, if the substrate is hydrophobic, the deposition of the thin film will occur during the immersion, and the hydrophobic alkyl chains will interact with the surface, and the slide becomes hydrophilic. With each additional layer transferred from the air/water interface onto the solid support, the latter changes its character from hydrophobic to hydrophilic. If the deposition starts with a hydrophilic substrate, the slide becomes hydrophobic after the first deposition and the second monolayer will be transferred during the immersion [2]. This process, in which layers are deposited each time the substrate moves across the phase boundary, is known as Y-type deposition [76] (*Figure 1.21 a*). As a result, the interactions between adjacent monolayers are either hydrophobic-hydrophobic or hydrophilic-hydrophilic [2] and, therefore, an even number of layers is deposited during a complete cycle. *Figure*

1.21 *b* and *c* picture two other deposition types, affording so-called X- and Z-type LB multilayers. In these cases transfer occurs only when the slide enters (X) or leaves (Z) the subphase, the choice of protocol depending on the nature of the monolayer, the substrate, the subphase, and the surface pressure. During the deposition of an individual LB layer, the surface area of the *Langmuir* monolayer on the water surface decreases due to the loss of molecules to the substrate. A simple diagnostic parameter of the deposition, the transfer ratio TR , is defined as (equation 1.4) [97]:

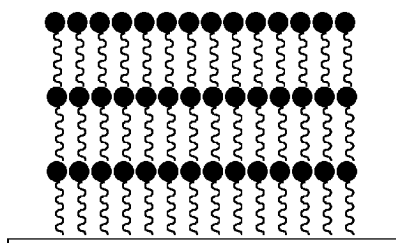
$$TR = A_L/A_T \quad (1.4)$$

where, A_L is the decrease in *Langmuir* monolayer surface area, and A_T is the total surface area of the solid substrate (slide). According to conventional wisdom, a $TR = 1$ is indicative of good deposition. The acceptance of the value of unity as ideal, however, reflects the assumption that the deposition process simply consists of transferring the constituent molecule from the water subphase to the solid support. This assumption is incorrect because the LB transfer is a complicated process in which the amphiphilic molecules generally attempt to reach a new thermodynamic minimum as they interact with the solid surface [98].

a) Y-type



b) X-type



c) Z-type

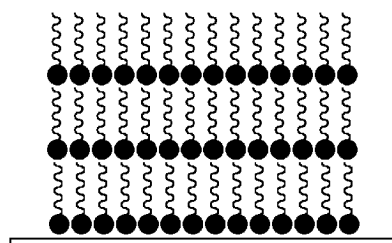


Figure 1.21 Structures of: a) Y-, b) X-, and c) Z-type LB multilayers [92].

Since the LB film deposition technique allows the preparation of highly ordered monolayers with a dense packing and precisely controlled thickness, LB monolayers have been used for immobilization of enzymes and other biomolecules in the development of various types of biosensors [99-107]. A biosensor is an analytical device which uses the specific interaction of the analyte with a biological molecule along with a physicochemically incorporated transducer to convert a molecular recognition event into an optical/electrochemical signal. Recently, *Malhotra* and co-workers [108] studied the immobilization of urease on LB films of poly(N-vinyl carbazole)/stearic acid with the intent of building a urea biosensor. The immobilization was achieved by transferring the monolayer of PVNK/SA/urease from the pure water surface onto the indium-tin oxide (ITO) coated glass plates. When the sensor is placed in a solution containing urea, the latter reaches the immobilized enzyme by diffusion and is decomposed to ammonium and bicarbonate ions. Detection of the ammonium ions was achieved by potentiometric measurements using an ammonium ion selective electrode. The detection limit and sensitivity of such an electrode were found to be 5 mM and 10 mV/mM, respectively. The same authors also prepared LB films of poly(3-dodecyl thiophene)/stearic acid (P3DT/SA) as part of a glucose biosensor [109]. The desired enzyme-containing monolayer was prepared by dispersing glucose oxidase (GOX) together with P3DT/SA on the water subphase to form a *Langmuir* film. The latter was transferred from the water subphase onto ITO-coated glass plates, and the activity of the immobilized GOX was measured by amperometry. The sensing process is based on the catalytic oxidation of glucose by GOX, followed by an amperometric determination of H₂O₂ which is a product of the oxidation. This biosensor can be used for the estimation of glucose concentrations of 100 and 400 mg/dl.

1.3.4 Characterization and Properties of Monolayers

This *Section* concentrates on the characterization of *Langmuir–Blodgett* monolayer films on solid support, by the techniques used in the context of the present thesis: *Brewster* angle microscopy, and grazing X-ray diffraction.

1.3.4.1 *Brewster* Angle Microscopy (BAM)

Brewster angle microscopy (BAM) [110, 111] has been shown to be a powerful method to visualize the morphology of amphiphilic monolayers on a microscopic scale. The

principle of the microscope is based on the fact that the reflectivity of an interface between two media of refractive indices n_1 and n_2 depends on the polarization of the incident light and the angle of incidence, θ . For a *Fresnel*⁶ interface and for light polarized in the plane of incidence (p -polarization), there is an angle, called *Brewster* angle θ_B , for which the reflectivity vanishes ($\tan\theta_B = n_2/n_1$). At this specific angle of incidence, the dipole moments induced in the second medium by the incident beam point exactly in the direction of reflection. Thus, the dipoles do not radiate in this direction and the reflectivity vanishes (*Figure 1.22*).

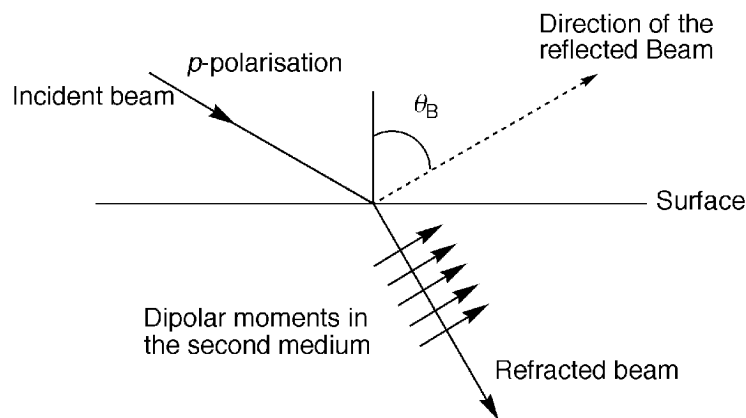


Figure 1.22 Schematic representation of the *Brewster* angle for the p polarization, as reported by *Meunier* [112].

For real interfaces, however, the refractive index n does not change quickly from one medium to the other and, secondly, these interfaces have a certain roughness. As a consequence, the reflection is minimal (the reflectivity at a surface of pure water is 1.2×10^{-8}) but it does not vanish completely at the *Brewster* angle. The (low) intensity of the reflection at the *Brewster* angle is strongly dependent on the interfacial properties. The presence of a surfactant monolayer leads to a change in the refractive index n and, thus, to a measurable change in reflectivity (*Figure 1.23*) [110, 111] which is related to the thickness of the interface, its actual roughness, and the anisotropy of the monolayer [113].

⁶ A *Fresnel* interface is an interface without roughness and for which the refractive index changes quickly from the refractive index of the lower phase, n_1 , to the refractive index of the upper phase, n_2 [110].

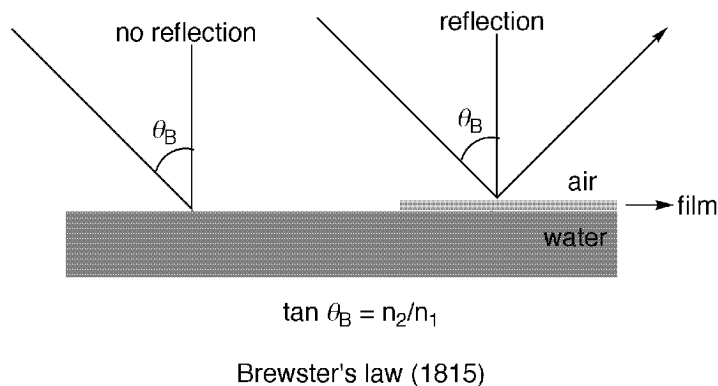


Figure 1.23 Schematic representation of *Brewster's* law at the air-water interface in the absence (left) and in the presence (right) of a thin film.

As an example, a layer with a thickness of 10 \AA and a refractive index of 1.4 increases the reflectivity by a factor of 35. Consequently, the difference between a two-dimensional gaseous and a condensed phase of a *Langmuir* film will also be detected easily by BAM microscopy. *Figure 1.24* shows a BAM image of a two-dimensional gas and a liquid phase coexisting in a *Langmuir* film of a fatty acid. The contrast between the two phases is very large because the surface densities of the fatty acid are very different in each of them [112]. The “gas” phase, with its relatively low density of molecules, appears in black whereas the liquid phase shows a much higher reflectivity.

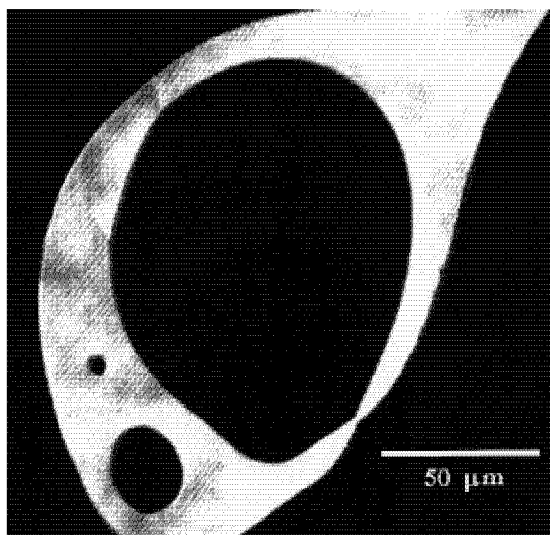


Figure 1.24 BAM image of a two-dimensional gas/liquid interface of a fatty acid, as reported by *Meunier* [112]. Gas phase = dark (black) and liquid phase = bright (white).

The *Brewster* Angle Microscope is schematically shown in *Figure 1.25*.

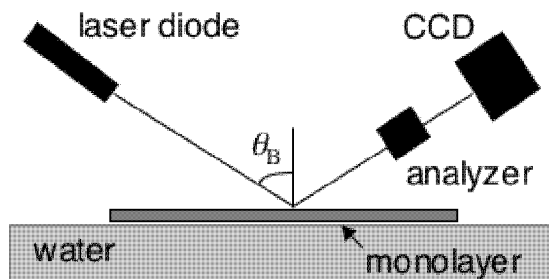


Figure 1.25 Schematic view of a *Brewster* angle microscope. The CCD (charge coupled device) is a camera which converts the incident light to images with a lateral resolution of about $< 20 \mu\text{m}$. The analyzer filters out the residual *s*-component background of the beam.

The *Brewster* angle microscope is operated with a laser diode as a light source (laser diode, $\lambda = 660 \text{ nm}$). The interface is illuminated at *Brewster* angle incidence (53° for the air-water interface) with a radiation that is nearly *p*-polarized (the electrical field vectors of the beam are in the plane of incidence) [114]. The light reflected from the monolayer passes through an analyzer, which filters out the residual *s*-component (component that is perpendicular to the plane of incidence) background, and is then transformed by a CCD camera into BAM images with a lateral resolution $< 20 \mu\text{m}$. The BAM image in *Figure 1.26 b* corresponds to the structure shown in *Figure 1.26 a* and represents the coexistence between an isotropic liquid expanded (LE) and a tilted liquid condensed (LC) phase. *Figure 1.26 b* reveals the presence of three distinct regions: The dark areas evidence the water subphase from which practically no light is reflected (see *Figure 1.24*), the gray areas correspond to the LE phase, and the brighter areas (white zones) to the condensed phase. The presence of an additional analyzer (a polarizer in the reflected beam) allows the detection of the in-plane optical anisotropy of the film which is induced by molecular tilt. Molecules differently tilted within the monolayer lead to different reflectivities [81, 115]. In *Figure 1.26 c*, each LC domain is subdivided in circular sectors differing in reflectivity. This is commonly attributed to different azimuthal orientations of the aliphatic chains inside each sector. The contrast between the regions with different brightness can be modified by simple rotation of the analyzer. The rotation angle of this additional analyzer corresponds to the tilt angle of the molecules within the monolayer. Then from the variation of the angle it is possible to determine the molecular orientation within the monolayer.

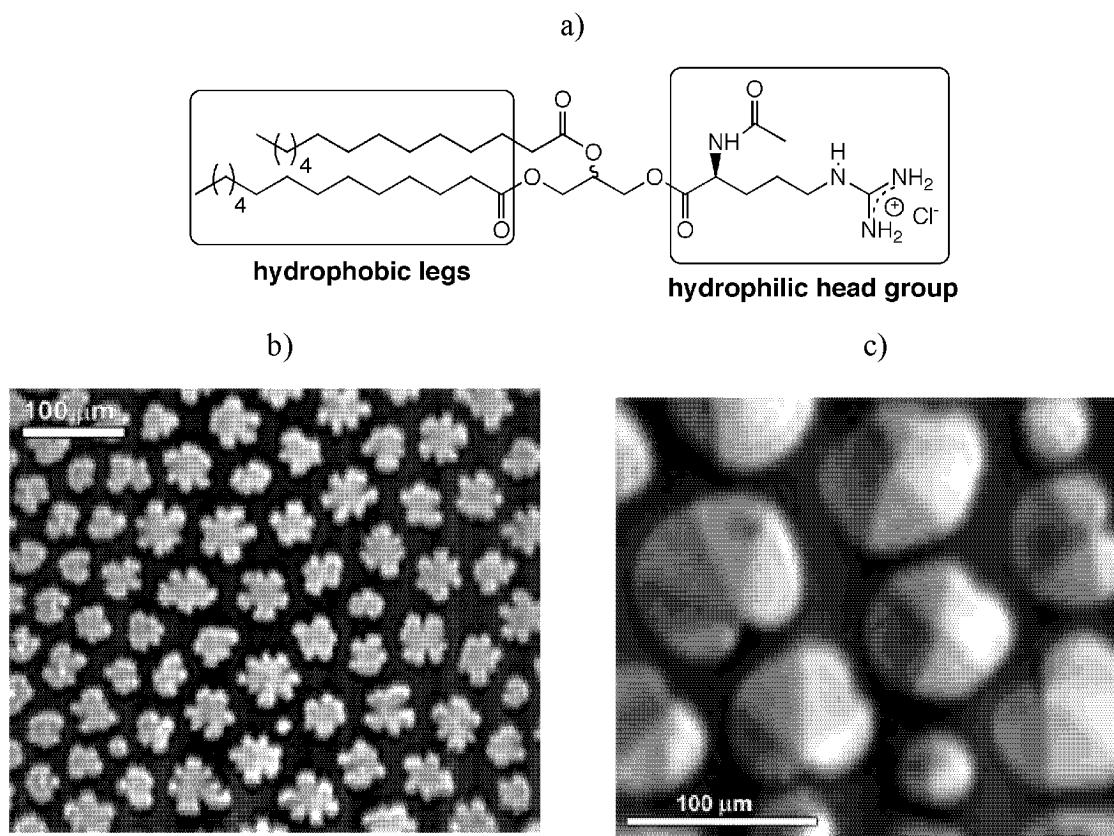


Figure 1.26 Arginino-triglyceride surfactant: a) molecular structure: BAM observations of a *Langmuir* monolayer of an arginino-triglyceride surfactant in the LE-LC coexistence region with the analyzer at 0° (b), and 60° (c) to maximize the inner texture, as reported by *Ignés-Mullol et al.* [116].

The calibration of the BAM used for the present thesis was accomplished using stearic acid (SA) as an amphiphile. The monolayer of SA exhibited a π - A isotherm (*Figure 1.27 a*) with a characteristic change in slope at $20 \text{ \AA}^2/\text{molecule}$ and $\pi = 25 \text{ mN m}^{-1}$, which reflects the transition from the liquid phase to the solid phase. When the linear part of the isotherm, corresponding to the solid-condensed phase, is extrapolated to zero pressure, the area per molecule is determined to 22 \AA^2 , which is consistent with the values reported in literature [83]. *Figure 1.27 b* shows BAM images of the stearic acid thin film that describe the morphology of the *Langmuir* monolayer at different points of the π - A isotherm. In picture 1, the bright islands represent SA molecules within the monolayer while the dark zones correspond to the water subphase. Upon compression, the bright areas gradually fuse to give a uniform image (picture 2) at the point where the liquid condensed phase appears.

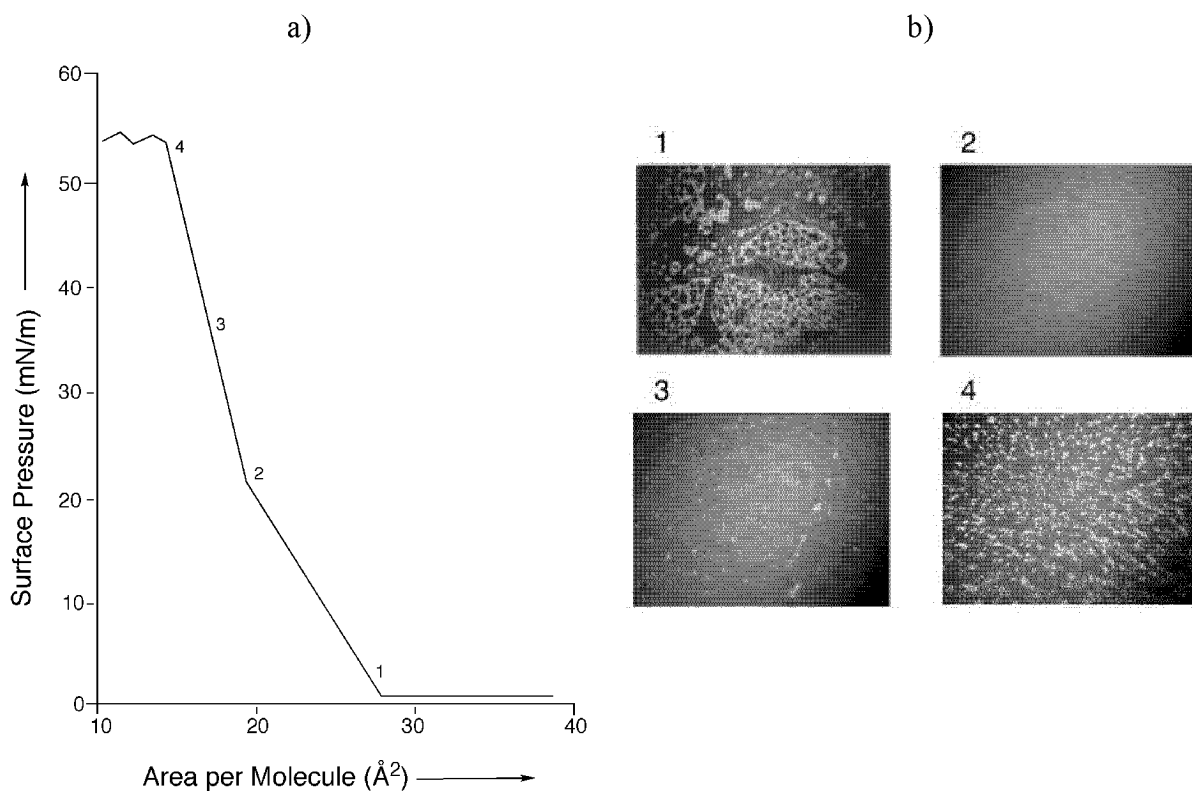


Figure 1.27 Langmuir layer of stearic acid at the air/water interface: a) *pressure–area* isotherm recorded at 25 °C, and b) BAM images corresponding to the points designated as 1, 2, 3, and 4 in the π – A isotherm.

This homogeneous image persists between points 2 and 3 even though the transition from liquid condensed to solid phase occurs at 25 mN m⁻¹. At a surface pressure of *ca.* 37 mN m⁻¹, image 3 shows bright spots, indicating the formation of small condensation nuclei or germs corresponding to the start of the monolayer collapse. These spots cluster (image 4) and fuse as the surface pressure is further raised, evidencing collapse of the monolayer. These results are in full agreement with those reported by *Seoane et al.* [83], demonstrating the accuracy of the employed instrument.

1.3.4.2 Grazing Incidence X-Ray Diffraction

X-Ray diffraction techniques have been extensively used in order to determine the monolayer thickness of LB films [117-119]. When electromagnetic radiation impinges on the surface of a material, a portion of it will be refracted and the rest reflected. The reflection at the surface and interfaces is due to the different reflective indices in the layers. Reflection therefore occurs at the top and the bottom of the surfaces of the film (*Figure 1.28*).

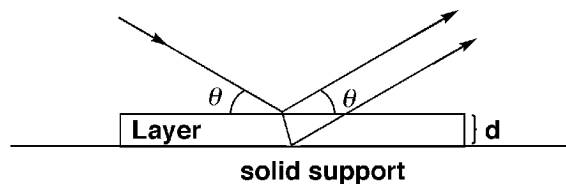


Figure 1.28 Schematic representation of X-Ray diffraction at a layered surface as reported by Datta [120].

The interference between the rays reflected from the top and the bottom of the film surfaces results in interference fringes (*Kiessig* fringes). The period of these fringes and the fall intensity are related to the thickness of the layer, whereas the interference is angle-dependent. Under the condition of *Bragg's* law (the angle of incidence is equal to the angle of reflection) equation 1.5 (*Bragg's* law) allows the calculation of the thickness of the layers:

$$n\lambda = 2d \sin\theta \quad (1.5)$$

where n is an integer ($n = 1, 2, 3, \text{etc.}\dots$), λ the wavelength of the incident X-ray beam, θ the angle of incidence, and d the thickness of the layer.

Figure 1.29 shows an X-ray reflectivity spectrum of a LB layer of a fullerene derivative, as reported by Gallani *et al.* [121].

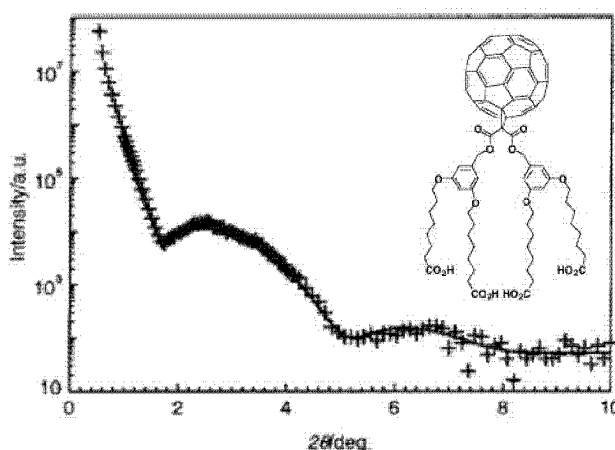


Figure 1.29 X-ray reflectivity spectrum of a LB layer of a fullerene derivative on silicon. The line is a fit to the data points [121].

The number of the *Kiessig* fringes depends on the transfer of the layer onto solid support. In fact, in Figure 1.29 the presence of only two *Kiessig* fringes is consistent with the low

transfer ratio that the authors observed (~ 0.75). Using a simulation or the least-square fit of the reflectivity pattern, they obtain accurate measurements of thickness and interface roughness for mono and multilayers.

2 Langmuir Investigations into the Vase–Kite Conformational Control of Amphiphilic Molecular Grippers

The studies of the monolayers of several amphiphilic cavitands (*Figure 2.1*) at the air-water interface are discussed in this *Chapter*.

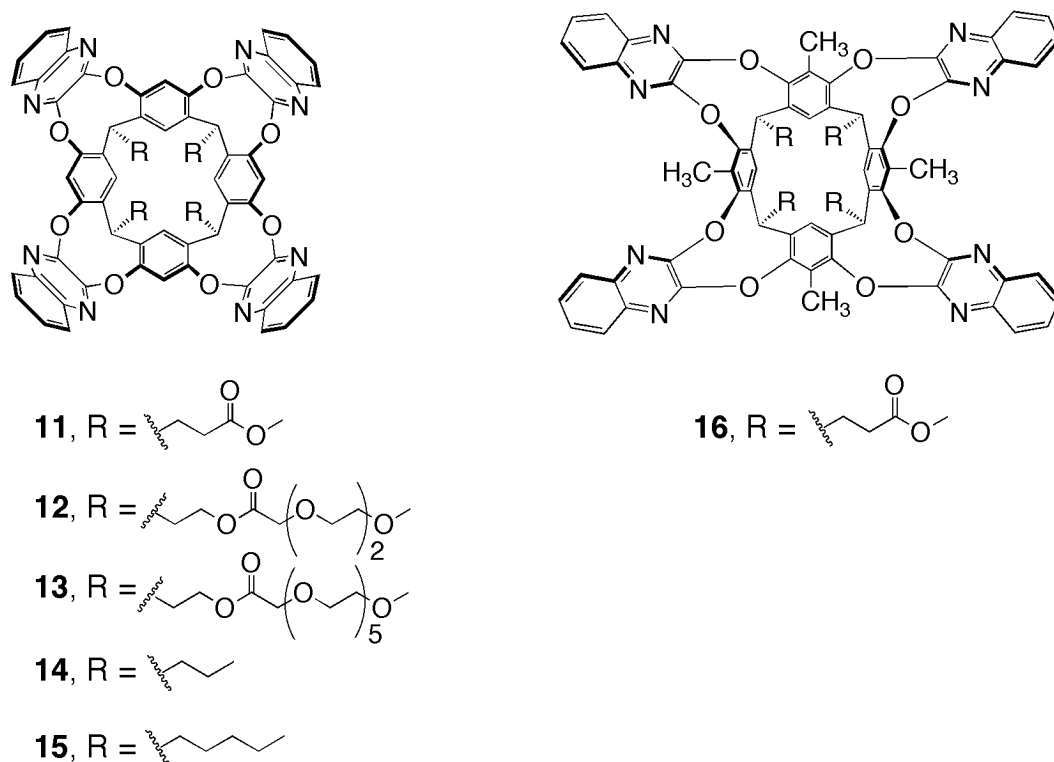


Figure 2.1 Chemical structure of amphiphilic cavitands in vase (**11–15**) and in kite (**16**) form.

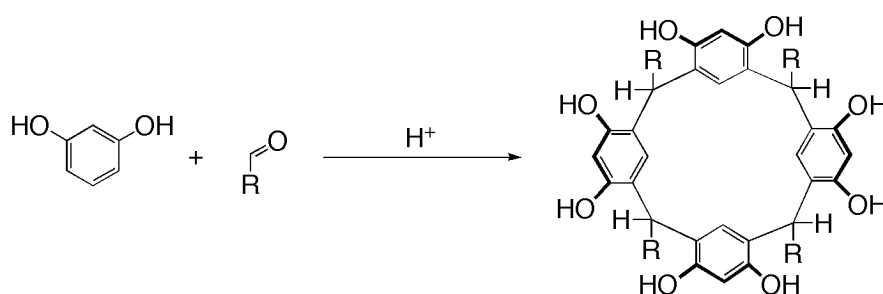
The *Chapter* is divided into six sections:

- *Section 2.1* is an introduction giving a general account of the properties of cavitands and their applications.
- *Section 2.2* describes the *Langmuir* investigation of the amphiphilic behavior of molecular grippers on pure water subphase.
- *Section 2.3* presents a comprehensive investigation of the *vase-to-kite* conversion of cavitand **11** at the air-water interface.

- *Section 2.4* describes the influence of the length of polyethylene glycol chain on the spreading behavior of cavitands **12** and **13**.
- *Section 2.5* describes the spreading behavior of cavitands **14** and **15**.
- *Section 2.6* gives a brief summary of the key findings of *Sections 2.3–2.5*.

2.1 Introduction

Recent efforts in chemical switching focused on the development of systems in which large changes in molecular or supramolecular geometry are induced by redox processes, light irradiation, or host/guest complexation. Representative examples are rotaxanes and catenanes [122-128], or calixarene ionophores, which undergo a large conformational change upon cation complexation [129]. Among the most fascinating systems, featuring two dramatically different, reversible, and switchable geometries, are the so-called cavitands. The name *cavitand* was given by *Cram* in 1982 [130] to a class of synthetic organic compounds that define a cavity large enough to accommodate other molecules or ions. These bowl-shaped macrocycles are readily synthesized by bridging the hydroxy groups of neighboring aromatic rings of resorcinarenes. *Cram* [131] made a breakthrough in the methodology to construct various kinds of cavitands [12, 17, 27, 130, 132-135] from *Högberg's* resorcinarenes (commonly called octols) [136, 137], which are easily obtained in high yield by the acid-catalyzed condensation of resorcinol with aldehydes [138] (*Scheme 2.2*).



Scheme 2.2 General synthesis of *Högberg's* resorcinarenes.

As a consequence of the non-planarity of resorcinarenes, it was found that octols can in principle exist as a mixture of four possible configurational diastereoisomers. Different relative configurations of the substituents at the methylene bridges of a resorcin[4]arene can lead to *cis-cis-cis* (*ccc*), *cis-cis-trans* (*cct*), *cis-trans-trans* (*ctt*), or *trans-cis-trans* (*tct*) arrangements (*Figure 2.3*).

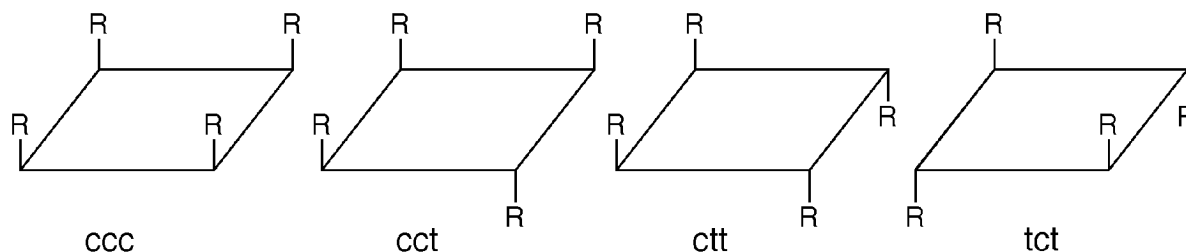


Figure 2.3 Possible configurational diastereoisomers of Högberg's resorcin[4]arene.

In the condensation of resorcinol with benzaldehyde [136, 139] only two diastereoisomeric tetrameric macrocycles are observed. One is a C_{4v} -symmetric isomer⁷ with all four substituents in axial position and *cis*-configuration (*ccc*) and the other a C_{2h} -symmetric isomer adopting a chair-like conformation (*ctt*) (Figure 2.3). The final diastereoselectivity of the condensation is controlled by the difference in the solubilities of the two macrocyclic products and the reversibility of the carbon-carbon bond formation [141]. The precipitation of the less soluble isomer (*ccc*) constitutes a thermodynamic sink, shifting the reaction equilibrium entirely toward its formation as the final product. Because of the reversibility of the reaction, *Abis et al.* [142] observed that the kinetically favored (*ctt*) isomer converts rapidly to the thermodynamically more stable (*ccc*) isomer. The intramolecular hydrogen bonds between the eight hydroxy groups make the macrocycle more rigid stabilizing the C_{2v} -symmetric boat conformations. Reaction of the OH groups of resorcinarenes with other residues, for example (hetero)aryl halides, creates cavitands and velcrands⁸ (Figure 2.4) which are particularly attractive molecules because the rims of the bowls can be varied by different substituents R^2 and bridging groups R^3 (Figure 2.4) [143]. These modifications allow for shaping of the cavity and manipulation of the solubility of the cavitands.

⁷ The average C_{4v} -symmetry results from two rapidly interconverting boat conformers with C_{2v} -symmetry [140].

⁸ Velcrands represent a class of cavitands that dimerize to form molecular velcro-like systems due to the presence of a methyl substituent *ortho* to both ether functions of each benzene ring.

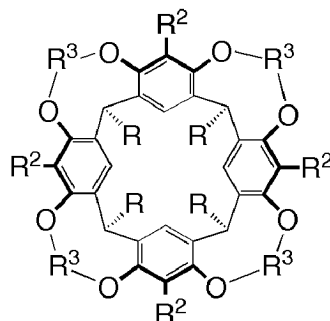
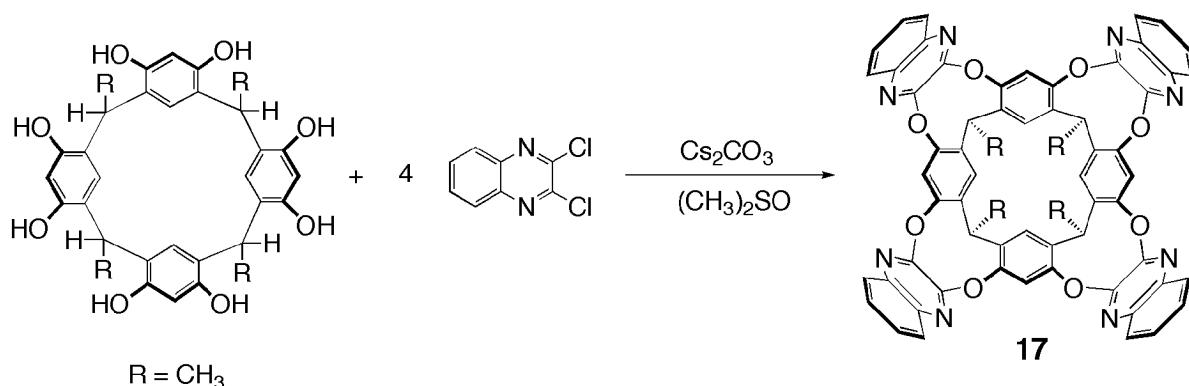


Figure 2.4 Possible structural modifications of cavitands by introduction of substituents R² or bridges R³.

If R³ is a polycyclic aromatic spacer, a much deeper cavity results which is interesting for host/guest complexation. Receptor **17** (Scheme 2.5) was thus prepared in good yield starting from the corresponding octol and 2,3-dichloroquinoxaline [27, 132].



Scheme 2.5 Synthesis of cavitand **17** containing quinoxaline-2,3-diyl bridges.

In this cavitand, the quinoxaline moieties act as conformationally mobile flaps. In one conformation the flaps come together in a nearly parallel array, resembling a *vase* with C_{4v}-symmetry. [14, 15, 17, 144, 145]. When the flaps are more or less orthogonal to the symmetry axis, a *kite* type conformer⁹ with a large flat surface results [27]. As described by *Cram*, the resonance of the methine proton in the skeleton of the octol is highly conformation-dependent, with a difference in chemical shift ($\Delta\delta = 2$ ppm) between *vase* ($\delta \sim 5.5$ ppm) and *kite* conformers ($\delta \sim 3.7$ ppm) [27]. VT (variable temperature) ¹H NMR

⁹ The *kite* conformer exists as equilibrium between two conformers *kite 1* and *kite 2*. The symmetry of both conformers is C_{2v}. Nevertheless, the equilibrium *kite 1* – *kite 2* is fast on the NMR time scale at room temperature. Thus, the ¹H-NMR spectrum of the *kite* conformer is dynamically averaged and indicates an apparent fourfold symmetry for the macrocycle [146].

spectroscopy in CHCl_3 showed that at elevated temperatures ($>318\text{ K}$) the *vase* conformation is preferred, whereas the *kite* conformation dominates at low temperatures ($<213\text{ K}$). This unique conformational behavior is related to the release of solvent molecules into the bulk solvent during the *kite*-to-*vase* conversion: The *kite* conformer is in contact with more solvent molecules than the *vase* conformer on account of its more extended surface. The higher degree of solvation in the *kite* form is stabilizing enthalpically but destabilizing entropically. At low temperatures, the favourable enthalpy of solvation overrides both the unfavourable entropy of solvation and the greater strain in the *kite* conformation. As the temperature rises, the unfavorable entropy effect becomes more important and the equilibrium is shifted towards the less strained *vase* conformation [27, 132]. *Diederich et al.* [146] estimated the thermodynamic parameters (ΔH and ΔS) for the equilibration between *vase* and *kite* conformational states. The authors calculated ΔH and ΔS for the *vase* \rightarrow *kite* transition to be *ca.* -6 kcal mol^{-1} and $-26\text{ cal mol}^{-1}\text{ K}^{-1}$, respectively, confirming that the transition between *vase* and *kite* form is enthalpy-driven at low temperature, as predicted earlier by *Cram* and co-workers [27]. Thanks to the *vase*-*kite* interconversion, such cavitands can be integrated into suitable devices where they should be able to capture, by complexation, a single molecule in the *vase* form, hold it during a possible translocation and finally release it upon switching to the non-complexing *kite* conformation. Because of this potential application, investigation of the various ways to induce the conformational switching is of high interest. *Diederich et al.* [147] have recently made a breakthrough in this context when they discovered that, at room temperature, the *vase*-to-*kite* conversion can also be induced by protonation with common organic acids such as CF_3COOH . In this case, the change in molecular geometry can be attributed to the protonation of the mildly basic quinoxaline N-atoms, resulting in an electrostatic repulsion among the cationic cavitand walls in the *vase* form. The switching is reversible and the *vase* can be regenerated by neutralization with K_2CO_3 . The acid-induced *vase*-to-*kite* switching is accompanied by a ^1H -NMR upfield shift of the methine proton from ~ 5.5 to ~ 3.7 ppm. The binding properties of switchable cavitands (see *Section 1.2.1.1*) were investigated in the solid state, in the gas phase, and in solution [13, 14, 148-151]. The adsorption on a metal surface [15, 23, 152-158] would be very interesting for single-molecule manipulation [159-162]. Some examples of *Langmuir* monolayers of cavitands are given in the following *Section*.

2.2 *Langmuir* Monolayers of Amphiphilic Calix[4]arene- and Resorcin[4]arene-Based Cavitands

It is known that amphiphilic resorcin[4]arene-derived cavitands form self-assembled thin solid films at the air-water interface [163-165]. In these films, the orientation of the molecules is defined by the way head and tail of cavitand molecules interact with the water subphase in *Langmuir* monolayers [166]. Similarly, the interactions with the solid substrate define the structure of *Langmuir-Blodgett* monolayers [164]. The possibility of forming well-organized films of receptor molecules (the *vase* conformers) extends possible applications of cavitands in the field of molecular recognition and supramolecular sensors [167-171]. Furthermore, the possibility of introducing different functional groups at the lower rim of cavitands delivers a great variety of receptors.

The *Langmuir* film technique can be used to control molecular recognition events at the air-water interface [169, 172, 173]. Such experiments can be performed by spreading a solution of hosts, for example cavitands, on a water subphase containing the species to be recognized. Variations in the collapse pressure and in the measured area per molecule, which can be shifted either to smaller or to larger values compared to the isotherm obtained on pure water as a subphase, are a proof that a molecular recognition event takes place. Recently, *Liu* and co-workers [170] studied the properties of monolayers of 5,11,17,23-tetra-*tert*-butyl-25,27-bis(2-aminoethoxy)-26,28-dihydroxycalix[4]arene (BAC) at the air-water interface and their recognition capacity for 5'-AMP⁻ and 5'-GMP²⁻. *Figures 2.6 a* and *b* show π -*A* isotherms of BAC in the presence of 5'-AMP⁻ and 5'-GMP²⁻, respectively, on water as a subphase. On pure water, the isotherm of BAC shows a compression plateau (25-40 mN m⁻¹) which indicates orientational change of the calix[4]arene at the air-water interface. The authors hypothesized that the molecules assume two kinds of orientation: One is parallel, with the calix[4]arene disposed with its lower rim anchoring into the aqueous subphase, and the other orientation is perpendicular with the calix[4]arene disposed with the lateral side contacting with the water subphase. After spreading, the molecules adopt a parallel orientation and upon compression they re-orient toward the perpendicular orientation. In the presence of nucleotide in the water subphase, the area per molecule at the lower pressure gets larger and the compression plateau gets longer, evidencing that interactions between BAC and 5'-AMP⁻ and 5'-GMP²⁻ occurred.

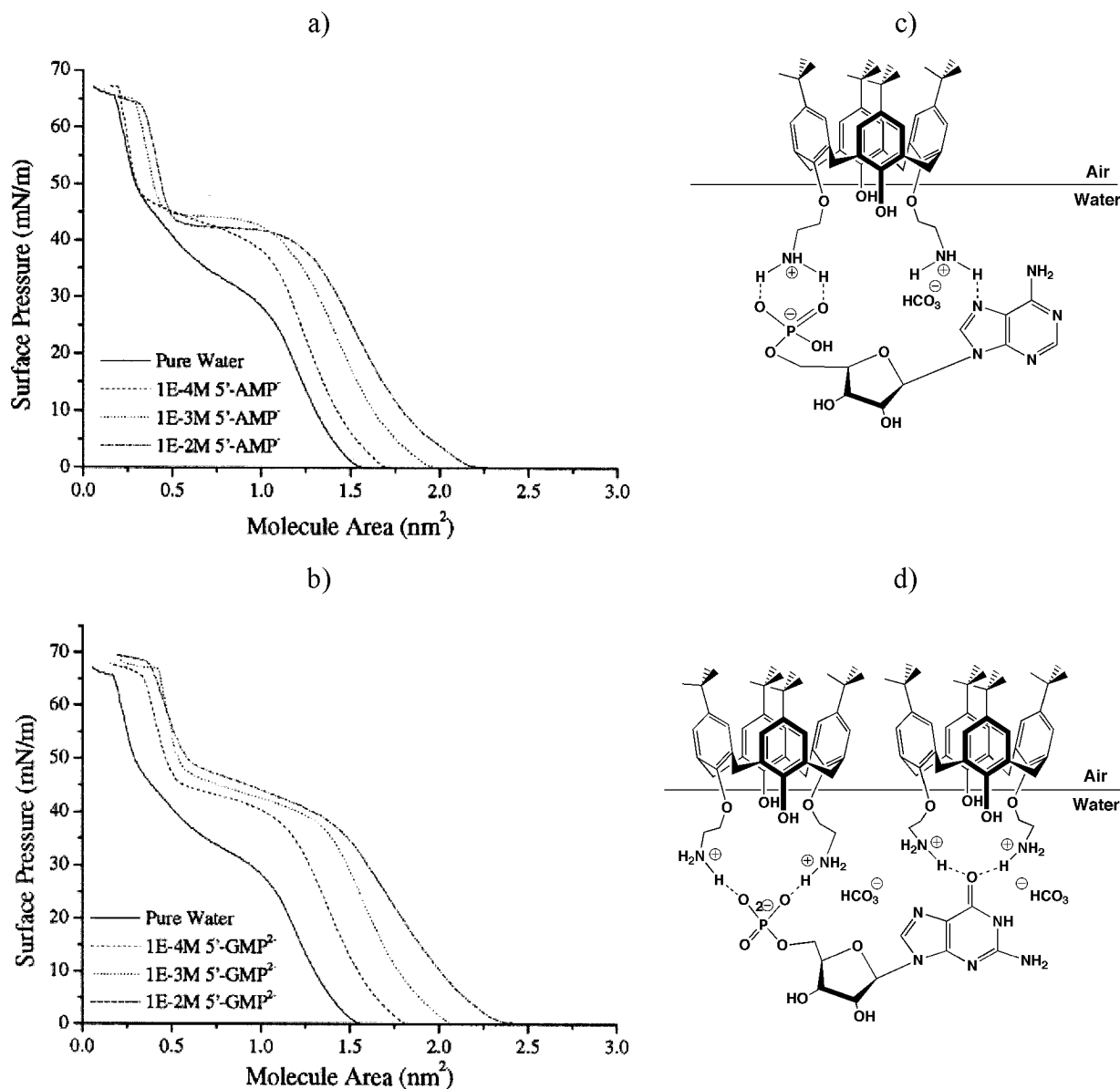


Figure 2.6 π -A Isotherms of monolayers of BAC in presence of a) 5'-AMP⁻ and b) 5'-GMP²⁻ at the air/water interface, as reported by Liu *et al.* [170]. The corresponding interaction patterns are shown on the right for c) 5'-AMP⁻ and d) 5'-GMP²⁻.

Comparison between Figures 2.6 a and b reveals that the monolayers in contact with the 5'-AMP⁻-containing subphase possess a larger molecular area, while those on the 5'-GMP²⁻-containing subphase have a higher compression plateau. This suggests that the interaction modes between BAC and the two nucleotides are different. The authors proposed two possible interaction patterns (Figures 2.6 c and d) that are in accord with the results obtained for the Langmuir monolayers: At lower pressure, BAC molecules in parallel orientation bind the two nucleotides, leading to an increase of the area per molecule. Once the

supramolecular entities are formed, they stabilize this orientation with the ammonium groups sticking into the water and the hydrophobic calix[4]arene skeleton stretching out of the water subphase. Consequently, the orientational change from parallel to perpendicular is delayed and the compression plateau is observed at higher pressure, with respect to the pure water subphase. The potential of the *Langmuir* technique to detect variations of the molecular area within the monolayers was the starting point, in our work, for the investigation of the conformational *vase*–*kite* switching equilibrium of cavitands at the air-water interface. Theoretical calculations performed using PM3 (implemented in the Spartan SGI version 5.1.3 [174]) as a computational method, revealed the difference in the area per molecule¹⁰ for the two conformations. In particular, the molecular area increases on the transition from the *vase* to the *kite* form. Based on these calculations, amphiphilic cavitands in both conformations were prepared by modifying the lower rim with amphiphilic legs (*Figure 2.7*).

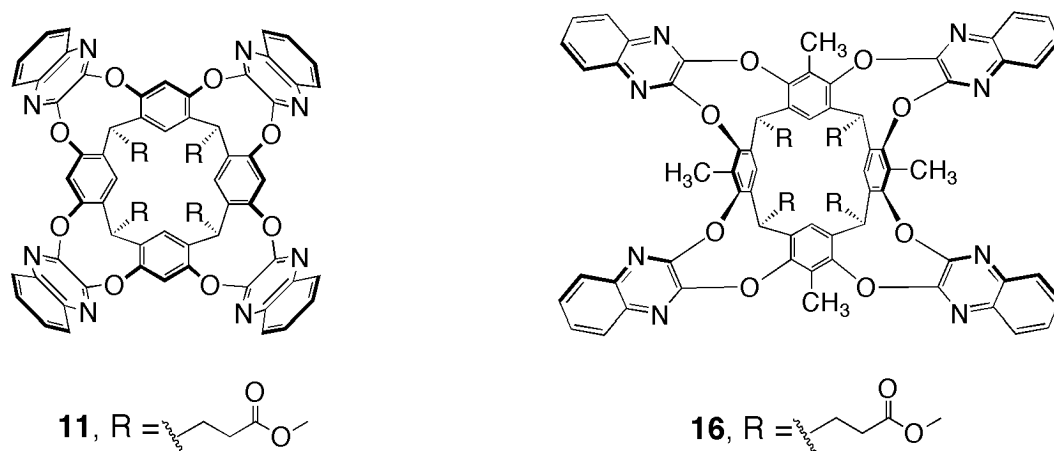


Figure 2.7 Cavitands containing amphiphilic legs at the lower rim for anchoring on the water subphase.

The different molecular area requirements were confirmed by X-ray crystal structure analysis for cavitand **11** [175] and velcrand **16**. For **11**, which prefers the *vase* conformation, a value of 120 \AA^2 was obtained whereas for **16**, which stays exclusively in the extended *kite* conformation [27], a value of 290 \AA^2 was obtained. Velcrand **16** cannot adopt the *vase* conformation because of the steric repulsions between the eight unshared electron pairs of the quinoxaline units and the four methyl groups *ortho* to both ether functions, whereas cavitand

¹⁰ The limiting area is mainly determined by the cross-sectional area of the upper rim of resorcin[4]arene.

11, which carries hydrogen atoms in that *ortho* position, can adopt the *vase* closed conformation.

Langmuir film studies were undertaken by spreading solutions of **11** and **16** on pure water subphases [2, 92]. The orientation of the cavitand molecules on the subphase is such that the most polar ester groups are in contact with water and the quinoxaline “flaps”, which represent the hydrophobic headgroup, extend away from the water surface (*Figure 2.8*)

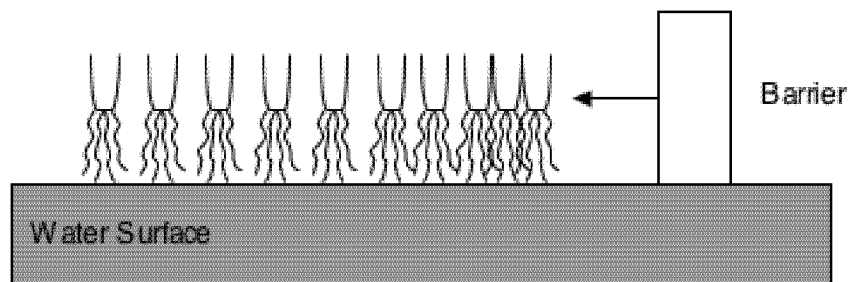
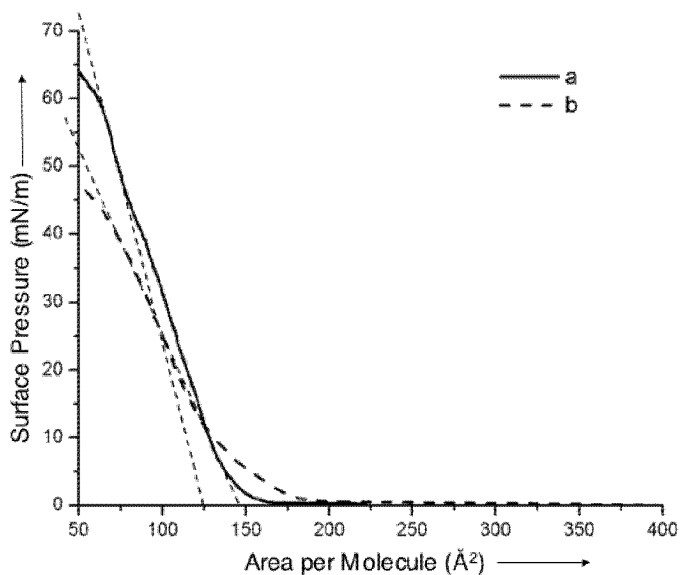


Figure 2.8 Orientation of amphiphilic cavitands at the air-water interface

According to equation 1.1 (*Chapter 1*), solutions of **11** (2.2 mg mL^{-1}) and **16** (0.32 mg mL^{-1}) in CHCl_3 were prepared and spread on the water surface in the *Langmuir* trough. After the chloroform had evaporated, a *Langmuir* film of cavitand molecules in the liquid-expanded phase was left on the water surface and subsequently compressed. Displayed in *Figure 2.9* are the surface pressure–area (π – A) curves for *Langmuir* films of **11** (solid line) and **16** (dashed curve). Cavitand **11** and velcrand **16** form a stable monolayer with a collapse pressure of 65 mN m^{-1} and 47 mN m^{-1} , respectively. The limiting area for **11**, estimated by extrapolating the linear region of the curve to zero pressure, is approximately 125 \AA^2 which is in good agreement with the calculated value (see table in *Figure 2.9*).



| | $A_E/\text{Å}^2$ | $A_T/\text{Å}^2$ |
|----------|------------------|------------------|
| a | 125 | 120 |
| b | 140 | 290 |

A_E = area per molecule experimentally estimated

A_T = area per molecule calculated from X-ray crystal structure

Figure 2.9 Surface pressure–area isotherms for monolayers of cavitand **11** (solid line) and velcrand **16** (dashed line) on a pure water subphase.

BAM photographs show a homogeneous monolayer of **11** (light gray) against the subphase (gray). At low pressure no coexistence of expanded and condensed domains was observed (Figure 2.10 a-c), nor was there any difference in brightness indicating different states or different orientations of the molecules within the monolayer [112, 176-178].

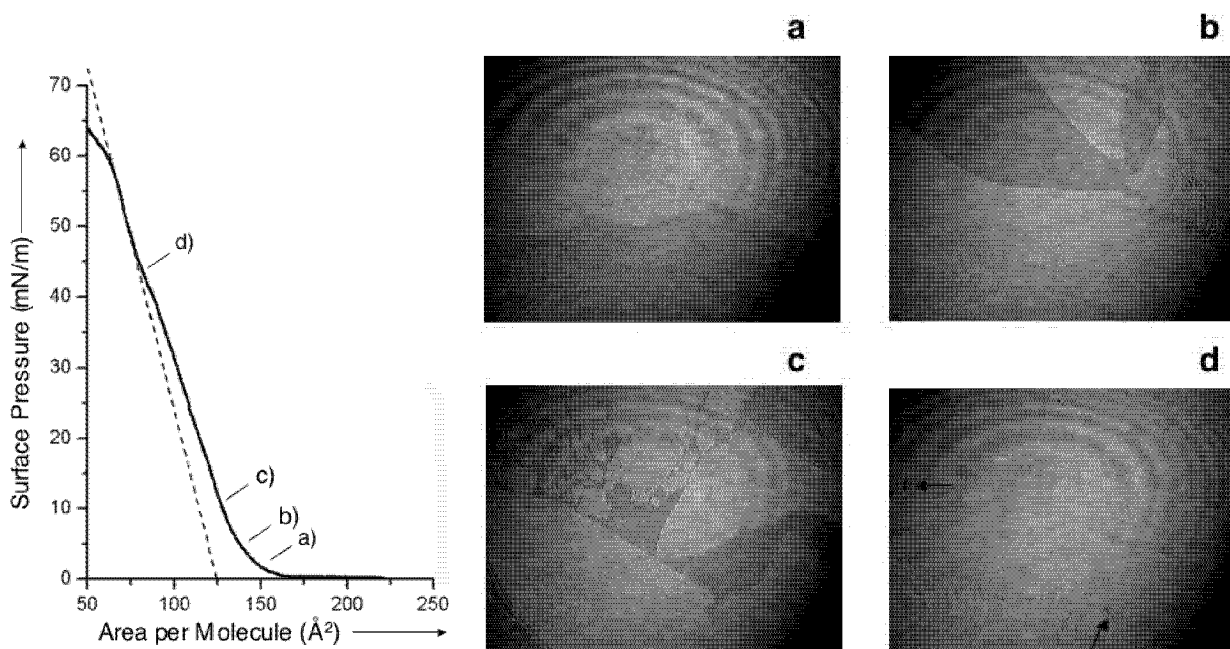


Figure 2.10 BAM photographs taken during the compression of cavitand **11** on water at a) $\pi = 0.3 \text{ mN m}^{-1}$, b) $\pi = 4 \text{ mN m}^{-1}$, c) $\pi = 10 \text{ mN m}^{-1}$, and d) $\pi = 42 \text{ mN m}^{-1}$. The two arrows in picture d show cavities indicating the collapse of the monolayer.

It seems that the monolayer is well organized even at the beginning of compression, and there is no change in its morphology during compression. At the collapse pressure, the BAM image shows very small cavities (*Figure 2.10 d*) [179] with reduced reflectivity (dark spots). These indicate the initial collapse of the film. On the other hand, the extrapolation of the isotherm of velcrand **16** gives an area per molecule of 140 \AA^2 , about half the value of 290 \AA^2 which was predicted for a single-molecule monolayer (see Table in *Figure 2.9*).

This unexpected value can be explained by considering that velcrand **16** exists as two equilibrating degenerate *kite* conformations **16a** and **16b** (*Figure 2.11*) which are highly preorganized for dimerization [27, 134].

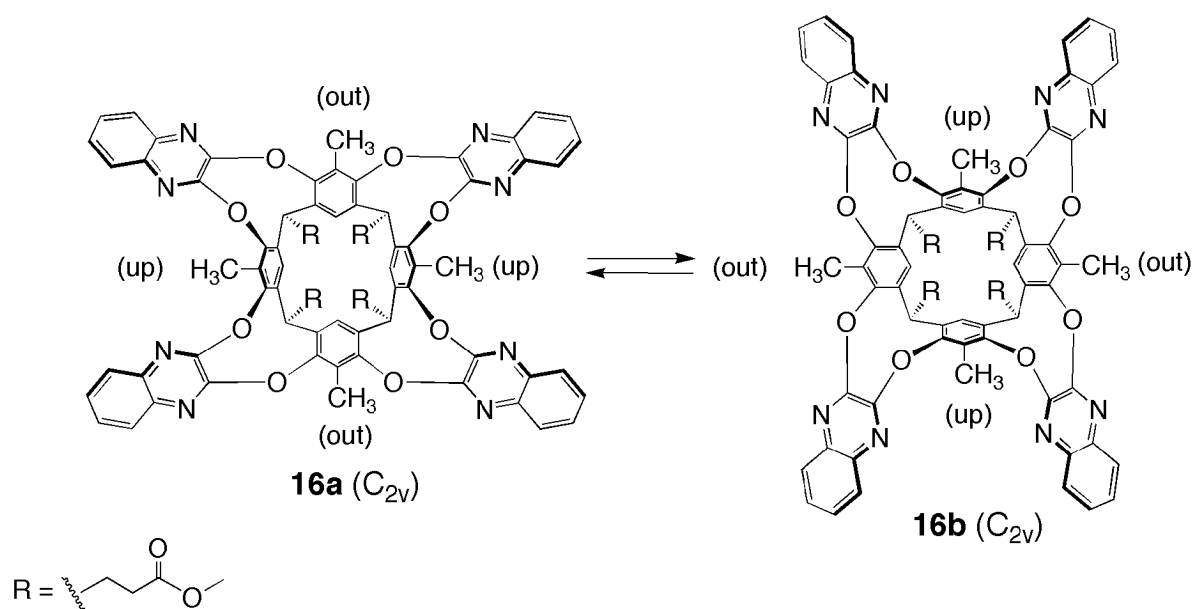


Figure 2.11 Interconversion between *kite 1* (**16a**) and *kite 2* (**16b**) conformations of resorcin[4]arene velcrands with four quinoxaline “flaps”.

The degenerate *kite* forms **16a** and **16b** possess a roughly rectangular face ($15 \times 20 \text{ \AA}$) containing two methyl groups protruding upward and oriented perpendicular to this face, two methyl groups pointing out horizontally, and two methyl sized indentations. These protrusions and indentations are shown in *Figure 2.12* as CH_3 and empty circles, respectively. The dimerization is illustrated by a schematic drawing $\text{A} + \text{B} \rightarrow \text{C}$. Rotation of A by 90° in the plane of the page produces B, which then fits on top of A to give the dimer C. The dimer has four methyl groups that occupy four host cavities that are stereoelectronically complementary to them. In complex C, the individual molecules cannot slip or rotate with respect to each other because the four methyl groups lock them.

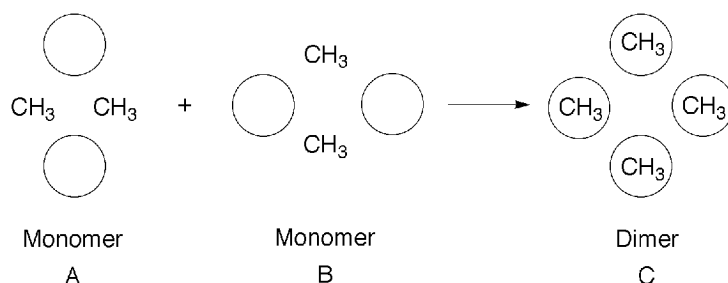


Figure 2.12 Scheme of the dimerization of two complementary velcrands **16a** and **16b**, as reported by *Cram et al.* [27, 134].

Cram [27, 134] observed that the binding free energy of the dimer increases with the solvent polarity because of solvophobic driving forces. In non polar solvents, such as CHCl_3 , the dimerization is entropy-driven and enthalpy-opposed because solvent molecules are detached from the surface of the two monomers and transferred to the bulk solvent. In the case of polar solvents, the dimerization is enthalpy-driven and entropy-opposed because the large hydrophobic surfaces of the velcrand monomers prefer to be in contact with each other rather than in contact with the solvent. This experimental evidence is well supported by the *Langmuir* isotherm of velcrand **16**.

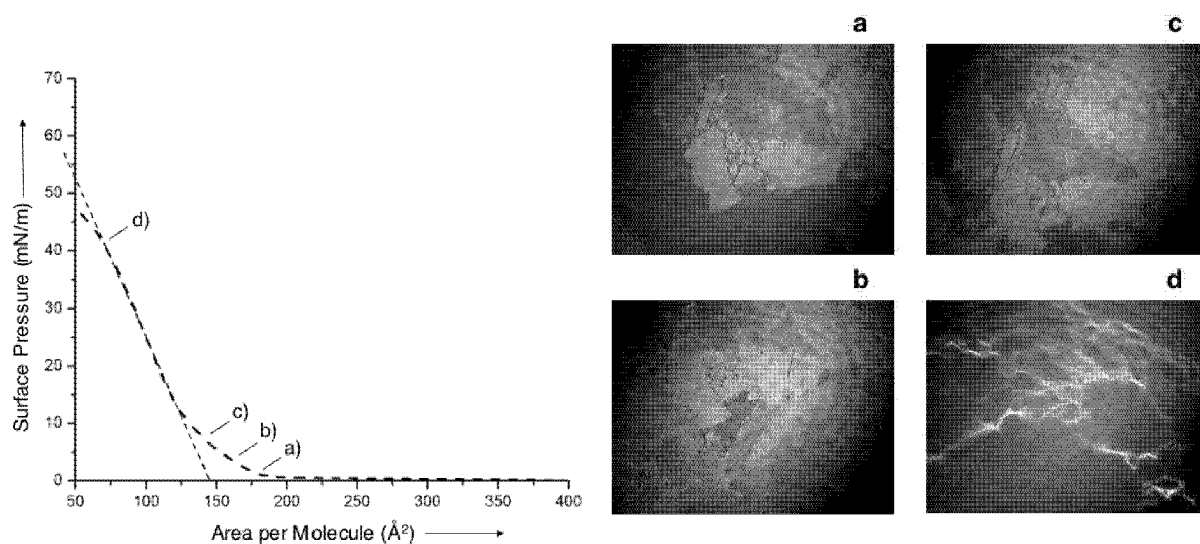


Figure 2.13 BAM photographs taken during the compression of cavitand **16** on water at a) $\pi = 0.6 \text{ mN m}^{-1}$, b) $\pi = 3.5 \text{ mN m}^{-1}$, c) $\pi = 7 \text{ mN m}^{-1}$, d) $\pi = 40 \text{ mN m}^{-1}$.

The obtained molecular area value suggests that dimerization of **16** occurs under formation of velcraplexes with the flat surfaces facing each other, resulting in a defined double layer at the air-water interface. BAM photographs taken during the compression of velcrand **16** show an inhomogenous image of the monolayer (*Figure 2.13 a-c*). At a pressure of $\sim 40 \text{ mN m}^{-1}$, BAM photographs show bright fracture lines which suggest a collapse of the monolayer (*Figure 2.13 d*). Successive compression/decompression cycles evidenced the formation of irreversible layers for both cavitands.

Considering these promising results, we investigated the conformational switching of cavitands at the air-water interface (*Figure 2.14*).

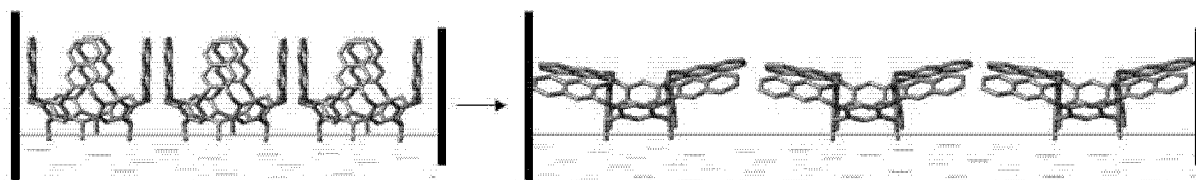


Figure 2.14 Visualization of the *vase-to-kite* conversion at the air/water interface.

2.3 *Vase-to-Kite* Conversion at the Air-Water Interface

2.3.1 pH-Induced Conformational Conversion¹¹ at the Air-water Interface

The starting point for the *Langmuir* investigations of the conformational switching was the reversible *vase-kite* isomerization of cavitands in solution induced by *Diederich et al.* at room temperature by pH-changes [147]. The switching was accomplished by addition of aliquots of trifluoroacetic acid (TFA) to a solution of cavitand ($c = 10^{-5} \text{ M}$) in CHCl_3 . Taking into account these results, pH-promoted conformational control was studied at the air-water interface by spreading a solution of amphiphilic cavitand **11** in CHCl_3 (2.2 mg mL^{-1}) on water as a subphase at different pH adjusted by addition of TFA. Isotherms were recorded at $\text{pH} = 7$, $\text{pH} = 3$, $\text{pH} = 2$, and $\text{pH} = 1$ (*Figure 2.15*). Further increase of the concentration of TFA in the water subphase was not allowed due to expected corrosion of the instrument.

¹¹ In this context, the term conversion is more appropriate than switching because no reverse process was achieved.

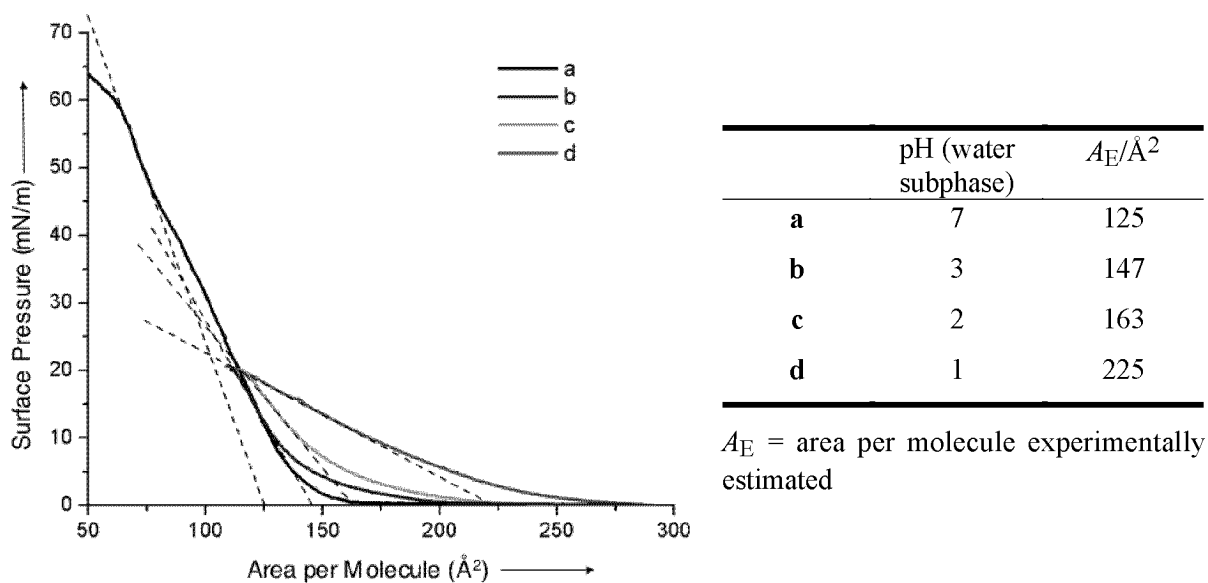


Figure 2.15 Langmuir isotherms of **11** recorded at 25 °C on neutral (pH = 7, black) and acidic (pH = 3, blue; pH = 2, green; pH = 1, red) subphases.

The four isotherms recorded at different pH exhibit similar behavior: the surface pressure departs from 0 mN m⁻¹ at a molecular area around 250 Å² and then increases gently until the collapse of the monolayer occurs at pressures between ~ 20 mN m⁻¹ (acidic subphases) and ~ 65 mN m⁻¹ (neutral subphase) (Figure 2.15). Isotherms **b**, **c**, and **d** show the so-called liquid condensed phase [113, 180]. It appears that the liquid-like molecular organization of the films correlates with the concentration of acid in the water subphase. At high concentrations of TFA, a continuous increase in the surface pressure with decreasing area per molecule suggests that there is no phase transition to the condensed state. On pure water, the limiting molecular area of **11** is $A \approx 125 \text{ Å}^2$ which is in agreement with the value predicted for the *vase* conformation ($A = 120 \text{ Å}^2$), as previously discussed in Section 2.2. In contrast, the π - A isotherms of **11** on the various acidic subphases show molecular limiting areas of $A \approx 146 \text{ Å}^2$, 162 Å^2 , and 225 Å^2 for pH = 3, 2, and 1, respectively. Because an increase in molecular area is associated with an increased prevalence of the *kite* conformation, the data suggest that the presence of acid brings about the *vase-to-kite* transformation. At pH = 1, the limiting area of 225 Å^2 suggests that the cavitand **11** predominately adopts the *kite* form within the monolayer. The value measured is consistent with the calculated value of $A = 290 \text{ Å}^2$ for the *kite* conformation, as previously discussed.

2.3.2 *Langmuir* Films of Resorcin[4]arene Cavitand **11** on Various Ion-Containing Subphases

The new application of the *Langmuir* technique for studying the *vase-to-kite* conversion at the air-water interface has stimulated further efforts to discover new switching methods. Preliminary $^1\text{H-NMR}$ investigations performed by adding silver salts to a solution of cavitand in CHCl_3 thus evidenced an upfield shift of the methine proton, similar to that observed for temperature- [132] and pH-induced conformational switching [147]. The coordination of the nitrogen atoms of the quinoxaline moieties to silver ions should favor the *vase-to-kite* switching. Unfortunately, comprehensive $^1\text{H-NMR}$ investigations could not be pursued because the high silver(I) ion concentration needed to drive the conformational change to completion was inaccessible for solubility reasons. By using the *Langmuir* technique it was possible, though, to investigate the influence of silver ions on the *vase-to-kite* conversion because of the possibility to work with high concentrations of the silver salt easily dissolved in the water subphase. A solution of **11** in CHCl_3 (2.2 mg mL^{-1}) was spread on water containing AgNO_3 in varying quantities. The according isotherms, displayed in *Figure 2.16*, reveal a slight increase of the limiting area per molecule with increasing concentration of silver salt in the water subphase. Of particular note is the molecular area increase from $A \approx 125 \text{ \AA}^2$ (pure water) to $A \approx 145 \text{ \AA}^2$ ($2 \times 10^{-1} \text{ mM}$ aq. solution of AgNO_3) (*Figure 2.16*). Each of the isotherms **b**, **c**, and **d** shows two inflection points which are most pronounced in curve **d** (higher concentration of AgNO_3 in the water subphase). This behavior can be explained by considering the coexistence of two phases. The coordination of silver(I) with the nitrogen atoms of the quinoxaline moieties in two neighboring cavitands causes them to be closer and consequently aggregated. This coordination leads to the formation of condensation nuclei dispersed in the liquid expanded phase [181-184] and to the premature collapse of the monolayers [93, 185]. In fact, by increasing the concentration of silver salt in the water subphase, the collapse pressure decreases.

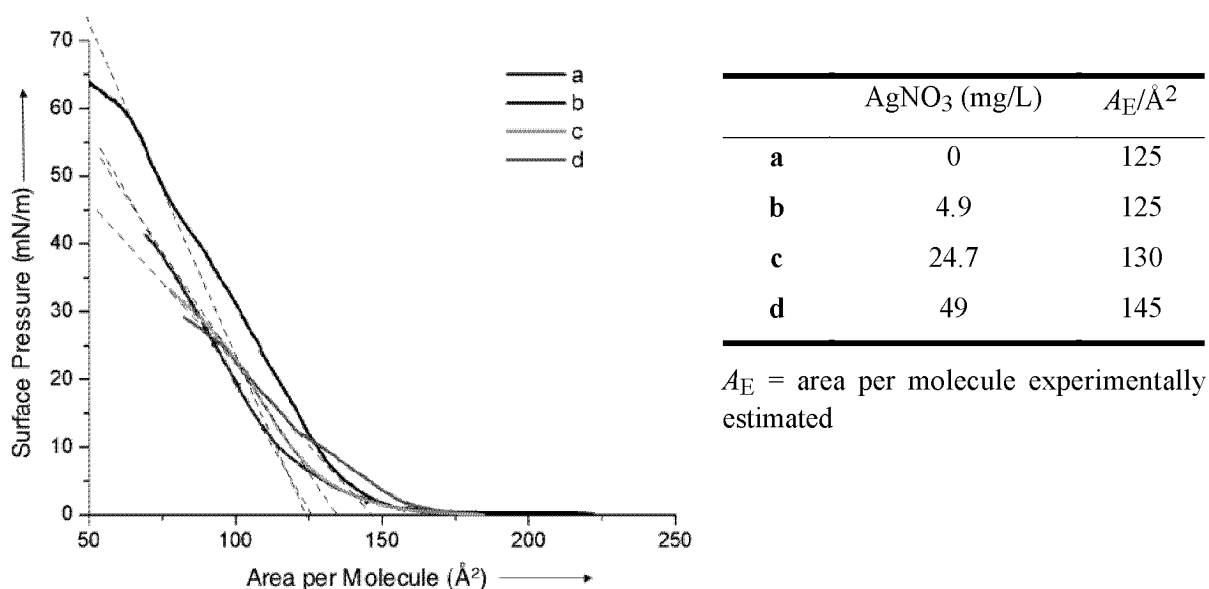


Figure 2.16 Langmuir isotherms recorded for **11** at 25 °C on a) pure water (black curve) and on water containing AgNO₃ at concentrations of b) 4.9 mg L⁻¹ (blue curve), c) 24.7 mg L⁻¹ (green curve), and d) 49 mg L⁻¹ (red curve).

It seems that the preferred linear geometry of silver complexes does not favor the coordination with two quinoxaline nitrogens of the same cavitand, whereas it may prefer the coordination with two nitrogens of neighboring cavitands. Molecular modeling of the cavitand **11** in *kite* form shows that neighboring quinoxalines are tilted with respect to each other and the complex with a silver ion gives an angle N-Ag-N of 110°, which is significantly lower compared to the linear geometry (180°).

Therefore, we carried out further studies with other metals, such as Cu²⁺ [186] and Fe³⁺ [163]. The isotherms reported in *Figure 2.17* were obtained by spreading a solution of **11** in chloroform (2.2 mg mL⁻¹) on water containing iron trichloride at varying concentrations. The onset of the π - A isotherms **b**, **c**, and **d** displayed in *Figure 2.17* is shifted towards smaller areas with respect to curve **a**. This shift suggests that the films are more compact [187] but less stable (the collapse pressure decreases on the transition from **a** to **d**) in the presence of iron(III) ions as compared to pure water. Increasing the Fe³⁺ concentration enhances this phenomenon up to the threshold of 47 mg mL⁻¹, above which no more changes in the isotherm were observed. Due to the affinity of Fe³⁺ ions for oxygen, we may hypothesize that their presence causes a significant reorganization of the water subphase, leading to a change of its molecular structure and altering the spreading behavior of the cavitands.

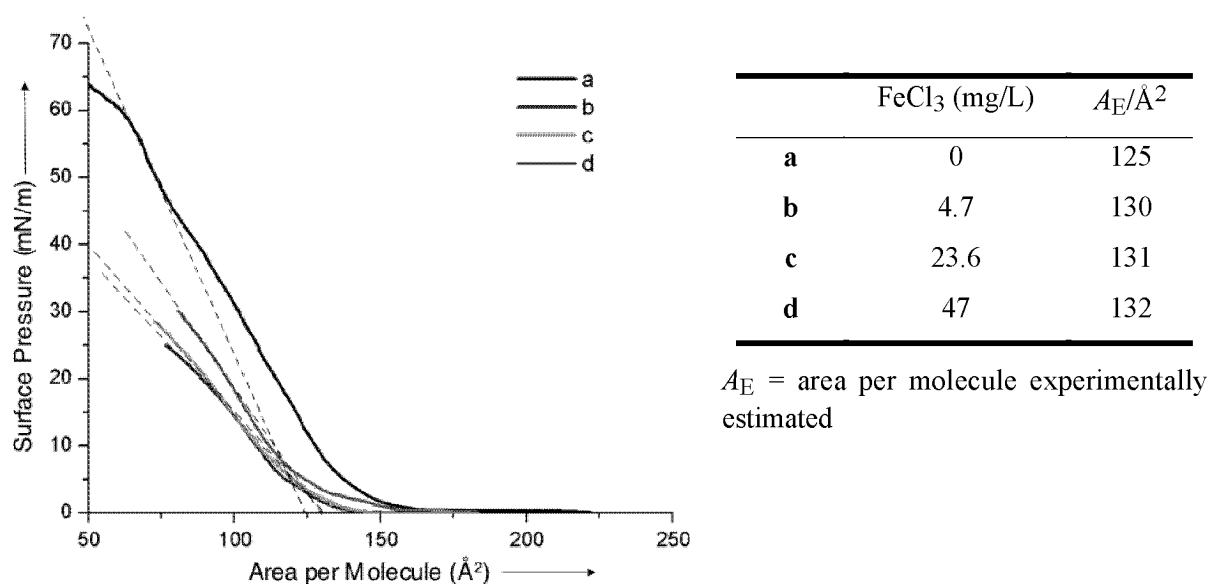


Figure 2.17 Langmuir isotherms of **11** recorded at 25 °C on a) pure water (black curve), and on water containing FeCl₃ at concentrations of b) 4.7 mg L⁻¹ (blue curve), c) 23.6 mg L⁻¹ (green curve), and d) 47 mg L⁻¹ (red curve).

Finally, the influence of copper(II) ions on the conformational control of **11** was studied by using a water subphase containing CuSO₄. The corresponding isotherms are displayed in Figure 2.18.

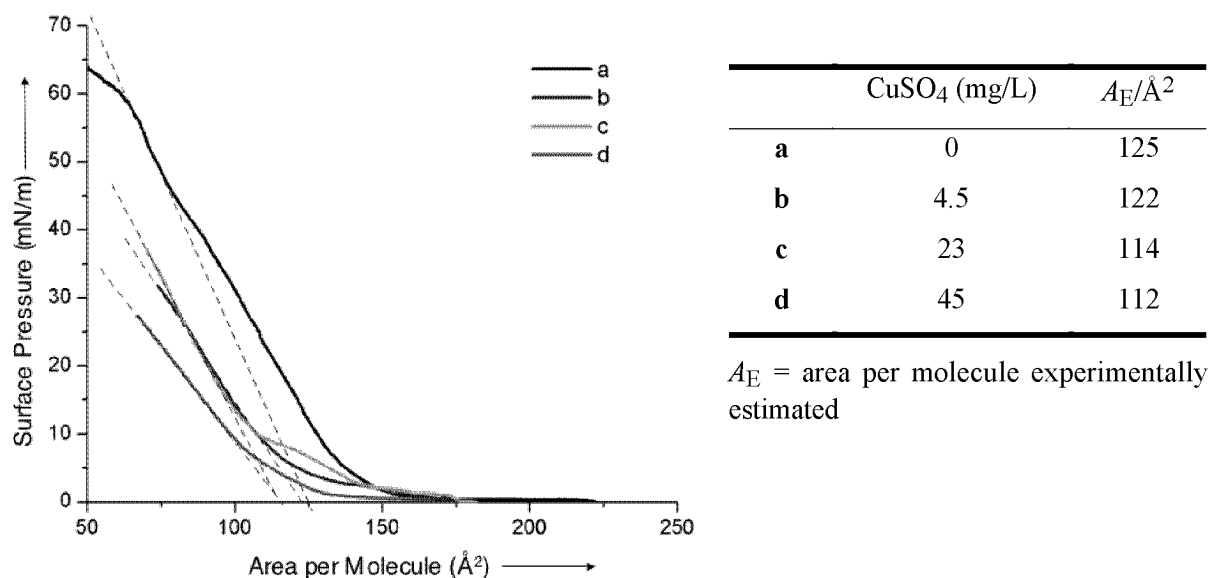


Figure 2.18 Langmuir isotherms of **11** recorded at 25 °C on a) pure water (black curve), and on water containing CuSO₄ at concentrations of b) 4.5 mg L⁻¹ (blue curve), c) 23 mg L⁻¹ (green curve), and d) 45 mg L⁻¹ (red curve).

Also in this case, the onset of the isotherms show the same general behavior as in the case of iron(III) chloride: The isotherms shift toward smaller area per molecule by increasing the concentration of CuSO_4 in the water subphase.

From the analysis of the π - A isotherms, the following conclusions can be drawn:

1. A progressive increase of the amount of Cu^{2+} ions up to 50 equivalents (*Figure 2.18*, isotherm **b**) does not lead to a significant variation in the area per molecule for **11**.
2. At even higher concentrations of Cu^{2+} ions (>50 equivalents) (*Figure 2.18*, curves **c** and **d**), the area per molecule decreases again slightly to the value of 112 \AA^2 (**d**).

Analogously to the Fe(III)-behavior, a possible explanation for these results may be the affinity of copper(II) for water [188], which may cause some changes in the molecular structure of the subphase.

To understand if the role of iron(III) and copper(II) is related to the reorganization of the water subphase, we performed experiments in the presence of metal ions (K^+) that cannot coordinate to the nitrogen atoms of quinoxalines. For this purpose, a water subphase containing varying concentrations of KCl was used and the resulting isotherms are shown in *Figure 2.19*.

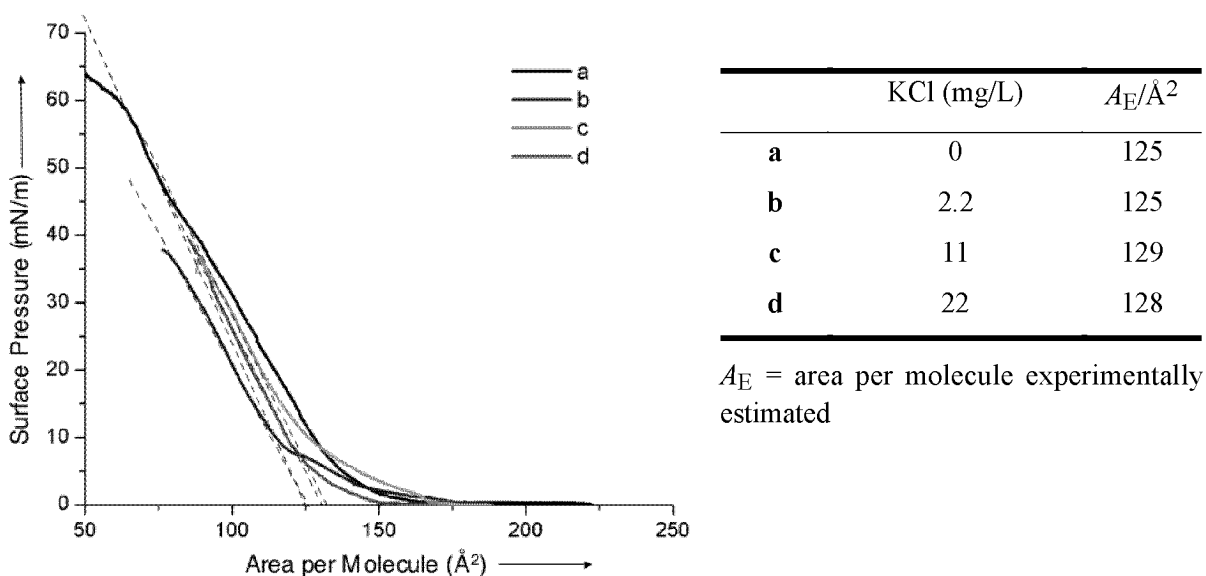


Figure 2.19 Langmuir isotherms of **11** recorded at $25 \text{ }^\circ\text{C}$ on a) pure water (black curve), and on water containing KCl at concentrations of b) 2.2 mg L^{-1} (blue curve), c) 11 mg L^{-1} (green curve), and d) 22 mg L^{-1} (red curve).

As expected, the intercepts to zero pressure of the isotherms evidenced no sizeable variation of the limiting molecular area with changing concentrations of KCl. This is expected because there are no interactions between K^+ ions and the quinoxaline nitrogen atoms. Nevertheless, the onset of the π - A isotherms (*Figure 2.19; b, c, and d*) collected in the presence of KCl is slightly shifted towards smaller areas with respect to the isotherm **a** (pure water as subphase) showing an influence of the K^+ ions on the morphology of the monolayers. This shift which is analogous to one seen with the other metal ions may suggest that the main interaction occurs between the ester groups at the lower rim of cavitand **11** and the water subphase reorganized by the interaction with the metals (Ag^+ , Fe^{3+} , Cu^{2+} , and K^+). However, silver(I) ions interact to some extent with the nitrogen atoms of the quinoxaline moieties, leading to an increase of the limiting molecular area.

2.3.3 Zn(II)-induced Conformational Control of Amphiphilic Cavitand **11**

The negligible variations in the area-per-molecule values obtained with *Langmuir* monolayers of **11** on Ag^+ -, Fe^{3+} -, and Cu^{2+} -containing subphases could be attributed to the low capacity of quinoxaline moieties to coordinate to these metals. The nitrogen-metal coordination is impeded by the fact that two neighboring quinoxaline moieties are not close enough. Because of its amphiphilic character, the resorcin[4]arene cavitand **11** places the nitrogen atoms at the air-water interface, whereas the metals are completely solubilized in the water subphase where they form aquo-complexes [188] (*Figure 2.20*).

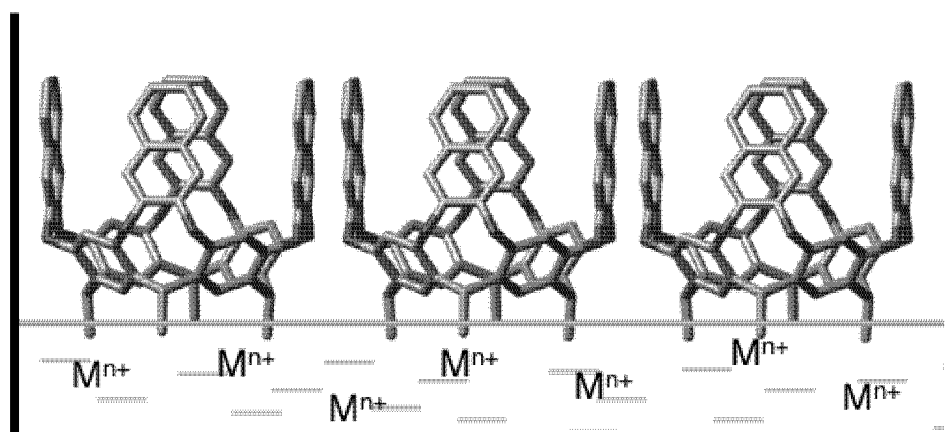


Figure 2.20 Schematic representation of the amphiphilic cavitand on the water subphase containing metal ions (M^{n+}).

The schematic representation in *Figure 2.20*, gives an impression of how difficult the coordination between the quinoxaline nitrogen atoms at the air-water interface and the metal ions in the water subphase is. Based on these considerations, new *Langmuir* experiments were done under different conditions, and in presence of Zn^{2+} ions [189], which should better coordinate to the nitrogen atoms of the quinoxalines [186].

Figure 2.21 shows the results of experiments performed with a water subphase containing different concentrations of zinc acetate.

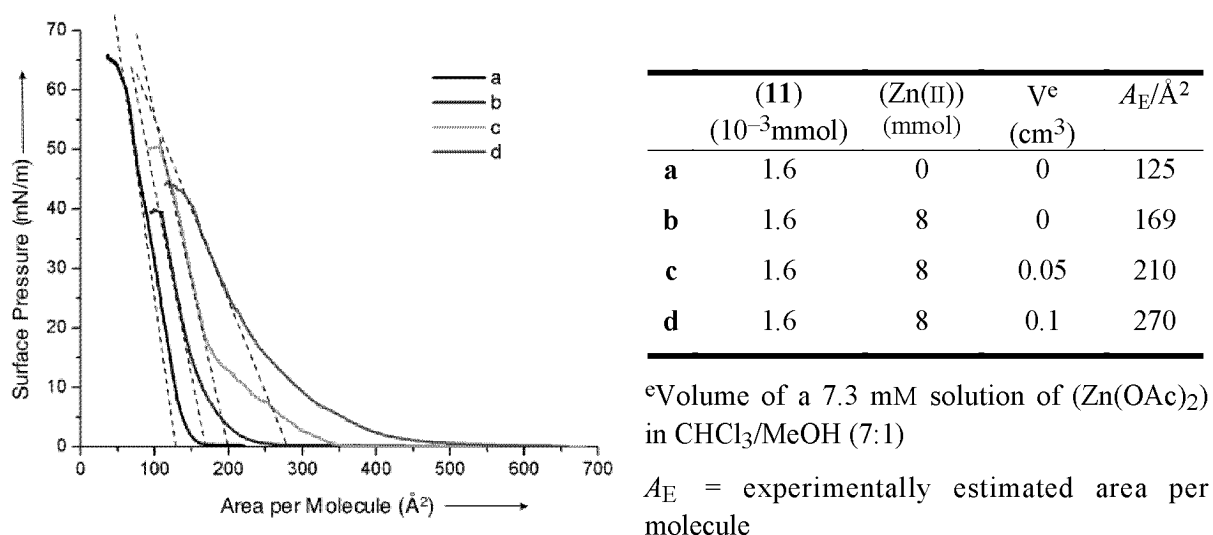


Figure 2.21 *Langmuir* isotherms of **11** recorded at 25 °C on a) pure water (black curve), b) on water containing $\text{Zn}(\text{OAc})_2$ (**11**) : $(\text{Zn}(\text{II})) = 1 : 5000$). Isotherms recorded by spreading a solution of cavitand **11** in CHCl_3 and a solution (7.3 mM) of $\text{Zn}(\text{OAc})_2$ in $\text{CHCl}_3/\text{MeOH}$ in volume of c) 0.05 cm^3 , and d) 0.1 cm^3 on the subphase almost saturated with $\text{Zn}(\text{OAc})_2$.

The black and blue curves were collected after spreading a solution of **11** in CHCl_3 (2.2 mg mL^{-1}) on a pure water subphase and on a $\text{Zn}(\text{II})$ -containing subphase (**11**) : $(\text{Zn}(\text{II})) = 1 : 5000$), respectively. The observed variation in the limiting area per molecule from $A \approx 125 \text{ Å}^2$ (isotherm **a**) to $A \approx 169 \text{ Å}^2$ (isotherm **b**), led us to spread a solution of cavitand **11** in CHCl_3 and different volumes of a 7.3 mM solution of $\text{Zn}(\text{AcO})_2$ in a mixture of $\text{CHCl}_3/\text{MeOH}$ 7 : 1 on the water subphase nearly saturated with $\text{Zn}(\text{AcO})_2$. The monolayers ($\text{Zn}(\text{II})$ and **11**) were allowed to equilibrate for 20 min before compression was started. After the solvent evaporated, the additional Zn ions and cavitand **11** molecules should remain at the air-water interface because of the nearly saturated water subphase. In this situation the metal

ions should be close enough to the nitrogen atoms for coordination, resulting in the *vase*-to-*kite* conversion. The green and red isotherms were measured under these experimental conditions. The determined molecular area values are now significantly higher, becoming nearly identical (270 \AA^2 for the red isotherm) to the theoretical value of 290 \AA^2 calculated for a monolayer of **11** in the *kite* form.

Molecular models (Spartan v. 5.1.3 [174]) suggest that the intramolecular distance between two neighbouring quinoxaline nitrogen atoms in the *kite* form is suitable for Zn(II) coordination ($d(\text{N}\cdots\text{Zn(II)}) \approx 2.5 \text{ \AA}$). We hypothesize that the coordination of two Zn(II) ions by the two pairs of neighboring N-atoms can provide the driving force for the observed *vase*-to-*kite* conversion (Figure 2.22). The stoichiometry was determined as 1 : 2 (cavitand : Zn(II)) by using Job's method of continuous variation.

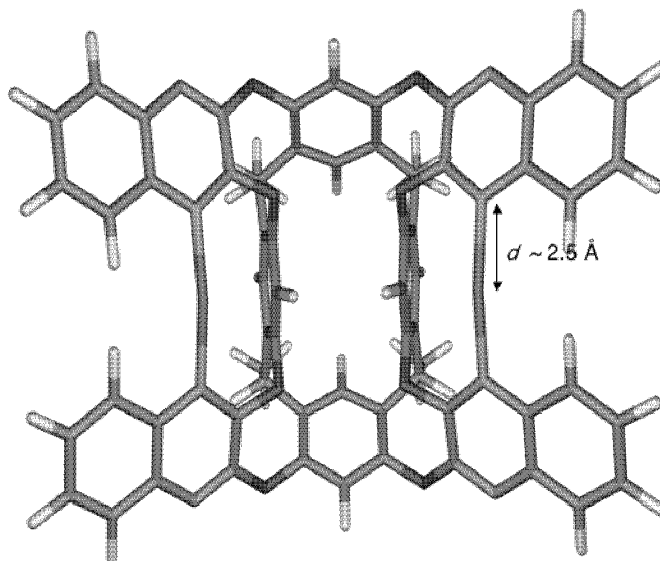


Figure 2.22 Top view of the *kite* form stabilized by coordination of two Zn(II) ions to neighboring quinoxaline N-atoms. Atom colors: gray C, violet N, magenta Zn, red O.

This new metal-induced *vase*-to-*kite* conformational change observed for **11** in the above *Langmuir* experiments was confirmed also in solution (solvent) by $^1\text{H-NMR}$ spectroscopy through monitoring of the methine resonance [130, 132, 134]. As previously reported by *Cram et al.* [132] and *Diederich et al.* [146, 147, 190], the methine protons appear as a triplet at $\sim 5 \text{ ppm}$, characteristic of the *vase* form. Addition of TFA or lowering of the temperature to 193 K shifts the resonance upfield to $\sim 3.8 \text{ ppm}$ which is typical of the *kite* conformer.

Addition of ZnI_2 to a solution of **11** in CD_3OD shifted the triplet in question to 3.90 ppm, thus providing good evidence for the *vase-to-kite* conversion.

2.4 Conformational Transitions of *Langmuir* Monolayers of Resorcin[4]arene-Based Cavitanes bearing Polyethylene Glycol Chains at the Lower Rim

Based on the evidence for the pH-driven switching on the water subphase (*Section 2.3.1*), cavitant **12** (*Figure 2.1*) was synthesized. The presence of four polyethylene glycol chains at the lower rim should improve the spreading behavior of the cavitant. Consequently the *vase-to-kite* conversion should be even easier to observe under the experimental conditions used with **11**. The first step was the investigation of pure **12** at the air-water interface. Several π - A isotherms, recorded at different concentrations of the spreading solution (**12** in CHCl_3), are presented in *Figure 2.23* along with the observed molecular areas.

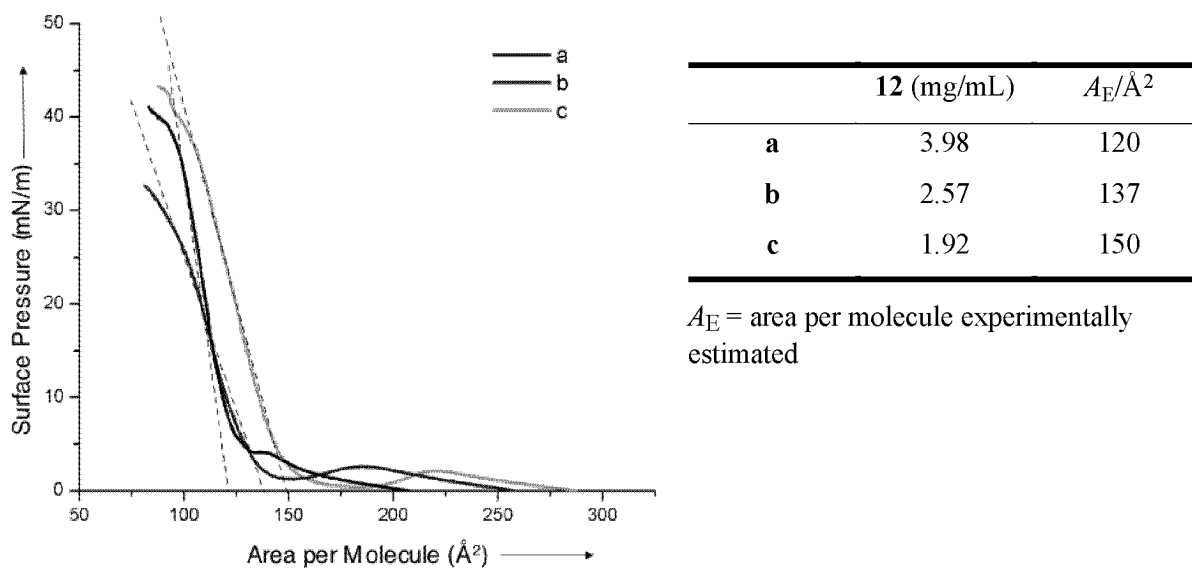


Figure 2.23 Langmuir isotherms recorded at 25 °C after spreading a solution of **12** in CHCl_3 on pure water as a subphase.

For all concentrations, the surface pressure begins to increase in a nearly linear fashion, but for the concentrations of 1.92 mg mL^{-1} and 2.57 mg mL^{-1} , the isotherms show a kink appearing around 3 mN m^{-1} and 4 mN m^{-1} , respectively. Upon further compression, a small

maximum is followed by a slight decrease of the surface pressure before it increases steeply again. The shape of the trough of low pressure is concentration-dependent: the higher the concentration of **12** in CHCl_3 , the less pronounced this depression was. At the concentration of 3.98 mg mL^{-1} , the kink is less pronounced and the surface pressure increases smoothly until the monolayers collapse at around 40 mN m^{-1} . Different explanations can be discussed for this unexpected behavior.

1. Solubility of **12** in the water subphase. Curves **b** and **c** show a region of decreasing pressure probably due to the solubilization of cavitand molecules in the water subphase. Saturation of the subphase is reached rapidly, and the remaining molecules at the air-water interface are compressed which leads to an increase of the pressure. In isotherm **a**, the depression range is less marked because the fraction of solvated molecules is less with respect to the total number of molecules spread on the water surface.

2. Polymer PEG2000¹² attached to a hydrophobic headgroup, which behaves like a highly dynamic random coil in aqueous solution, can readily pack and form a solid crystalline under conditions of high concentration, elevated temperature, or high pressure [191-198]. Furthermore, *Langmuir* measurements on monolayers of PEG2000 attached to an apolar head (PEG2000+)¹³ reveal two phase transitions in the surface *pressure–area* isotherm. This is very similar to what we observed in the case of **12** (*Figure 2.23*). The low pressure transition is generally interpreted as a “pancake-to-mushroom” [191, 193, 199] conformational change in the PEG chain. The second conformational transition is called “mushroom-to-brush” [191, 200-202] (*Figure 2.24*).

In the low surface pressure region (A) ($\pi < \text{the first transition pressure, } \pi_1$), PEG2000+ spreads to form a thin two-dimensional layer. In the medium surface pressure region (B) ($\pi_1 < \pi < \text{the second transition pressure, } \pi_2$) the adsorbed PEG chains partially desorb from the air-water interface and extend into the aqueous subphase. The PEG chains can adopt either a mushroom or a brush conformation. At high surface pressure (C) ($\pi > \pi_2$) PEG chains dehydrate by expelling the associated water and they adopt a more densely packed brush conformation. At this stage, the area per molecule is smaller than in situations A or B and the molecules are highly compressed at the air-water interface.

¹² PEG2000 is a polymer constituted by 40 polyethylene glycol units.

¹³ PEG2000+ is a notation referring to a PEG polymer derivatized with a hydrophobic headgroup.

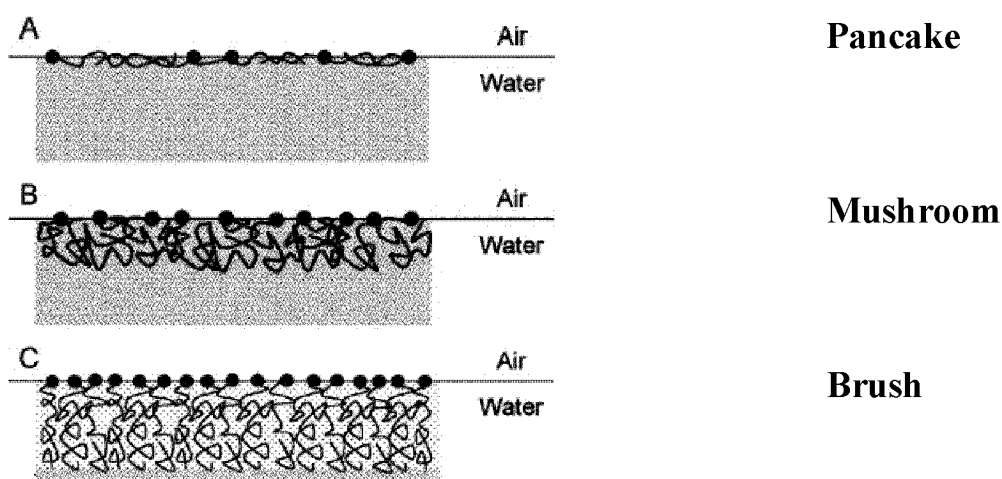


Figure 2.24 Schematic illustration of different conformations of PEG2000+ at the air-water interface as reported by Marchant *et al.* [191]. The surface pressure π increases in the order A, B, C.

Analogously to the isotherm of PEG2000+, the two phase transitions observed in the isotherms reported in Figure 2.23 can be rationalized by considering the different conformations that the polyethylene glycol chains of **12** can assume on the water subphase. At low pressure, the chains occupy a large surface area (Figure 2.24 A for PEG2000+). Under mechanical compression, the polyethylene glycol chains expell the associated water and they extend deeper into the water subphase. This situation corresponds to the pancake-mushroom transition observed for PEG2000+ (Figure 2.24 B). At higher pressure, the polyethylene glycol chains are completely immersed in the subphase and the limiting areas per molecule are determined only by the hydrophobic part of cavitand **12**, in analogy to PEG chains of PEG2000+ in the brush arrangement (cf. Figure 2.24 C). The area per molecule value observed at high pressure is consistent with this hypothesis and corresponds to the *vase* conformation of cavitand **12**. Nevertheless, it was observed that when more concentrated solutions of **12** (Figure 2.23, isotherm a) are spread on the water subphase, polyethylene glycol chains are pushed into the water subphase from the beginning and the above-described transitions are less pronounced upon compression of the monolayer. To confirm this hypothesis, cavitand **13** (Figure 2.25) with longer polyethylene glycol chains was synthesized and its spreading behavior investigated.

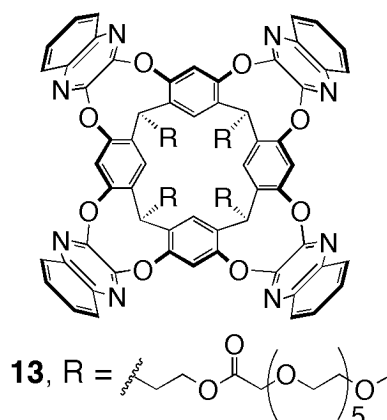


Figure 2.25 Amphiphilic cavitand **13**.

Figure 2.26 shows π - A isotherms of **13** along with the concentration of the used spreading solutions and the observed limiting molecular area.

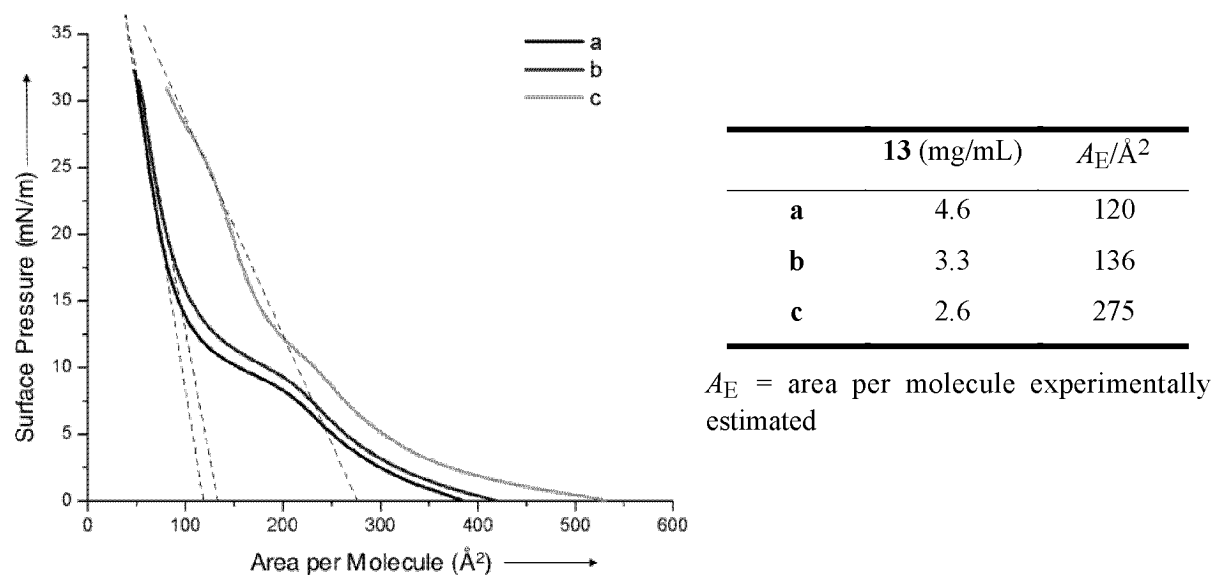


Figure 2.26 Langmuir isotherms recorded by spreading solutions of **13** (CHCl_3) of various concentrations on a pure water subphase at 25 °C.

Cavitand **13** basically shows similar behavior as **12**. The two transition phases and the determined areas per molecule indicate that the polyethylene glycol chains influence the spreading behavior of both cavitands **12** and **13** in a similar way at the air-water interface:

1. At low pressure (see isotherms **a**, **b**, and **c** in *Figures 2.23* and *2.26*) and at low concentration (see isotherms **c** in *Figures 2.23* and *2.26*) monolayers of cavitand **13** show a larger area per molecule than those of cavitand **12**. Supposing that the polyethylene glycol chains are spread at the interface at the beginning of the compression, the larger areas per molecule observed for **13** are due to its longer hydrophilic “legs”. Three additional glycolic units extending at the air-water interface occupy more space.
2. At higher concentrations, both transition phases are observed (isotherm **a**). Chains with five glycolic units (**13**) instead of two (**12**) better approximate the PEG2000+ system for which the described conformational changes due to different orientations at the interface and into the subphase are most dramatic.
3. At high pressure, the determined limiting areas per molecule are similar for both cavitands (**12** and **13**) (see *Figures 2.23* and *2.26*, isotherms **a** and **b**). This could be evidence that at high pressure the PEG chains extend into the water and the area per molecule is determined mainly by the apolar headgroups.

2.5 *Langmuir* Monolayers of Cavitands with Alkyl Chains at the Lower Rim

The presence of alkyl chains at the lower rim of resorcin[4]arene-based cavitands causes different spreading behavior at the air-water interface. This is due to the fact that the cavitand molecules are adsorbed on the water surface with opposite orientation when compared to cavitand **11**. The more polar head (quinoxaline moieties) is in contact with the water and the alkyl chains extend away from the surface [203]. Solutions of **14** (1.95 mg mL⁻¹) and **15** (2.12 mg mL⁻¹) (see *Figure 2.27*) in CHCl₃ were prepared and spread on water. The corresponding π -*A* isotherms are displayed in *Figure 2.27* (**14**: solid line; **15**: dashed line). Both films undergo two successive transitions. In the liquid-expanded (LE) phase the alkyl chains spread out in the plane. The average area per molecule, limited by chain-chain interaction of neighboring molecules is correspondingly large ($A \approx 160 \text{ \AA}^2$). In the liquid condensed phase, the chains are forced to straighten up and the average molecular area is now determined by the average cross section of the upper rim of the cavitands. Finally, in the solid phase, the heads are so tightly packed that the obtained area per molecule is almost equal to the theoretical value calculated for the *vase* conformation [203].

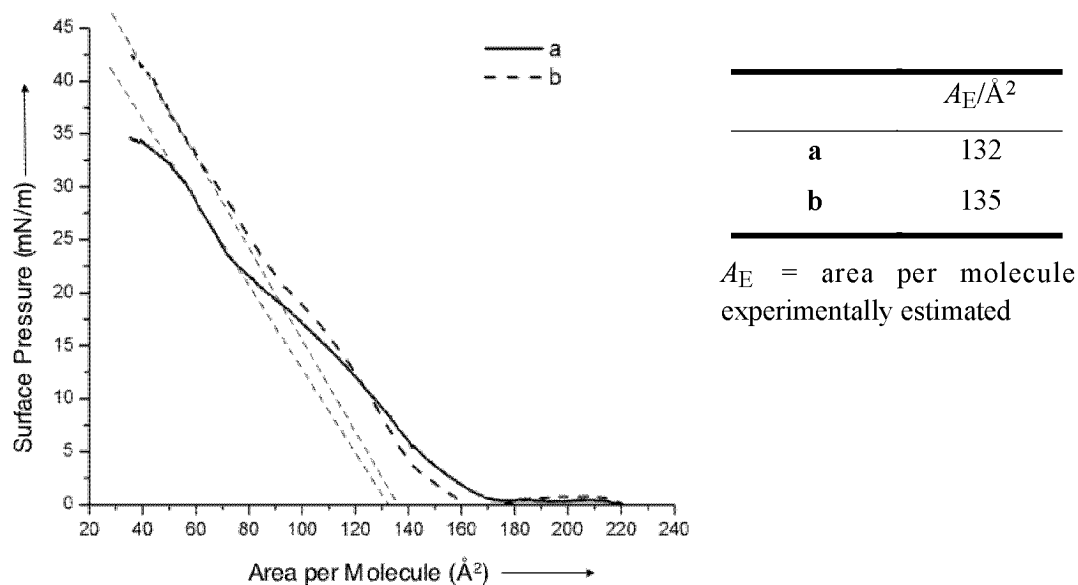


Figure 2.27 Surface pressure–area isotherms measured for cavitands **14** (solid line) and **15** (dashed line) on water as a subphase.

2.6 Conclusion

Langmuir monolayers of resorcin[4]arene-based cavitand **11** were studied on water as a subphase at different pH values (**A**) and in the presence of different metals (Ag^+ , Fe^{3+} , Cu^{2+} , Zn^{2+}) (**B** - **E**); the results are summarized in *Table 2.1*.

Table 2.1 Summary of the *Langmuir* experiments performed with cavitand **11**.

| | | A_0^f | A^g | ΔA^h |
|----------|--------------------|--|--|--|
| | | ($\text{\AA}^2 \text{ molecule}^{-1}$) | ($\text{\AA}^2 \text{ molecule}^{-1}$) | ($\text{\AA}^2 \text{ molecule}^{-1}$) |
| A | pH = 1 | 125 | 223 | 98 |
| B | AgNO_3 | 125 | 145 | 20 |
| C | FeCl_3 | 125 | 130 | 5 |
| D | CuSO_4 | 125 | 114 | -11 |
| E | Zn(OAc)_2 | 125 | 270 | 145 |

- f) Area per molecule obtained by spreading a solution of **11** in CHCl_3 on pure water.
g) Area per molecule obtained by spreading a solution of **11** in CHCl_3 on water containing: A) pH = 1, B) AgNO_3 (27 mg), C) FeCl_3 (26 mg), D) CuSO_4 (25 mg), and E) Zn(OAc)_2 (2 g).
h) $\Delta A = A - A_0$

In the case of acid and zinc(II) ions, the *Langmuir* experiments as well as $^1\text{H-NMR}$ solution measurements demonstrated the feasibility of metal ion-induced *vase-to-kite* conversion.

Monolayers of resorcin[4]arene cavitands **12** and **13** are strongly affected by the presence of polyethylene glycol chains at the lower rim. Film balance measurements reveal two phase transitions in the π -*A* isotherms that crucially depend on the presence of polyethylene glycol chains. It was observed that the area per molecule is larger at low pressure than at high pressure. In particular, cavitand **13**, which has hydrophilic “legs” of five glycolic units, has a larger area per molecule at low pressure than cavitand **12** with only two such units. The different length of the hydrophilic chains at the lower rim also explains the behavior of monolayers at high concentrations: whereas no phase transitions are observed with cavitand **12** at high concentrations, both of them (*vide supra*) are seen with **13**. Legs with five ethylene glycol units approximate the PEG2000 systems for which both phase transitions are very pronounced.

Finally, *Langmuir* investigations on cavitands **14** and **15** (*Figure 2.1*) reveal that these molecules, carrying alkyl chains at their lower rim, orient themselves in such a way that the quinoxaline moieties make contact with the water subphase whereas the hydrophobic chains extend into the air. The presence of two inflection points in the isotherms (*Figure 2.27*) can be ascribed to conformational changes in the alkyl chains. It was found that at low pressure the area per molecule is limited by intermolecular interactions among the conformationally mobile chains, whereas at high pressure, the alkyl groups are well packed and the limiting molecular area is determined by the upper rim of the cavitand.

3 Fullerene-Ionophore Conjugates: Formation of Complexes with Metal Cations at the Air-Water Interface

The special electrochemical and photophysical properties of fullerene-containing monolayers are currently being investigated for their potential applications in microsensors [204], conductive films, and optoelectronic devices [205]. Fullerene monolayers have been created through self-assembly of appropriate derivatives (*Section 1.2.1.2*) or by the *Langmuir* and *Langmuir-Blodgett* techniques [206-211]. Monolayers of pure C₆₀ on water as a subphase are difficult to obtain due to the nonamphiphilic nature of the compound and to the aggregation tendency resulting from strong fullerene-fullerene cohesive interactions. Two approaches are used to form stable fullerene monolayers at the air-water interface: The first consists of embedding pristine C₆₀ into amphiphilic monolayers of a matrix [212-215] to produce mixed *Langmuir* films. Amphiphilic receptor molecules containing a cavity able to incorporate fullerenes such as modified azacrowns [216] or calixarenes [217, 218] are found to be the most suitable matrices for the preparation of fullerene-containing composite *Langmuir* films of good quality. The second approach is characterized by covalent attachment of polar headgroups to the lipophilic fullerene core in order to obtain an adduct with amphiphilic character. In this chapter, we report on *Langmuir* investigations with fullerenes functionalized by hydrophilic groups that stabilize the formed monolayers by interaction with the water subphase [219, 220].

The Chapter is divided into four Sections:

- *Section 3.1* is an introduction giving a general account of the fundamental physical properties of C₆₀.
- *Section 3.2* investigates the amphiphilic behavior of [60]fullerene and crown ether macrocycles at the air-water interface.
- *Section 3.3* presents comprehensive investigations of fullerene-ionophore conjugated monolayers by *Brewster* angle microscopy.
- *Section 3.4* gives a brief summary of the key findings of *Section 3.3*.

3.1 Introduction

Fullerenes were first experimentally observed in 1985 by *Kroto, Smalley, Curl*, and co-workers during experiments aimed at understanding the mechanism by which long-chain carbon molecules are formed in circumstellar shells and interstellar space [221]. The investigators observed that laser vaporization of graphite gave a cluster distribution strongly dominated by sixty- and seventy-carbon atom clusters of molecular masses $m/z = 720$ and 840, respectively. For the extraordinarily stable C_{60} corresponding to the m/z 720 peak, they proposed a spheroidal structure of sp^2 -hybridized carbon atoms with fully saturated valences. The truncated icosahedron, an I_h -symmetrical polygon with 60 vertices and 32 faces (twelve pentagons and 20 hexagons) seemed to best satisfy these requirements. The molecule was called *Buckminsterfullerene* in honor of the American architect *Richard Buckminster Fuller* whose geodesic domes obey similar geometrical rules. Subsequently, many efforts were made to produce and isolate [60]fullerene in macroscopic amounts and in 1990, *Krättschmer, Huffman*, and co-workers were able to find a versatile method: They observed that the soot produced by the vaporization of graphite rods in an electrical arc under an inert atmosphere of helium [222] showed infrared absorptions corresponding to those calculated for I_h-C_{60} [223-225]. Extraction of the soot with benzene allowed the isolation of a mixture of fullerenes. The separation of this mixture by column chromatography allowed the complete spectroscopic characterization of C_{60} and C_{70} and verification of the icosahedral structure of C_{60} [226, 227]. Later on, *Hawkins et al.* determined the X-ray crystal structure of an osmate derivative of C_{60} , which definitively confirmed the “soccer ball” framework of buckminsterfullerene [228].

3.1.1 The Structure of [60]Fullerene

Fullerenes are carbon cages composed of tricoordinate, sp^2 -hybridized carbon atoms assembled to a spheroidal network of five- and six-membered rings. According to *Euler's* theorem, the introduction of twelve pentagons into a plane of hexagons leads to a closed polygonal structure. In accord with this theorem, each fullerene contains $20 + 2n$ ($n > 1$) carbon atoms, where the integer n corresponds to the number of hexagonal faces. A second empirical rule that governs fullerene-type structures is the Isolated Pentagon Rule (IPR). This rule, based on both steric and electronic considerations, states that two pentagons may

never share a common edge. Indeed, among the 1812 distinct fullerene isomers of buckminsterfullerene, only I_h - C_{60} containing 12 pentagons isolated by 20 hexagons (soccer ball structure) is formed in accordance with the IPR. The precise geometric structure of this isomer was determined by X-Ray analysis of pristine C_{60} at low temperature [229-231], C_{60} derivatives [228], C_{60} solvates [232, 233], and solid-state ^{13}C NMR measurements [234]. Such experimental findings definitively confirmed the postulated I_h -symmetry with a mean diameter of ~ 7.1 Å for the sphere. Its *van der Waals* diameter is ~ 10.4 Å, and the distance across the cavity is ~ 3.5 Å. X-Ray crystal structure determinations of C_{60} also prove the existence of two different types of bonds: those common to two hexagons (6-6 bonds, mean distance = 1.391 Å), and those common to a hexagon and a pentagon (6-5 bonds, mean distance = 1.449 Å) [229, 235]. The measured bond lengths clearly show that the double bonds are located at the junctions of two hexagons and there are no double bonds in pentagonal rings (*Figure 3.1*).

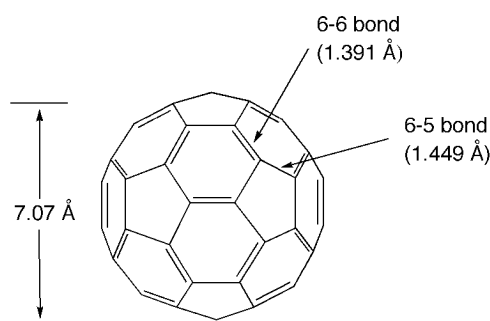


Figure 3.1 Representation of the two different types of bonds in C_{60} , and the nucleus-to-nucleus diameter.

The crystal structure of pristine C_{60} reveals poor π -electron delocalization, and the bond length alternation clearly defines a preference for the unique resonance structure in which the 30 double bonds are formally localized at 6-6 junctions. This can be considered as consequence of the pyramidalization of the sp^2 -carbon atoms which leads to a substantial rehybridization. This rehybridization is in part responsible for the high electron affinity of C_{60} since it considerably reduces the energy of the lowest unoccupied molecular orbital (LUMO). A more complete picture of the electronic structure of C_{60} is obtained by *Hückel Molecular Orbital* (HMO) theory which predicts an electronic configuration with a five-fold

degenerate HOMO (h_u) and a three-fold degenerate low-lying LUMO (t_{1u}) (Figure 3.2), separated by a moderate energy gap of ~ 1.8 eV [236-238].

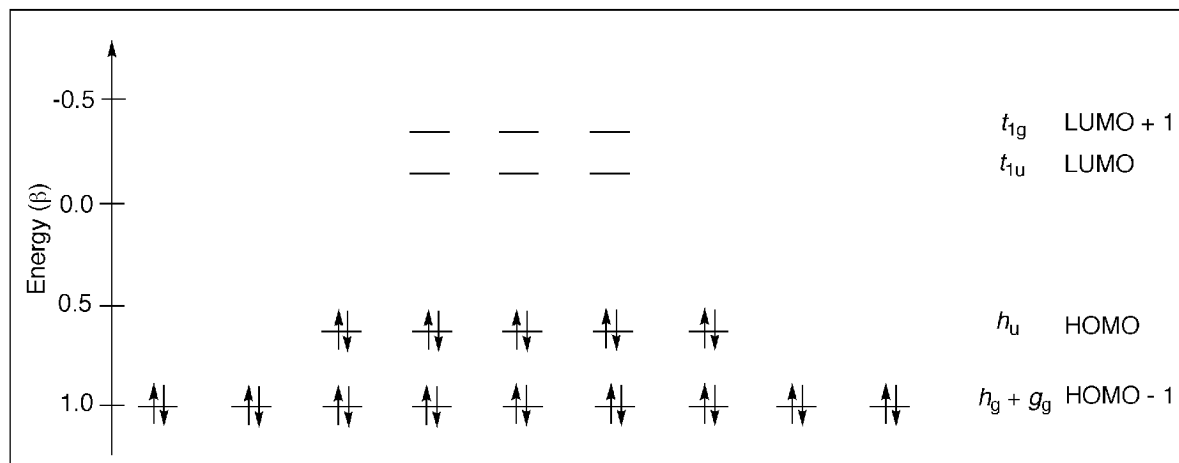


Figure 3.2 Schematic representation of the HOMO-1, HOMO, LUMO, and LUMO+1 Hückel molecular orbitals of C_{60} .

3.1.2 Electrochemical Properties of C_{60}

C_{60} possesses very interesting electrochemical properties which are related to its electronic configuration. In accord with the degeneration of the LUMO level, the redox chemistry demonstrates the ability of [60]fullerene to accept up to six electrons [239]. The systematic proof for the triple degeneracy of the LUMO level of C_{60} came with the detection of fullerene anions C_{60}^{2-} [240], C_{60}^{3-} [241], C_{60}^{4-} [242], and C_{60}^{5-} [243]. However, in 1992 all six one-electron reductions, leading to C_{60}^{6-} , were detected by three independent groups [244-246]. *Echegoyen* and co-workers first managed to generate and detect stable C_{60}^{n-} ($n = 1-6$) using cyclic voltammetry (CV) and differential pulse voltammetry (DPV) [245]. The potentials measured ($E^{1/2}$) were -0.98 , -1.37 , -1.87 , -2.35 , -2.85 , and -3.26 V vs Fc/Fc⁺ (in PhMe/MeCN 1:5) [245]. The separation between any two successive reductions is relatively constant and amounts to $\sim 450 \pm 50$ mV. This correlates well with the triple degeneracy of the LUMO level. Considering the HMO diagram (Figure 3.2), oxidation of C_{60} consists in the removal of an electron from the low-lying HOMO, leading to an important destabilization of the π -electron system. Correspondingly, the first one-electron oxidation of C_{60} occurs at a highly positive potential, 1.26 V vs Fc/Fc⁺ in 1,1,2,2-tetrachloroethane. The difference in potential between the first oxidation and the first reduction of C_{60} ($E^{1/2}_{ox} - E^{1/2}_{red} = 2.32$ V)

is a good measure of the HOMO-LUMO gap in solution and correlates well with the calculated value (1.5 - 2.0 eV) [247].

3.1.3 Spectroscopic Properties

The UV-VIS spectrum of C₆₀ shows intense absorption bands between 190 and 410 nm (maxima at 328, 256, and 211 nm). These bands are due to symmetry-allowed singlet-singlet transitions from the HOMO to the LUMO+1 (*Figure 3.2*). In the visible region, the spectrum is characterized by a weak broad band between 440 and 620 nm with two maxima located at 598 and 543 nm [248-250] which correspond to symmetry-forbidden singlet-singlet transitions from the HOMO to the LUMO and LUMO+1. Chemical functionalization of buckminsterfullerene modifies the electronic structure of the fullerene chromophore. This is strongly reflected in the UV-VIS spectra of its derivatives. The degree of variation is dependent on *i*) the number of addends, *ii*) the geometric addition pattern in multiadducts, and *iii*) the electronic structure of the functional group [248, 251]. The derivatization of the fullerene core reduces its symmetry, thereby enhancing transition probabilities. Consequently, C₆₀ derivatives show stronger absorptions in the visible region with respect to pristine C₆₀. The absorptions at 257 and 329 nm are hardly shifted as a result of the functionalization but less intense, which is consistent with the transition from a 60- to a 58- π -electron system [248]. Very characteristic for all 6-6 closed monoadducts are the absorptions at ~ 430 and ~ 695 nm [252-254].

3.2 Fullerene- and Crown Ether-containing *Langmuir* Films

3.2.1 Thin Film Fullerene-Based Materials

Due to the unique characteristics of C₆₀, the investigation of its redox and photophysical properties in monomeric and in aggregated forms has become a focus of considerable interest [59]. C₆₀ is known to exhibit some marvelous properties, such as superconductivity observed upon doping with metals [255, 256], non-linear optical properties [257], and unique electrochemical properties [208, 228, 258, 259]. As a consequence, new materials with a wide range of distinguished physicochemical properties have been discovered that encouraged the exploration of potential applications in advanced (nano-)materials science [260, 261]. Many advanced materials applications of [60]fullerene require an arrangement of

molecules in well-ordered two- or three-dimensional networks. One of the most useful methods for the construction of ordered networks is to make thin solid films of high quality. The LB technique is one of the simplest methods for obtaining organized thin solid films of fullerene derivatives [213, 262, 263]. Despite the fact that C_{60} itself does not possess any amphiphilic character, many rather unsuccessful efforts have been made to form *Langmuir* or LB monolayers of this fullerene [206, 209, 264-267]. *Langmuir* and BAM investigations of pure monolayers of C_{60} at the air-water interface reveal unambiguous evidence for the formation of multilayers [212], even with dilute solutions ($\sim 10^{-5}$ M in various solvents) and at low compression rates. A typical π - A isotherm of buckminsterfullerene on a water subphase is shown in *Figure 3.3 a*. The fully compressed fullerene monolayer is remarkably rigid and visibly patchy as seen in the optical micrograph of the film (*Figure 3.3 b*) on the hydrophobic substrate [268]. In *Figure 3.3 b*, it is possible to see the morphology of two-dimensional crystalline islands, formed by aggregation of the carbon spheres immediately after spreading them on the pure water subphase. The arrow points at one of these crystalline particles in the thick layers.

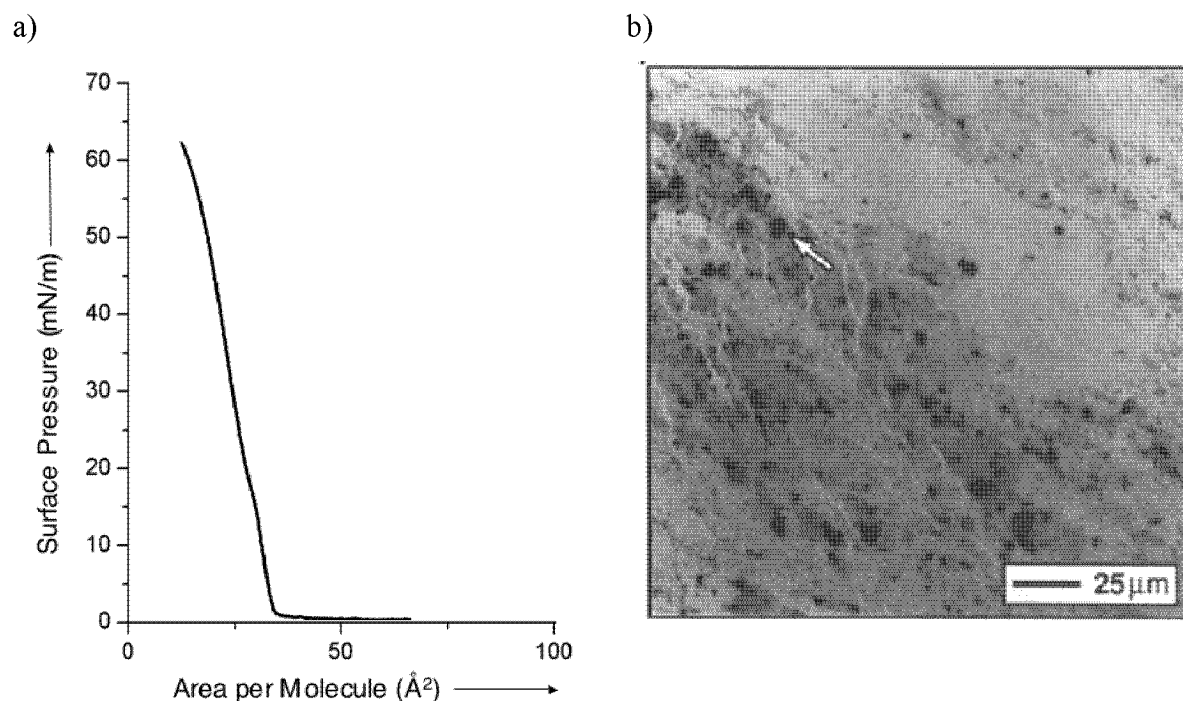


Figure 3.3 Spreading behavior of [60]fullerene at the air-water interface: a) π - A isotherm measured in the context of the present thesis (spreading solution: 10^{-4} M in toluene); b) optical micrographs of *Langmuir* films on the hydrophobic substrate, as reported by Tomioka *et al.* [268].

The limiting area per molecule (A), obtained by extrapolating the linearly ascending part of the π - A isotherm in *Figure 3.3 a* to zero pressure, ranges between 20 and 30 Å² [206, 264, 269] which is only about 1/4 of the value calculated for C₆₀ (86.6 Å²), assuming a tight hexagonal packing with a nearest center-to-center distance of 10 Å [222, 270].

Such a reduced area per molecule suggests that the floating film of pure C₆₀ on water consists of more than a single molecule in thickness. This is a direct consequence of the pronounced hydrophobic character of the fullerene and its high cohesive energy (31 kcal mol⁻¹) that play a key role in (mono)layer formation (*Figure 3.4*).

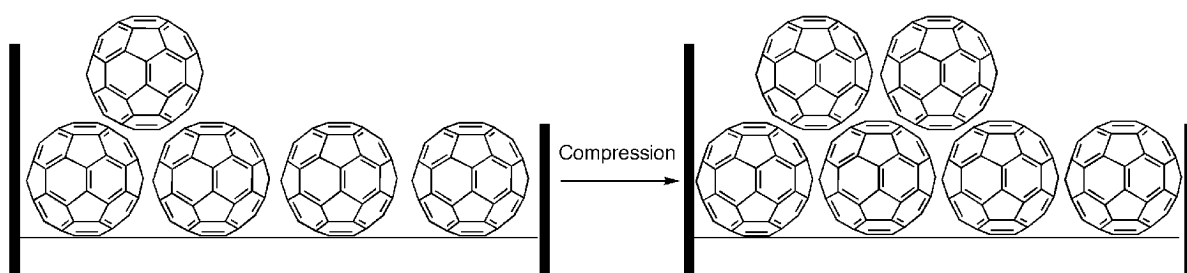
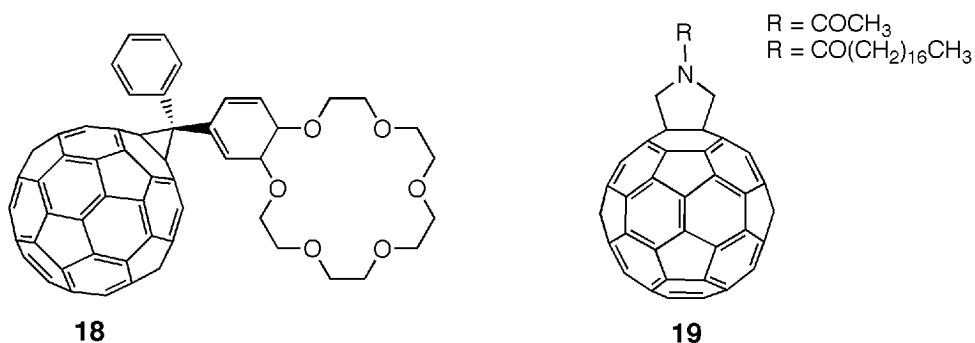


Figure 3.4 Aggregates of C₆₀ obtained by compression of a fullerene film at the air-water interface.

The first idea to overcome the tendency to aggregate was a chemical derivatization of the fullerene core with hydrophilic groups [207, 265, 271-278]. This confers an amphiphilic character to the molecule and enhances its interaction with the water subphase. This strategy gave promising results in terms of seeing agreement between experimentally observed and calculated area per molecule [270].



Leblanc and coworkers prepared *Langmuir* monolayers of fullerenes functionalized with benzocrown ether **18** [279]. The limiting molecular area observed is in good agreement with

that reported for C_{60} , indicating the formation of a monolayer in which the polar crown ether is directed into the water subphase. However, BAM images recorded during compression reveal the presence of solid domains even at very low pressure. *Maggini et al.* prepared a series of *N*-acylated fulleropyrrolidine derivatives of type **19** [280, 281]. Due to the hydrophilicity of the amide group, the fullerene is better anchored on the subphase, favoring the formation of monomolecular layers. Nevertheless, aggregation still occurs and no transfer to a solid substrate was possible.

In both systems the presence of hydrophilic headgroups increases the amphiphilic character of the molecules and improves their spreading behavior, thus leading to limiting molecular areas that are significantly larger than those obtained with pristine C_{60} . However, the hydrophilic moiety is not bulky enough to prevent fullerene-fullerene aggregation, as schematically shown in *Figure 3.4*. Therefore, to prepare a “well-behaved” monolayer of a C_{60} -derivative at the air-water interface, it is necessary to expand the size of the headgroup to keep the carbon spheres apart. This way the corresponding intermolecular interactions should be entirely disrupted (*Figure 3.5*).

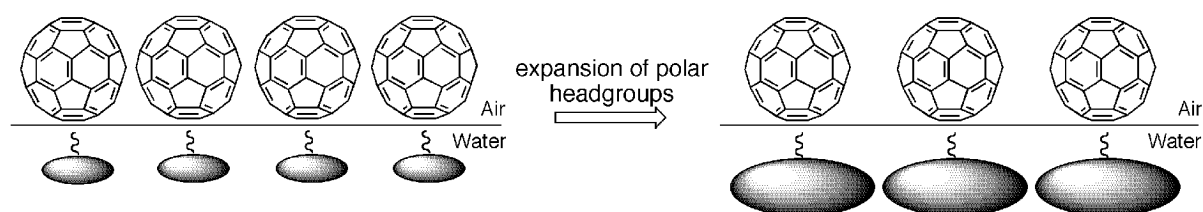
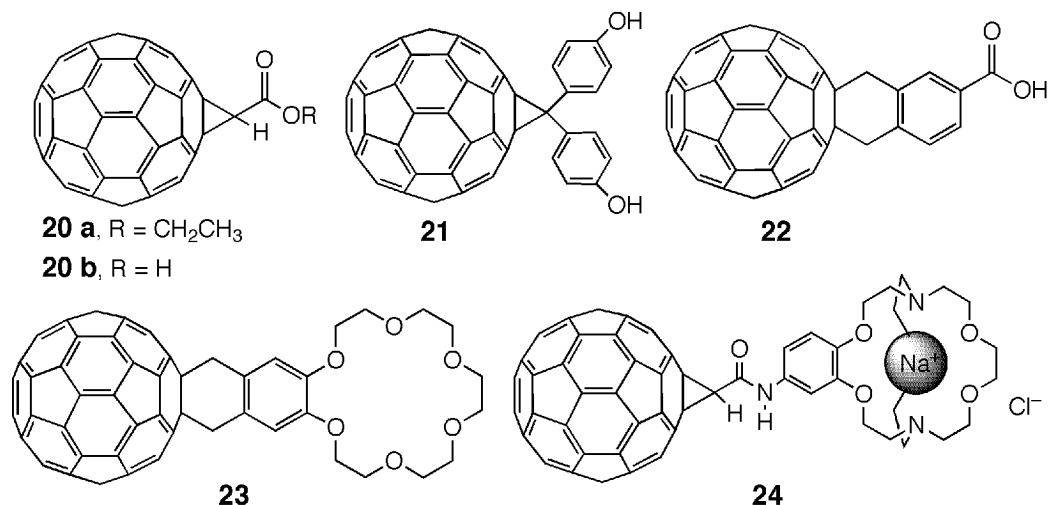
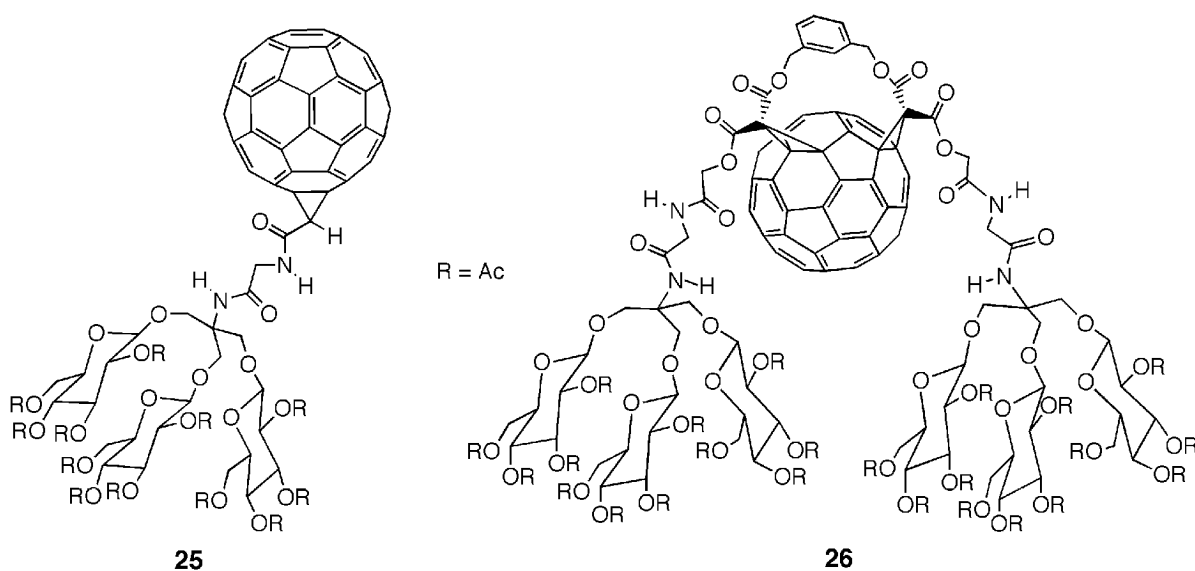


Figure 3.5 Schematic representation of the effect of the size of the headgroup on the aggregation of neighboring carbon spheres of fullerene derivatives at the air-water interface.

Diederich et al. studied the effect of the structure of the headgroup on the spreading behavior of monofunctionalized buckminsterfullerenes. They prepared a series of amphiphilic monoadducts by cyclopropanation of C_{60} (**20 a** and **b**, **21**, **24**) and by *Diels–Alder* addition of *ortho*-quinodimethane intermediates (**22**, **23**). They observed that the larger the headgroup, the greater is the experimentally determined molecular area requirement. The limiting area per molecule increases from compounds **20 a** and **b** ($A \approx 28 \text{ \AA}^2$) to compounds **23** ($A > 90 \text{ \AA}^2$) [278] and **24** ($A \approx 80 \text{ \AA}^2$), leading to monolayers of enhanced quality in the case of the last two fullerene-derivatives.

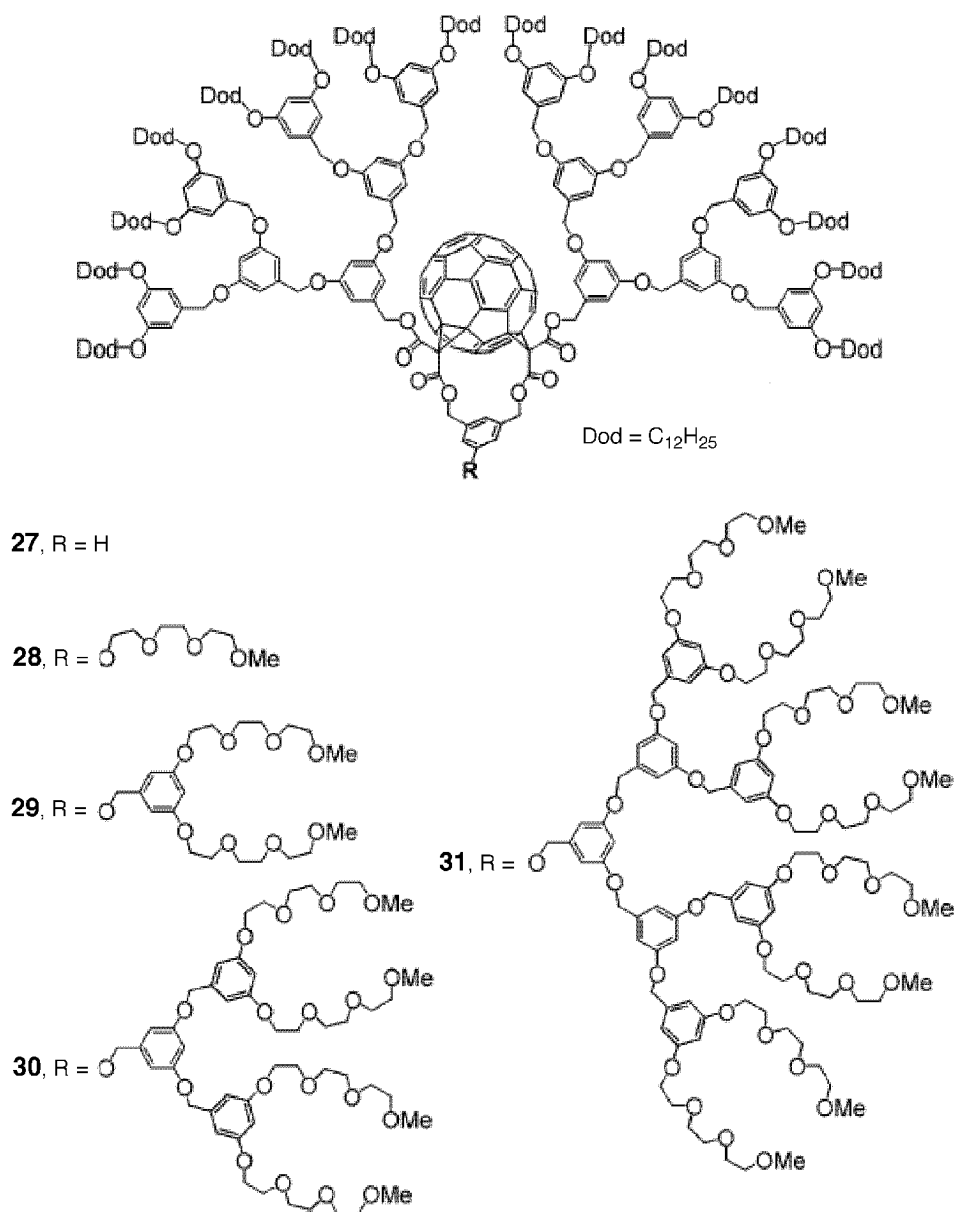


However, light microscopy observation and compression/expansion cycles still reveal an irreversible aggregation in *Langmuir* films, even of **23** and **24**, thereby demonstrating that the polar headgroup is not completely effective at preventing fullerene aggregation [220, 278]. Subsequently, an impressive example of stable, ordered, and reversible monomolecular fullerene layers at the air-water interface was reported by *Diederich* and co-workers, who took advantage of the versatile regioselective *Bingel* reaction [282, 283] of *m*-xylylene-bismalonates to prepare, besides C₆₀-derived amphiphilic monoadduct **25**, bis-adduct **26** bearing polar and bulky glycodendron tail groups [284].



These derivatives displayed reversible behavior in successive compression/expansion cycles. The hydrophilic parts are bulky enough to prevent contact between neighboring fullerene

cores when the film is compressed. Thus, the irreversible aggregation previously observed did not occur. The monolayers could also be successfully transferred onto quartz slides and the resulting films are likely X-type (head-to-tail arrangement) (see *Section 1.33*). Following a similar strategy, *Nierengarten* and co-workers [118, 119, 274, 285] prepared a series of amphiphilic dendrimers with fullerene cores (**27** - **31**) [286].



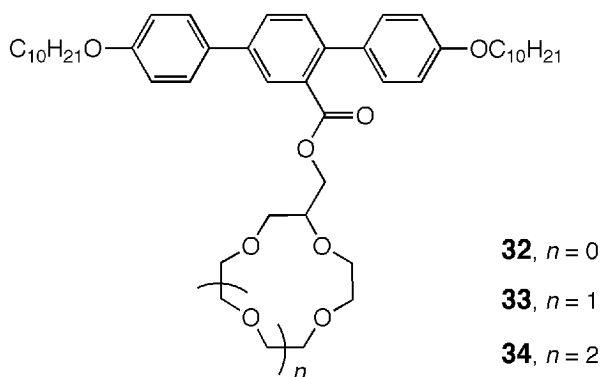
Owing to the good hydrophobicity/hydrophilicity balance, all these compounds formed stable films with reversible behavior upon successive compression/expansion cycles. Compounds **28-30** were transferred onto hydrophilic silicon (111) wafers, creating LB films of excellent quality.

In the cases of **28** and **29**, the UV-VIS spectrum of the LB layers revealed a broadening of the absorption in the film compared to that in solution. This observation is indicative of fullerene-fullerene interactions [286], which may be ascribed to the contact of carbon spheres from neighboring layers. In fact, the presence of the dendritic shell segregates C₆₀ cores, preventing interactions between fullerenes within a layer.

The broadening of the UV-VIS absorptions almost vanishes for **30** and **31**, suggesting that the dendritic shell completely covers the fullerene core, consequently preventing any fullerene-fullerene interactions. To put it in “*Orwellian*” style: no head, no film, small head, weak films” [286].

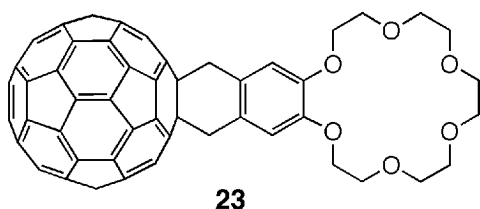
3.2.2 Langmuir Monolayers Containing Macrocyclic Ionophores

The pioneering work of *Pedersen* [287, 288] led to extensive studies of synthetic macrocyclic molecules [289, 290]. More recent interest focuses on their properties as constituents of membranes and thin solid films. In particular, the receptor and carrier characteristics of macrocyclic ionophores allowed the development of supramolecular devices for the investigation of ion transport through biological membranes and as sensitive elements in biosensors. Therefore, investigations into the behavior of natural and synthetic ionophores at the air-water interface are of great relevance [291]. Crown ethers represent the most important class of synthetic ionophores. However, crown ethers themselves do not form stable monolayers because of an insufficient balance between hydrophilicity and hydrophobicity. Modification of crown ethers [291-298] with long hydrocarbon chains allows the preparation of surface-active derivatives that are able to form stable monolayers at the air-water interface. To study the complexation in floating monolayers, changes in the isotherms due to the presence of different metal cations in the water subphase were investigated [299, 300]. Differences in the complexation selectivity of crown ethers can be determined at interfaces in the presence of various alkali metal cations [301]. The surface area occupied by the ionophores depends on the kind and concentration of alkali metal salts in the subphase. *Tschierske* and co-workers studied the ion selectivity at the air-water interface of a series of crown ether derivatives (**32** – **34**) that differ only in ring size [302]. They investigated the spreading behavior of **32** - **34** on water containing Li⁺, Na⁺, K⁺, Rb⁺, and Cs⁺ ions. All three compounds showed the same π -*A* isotherm on pure water.



When alkali metal salts were added to the subphase, profound changes in the isotherms were detected such as an increase of the limiting molecular area as well as of the surface pressure. These effects are due to the complexation of alkali metal ions by the hydrophilic crown ether moiety which enhances the amphiphilic character of the crown ether derivatives and improves their spreading behavior at the air-water interface. The monolayers of **32** are significantly stabilized by Li^+ ions, whereas those of **33** interact best with Na^+ , and those of **34** with K^+ . The different selectivities are related to the size of the crown ether and the radii of the cations in the subphase [291]. Potassium ions, for example, are too large for the small cavity of **32**, whereas they fit better in the larger cavity of **34**. In general, as observed by *Pedersen* [287, 288], the factors influencing the stability of the complexes stabilized by ion-dipole interactions between the cation and the oxygen atoms with their lone pairs, include the relative sizes of cyclopolyether and cation, the number of oxygen atoms in the former, the orientation of the lone pairs (conformational preference of the macrocycle), and the tendency of the ions to interact with the solvent which – in the alkali metal series – is a function of the charge density.

Diederich et al. reported the first example of monolayers of a fullerene-ionophore conjugate (**23**). They studied the influence of K^+ ions on its spreading behavior [278] and found that the quality of the monolayers is strongly influenced by the presence of potassium ions. The limiting molecular area increases from 80 to 90 \AA^2 when the water subphase is replaced by a 1M aq. solution of KCl.



The measured surface requirements suggest the formation of a real monolayer at low pressure, stabilized by the hydrophilic headgroup which consists of the crown ether complex. As reported by *Leigh et al.* [303], the morphology of such monolayers can change after addition of cations to the subphase (*Figure 3.6*). Complexation can cause tilting of the fullerene-crown ether molecular axis (*Figure 3.6 b*) or induce a conformational change in the crown ether moiety (*Figure 3.6 c*) when compared to the monolayer on a pure water subphase (*Figure 3.6 a*).

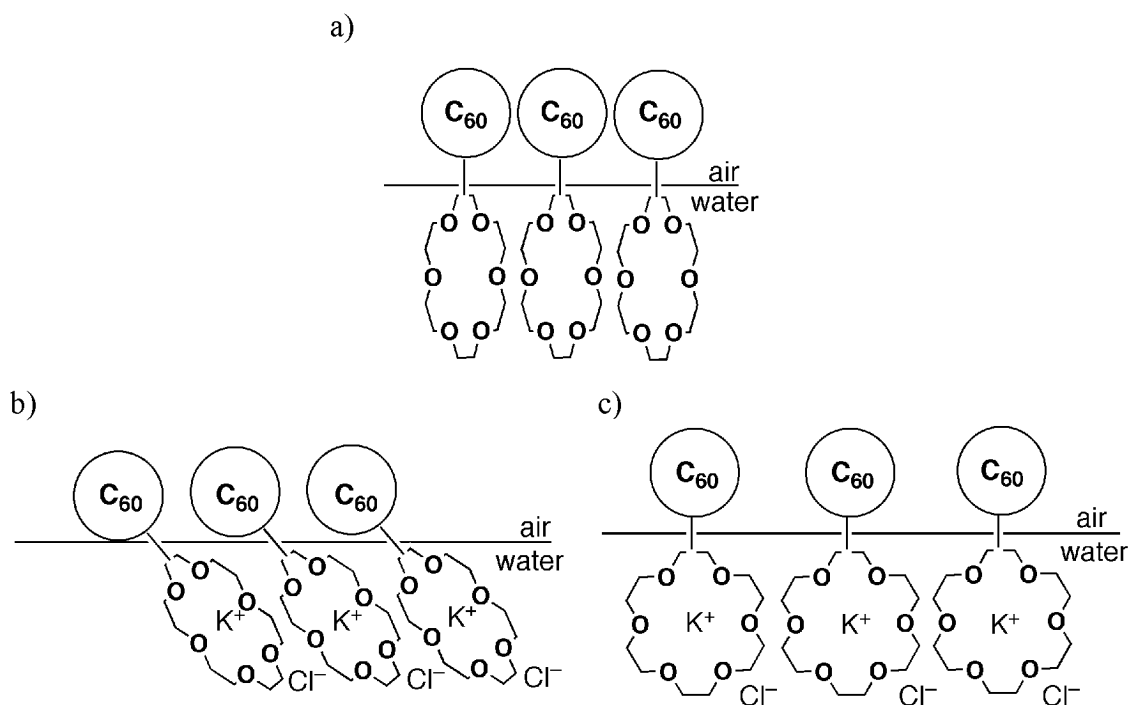


Figure 3.6 Schematic representation of different morphologies adopted by C₆₀-crown ether conjugate in *Langmuir* films on a) pure water, and b) and c) 1M aq. KCl.

Although the limiting area per molecule of **23** increases upon addition of K⁺ to the subphase, BAM investigations revealed film damage upon re-expansion following the initial compression [220]. Again, the irreversible aggregation of neighboring fullerenes is not prevented by the moderately bulky headgroups and causes the formation of a rigid monolayer at the air-water interface.

With this in mind, two new fullerene-ionophores, **35** and **36**, were designed in the context of the present thesis. They include one (**35**) and two (**36**) dibenzo[24]crown-8 ether moieties that were attached to the fullerene core by the *Bingel* reaction (*Figure 3.7*).

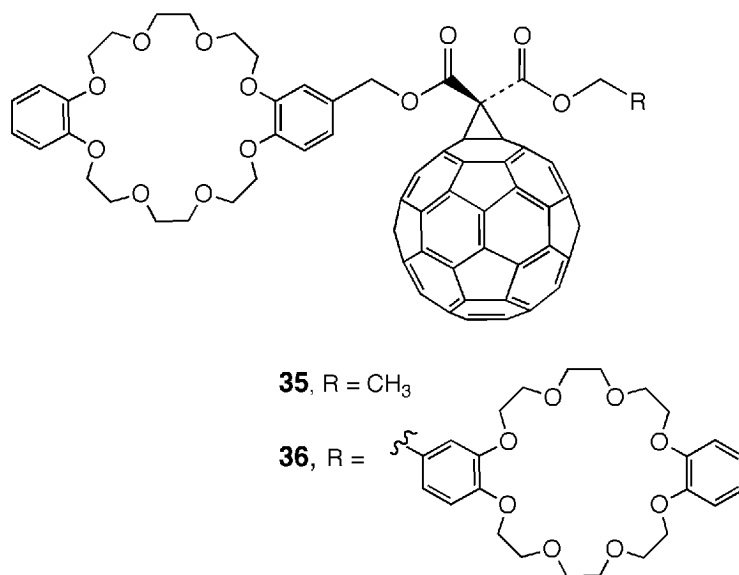


Figure 3.7 Molecular structures of C₆₀-derived ionophores **35** and **36**.

These two derivatives should be more hydrophilic than compound **23** because of the larger crown ether (**35**) or the presence of two such units (**36**). Moreover, the cyclopropanedicarboxylate moiety in **35** and **36** is more hydrophilic than the tetrahydronaphthalene connector of **23**. Besides, the way the ionophores are attached to the fullerene core gives them a greater conformational freedom in the water subphase as compared to **23**.

In the next *Section*, we describe *Langmuir* and BAM investigations of the spreading behavior of C₆₀-derivatives **35** and **36** on pure water and on aqueous subphases containing different alkali metal salts.

3.3 *Langmuir* Monolayers of Fullerene-Ionophore Conjugates **35** and **36**

Due to the ability of crown ethers to bind alkali metal ions with a certain selectivity [291, 292, 300, 304, 305], the *Langmuir* experiments with **35** and **36** were carried out on both pure water and on 1M aqueous solutions of different alkali metal salts (LiCl, NaCl, KCl, CsCl) and CaCl₂. We expected that cations with a larger radius would bind better to the dibenzo[24]crown-8 moieties and thus have a more pronounced impact on the π -*A* isotherms of both compounds.

3.3.1 Langmuir Monolayers of **35** and **36** on Pure Water and on 1M aq. LiCl, CaCl₂, NaCl, KCl, and CsCl as Subphases

The surface pressure–molecular area isotherms obtained for fullerene derivatives **35** (solid line) and **36** (dashed line) on pure water are shown in *Figure 3.8*. The observed limiting molecular areas are 60 Å² and 75 Å² for **35** and **36**, respectively. Even if they are smaller than the theoretical value calculated for pristine C₆₀, the two values suggest that the area per molecule is determined by the fullerene moieties, evidencing that the molecules line up with their long axes perpendicular to the air-water interface (cf. *Figure 3.6 a*). The C₆₀ cores are close to each other, and the strong fullerene-fullerene cohesive interactions cause the formation of irreversible monolayers as usually observed with pristine buckminsterfullerene and its amphiphilic derivatives bearing compact headgroups [213, 285, 306].

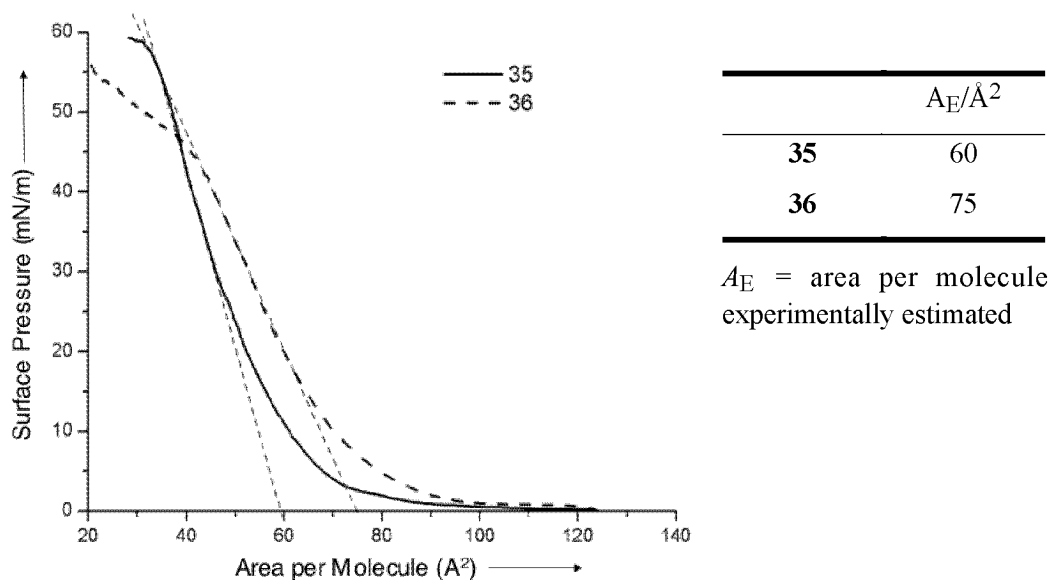


Figure 3.8 π - A Isotherms of fullerene-crown ether conjugates **35** (solid line) and **36** (dashed line) on a pure water subphase.

Important information on the spreading behavior of **35** and **36** was obtained by means of *Brewster* angle microscopy. BAM images reveal an immediate aggregation of the C₆₀-derivatives after spreading of the samples at the air-water interface (*Figure 3.9 a*, picture 1 and *b*, picture 1).

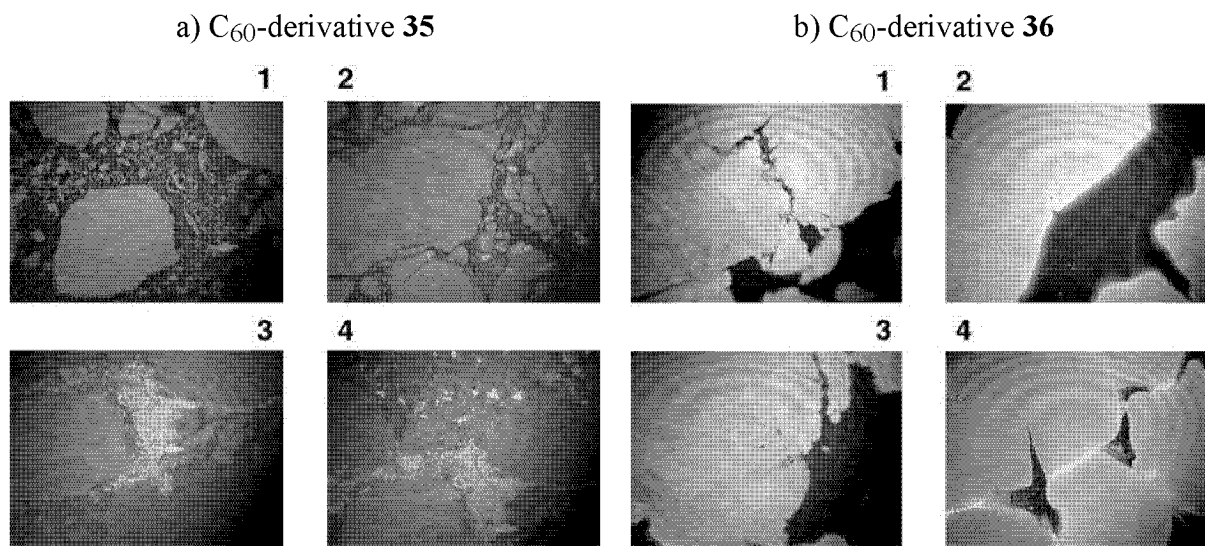


Figure 3.9 BAM images of monolayers of C_{60} -crown ether conjugates a) **35** and b) **36** at pressures of: 1) 0 mN m^{-1} , 2) 0.7 mN m^{-1} , 3) 11 mN m^{-1} , and 4) 45 mN m^{-1} . Subphases: pure water.

The aggregates are pushed together by lateral compression without any apparent change in the general appearance (BAM images). It ensues that the morphology of the layers does not change (pictures 1-3 in *Figures 3.9 a* and *b*), and the aggregates persist until the film collapses, providing evidence for the formation of non-homogeneous layers (*Figures 3.9 a*, picture 4 and *b*, picture 4). The surface pressure–molecular area isotherm of **35** is steep as that of pristine buckminsterfullerene (*Figure 3.3 a*) suggesting formation of a rigid film. Even if the limiting area per molecule **35** (60 \AA^2) is larger than that of pure C_{60} ($20\text{--}30 \text{ \AA}^2$), a strong tendency to escape from the air-water interface to form three-dimensional aggregates is observed. In fact, BAM images show areas of different brightness confirming the formation of multilayers with C_{60} -derivatives stacked on top each other (*Figure 3.9 a*). The steep slope in the π – A isotherm of **35** indicates the presence of incompressible and condensed two-dimensional phases [277]. Rather different BAM images were obtained with derivative **36**. The homogeneous distribution of light intensity within the bright domains demonstrates the monomolecular nature of the freshly spread film. The domains, formed even at low surface pressure, expand gradually upon compression without changing their brightness up to film collapse (picture 4 in *Figure 3.9 b*), at which point a non-homogeneous structure can be observed. But a comparison of the collapse pressure values (*Figure 3.8*) shows that the

monolayers formed by **36** are less stable than those of derivative **35**, possibly due to the presence of two crown ether moieties in the molecule. On one hand, the two hydrophilic headgroups in **36** enhance the amphiphilicity of the fullerene core and lead to better anchoring in the water subphase and, accordingly, the surface requirement increases from 58 Å² (**35**) to 75 Å² (**36**). On the other hand, if both derivatives are positioned at the air-water interface as shown in *Figure 3.6 a*, compression may lead to unfavorable intra- or intermolecular interactions of the densely packed crown ethers of **36**, destabilizing the monolayer and causing a premature collapse.

When both compounds are spread on a 1M aq. LiCl (*Figure 3.10*) subphase, no variation in the spreading behavior of **35** and **36** was detected with respect to the case of a pure water subphase (*Figure 3.8*). In fact, the limiting areas per molecule do not change appreciably: The values observed are 60Å² and 78Å² for **35** and **36**, respectively. The π - A isotherms (*Figure 3.10*) basically show the same shape, except at low pressures where the isotherm of **35** appears less steep than that recorded on pure water (black curve in *Figure 3.8*), an effect that is indicative of a less rigid behavior. The isotherm of **35** on 1M aq. LiCl (blue isotherm in *Figure 3.10*) displays a phase transition at 5 mN m⁻¹ with a liquid-like region at lower pressures and a condensed phase at higher pressures.

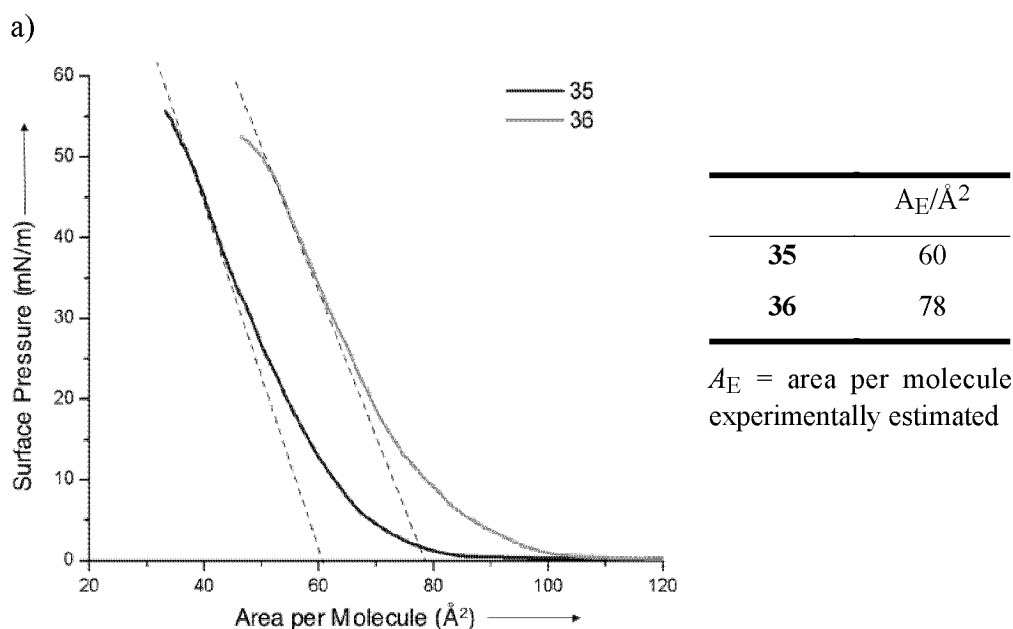


Figure 3.10 Surface pressure–molecular area isotherms of fullerene-crown ether conjugates **35** and **36** on a 1M aq. LiCl subphase.

BAM images reveal that both derivatives form aggregates on a 1M aq. LiCl subphase even at low pressures (pictures 1 in *Figures 3.11 a* and *b*).

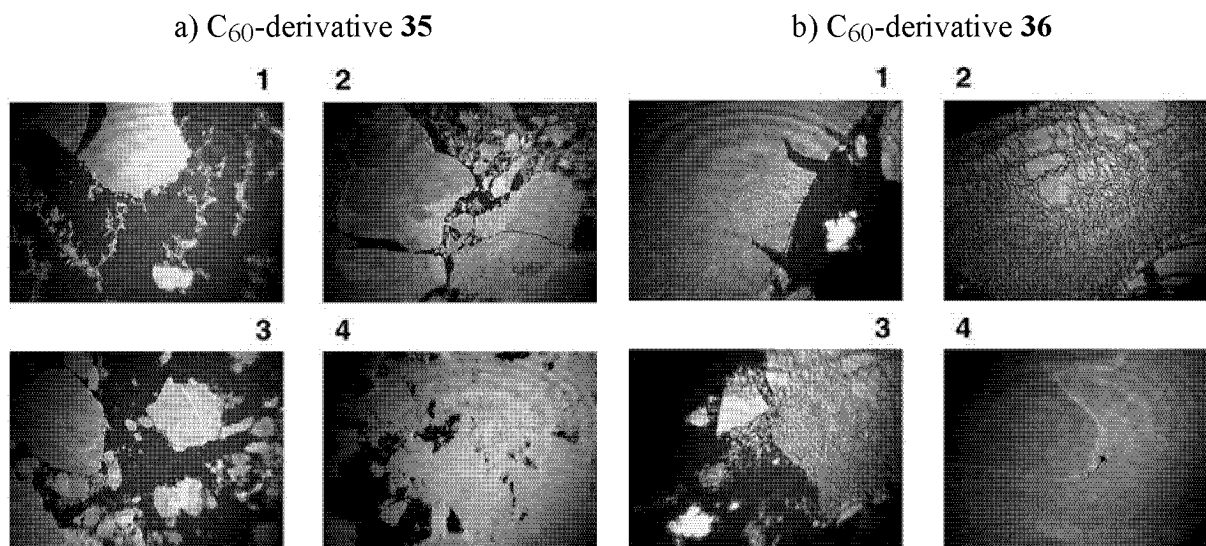


Figure 3.11 BAM images of monolayers of C_{60} -crown ether conjugates: a) **35** and b) **36** on 1M aq. LiCl subphase at pressures of: 1) 0.3 mN m^{-1} , 2) 0.6 mN m^{-1} , 3) 4 mN m^{-1} , and 4) 30 mN m^{-1} .

In the case of compound **35**, the images reveal the formation of a multilayered film. Areas of different brightness are detected (pictures 2 and 3 in *Figure 3.11 a*). Pictures 4 (*Figures 3.11 a* and *b*) show the monolayers at 30 mN m^{-1} . At this pressure, the layer of **35** appears discontinuous with holes through which the subphase can be seen (*Figure 3.11 a*), whereas the layer of **36** appears more homogeneous. This is attributed to the enhanced amphiphilic character of **36** as compared to **35**.

When spread on a 1M aq. CaCl_2 subphase, neither **35** nor **36** shows any appreciable variation in the limiting area occupied per molecule, when compared to the spreading on pure water (*Figure 3.12 a*).

The π - A isotherms recorded in the presence of Ca^{2+} ions (*Figure 3.12 a*) do not show any variation in shape aside from the collapse pressure which slightly increases for both monolayers (**35** and **36**) when compared to the situation of a pure water subphase (*Figure 3.8*). BAM investigations reveal that the molecules associate to form islands already at large molecular areas, similar to the cases of pure water and of Li^+ -containing subphases. These islands fuse to give irreversible layers of **35** and **36**, which appear more homogeneous than in the cases of 1M aq. LiCl subphase (*Figures 3.11 a* and *b*, pictures 4).

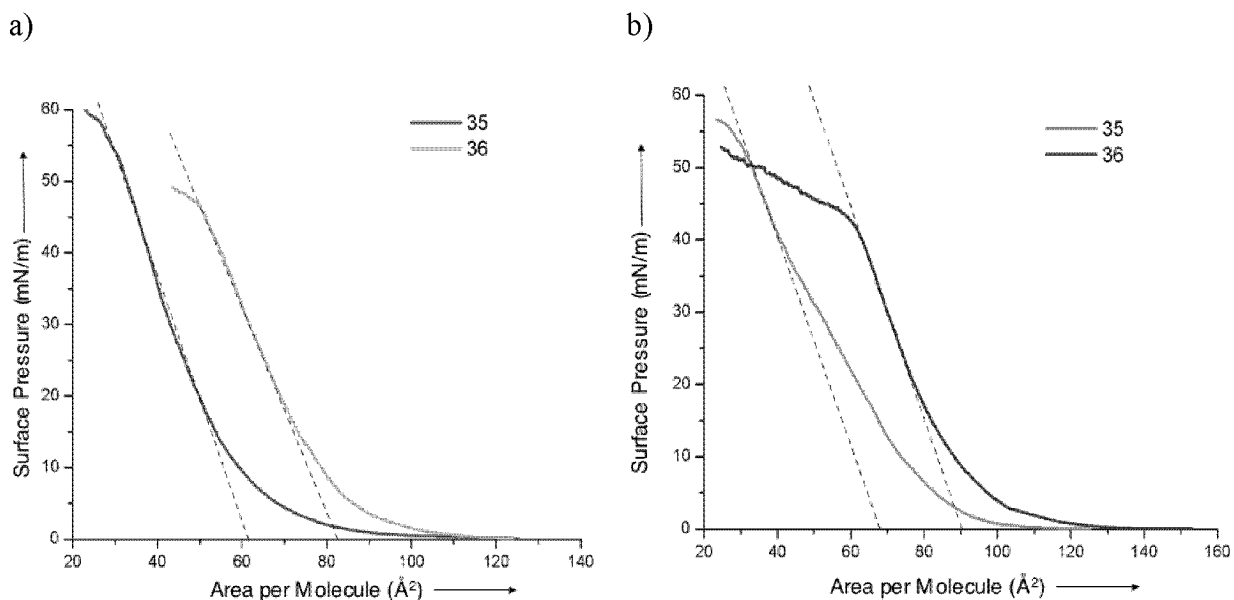


Figure 3.12 Surface pressure–molecular area isotherms of crown ether–fullerene conjugates **35** and **36** on a) 1M aq. CaCl_2 , and b) 1M aq. NaCl subphases.

On 1M aq. NaCl subphase, larger molecular area requirements are detected (Figure 3.12 b). In particular, the limiting molecular area of **35** increases from 60 \AA^2 (pure water subphase) to 67 \AA^2 , whereas that of **36** increases from 75 to 90 \AA^2 . The latter values are in agreement with areas measured by *Diederich et al.* [220] and *Leigh et al.* [303] for other C_{60} -crown ether derivatives. The monolayer at zero pressure shows the coexistence between the liquid-expanded (bright zone) and the liquid-condensed phases (gray zone) (Picture 1 in Figure 3.13 b) that fuse to form a nicely uniform image without any scattered defects (Picture 2 in Figure 3.13 b). During compression, no variations in the monolayer morphology are observed. Expansion/compression cycles evidence the irreversible nature of the monolayer. BAM investigations on the film of **35**, on the other hand, show non-homogeneous reflectivity. It seems that a second layer overgrows the first layer giving areas of different brightness. At the end of compression, the monolayer appears more uniform with some holes through which the subphase can be seen. The apparent better quality of the film of **36** (compared to **35**) may be related to the presence of two crown ethers that anchor it better to the water subphase, making it a better amphiphile.

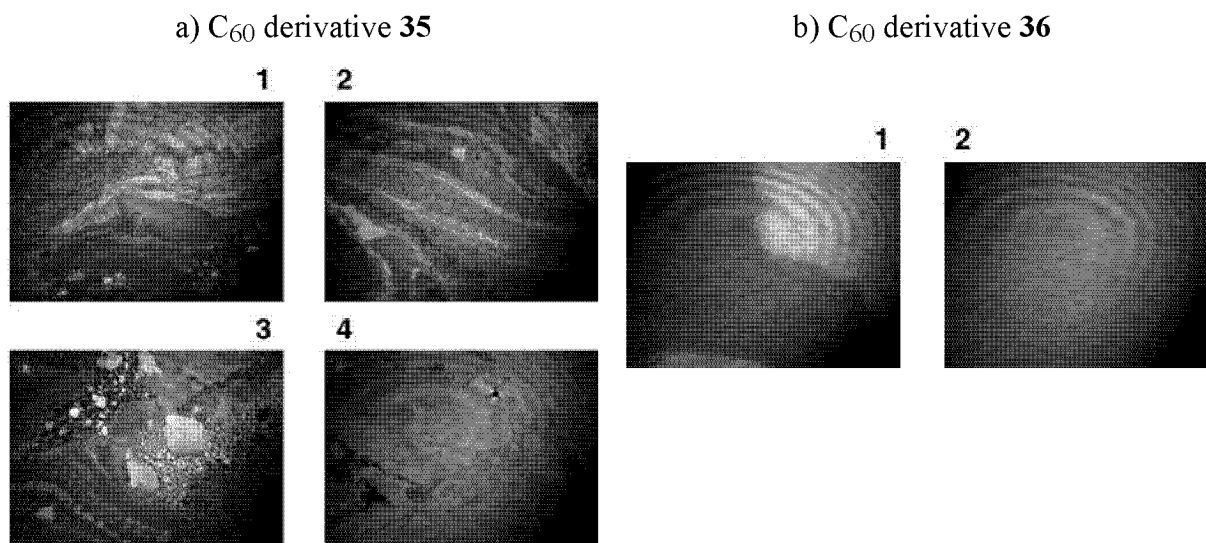


Figure 3.13 BAM images of monolayers of C_{60} -crown ether conjugates a) **35** and b) **36** on 1M aq. NaCl. Pressures: a) 0.2 mN m^{-1} (1), 0.4 mN m^{-1} (2), 3 mN m^{-1} (3), 30 mN m^{-1} (4); b) 0 mN m^{-1} (1), 30 mN m^{-1} (2).

Finally, *Langmuir* monolayers of both compounds were prepared on 1M aq. KCl and 1M aq. CsCl subphases. The limiting molecular areas extracted from the π - A isotherms are 87 \AA^2 for **35** and 100 \AA^2 for **36** (K^+ -containing subphase, Figure 3.14 a), whereas even larger values were obtained with the Cs^+ -containing subphase: 97 \AA^2 for **35** and 120 \AA^2 for **36** (Figure 3.14 b).

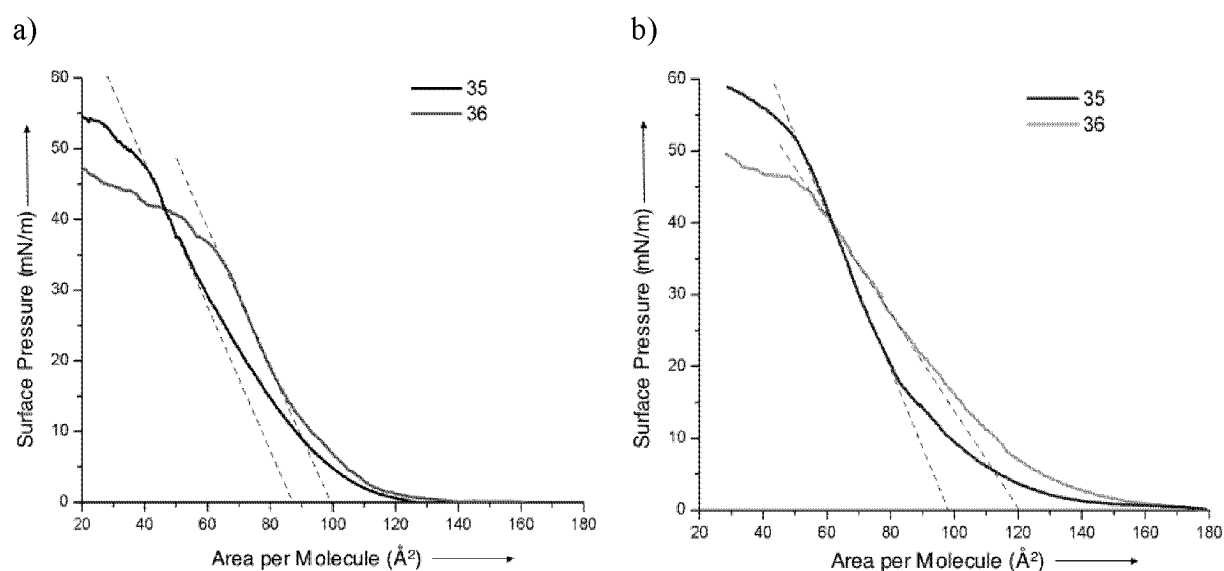


Figure 3.14 Surface pressure-molecular area isotherms of fullerene-crown ether conjugates **35** and **36** on a) 1M aq. KCl, and b) 1M aq. CsCl.

As indicated by the higher collapse pressures, the layers are more stable for derivative **36** as compared to **35** and in the presence of CsCl than of KCl. The morphology of the films does not change in the transition from K^+ to Cs^+ as subphase solute, and aggregation is already observed at large molecular areas, demonstrating that the fullerene-fullerene interactions cannot be prevented in this system. When reexpanded, the molecules stay aggregated and cracks appear in the film upon expansion showing the irreversibility of the monolayer formation. Attempts to transfer monolayers of **36** from either subphase to a glass support were unsuccessful.

Analysis of the obtained results leads to the following conclusions:

1. As expected, the presence of two crown ether moieties improves the hydrophilicity of fullerene-ionophore conjugate **36** as compared to **35** on pure water as well as on subphases containing different metal salts. In all the performed experiments, extrapolation of the linearly ascending part of the measured isotherms to zero pressure yields a limiting area per molecule that is larger for **36** than for **35** and almost equal to or even higher than the ideal value calculated for pure C_{60} (86 \AA^2 [270]). This is related to the presence of two crown ethers that improve the spreading behavior of **36** as compared to **35**. The presence of cations in the water subphase increases the amphiphilicity of the conjugates or, in other words, the metal ion complexes provide better anchoring on the subphase. Moreover, the complexation may also cause the crown ether moieties to assume a more extended conformation, leading to higher molecular area requirements (*Figure 3.6 c*).
2. A correlation is observed between the limiting area per molecule and the radius of the alkali metal ion solubilized in the water subphase. Ca^{2+} as a doubly charged alkaline earth metal ion does not fit into this series.

The ionic radii of the complexed cations, together with the measured ΔA^{14} (\AA^2) values and the logarithms of the association constants reported for the complexation of the cations by dibenzo[24]crown-8 in water are listed in *Table 3.1*. Considering the cavity size of dibenzo[24]crown-8 ($4.5 - 5 \text{ \AA}$ [307, 308]) and the ionic radii reported in *Table 3.1*, it can be argued that the crown ether has the highest affinity for K^+ and Cs^+ .

¹⁴ ΔA is defined as the difference between the area per molecule observed on the metal ion-containing aq. subphase and that observed on pure water (60 \AA^2 and 75 \AA^2 for **35** and **36**, respectively).

Table 3.1 Variation of the molecular surface requirement as a function of the ionic radius (\AA) of the cation dissolved in the subphase (anion = Cl^- in all cases).

| Cation | Radius (\AA) | $\log(K_a)$ | ΔA (\AA^2) for 35 | ΔA (\AA^2) for 36 |
|---------------|-------------------------|-------------------|---|---|
| Li^+ | 0.76 | a | 0 | 3 |
| Na^+ | 1.02 | 2.25 ^b | 8 | 15 |
| K^+ | 1.38 | 3.49 ^b | 27 | 25 |
| Cs^+ | 1.67 | 3.78 ^b | 37 | 55 |

^a Association constant not reported in literature.

^b Association constant in MeOH at 25 °C [309].

In line with this trend, the spreading behavior of fullerene derivatives **35** and **36** improves and the limiting area per molecule increases with the size of the ions present in the water subphase, the best results being obtained with K^+ and Cs^+ . The formation of complexes between the crown ethers of **35** and **36** and the ions increases the hydrophilicity of the cyclopolyether moieties and, consequently, the fullerene core is better anchored at the air-water interface. In addition, complexation may cause an orientational or a conformational change in the amphiphiles (cf. *Figures 3.6 b* and *c*), thus further hampering the strong fullerene-fullerene aggregation and leading to the formation of less rigid monolayers. Nevertheless, even the monolayers on aq. KCl and aq. CsCl subphases show an irreversible character, evidencing that the crown ether complexes in both compounds are not bulky enough to completely prevent close contacts between the fullerene cores of **35** and **36**. The higher ΔA observed with Cs^+ as compared to K^+ (*Table 3.1*) reflects the selectivity of the crown ether for the different alkali-metal ions [48, 310-313] as shown from the complexation constants [309, 314]. In the case of Li^+ which is much smaller than the cavity of the dibenzo[24]crown-8, the monolayers of both **35** and **36** show the same behavior as on the pure water subphase and no variation in the limiting molecular area (ΔA) is observed (*Table 3.1*). Due to the strong fullerene-fullerene interactions, molecules can escape the water subphase, leading to a three-dimensional aggregation and formation of multilayered films. On a NaCl-containing subphase, variations in the molecular area requirements (ΔA , *Table 3.1*) were observed for both fullerene derivatives, although Na^+ ions are smaller than the binding site of the macrocycle. This may be related to the formation of disodium complexes which is well known for dibenzo[24]crown-8 (*Figure 3.15*). In this 2:1 complex, two Na^+ ions closely interact with one side of the macrocycle while the opposite oligoethylene glycol

chain extends somewhat to relieve the charge repulsion between the two cations within the cavity [289].

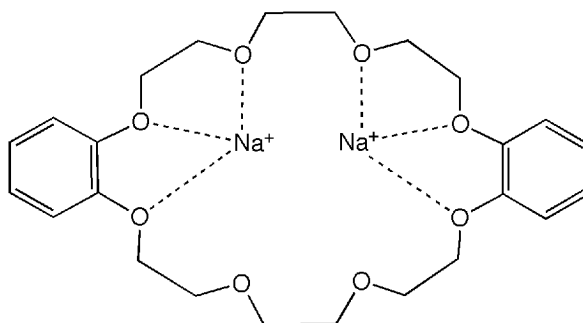


Figure 3.15 Geometry of the disodium complex of dibenzo[24]-crown-8, reported by Gokel [289].

In the case of the CaCl_2 -containing subphase, the variation in the molecular area (ΔA) is smaller (2 \AA^2 and 8 \AA^2 for **35** and **36**, respectively) than that measured on aq. NaCl, KCl, and CsCl subphases. Although the high charge density of Ca^{2+} (*ca.* twice that of Na^+) should favor ion-dipole interactions with the lone pairs of the crown ether oxygen atoms, it is also responsible for a strong solvation by water molecules, most of which need to be stripped off during complexation. Besides, the lack of knowledge on the structure of the calcium complex of dibenzo[24]crown-8 makes any prediction of the influence of Ca^{2+} on the spreading behavior of **35** and **36** difficult. On the other hand, taking into account the relation between the complexation constant and the spreading behavior in the cases of the alkali metals, we may simply hypothesize that the complexation of Ca^{2+} by dibenzo[24]crown-8 in water is rather weak¹⁵ [287, 288].

3.4 Conclusion

Pristine C_{60} does not form stable monolayers at the air-water interface due to its non-amphiphilic character. On the basis of strong cohesive forces, the fullerene molecules interact strongly with each other within the resulting *Langmuir* films which are extremely rigid and their formation irreversible. Modification of the fullerene core with polar headgroups affords surface-active derivatives that are able to form stable monolayers at the air-water interface, provided the headgroups are bulky enough to prevent fullerene-fullerene

¹⁵ The association constant for the dibenzo[24]crown-8•calcium(II) complex is not reported in literature.

aggregation. To this end, we prepared two fullerene derivatives bearing one (**35**) and two (**36**) dibenzo[24]crown-8 ether moieties (*Figure 3.7*) that anchor the fullerene core to the water subphase, thus improving their spreading behavior. In particular, we investigated the effect of the complexation of metal cations by the dibenzo[24]crown-8 moieties on the film-forming abilities of **35** and **36**. The spreading behavior on pure water and on aqueous metal salt solutions was studied by π -*A* isotherm measurements and the film morphologies investigated by *Brewster* angle microscopy. The comparison between **35** and **36** suggests that two crown ethers attached to the fullerene core improve its spreading behavior more than one. In fact, on a pure water subphase, the limiting molecular area increases from 60 Å² (**35**) to 72 Å² (**36**). *Langmuir* experiments performed with both derivatives on water subphases containing LiCl, NaCl, KCl, CsCl, and CaCl₂ evidenced a correlation between ionic radii and limiting molecular areas. Particularly large molecular area requirements were detected on aq. KCl (**35**: 87 Å², **36**: 100 Å²) and aq. CsCl (**35**: 97 Å², **36**: 120 Å²) subphases which are both larger than the theoretical value calculated for C₆₀ (86 Å). This trend is paralleled by the affinity of dibenzo[24]crown-8 for the used alkali metal ions and can be understood in terms of a further enhancement of the hydrophilicity of the polar headgroups by complexation and, therefore, a better anchoring of the studied molecules on the respective subphases. Na⁺ and Ca²⁺ have almost the same ionic radius but lead to different spreading behaviors of **35** and **36** when present in the aq. subphase, which is probably related to their different charge densities and different association constants with dibenzo[24]crown-8.

4 *Langmuir–Blodgett* Multilayers of Porphyrin- and [60]Fullerene-Containing Derivatives: Spectroscopic Investigations

Photosynthetic systems contain ordered assemblies of porphyrin derivatives that may be potentially useful as photoconductors [315, 316] and chemical sensors [317-321]. Consequently, the elucidation of the structural organization and photophysical properties of porphyrin derivatives assembled in ordered molecular arrays is a topic of high current interest [322]. In the past, the electronic and spectroscopic properties of porphyrins in thin solid films were examined [323-325]. Since the proximity and relative orientation of natural porphyrins in biological systems is very important for functions such as light-induced charge separation and energy transduction, the *Langmuir–Blodgett* (LB) [92] method is widely used as one of the most versatile techniques for fabricating organic thin films with well controlled composition, structure, and thickness [326]

In this *Chapter*, we report *Langmuir* and *Langmuir–Blodgett* investigations of two porphyrin-crown ether dyads, **42** and **43** (*Figure 4.6*), which differ only in the linker between the hydrophobic (porphyrin) and hydrophilic (crown ether) part, and of the porphyrin-fullerene-crown ether triad **44** (*Figure 4.6*).

The *Chapter* is divided into four Sections:

- *Section 4.1* is an introduction giving a general account of porphyrins, their structures and photochemical properties.
- *Section 4.2* discusses *Langmuir* monolayers formed by amphiphilic porphyrins and porphyrin-[60]fullerene dyads.
- *Section 4.3* presents a comprehensive investigation of *Langmuir–Blodgett* layers of porphyrin-crown ether conjugates **42** and **43** and of porphyrin-[60]fullerene-crown ether conjugate **44** (the work presented in this *Section* is the fruit of a joint effort with *Dr. Jean-Louis Gallani* at the *CNRS, Strasbourg*)
- *Section 4.4* gives a brief summary of the key findings of *Section 4.3*.

4.1 General Account of Porphyrins

The name ‘porphyrin’ derives from the Greek “πορφυρος” (*porphuros*) and has been used to denominate the basic skeleton of a series of deep purple or red tetrapyrrolic macrocycles [327]. These macrocycles, *e.g.* chlorins, bacteriochlorins, porphyrinogens, protoporphyrins, represent an ubiquitous class of naturally occurring compounds. They include many important biological representatives playing essential roles in various biological processes such as electron transfer, oxygen transfer, and light energy harvesting [328-331]. Two representative examples are heme and chlorophyll. Heme is an iron(II)-protoporphyrin-IX complex (*Figure 4.1 a*) which is the prosthetic group in hemoglobins and myoglobins. The latter two biomolecules are responsible for oxygen transport and storage in living tissues [4]. Chlorophylls (chlorophyll *a*: *Figure 4.1 b*) are the green photosynthetic pigment that plays a key role in the transformation of solar (photonic) energy into chemical energy during natural photosynthesis in which the energy absorbed by chlorophylls is used to transform carbon dioxide and water into carbohydrates and oxygen [332, 333].

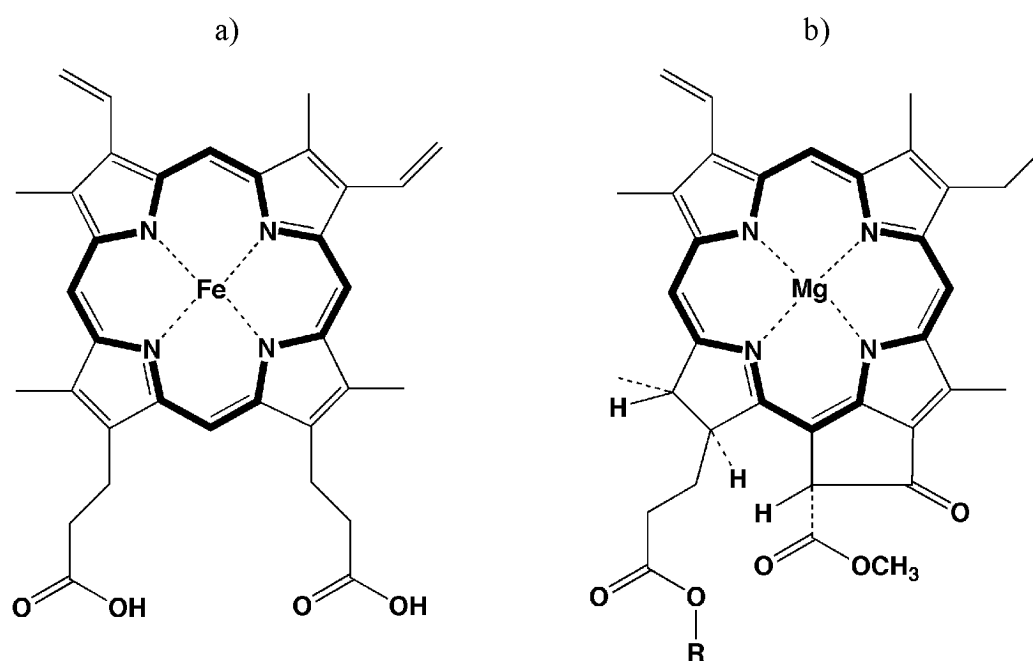


Figure 4.1 Structure of tetrapyrrolic macrocycles: a) heme and b) chlorophyll a.

The basic porphyrin skeleton consists of four pyrrole-type heterocycles interconnected by four methine groups at positions 2 and 5 (*Figure 4.1*). This conjugated macrocycle includes a perimeter with 18 π -electrons which is aromatic according to *Hückel's* rule ($4n + 2$

delocalized π -electrons, with $n = 4$) [334]. The UV-VIS absorption spectrum of a porphyrin system exhibits very characteristic bands: *i*) the *B* band, also called *Soret* band, appears between 380 and 420 nm and corresponds to a strong transition from the ground state to the second excited state $S_0 \rightarrow S_2$ (ϵ between 2×10^5 and $4 \times 10^5 \text{ M}^{-1} \text{ cm}^{-1}$), *ii*) the *Q* bands between 500 and 600 nm relate to the weak transition from the ground state to the first excited state $S_0 \rightarrow S_1$ (ϵ between 1.2×10^4 and $2 \times 10^4 \text{ M}^{-1} \text{ cm}^{-1}$). The *B* and *Q* band arise from π - π^* transitions and can be explained by considering the four frontier orbitals of the porphyrin: two almost isoenergetic π orbitals (a_{1u} and a_{2u}) and two degenerate π^* orbitals (e_{gx} and e_{gy}).

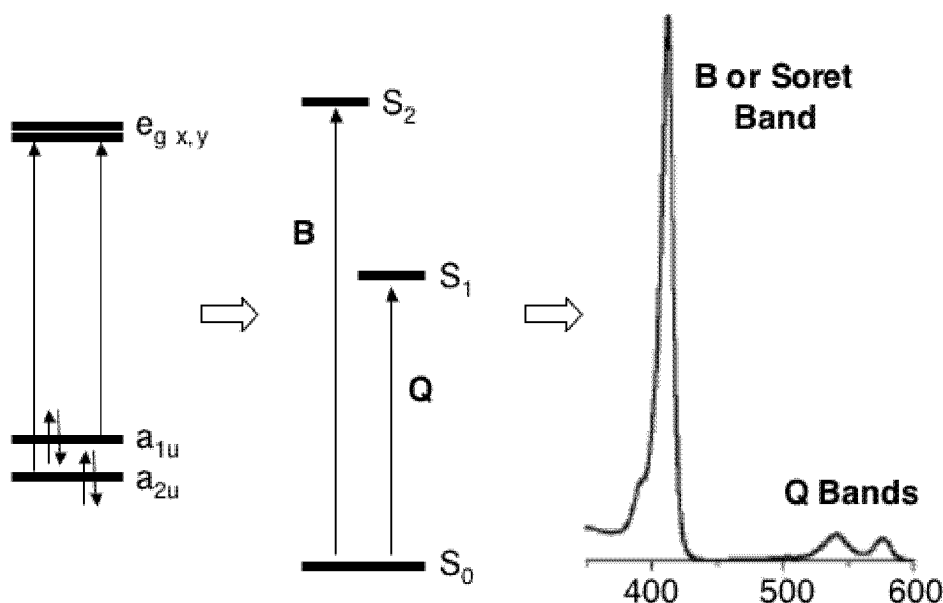


Figure 4.2 The four molecular orbitals explaining the absorption spectrum of a porphyrin macrocycle, as reported by *Anderson* [335].

Supposing that the $a_{1u} \rightarrow e_g$ and $a_{2u} \rightarrow e_g$ transitions have the same energy and lead to two almost coincident absorptions, the two bands mix together by a process known as configurational interaction and resulting in two bands with very different intensities and positions, as schematically shown in *Figure 4.2*. In particular, constructive interference leads to the intense short-wavelength *B* band, while the weak long-wavelength *Q* band result from destructive combination [335]. Due to their distinctive optical and electrochemical properties, porphyrins have been extensively studied to mimick biological functions [336, 337] or as sensing material for gas sensors [61, 338]. However, control over structural organization at the molecular level is an essential requirement for molecular electronics

applications or for assembling new materials mimicking the photosynthetic processes [54, 66]. Consequently, the arrangement of functional molecules and their relative orientation play an important role for the efficiency of these molecular photodevices. Different approaches can be taken to fix position and orientation of the porphyrins by incorporating them into molecular assemblies. Among these, the *Langmuir–Blodgett* technique is one of the most versatile methods [91, 339–344]. In the next *Section*, some elegant examples of *Langmuir–Blodgett* layers of porphyrins are presented.

4.2 Thin Films of Porphyrin Derivatives

The first study of a monomolecular film of porphyrins (chlorophyll a and hemin) on a water subphase was reported by *Alexander* [345]. He studied the spreading behavior of different porphyrins at the air-water interface. From the observed area per molecule and the general stability of the films, he concluded that the porphyrins were packed face-to-face and oriented vertically with respect to the water subphase. Later on, *Bergeron et al.* [346] observed that the absorption spectra of porphyrin monolayers differ from those recorded in solution. In particular, a red-shift of the *Soret* band was observed. After these pioneering studies, thin films of porphyrin derivatives have attracted considerable attention and many of them have been investigated as *Langmuir* monolayers or LB films [339, 347, 348]. Most *Langmuir–Blodgett* studies have been focused on the structural characterization of the layers [340, 349]. Porphyrins without any functional modification, such as 5,10,15,20-tetraphenylporphyrin [350], do not form high-quality LB films. This is due to their lack of amphiphilicity and the attractive intermolecular π - π interactions that cause strong aggregation even at low surface pressure. Two main approaches are used to reduce this aggregation and to enhance the amphiphilicity [351]: chemical modification of the tetrapyrrolic ring and preparation of mixed monolayers formed by porphyrins in conjunction with amphiphilic compounds. Porphyrins are often functionalized with hydrophilic groups to enhance their amphiphilic character [352, 353].

In this context, *Suslick* and co-workers prepared a series of nitrophenyl- and octadecanamidophenyl-substituted porphyrins **37** – **40** (*Figure 4.3*). They observed that the area per molecule smoothly increases from 80 Å² (**37**) to 230 Å² (**40**) as the number of aliphatic chains increases from 1 to 4.

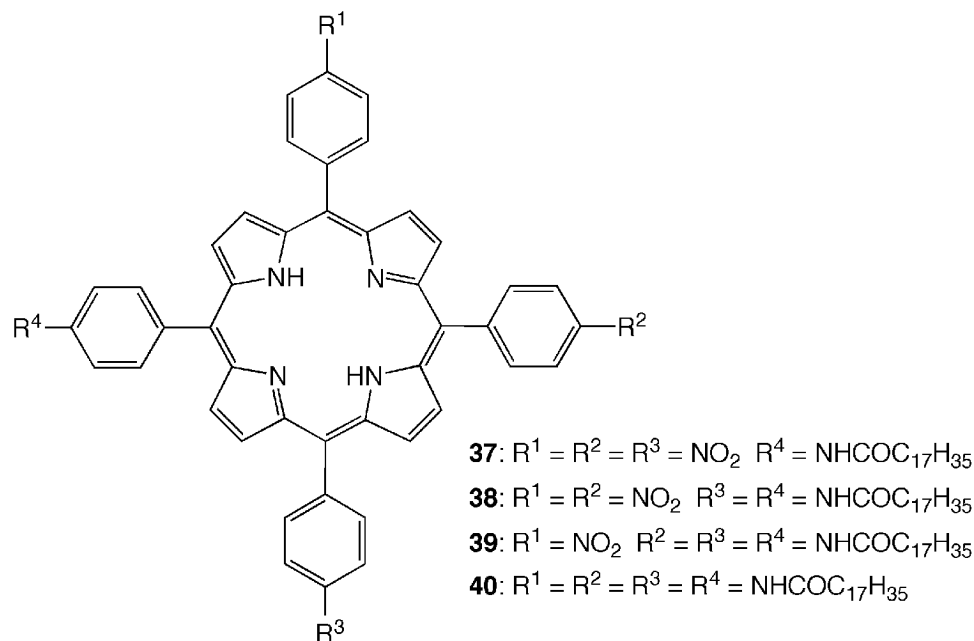


Figure 4.3 Structure of amphiphilic porphyrins as reported by *Suslick et al.* [349].

The aliphatic chains seem to be the responsible for the packing density and the aggregation between porphyrin rings that becomes less significant with increasing number of $n\text{-C}_{17}\text{H}_{35}$ chains [349]. In the presence of only one such chain, the porphyrins get close enough to interact with each other and porphyrin-porphyrin stacking occurs. Consequently, the area per molecule is small and corresponds to a vertical orientation of the macrocycle with respect to the water surface. As the number of peripheral octadecanamido groups increases, however, the macrocycles must pack more loosely. The area per molecule increases and the observed value seems to correspond to a parallel orientation of the porphyrins with respect to the water surface [349]. This improves the quality of the monolayers by preventing the strong interporphyrin interactions that cause formation of rigid and unstable films.

The second method used to prevent $\pi\text{-}\pi\text{-}$ stacking consists of spreading porphyrins together with amphiphilic compounds in mixed monolayers [350, 354]. *Li* and co-workers reported the formation of mixed monolayers of hemin (*Figure 4.1 a*) and $n\text{-octadecylamine}$ (ODA) (1:2) on a water subphase containing CdCl_2 [355]. The addition of Cd^{2+} ions to the water subphase should improve the spreading behavior of hemin due to the interaction with the carboxylic acid functions in the porphyrin moieties. It was observed that the spreading

behavior of the mixture hemin/ODA (curve b, *Figure 4.4*) differs strongly when compared to that of pure hemin (curve a, *Figure 4.4*)¹⁶

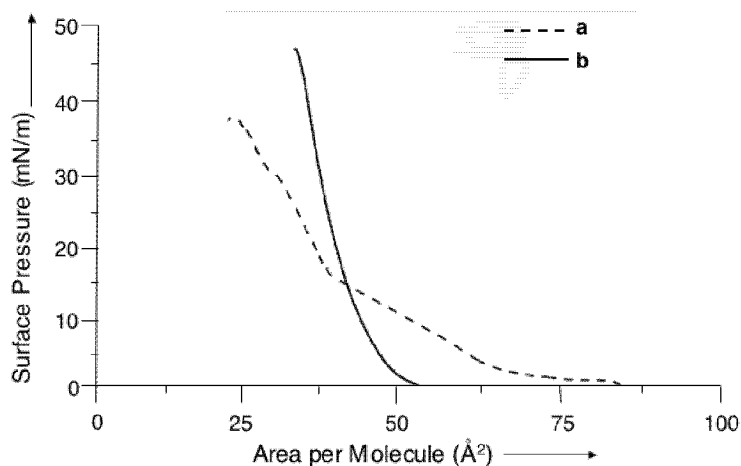


Figure 4.4 π -A Isotherms of a) pure hemin and b) mixed hemin/ODA (1 : 2) monolayers on water containing CdCl₂ (10⁻⁴ M).

For the isotherm of pure hemin (curve a, *Figure 4.4*), the larger slope indicates a relatively stronger interaction between hemin molecules which causes significant aggregation even prior to the compression of the *Langmuir* monolayer. The area per molecule obtained ($\sim 50 \text{ \AA}^2$) suggests a vertical orientation of the tetrapyrrolic ring. In case of the mixed monolayer (hemin/ODA), the limiting molecular area of hemin can be obtained from the area of ODA which is about 20 \AA^2 and the molar ratio of hemin/ODA (1 : 2). The calculated result shows that the molecular area of hemin in the mixed monolayer is $\sim 40 \text{ \AA}^2$, which is smaller than that obtained for pure hemin. The authors suggested that this decrease in the molecular area is due to the presence of ODA molecules. They are positioned between the hemin rings decreasing the repulsive force between hemin molecules and causing them to pack more densely [355].

These experiments illustrate that the orientation of porphyrins may be controlled within monolayers, by changing the hydrophilic substituents which are responsible for anchoring the tetrapyrrolic rings to the water subphase. For this reason, the LB technique was used to prepare molecular systems designed to mimic the photosynthetic process (photoinduced charge separation) in which the relative orientation of the different components is important.

¹⁶ The isotherms **a** (black curve) and **b** (magenta curve) were recorded in our laboratories by spreading a solution of hemin in DMF ($1.2 \times 10^{-5} \text{ M}$) on pure water and on water containing CdCl₂ ($2 \times 10^{-4} \text{ M}$), respectively. The results are in agreement with those reported in literature [355].

Guldi and co-workers studied the spreading behavior of the fullerene-porphyrin (C_{60} -NiP) conjugate **41** reported in *Figure 4.5* [356]. In this dyad, the tetraphenylporphyrin moiety acts as electron donor and the fullerene as electron acceptor (cf. *Section 3.1.2*).

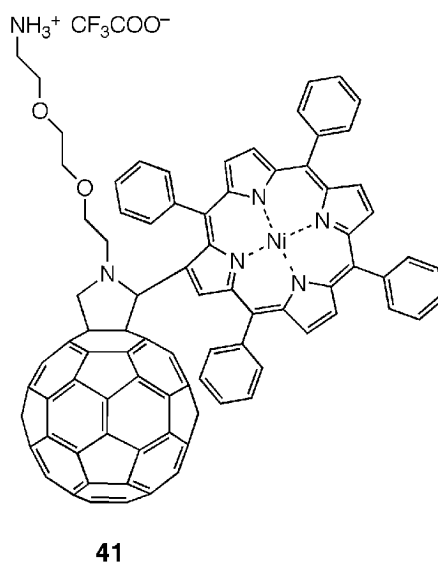


Figure 4.5 Structure of a fullerene-porphyrin dyad (**41**, C_{60} -NiP) as reported by *Guldi et al.* [356].

The authors prepared a *Langmuir* monolayer of **41** on water but the corresponding isotherm displays a behavior typical for non-amphiphilic fullerene derivatives. The floating film is rigid due to the high cohesive interactions between the carbon cages which predominate over the favorable interactions of the $-NH_3^+$ termini with the water subphase. Nevertheless, the layers have been transferred from the water subphase to an ITO substrate by the *Langmuir-Schäfer*¹⁷ technique at several pressures (*i.e.* 2 mN m^{-1} , 10 mN m^{-1} , 15 mN m^{-1} , and 25 mN m^{-1}). The authors observed that the photocurrents increase notably with increasing surface pressure, due to a closer packing of the dyad **41**. The photocurrent is generated by electron transfer from the tetrapyrrolic macrocycle to the fullerene core and from the fullerene moiety to the ITO electrode. In the presence of oxygen, the photocurrent increases three times due to the reduction of oxygen and consequent formation of oxide radical anion that acts as a very mobile electron carrier to transport the negative charge to the ITO electrode.

¹⁷ This method, consisting of horizontal depositions, is useful for the transfer of a very rigid film. A flat substrate is placed horizontally on the floating monolayer film. When the substrate is lifted from the water subphase, the monolayer is transferred to the solid substrate, keeping the molecules in their original orientation [2].

4.3 *Langmuir–Blodgett* Investigations of Porphyrin Derivatives

Taking into account the general properties of porphyrin monolayers (*vide supra*), we decided to study the spreading behavior of porphyrin derivatives **42**, **43**, and **44** bearing crown ethers as pendant hydrophilic headgroups (*Figure 4.6*) [357]. Similar to conjugate **41**, LB multilayers of derivative **44** appear promising in view of their potential photoinduced charge-separation properties.

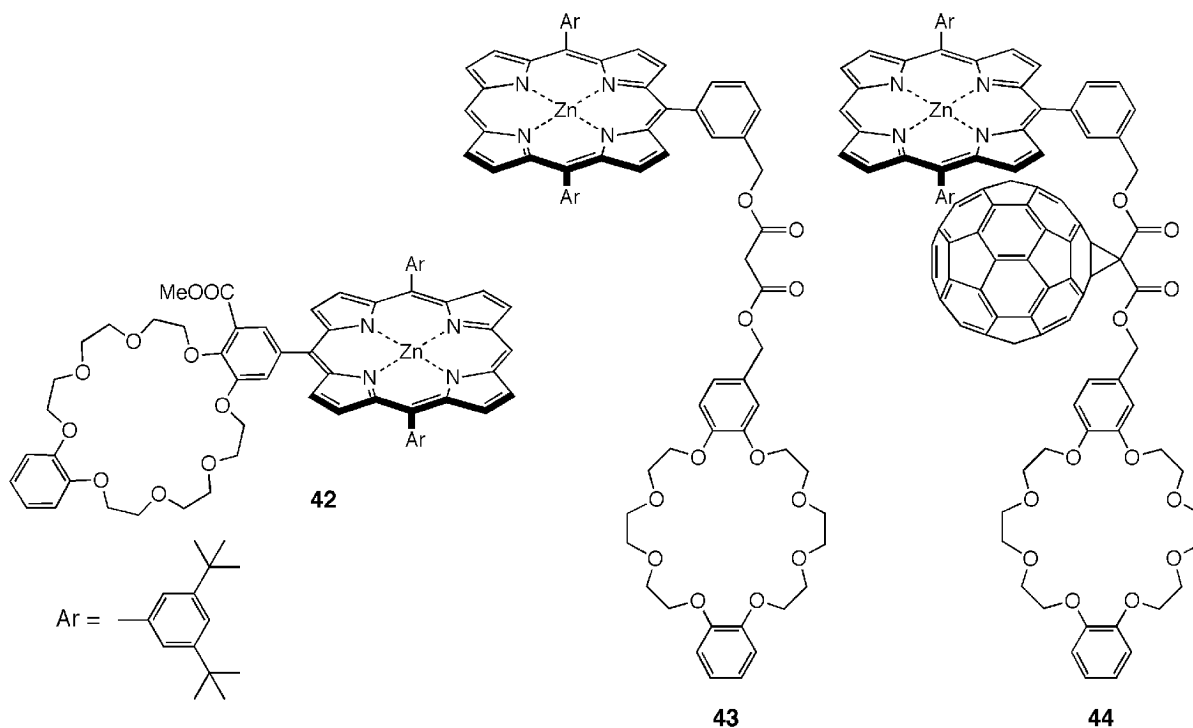


Figure 4.6 Structures of porphyrin-crown ether dyads **42** and **43**, and of porphyrin-crown ether-fullerene triad **44** [357].

4.3.1 Porphyrin-Crown Ether Derivative **42**: *Langmuir* and *Langmuir–Blodgett* Films

Because of the relatively high affinity of dibenzo[24]crown-8 for the larger alkali metal ions (see *Section 3.3*), *Langmuir* investigations of conjugate **42** were performed on pure water (*Figure 4.7*, black curve), on 1M aq. KCl (blue curve) and on 1M aq. CsCl (green curve) subphases. The extrapolation of the linear part of the three isotherms to zero pressure gives mean molecular areas of a) 85 Å², b) 110 Å², and c) 137 Å². The differences among these values suggests that the presence of K⁺ in the water subphase improves the spreading

behavior of **42** less, compared to Cs^+ in which case the observed molecular area requirement is significantly larger. This is further evidence for the selectivity of dibenzo[24]crown-8 within the alkali metal ion series.

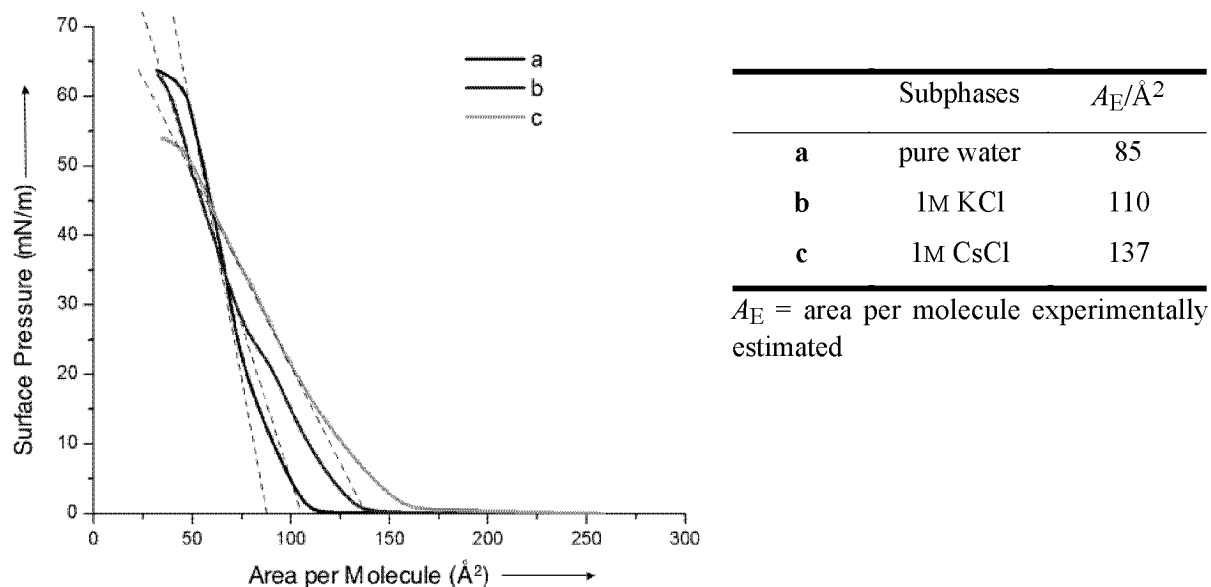


Figure 4.7 Surface pressure–area isotherms of porphyrin derivative **42** recorded a) on pure water, and on aqueous subphases containing b) KCl, and c) CsCl.

The increase in the area per molecule related to the presence of K^+ and Cs^+ ions in the water subphase confirms that the crown ether adopts a more extended conformation (see Section 3.2.2) upon coordination with the alkali metal ions (Section 3.3). The porphyrin rings can assume different orientations at the air-water interface: They can either stand vertically on the water surface (“edge-on”) or they can lie horizontally on it (“face-on”) with molecular area requirements of $\approx 70 \text{ \AA}^2$ and $\approx 170 \text{ \AA}^2$, respectively [349, 358, 359]. The molecular area value obtained for **42** on pure water suggests that the orientation of the porphyrin ring is slightly tilted with regard to the vertical position.

Isotherm **a** in Figure 4.7 shows a phase transition around 25 mN m^{-1} which suggests a change in the orientation of the porphyrin ring from a nearly horizontal to a nearly vertical position during compression [354, 359-361]. This change may be related to π - π interactions between macrocyclic rings. At low pressure, the porphyrins are not close enough to strongly interact with their neighbors. At higher pressures, the porphyrins sense each other and the

strong interaction causes a change in orientation. Surface potential measurements¹⁸ confirm the reorientation of the porphyrin units within the monolayer [359, 360]. *Figure 4.8* shows the surface pressure–area isotherm (solid curve) and the surface potential as a function of the area per molecule (dotted curve) recorded during the compression of a monolayer of **42** on a pure water subphase.

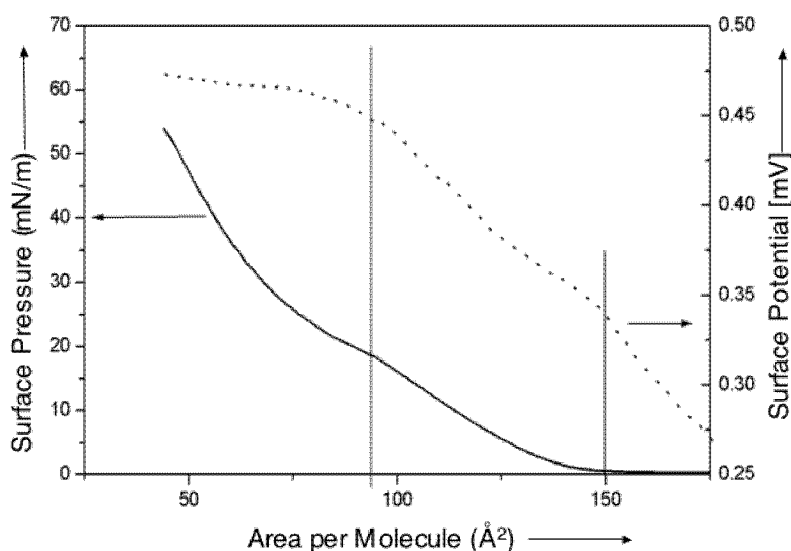


Figure 4.8 Surface potential difference ΔV (dotted curve) and π - A isotherm (solid curve) as functions of the mean molecular area measured for porphyrin derivative **42** during the compression of a *Langmuir* layer on pure water.

The surface potential difference curve shows two distinctive points, **a** and **b**, that correspond to a clear change in its slope. These two points also correspond to the phase transitions observed in the π - A isotherm, suggesting an orientational change of the porphyrin moieties. Approximating the molecule to a cylinder, the height h of the latter is given by the following expression (equation 4.1) [121]:

$$h = M_W (N_A \rho A)^{-1} \quad [\text{\AA}] \quad (4.1)$$

where M_W is the molecular weight (g mol^{-1}), N_A is the *Avogadro* number (mol^{-1}), ρ is the density (*ca.* 1 g cm^{-3} for organic molecules), and A is the area per molecule (\AA^2).

¹⁸ The surface potential technique is a non-destructive powerful tool to measure the potential variations at the air-water interface. The surface potential difference ΔV of a floating monolayer is defined as the difference in potential between a monolayer-covered surface and a clean water surface [362].

By using equation 4.1, the height values calculated for the two distinctive points (*Figure 4.8*) are 14 Å (**a**) and 22 Å (**b**). These correspond to the values obtained from theoretical calculations performed using PM3 (implemented in the Spartan SGI version 5.1.3 [174]) for the tetrapyrrolic macrocycle of **42** when vertically ($h = 25$ Å) or horizontally arranged ($h = 12$ Å) on the aqueous subphase. These two values suggest that the porphyrin planes change orientation from parallel to almost perpendicular to the water subphase during the compression of the monolayer, thus forming a well-packed and uniform monolayer (see picture 8 in *Figure 4.9*)

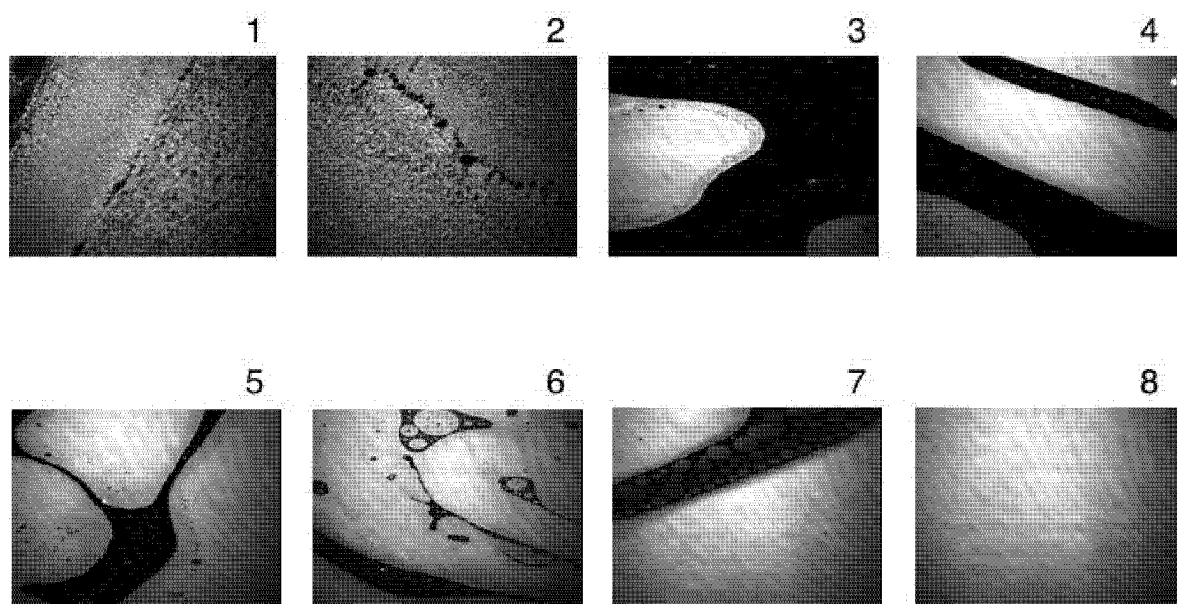


Figure 4.9 BAM images of a monolayer of porphyrin-crown ether conjugate **42** on pure water, compressed at 1) 0.1 mN m⁻¹, 2) 0.1 mN m⁻¹, 3) 0.3 mN m⁻¹, 4) 0.5 mN m⁻¹, 5) 0.7 mN m⁻¹, 6) 1.8 mN m⁻¹, 7) 10 mN m⁻¹, and 8) 15 mN m⁻¹.

The morphology of the monolayers of **42** during compression was investigated by BAM (*Figure 4.9*). In all pictures, the bright zones correspond to the monolayer, while the dark zones, where no reflection occurs, correspond to the water subphase. Pictures 1 and 2 (*Figure 4.9*) show the monolayer after the spreading of **42** (CHCl₃, 10⁻⁴ M), before compression. They show that the porphyrin derivative **42** has a tendency to self-aggregate. Pictures 3 and 4, taken at 0.3 and 0.5 mN m⁻¹, respectively, confirm that the molecules are not uniformly distributed but clustered in domains. Under increasing pressure, these clusters eventually coalesce into broader and larger domains (pictures 5, 6, and 7). The only perceptible variation in these images is the monotonous and continuous contraction of the

black areas up to the point of their disappearance and the generation of a uniform and condensed layer on the water subphase (picture 8). The monolayer shows a strong hysteresis effect: The molecules “remember” the close-packing of the condensed phase and do not separate upon expansion.

Nevertheless, the monolayer was successfully transferred onto a glass support at a pressure of 20 mN m^{-1} . The transfer occurred during the upstroke movement, suggesting a Z-type deposition (*Section 1.3.3*) for the LB multilayers [363].

The UV-VIS analysis of porphyrin derivative **42** in LB films (dotted line) reveals a considerable red-shift of the Soret band (*B*) and the *Q*-band in comparison to the spectra recorded in solution (CHCl_3) (solid line) (*Figure 4.10*).

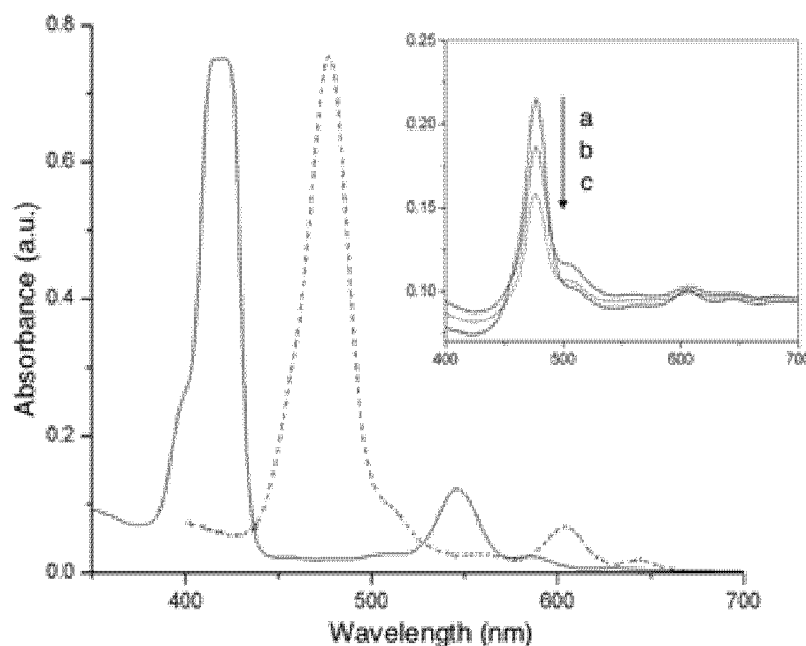


Figure 4.10 UV-VIS spectra of porphyrin derivative **42** in CHCl_3 solution (solid curve) and on a solid support (glass; 11 LB layers) (dotted curve). *Inset*: UV-VIS spectra of a) 1 LB layer, b) 5 LB layers, and c) 11 LB layers.

This shift is indicative of strong intermolecular interactions within the film. The location of the *B*- and *Q*-bands remains the same for films with differing numbers of layers (see *inset* in *Figure 4.10*). This implies that the interactions exist within rather than between layers. On the other hand, the absorption intensity decreases with increasing number of layers, confirming the difficult deposition of the layers and removal rather than addition of molecules upon deposition of new layers. The transfer ratio which measures the quality of the LB

layers (*Section 1.1.3*) is close to 0.5 for the first deposition but rapidly decreases to zero after eleven depositions.

Band splitting in the absorption spectra of LB films with aggregated species, relative to the “monomeric” absorptions of spectra in solution, is mostly interpreted by the exciton model developed by *Kasha et al.* [364]. It predicts that the shifting of absorption bands in weakly coupled electronic systems is caused by interactions between localized transition dipole moments. The shifting is determined by the center-to-center distance between interacting dipoles, their relative orientation, the oscillator strength of the transition of the monomer, and the number of monomers in the domains [365]. The simplest possible domain is a dimer for which the transition energies to the exciton-split states are given by equation 4.2:

$$E_{\text{dimer}} = E_{\text{monomer}} + D \pm \varepsilon \quad (4.2)$$

where E_{monomer} is the transition energy of the monomer species, D is a dispersion energy term and reflects the change in environment on the transition from monomer to oligomer, and ε is the exciton interaction energy, which is related to the magnitude of the transition moment, the geometry of the aggregate, and the angle between the transition dipoles and a line connecting the centers of the dipoles [348, 352]. A schematic energy diagram for this situation is shown in *Figure 4.11*, where E_G is the energy of the ground state, E the energy of the excited state, and E' and E'' are the energy levels arising from the splitting of E as a result of the exciton interaction between monomers.

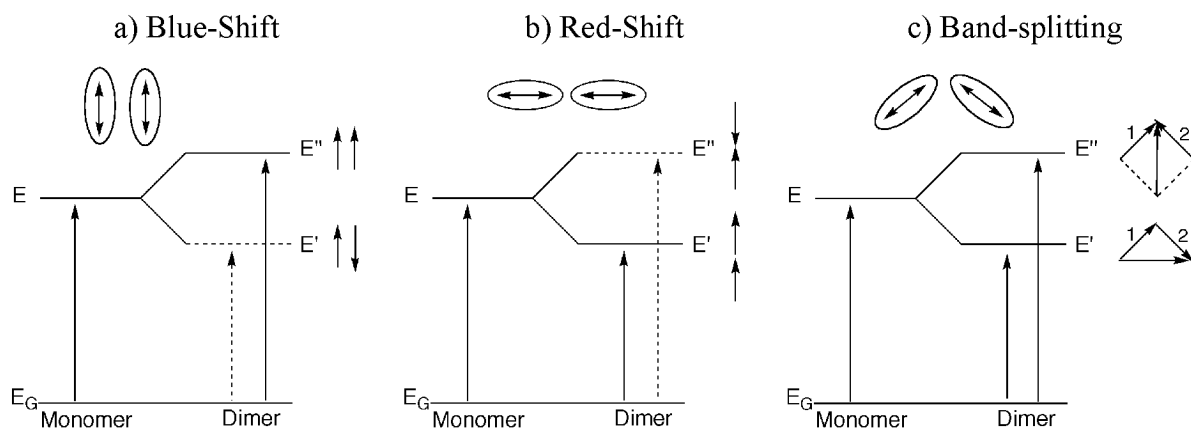


Figure 4.11 Schematic representation of exciton splitting in a) a parallel dimer, b) a head-to-tail dimer, and c) an oblique dimer, as reported by *Kasha* [366].

Kasha predicted that in the case of a parallel dimer (*Figure 4.11 a*), the exciton energy displacement is electrostatically repulsive for the two in-phase dipole vectors. Then, the energy level E'' of the dimer is raised. The out-of-phase transition moment array is attractive and, consequently, the energy level E' is lowered. For the parallel dimer, the vector sum for E'' is finite and equal to the sum of the two transition moments, whereas for E' the vector sum of the two transition moments is zero. Consequently, the only allowed transition is $E \rightarrow E''$ and the absorption spectrum appears blue-shifted. For the head-to tail dimer (*Figure 4.11 b*), the in-phase arrangement of the transition dipoles leads to a finite vector sum, whereas for the out-of-plane arrangement the vector sum is zero. The transition to the lower exciton state is allowed, that to the upper state forbidden (*Figure 4.11 b*), and the absorption of the dimer will be red-shifted. In the case of an oblique geometry (*Figure 4.11 c*), both excited states become allowed in the dimer with intensities depending on the angular relation between transition moments 1 and 2. In such cases a band splitting is expected relative to the single electronic transition of the monomer [364, 366].

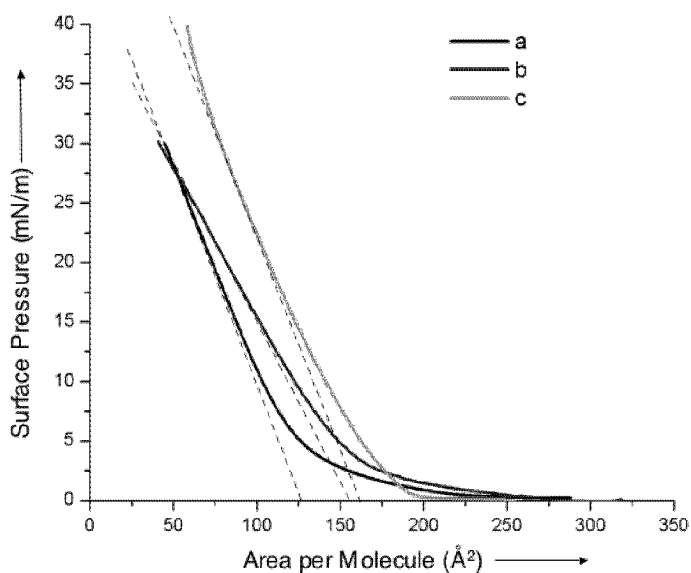
Taking into account these considerations, the most plausible structural model for the LB films of **42** that is consistent with the UV-VIS data and the molecular area measurements¹⁹, corresponds to *J*-aggregates²⁰ [369, 370] of offset porphyrins [353, 363] tilted by an angle θ with respect to the monolayer normal [371]. This arrangement may explain the bathochromic shift and the little shoulder of the *Soret* band (*Figure 4.10*). The extent of the shift linearly depends on five factors: (1) the degree of aggregation, (2) the interplanar distance, (3) the relative orientation of the monomers in the aggregate, including the tilt angle of the molecular stack, and (4) the electronic transition probabilities [353, 372]. Considering the large red-shift (56 nm), compared to those reported in literature (~ 20 nm [348, 352, 371]), in the according LB layers, we may hypothesize that the distance between the porphyrin units of **42** is small and the degree of aggregation is high. Emission studies reveal a fluorescence quenching for the aggregates of conjugate **42**. The fluorescence of a solid film or monolayer is usually quenched relative to that of the monomer [373]. The degree of quenching is directly related to the extent of aggregation of the molecules in the layer [373]. This correlation is attributed to an increase in the number of available vibrational modes which leads to an enhanced rate of internal conversion.

¹⁹ The molecular arrangement is supposed not to undergo a substantial change upon transfer from the air-water interface to the solid support.

²⁰ The monomers form a face-to-face array [354, 367, 368].

4.3.2 Porphyrin-Crown Ether Derivative **43** : *Langmuir* and *Langmuir-Blodgett* Films

Monolayers of conjugate **43** were prepared similarly to those of **42** by spreading a solution (CHCl_3 , 4.3×10^{-4} M) of the dyad on pure water and on 1M aq. KCl and 1M aq. CsCl subphases. *Figure 4.12* shows the π - A isotherms of **43** on pure water (black curve) and in the presence of KCl (blue curve) or CsCl (green curve). Limiting molecular areas of 125 \AA^2 , 154 \AA^2 , and 160 \AA^2 were obtained for pure water, aq. KCl, and aq. CsCl subphases, respectively. These values suggest that the presence of KCl and CsCl in the subphase changes the amphiphilic characteristics of conjugate **43** less dramatically than those of **42**. This may be due to the flexible malonate linker between the hydrophobic (porphyrin) and hydrophilic (crown-ether) moieties, allowing the porphyrin to adopt the same orientation under all conditions.



| | Subphase | $A_E/\text{\AA}^2$ |
|----------|------------|--------------------|
| a | pure water | 125 |
| b | 1M KCl | 154 |
| c | 1M CsCl | 160 |

A_E = area per molecule experimentally estimated

Figure 4.12 Surface pressure–area isotherms of porphyrin-crown ether conjugate **43** recorded a) on pure water and on aqueous subphases containing b) KCl (1M), and c) CsCl (1M).

The planes of the porphyrin macrocycles appear to be nearly parallel to the water subphase, diminishing the porphyrin-porphyrin stacking. Indeed, the molecular area occupied by derivative **43** is generally larger than in the case of **42** although still smaller than the theoretical value ($\approx 170 \text{ \AA}^2$) expected for a porphyrin lying flat on water subphase. At low pressure, the porphyrin of conjugate **42** is oriented parallel to the water surface and its area requirement is predominant compared to the crown ether. Under compression, the molecules

get into closer contact and due to porphyrin-porphyrin interactions, the tetrapyrrole macrocycle changes orientation from parallel to tilted with respect to the normal at the air-water interface, and the molecular area requirement of the crown ether becomes predominant. Complexation of the metal ions, which involves a conformational change of the crown ether, shows a more pronounced effect than in case of the porphyrin-crown ether conjugate **43**. In fact, the porphyrin unit of **43** does not change orientation dramatically and its plane stays nearly parallel to the water surface during the whole compression. As a result, the area occupied by the nearly horizontal porphyrin of **43** is larger than the area of the crown ether regardless of whether alkali metal ions are present or absent in the subphase. But in case of derivative **42** the area occupied by one molecule strictly depends on the orientation of the porphyrin. Therefore, the complexation alters the spreading behavior of derivative **43** to a lesser extent as compared to **42**. Compression/expansion cycles reveal that the monolayer of **43** is completely reversible, even though it is not homogeneous, as shown in *Figure 4.13*.

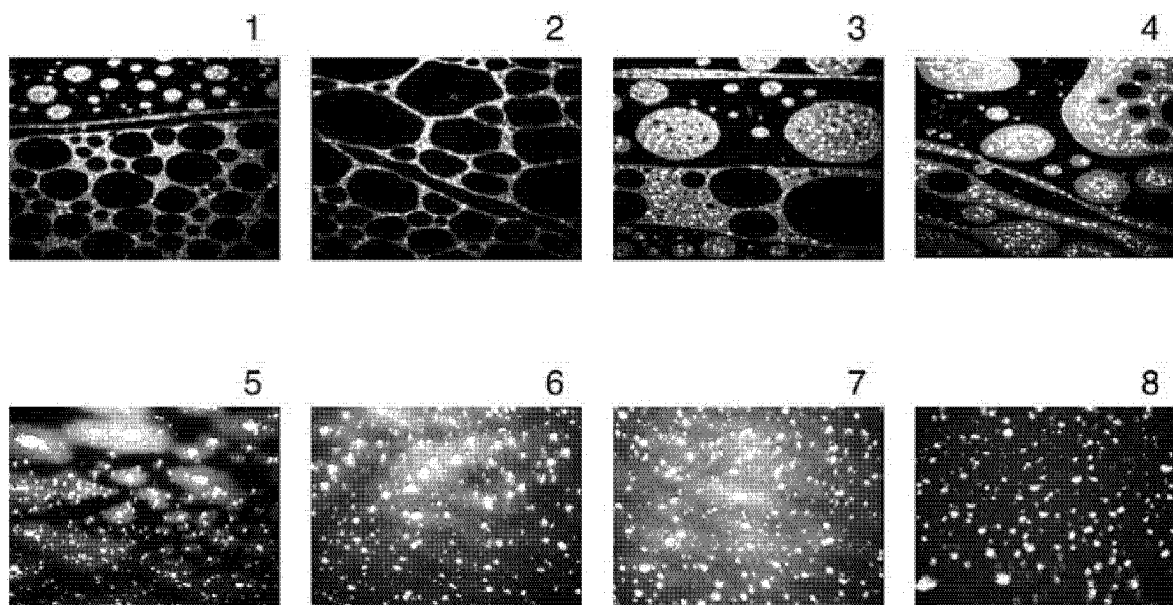


Figure 4.13 BAM images of porphyrin-crown ether conjugate **43** at 1) 0.2 mN m^{-1} , 2) 0.4 mN m^{-1} , 3) 0.7 mN m^{-1} , 4) 1.1 mN m^{-1} , 5) 2 mN m^{-1} , 6) 3.4 mN m^{-1} , 7) 5 mN m^{-1} , and 8) 10 mN m^{-1} .

BAM investigations reveal that after spreading, the monolayer is biphasic (*Figure 4.13*, picture 1). The liquid-expanded phase, corresponding to a relatively low density of molecules, appears in grey. The condensed domains are bright because of the higher reflectivity associated with the higher surface density (see *Section 1.3.4.1*) and the dark areas

correspond to the water subphase. The morphology of the monolayer does not change during compression (pictures 2 - 4) and the coexistence of two phases is observed up to a pressure of 10 mN m^{-1} . At this pressure, only the condensed phase is present as small domains floating in the water subphase (picture 8). During compression (pictures 1 - 8), the concentration of these bright solid domains increases but no coalescence is observed. The monolayer does not appear homogeneous at the collapse pressure. Generally, the morphology of the floating film does not appear to be very sensitive to variations in surface pressure.

At a surface pressure of 15 mN m^{-1} , the monolayers were transferred to a glass support, but only during the upstroke movement which led to the formation of Z-type LB multilayers. The UV-VIS analysis of the LB multilayers (*Figure 4.14*) reveals a similar situation as in the case of derivative **42**: the absorption intensity decreases as the number of layers (n) increases on the transition from $n = 1$ (a) to $n = 5$ (b) (see *inset*).

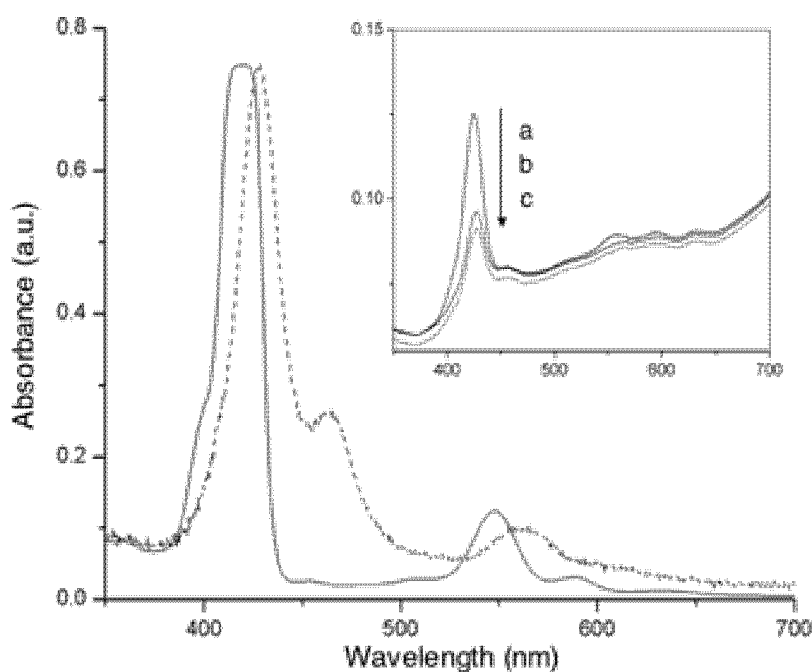


Figure 4.14 UV-VIS spectra of porphyrin-crown ether conjugate **43** in CHCl_3 solution (solid curve) and on a glass support (11 LB layers) (dotted curve). *Inset*: UV-VIS spectra of a) 1 LB layer, b) 5 LB layers, and c) 11 LB layers.

After five layers, the intensity does not change significantly, showing that layers may be lost in the water subphase during the downstroke movement when no deposition is observed.

Nevertheless, even a transfer ratio < 0.5 evidences monolayer transfer to the glass support up to the eleventh layer, after which the transfer ratio drops almost to zero.

In analogy to conjugate **42**, the *B* and *Q*-bands of the LB layers of **43** are red-shifted relative to the absorptions of monomeric **43** (CHCl₃) (*Figure 4.14*).

The *Soret* band of the LB multilayer of porphyrin conjugate **43** is split into two components whereas the *Q*-band remains a single feature (*Figure 4.14*). The analysis of exciton interactions suggests that the *Soret* band splitting is due to an oblique geometry (cf. *Figure 4.11*). Since exciton splittings are proportional to the oscillator strength of the corresponding electronic transition, the *B*-state exciton interactions will be much larger than *Q*-state interactions [374].

Nevertheless, the observed red-shift is less pronounced for conjugate **43** as compared to **42**, a fact related to the different structures of their aggregates. The frequency shift of the absorption peak of an aggregate relative to the monomer is inversely proportional to the cube of the distance between individual molecules [349].

In molecule **42**, the lack of a linker, such as malonate (cf. **43**), between the porphyrin and the crown ether restricts the conformational mobility and forces the molecules closer to each other. Consequently, they pack more efficiently [347, 373, 375, 376], leading to the formation of “rigid” *Langmuir* and *Langmuir-Blodgett* layers. The isotherms of both derivatives recorded on pure water (isotherms **a** in *Figures 4.7* and *4.12*) reveal that the “rigidity” of the film becomes less pronounced as the length of the linker between the porphyrin and the crown ether increases. Thus, derivative **42** shows a more solid-like behavior, while the *Langmuir* film of **43** is more fluid [348].

This is clearly reflected by the decreasing steepness in the slope [348] of the isotherms of conjugate **43** as compared to those of **42**. This effect is commonly expressed by the compressibility α [94], which is defined as follows (equation 4.5):

$$\alpha = A^{-1} (\partial A / \partial \pi)_T \quad [\text{m mN}^{-1}] \quad (4.3)$$

where A is the area per molecule, π the surface pressure, and T the temperature of the subphase. The compressibilities of **42** and **43** are included in *Table 4.1*.

Table 4.1 Position of the *Soret* band of conjugates **42** and **43** (LB films) as a function of the limiting area per molecule, compressibility of the isotherm (water), and transfer type of LB layers.

| Compound | Limiting area per molecule (\AA^2) | α (m mN $^{-1}$) | Type of transfer | λ_{max} (nm) (CHCl $_3$) | λ_{max} (nm) (11 LB layers) |
|-----------|---|--------------------------|------------------|--|--|
| 42 | 85 | 0.00564 | Z | 420 | 476 |
| 43 | 125 | 0.00702 | Z | 420 | 428 |

For LB layers of **42** and **43**, the red-shift of the *Soret* band amounts to 56 nm and 8 nm, respectively (Table 1), when compared to solution (CHCl $_3$) spectra. This shift reflects better a packing of **42**, related to the better stacking of the porphyrin in this conjugate.

The structural quality of one LB monolayer of derivative **43** was investigated by grazing incidence X-ray diffraction (Section 1.1.4.2). Figure 4.15 shows the diffraction pattern of one LB monolayer.

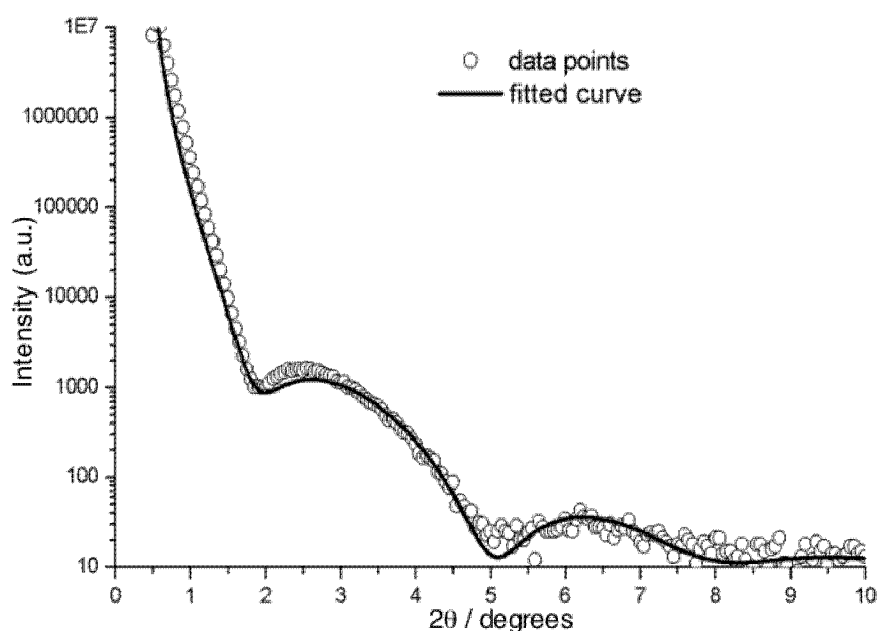


Figure 4.15 X-ray diffraction of one LB layer of porphyrin derivative **43**.

The monomolecular film shows only two *Kiessig* fringes (Section 1.1.4.2), for which the best mathematical fit (red curve) gives a thickness of $27.3 \pm 1 \text{ \AA}$ and a roughness of about 2.7 \AA . Unfortunately, it was impossible to investigate the quality of a LB layer of **42** by grazing incidence X-ray diffraction because of the difficult transfer onto a solid support, confirming the rigidity of the monolayer.

4.3.3 Porphyrin-Crown Ether-Fullerene Conjugate **44**: *Langmuir* and *Langmuir-Blodgett* Films

Porphyrin-fullerene conjugates are efficient artificial donor-acceptor (DA) systems due to the small reorganization energies associated with photoinduced electron-transfer reactions between them [32, 58, 377-380]. For this reason, they were proposed for applications in molecular electronics and as key components of artificial photosynthetic systems [57, 381, 382]. The photochemistry of such systems has mainly been studied in solution [357, 383] and solid phase [384, 385] revealing unusual short porphyrin-fullerene distances. The close proximity of the porphyrin and fullerene moieties results in the formation of an emitting charge-transfer (CT) state (*Chapter 5*). This manifests itself by the appearance of a new emission in the near infrared (NIR) region between 800 and 900 nm [357, 386, 387]. The transition from a solution to a solid phase may change the electron transfer (ET) properties of the compounds. This is related to a new rigid environment which restricts the reorganization of the compounds and the high density of chromophores which reinforces the intermolecular interactions [381]. Motivated by these findings, we decided to study the solid films of molecule **44** by using the *Langmuir-Blodgett* technique [377].

Figure 4.16 shows the π - A isotherms of compound **44** on pure water (black curve), on 1M aq. KCl (blue curve), and on 1M aq. CsCl (green curve) subphases.

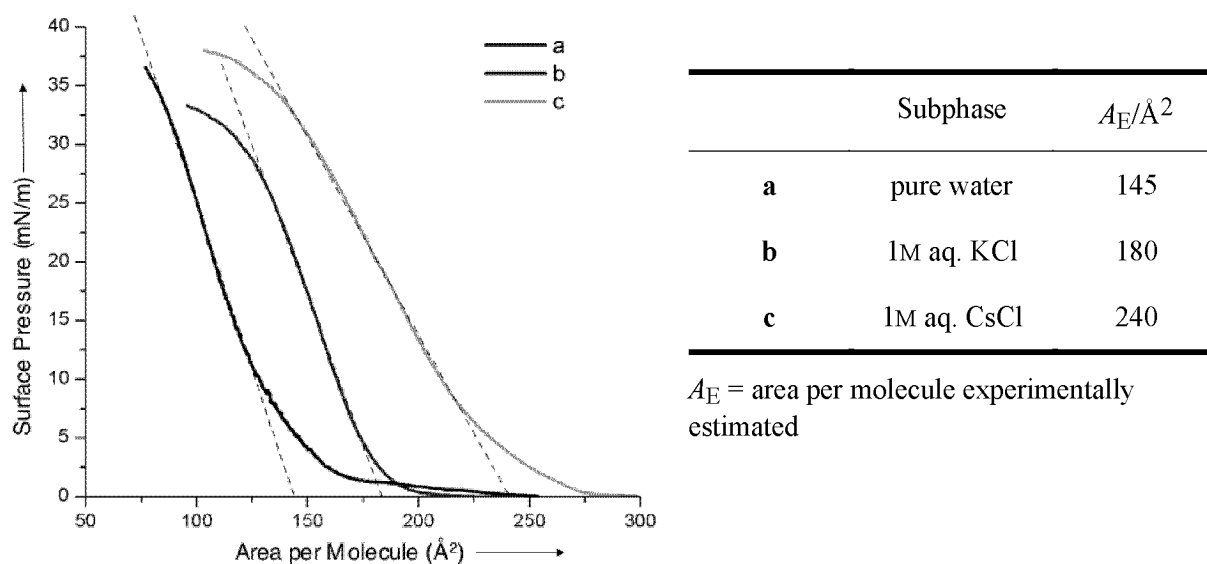


Figure 4.16 Surface pressure–area isotherms of conjugate **44** recorded a) on pure water and on water subphases containing b) KCl (1 M), and c) CsCl (1 M).

The molecular area requirements, obtained by extrapolating the isotherms to zero pressure, are 145 \AA^2 on pure water and 180 \AA^2 and 240 \AA^2 on aq. KCl and aq. CsCl subphases, respectively. The latter values evidence a strong influence of both alkali metal salts on the spreading behavior of **44**. This effect is significantly more pronounced with conjugate **44** than with the other porphyrin derivatives (**42** and **43**) because of the presence of the fullerene core. The fullerene increases the hydrophobic character of the molecule and consequently shifts the balance between the hydrophilicity and hydrophobicity, which is responsible for the formation of stable monolayers at the air-water interface, in an unfavorable way. This can be at least partially compensated by coordination of the crown ether moiety to alkali metal ions, thereby increasing its hydrophilicity and better anchoring the molecule in the water subphase. This balance may also explain the previously observed reduced influence of alkali metal ions on the spreading behavior of derivative **43** which lacks the fullerene unit. The increase in the molecular area requirement on the transition from aq. KCl to aq. CsCl subphases is understandable when considering the selectivity of dibenzo[24]crown-8 for the various alkali metal ions as observed in other cases of fullerene-ionophore conjugates (*Section 3.3*).

The π - A isotherms of derivative **44** (*Figure 4.16*) did not show any variation in the slope that would suggest a flipping of the porphyrin moiety. The limiting area per molecule observed on pure water suggests that the porphyrin sits tangentially atop the fullerene in a nearly parallel orientation with respect to the air-water interphase. This conformation benefits from favorable fullerene-porphyrin interactions and was found in other conjugates including these moieties and is also most apt to electron transfer between the donor and acceptor [357, 386]. Monolayers of **44** could be transferred to a glass support to form LB multilayers. Transfer was possible during upstroke and downstroke movements and the resulting multilayers were Y-type. Transfer ratios were close to 0.5 for the first two depositions but, similar to the cases of **42** and **43**, decreased progressively to reach zero after eleven depositions. The structure of a single LB layer, transferred at a surface pressure of 15 mN m^{-1} , was investigated by grazing incidence X-ray diffraction (*Figure 4.17*). The best mathematical fit (red curve) of the grazing incidence X-ray diffraction pattern gives a thickness of $37.3 \pm 1 \text{ \AA}$ and a roughness of $\sim 4.6 \text{ \AA}$. The estimated value of the thickness of a layer of conjugate **43** is $27.3 \pm 1 \text{ \AA}$, 10 \AA less than the measured value for **44**, which corresponds exactly to the diameter of C_{60} .

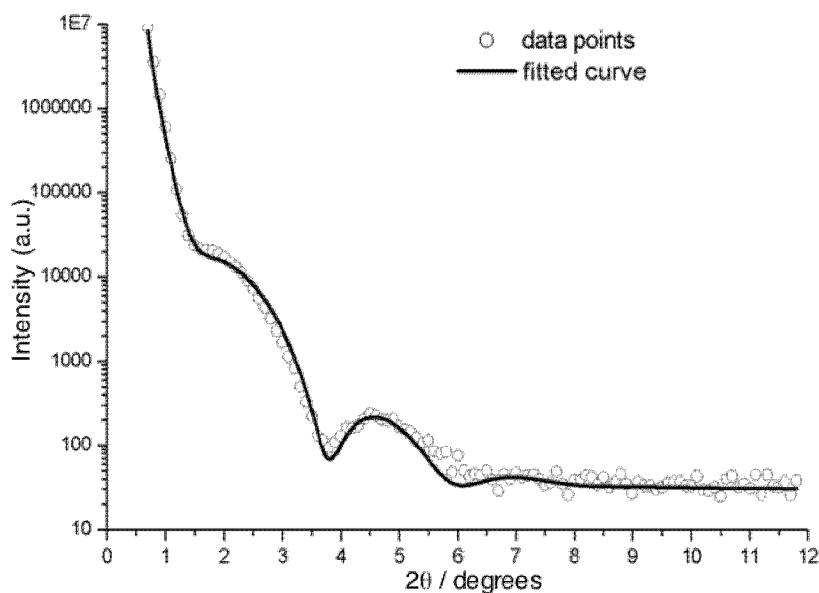


Figure 4.17 X-Ray diffraction of one LB layer of porphyrin-fullerene-crown ether conjugate **44**.

Considering the X-ray analysis, the red-shift of the *Soret* band, and the presence of fullerene which locks the porphyrin in horizontal position, we propose that the porphyrin-fullerene-crown ether conjugate adopts the molecular arrangement shown in Figure 4.18 a. This arrangement and the above X-ray diffraction results for **43** (cf. Section 4.3.2 and Figure 4.15), suggest that this porphyrin-crown ether conjugate adopts the same conformation as derivative **44** in a LB layer (Figure 4.18 b).

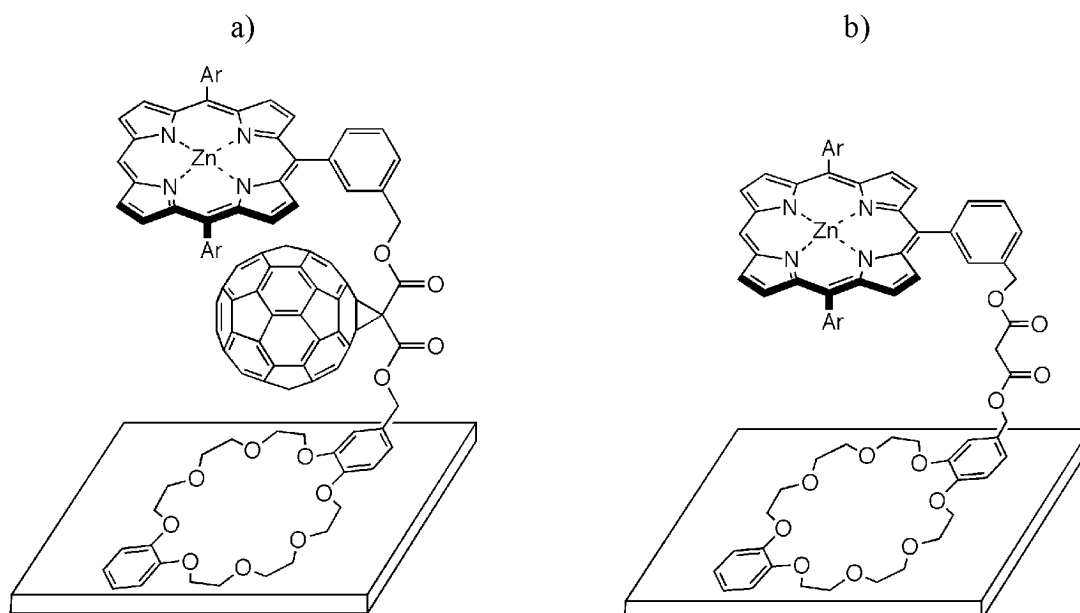


Figure 4.18 Schematic illustration of the arrangement of a) compound **44** and b) compound **43** within a LB monolayer on a glass support.

Nevertheless, the difference in the thicknesses suggests that the malonate is folded and the height of the conjugate **43** shorter by 10 Å compared to conjugate **44**.

The UV-VIS-spectroscopic analysis of a LB film of **44** (Figure 4.19) reveals a red-shift of the *Soret* band relative to the solution spectrum (CHCl₃) as in the case of derivatives **42** and **43** (Figures 4.10 and 4.13). This red-shift suggests *J*-type aggregation [354, 367, 368]. The *B*-band is further red-shifted (14 nm) with respect to conjugate **43** (8 nm), indicating an additional intermolecular interaction between the porphyrin and the C₆₀ moieties in the LB films of **44** [357, 377, 381, 383]. The absorption intensity, as previously observed with the other two porphyrin derivatives (**42** and **43**), decreases with increased number of deposited layers of **44** (see inset of Figure 4.20). As in the case of derivative **43**, the decrease in the absorption intensity is remarkable on going from $n = 1$ to $n = 5$, but after five layers little change is recorded. This is in agreement with the transfer ratio which decreases with increasing number of deposited layers and with the loss of deposited molecules in subsequent dipping cycles.

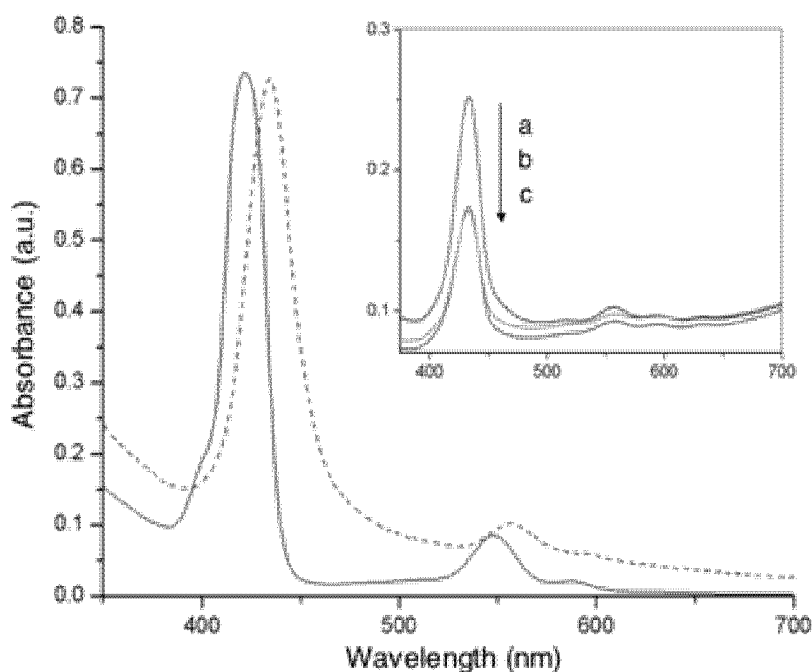


Figure 4.19 UV-VIS spectra of porphyrin-fullerene-crown ether **44** in CHCl₃ solution (solid curve) and on a glass support (dotted curve). *Inset*: UV-VIS spectra of a) 1 LB film, b) 5 LB films, and c) 11 LB films.

The compressibility values (Table 4.2) show that in the case of conjugate **44**, the molecules are well packed to form more ordered and better aggregated monolayers when compared to **43**. The isotherm of molecule **44** (isotherm **a**, Figure 4.16) appears steeper than that of **43**

(isotherm **a**, *Figure 4.12*). This is probably due to the presence of the hydrophobic fullerene, which results in a more rigid monolayer.

Table 4.2 Red-shift of the *Soret* band as a function of the limiting area per molecule, the compressibility (α) of the isotherm, and the transfer type of LB layers.

| Compound | Limiting area per molecule (\AA^2) | α (m mN ⁻¹) | Type of transfer | λ_{max} (nm) (CHCl ₃) | λ_{max} (nm) 11 LB layers |
|-----------|---|--------------------------------|------------------|---|---|
| 43 | 125 | 0.00702 | Z | 420 | 428 |
| 44 | 145 | 0.00603 | Y | 420 | 434 |

4.4 Conclusion

Porphyrim derivatives **42**, **43**, and **44** form stable monolayers at the air-water interface due to the presence of the hydrophilic dibenzo[24]crown-8 ether moiety. The spreading behavior of all derivatives, in particular of conjugate **44**, is improved by addition of KCl (1M) and CsCl (1M) to the water subphase. The selectivity of the crown ether for the different alkali metal ions favors a larger increase of the area per molecule in the case of CsCl, compared to KCl.

LB multilayers on glass slides could be obtained with all three conjugates (**42-44**). They evidenced that the transfer of *Langmuir* monolayers of complex molecules from a liquid to a condensed phase brings about new inter- and intramolecular interactions resulting in new types of conformers or associates. These formations can dramatically change the photochemical behavior of the compounds as compared to solutions. In the cases of **42-44**, the absorption spectra of single LB layers evidenced a bathochromic shift of the porphyrin-centered *B*- and *Q*-bands.

We observed that the presence of a spacer between the crown ether and the porphyrin changes the spreading behavior of the molecules, making the resulting monolayer less rigid. Moreover, the isotherm of the spacerless molecule **42** (black curve in *Figure 4.7*) is steeper than that of molecule **43** which includes a malonate spacer (black curve in *Figure 4.12*). The different packing of the monolayer explains the larger UV-VIS red-shifts observed for conjugate **42**. The *Soret* band is bathochromically shifted as the porphyrin-porphyrin stacking increases [347, 375, 376]. The isotherms obtained for molecules **42** and **43**

(isotherm a in *Figures 4.6* and *4.12*, respectively) during the compression of the monolayers show a transition phase which suggests that, especially in case of **42**, the molecules undergo a slow rearrangement [373]. The spreading behavior of conjugate **44** shows a particularly strong dependence of the presence of alkali metal ions in the water subphase. Even if the porphyrin is locked atop the fullerene at some distance from the water surface, the complexation of the crown ether by alkali metal ions has a stronger effect as compared to dyad **43** in which case the orientation of the porphyrin moiety is influenced by its interactions with the subphase. This apparent contradiction can be resolved by considering that the fullerene dramatically increases the hydrophobic character of the molecule and the coordination of the crown ether with K^+ or Cs^+ is needed to reestablish a more favorable balance between hydrophilicity and hydrophobicity. In the solid state (LB film), derivative **44** shows red-shifts of the *Soret* and *Q*-bands which are larger than in the case of dyad **43** ($\Delta\nu(\textit{Soret}) = 14$ nm and 8 nm, respectively), because of the additional interactions between the fullerene core and the porphyrin macrocycle. In accord with the low transfer ratios and the rather poor quality of all LB multilayers, the absorption intensities decrease upon successive depositions (in fact, previously deposited molecules are lost in subsequent dipping cycles). Upon depositing further layers no additional red-shifting of the *Soret* band was observed, suggesting that the exciton interactions are related to intralayer rather than interlayer interactions.

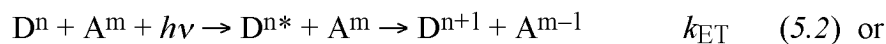
5 Towards Novel Fullerene-porphyrin Architectures: Attempted Synthesis of Fullerene-sandwiching Macrocyclic Bis(Metallo Porphyrin) and Porphyrin-Crown Ether

The photosynthetic system is regarded as the most elaborate nanoscale biological machine in nature [388-391]. It converts solar energy into chemical energy by way of two basic photochemical processes: The absorption of light of the appropriate wavelength by ensembles of light-harvesting chromophores and the photoinduced electron transfer between donor and acceptor molecules as a result of the photoexcitation of the donor components (chromophores).

The photoexcitation process consists of a transition from the lowest vibrational level (called the zero-point) of the electronic ground state to a higher-energy electronic level via a vertical transition (*Franck-Condon* transition). After initial population of the higher excited states, the system often relaxes rapidly (10^{-11} - 10^{-13} s) to the first excited state. The necessary energy release can be accomplished by different pathways which can be classified as radiative (*i.e.*, the transition to the lower states by light emission), non-radiative (*i.e.*, the transition to the lower states involves a release of translational, vibrational, and rotational energy), and quenching (*i.e.*, the deactivation of an excited sensitizer involves an external component, called quencher). The quenching process consists of an energy or electron transfer between a sensitizer and a quencher which can be separated or attached to each other via a flexible or rigid spacer. In the case of energy transfer, a donor molecule in an electronically excited state, D^* , may transfer its energy to an acceptor molecule, A. In the course of the process illustrated in *Scheme 5.1*, D^* is being deactivated and the excited state A^* is produced:



where D and A are the energy donor and acceptor, respectively, and k_{EN} is the rate constant for the transfer [392]. In the electron transfer process illustrated by *Schemes 5.2* and *5.3*, the excited states operate as an electron donor or acceptor leading to the formation of an ion pair which is often called a charge-separated intermediate:



where m and n indicate the charges of the molecules in the ground state, $h\nu$ is the energy necessary to excite the species, and k_{ET} the rate constant of electron transfer [393]. The energy and electron transfer processes generally require orbital overlap which needs short intermolecular distances between the reactants and also a good selection of the donor-acceptor pair [392]. These requirements accelerate photoinduced charge separation and retard charge recombination. In addition, the donor should efficiently harvest visible light (400-800 nm), which corresponds to the main region of the solar spectrum. Examples of good electron-donors are the porphyrins which can be covalently linked to electron acceptors such as quinones, aromatic imides, and fullerenes [57, 394-396]. Excitation of a porphyrin moiety is followed by photoinduced electron transfer to a nearby acceptor group to generate a charge-separated state. In particular, dyads consisting of a tightly bound porphyrin and fullerene evidenced exceptional photochemical behavior [397]. With its strong electron-accepting properties [241, 242, 245], [60]fullerene is one of the most popular molecular moieties that have been incorporated in molecular dyads [57, 398]. A variety of systems containing a porphyrin attached to C_{60} by a single linker have been prepared [38, 380, 399-405].

Recently, *Diederich* and coworkers [386] prepared two interesting photosynthetic model systems: One (**45**) consists of the tetrapyrrolic macrocycle doubly attached to the C_{60} core, and the other system (**46**) consists of two fullerene cores appended to a single porphyrin. It was observed that both porphyrin conjugates have similar photophysical and electrochemical properties. In particular, upon light excitation, both the porphyrin- and the fullerene-centered excited states are deactivated to a lower-lying charge transfer (CT) state, emitting in the NIR spectral region.

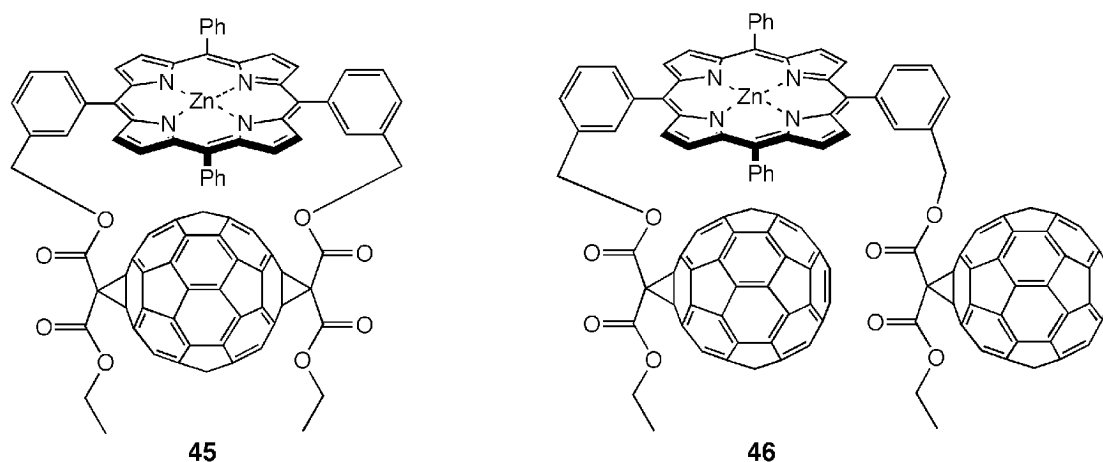


Figure 5.1 Fullerene-porphyrin conjugates reported by Diederich *et al.* [383, 386].

The spectroscopic observations suggest that a tight donor-acceptor distance can be established not only in bridged cyclophane-type structures (**45**) but also in singly-linked conjugates such as **46**, by taking advantage of the generally strong fullerene-porphyrin interactions [357, 386].

As an extension of this work, we decided to prepare the C₆₀-porphyrin triad **47**, with the *trans-1* bis-adduct of C₆₀ bearing a porphyrin moiety on each side of the carbon sphere (Figure 5.2).

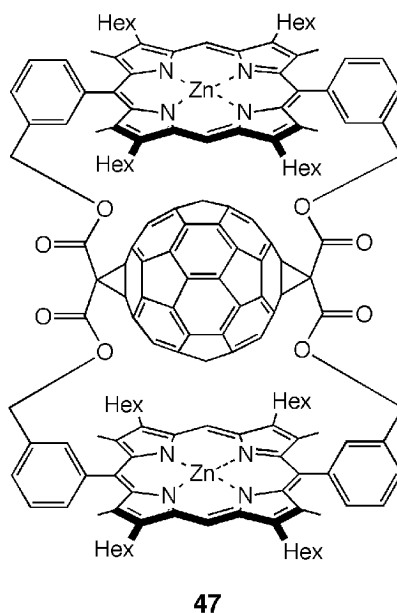


Figure 5.2 Targeted bisporphyrin-fullerene conjugate **47**.

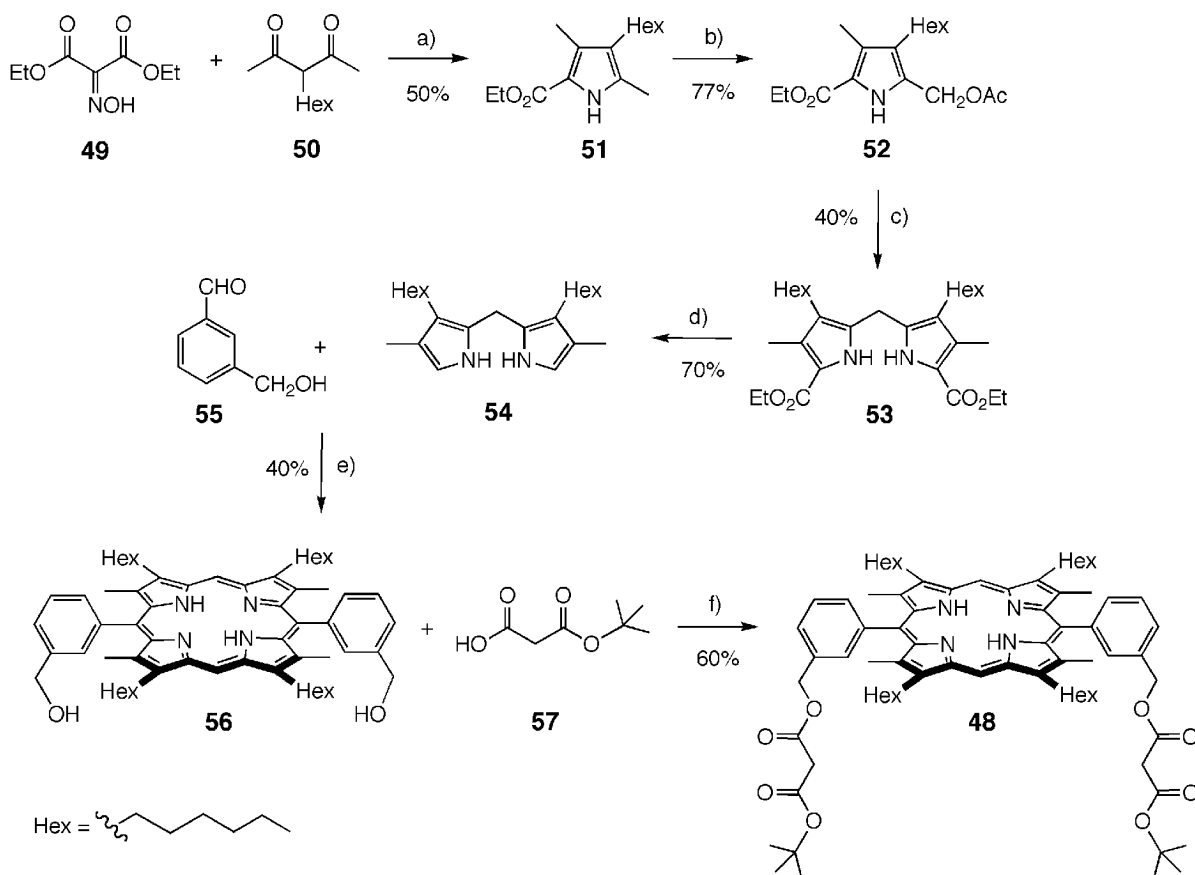
This *Chapter* is a description of the attempts toward the preparation of bisporphyrin-fullerene derivative **47**.

5.1 Attempted Preparation of Porphyrin-containing Macrocycles

5.1.1 Synthesis of porphyrin **48**.

The first stage toward the synthesis of bisporphyrin-fullerene conjugate **47** is the synthesis of the tetrapyrrolic macrocycle **48**, which can be prepared in six steps (*Scheme 5.3*) [406]. The synthesis started with the preparation of compounds **49** [324] and **50** [407] according to literature protocols. Reaction of **49** with **50** in the presence of Zn and AcOH afforded tetrasubstituted pyrrole **51** in good yield (50%) [408]. Oxidation and esterification of methylpyrrole **51** with Pb(OAc)₄ in AcOH yielded acetate **52** [409], which was further transformed to dipyrromethane **53** by treatment with EtOH and HCl_{conc} [409]. Saponification of **53** with EtOH in the presence of 10% aq. NaOH and subsequent decarboxylation by heating to reflux in ethanolamine yielded dipyrromethane **54** [410]. Aldehyde **55**, prepared according to a literature procedure [411], was reacted with dipyrromethane **54** following *Lindsey's* protocol [412] in the presence of Cl₃CCOOH to yield, after oxidation with *p*-chloranil, the desired porphyrin derivative **56** in good yield (40%) [406]. The regioselectivity in the macrocyclization reaction is quite high due to the absence of a phenyl substituent in *meso* position of dipyrromethane **54** which avoids scrambling²¹ [416]. The purification of **56** proceeded quite smoothly by single-step column chromatography on SiO₂ with a mixture CH₂Cl₂/AcOEt (9 : 1) as eluent. Malonic acid monoester **57** was obtained by reacting *Meldrum's* acid with *tert*-BuOH [417]. Diol **56** was transformed into tetraester **48** by reaction with *tert*-butyl hydrogen malonate (**57**) in the presence of DCC and DMAP as condensation agents in DMF at room temperature.

²¹ The scrambling process is a phenomenon related to the reversibility of the porphyrinogen formation which leads to rearrangements among the substituents and, consequently, to formation of isomeric porphyrins. The scrambling is a consequence of two processes: i) acidolysis (retro-condensation) of the dipyrromethanes and ii) recombination (re-condensation) of the fragments leading to isomeric mixtures. In the above-discussed example, the use of dipyrromethane **54** in the cyclization reaction inhibits the first process because the absence of a phenyl substituent in *meso* position prevents stabilization of the positively charged intermediates [413-415].

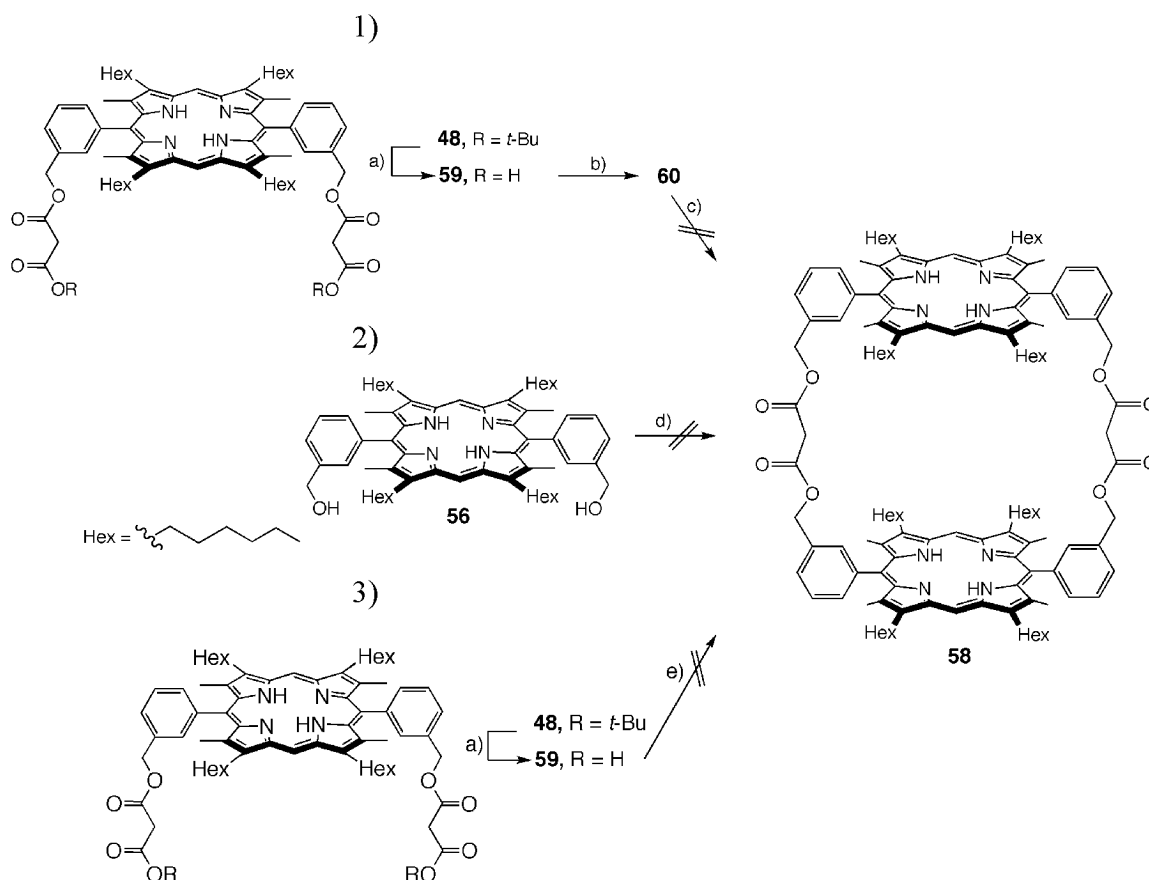


Scheme 5.3 Synthesis of porphyrin **48**. Reagents and conditions: a) Zn, NaOAc, AcOH, 80 °C, 2 h; b) Pb(OAc)₄, AcOH, r.t., 2 h, c) EtOH, HCl_{conc}, reflux, 1 h; d) i. EtOH, NaOH 10%, reflux, 5 h, ii. HOCH₂CH₂NH₂, reflux, 6 h; e) i. Cl₃CCOOH, CH₃CN, r.t., 14 h, ii. *p*-chloranil, THF, r.t. 6 h; f) DCC, DMAP, DMF, r.t., 14 h. DCC = *N,N'*-dicyclohexylcarbodiimide; DMAP = 4-(dimethylamino)pyridine.

5.1.2 Toward the synthesis of macrocyclic bis(metallo-porphyrin) **58**

Several approaches toward the synthesis of macrocyclic dimer bisporphyrin **58** have been tested. The first attempt included the removal of both *tert*-butyl protecting groups by TFA to yield diacid **59** which was subsequently reacted with oxalyl chloride to form the acid chloride **60**. The latter was reacted with the porphyrin-derived diol **56** under high-dilution conditions (*Scheme 5.4* (1)). However, the esterification between **56** and **60** yielded a complex mixture in which **58** could be identified neither by mass spectrometry nor by NMR spectroscopy. Subsequently, a one-step pathway was envisaged for the synthesis of macrocyclic bisporphyrin **58** starting from diol **56** and malonyl dichloride (*Scheme 5.4* (2)). The reaction was run under high-dilution conditions, but **58** could not be identified by any spectroscopic or spectrometric method. As a third approach, dicarboxylic acid **59** was

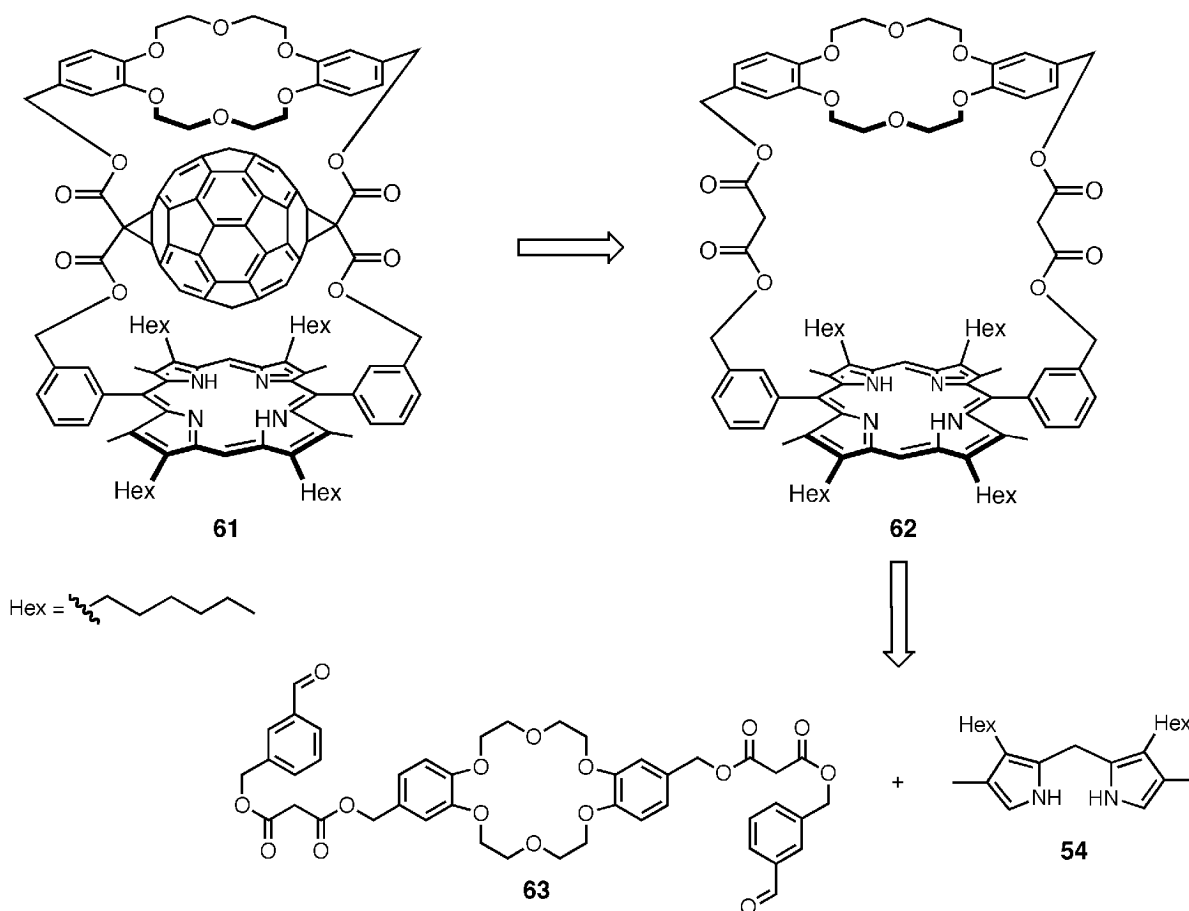
reacted with diol **56** in the presence of DCC and DMAP in DMF, again under high dilution [418] (Scheme 5.4 (3)). This procedure was not successful either.



Scheme 5.4 Attempted synthesis of bisporphyrin macrocycle **58**. Reagents and conditions: a) TFA, CH₂Cl₂, r.t., 14 h; b) (COCl)₂, CH₂Cl₂, 40 °C, 12 h; c) **56**, CH₂Cl₂, pyridine, r.t., 14 h, d) (COCl)₂CH₂, NEt₃, CH₂Cl₂, r.t., 12 h; e) i: DMAP, DCC, DMF, r.t., 12 h; ii: **56**, CH₂Cl₂, r.t., 12 h.

5.1.3 Toward the synthesis of the macrocyclic porphyrin-crown ether **61**

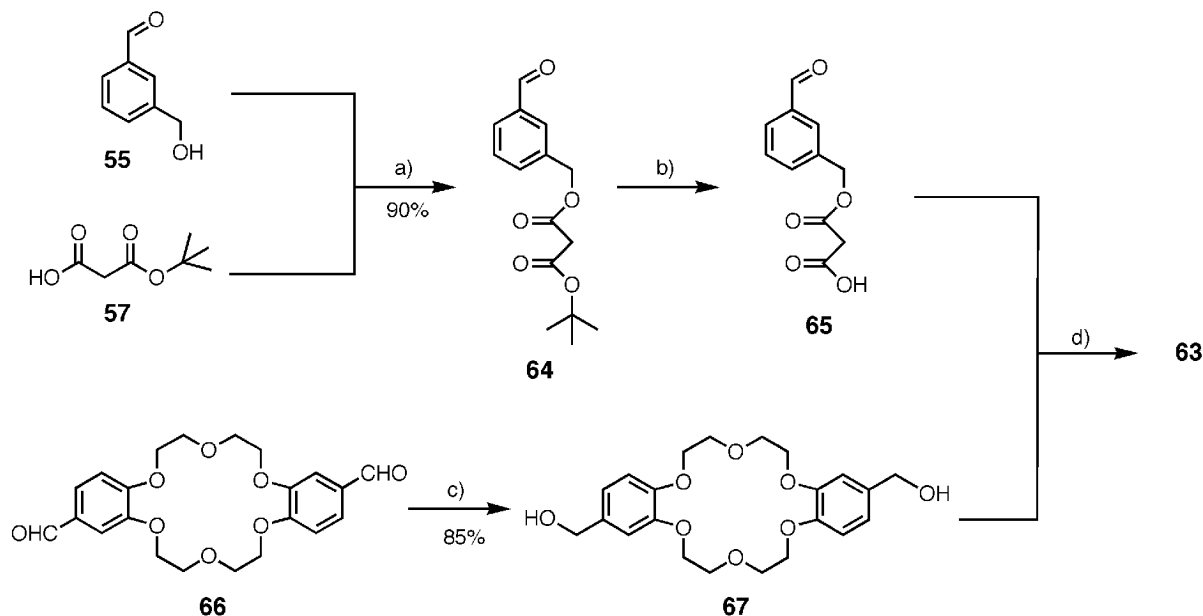
Taking into account the photophysical properties of porphyrin-fullerene conjugates **45** and **46** and the influence of the complexation of metal ions by a crown ether fixed with tangential orientation in close proximity to a fullerene, as observed for the first time by *Diederich et al.* [419], we decided to synthesize macropolycycle **61** in which a porphyrin and a dibenzo[18]crown-6 unit each bridge a *trans-1* type bismethano[60]fullerene (Scheme 5.5).



Scheme 5.5 Retrosynthetic approach aiming at the preparation of porphyrin-dibenzo[18]crown-6 conjugate **61**.

The envisaged retrosynthesis of conjugate **61** included the preparation of crown ether-derived dialdehyde **63** and its subsequent condensation with dipyrromethane **54** to give the macrocyclic intermediate **62** in one step [420-423]. For the synthesis of crown ether **63**, acid **65** was prepared in two steps (*Scheme 5.6*): Esterification of *tert*-butyl hydrogen malonate (**57**) with alcohol **55** mediated by DCC and DMAP afforded the mixed malonate **64** in 90% yield.

Subsequent removal of the *tert*-butyl group from **64** was achieved by addition of TFA to a solution of the malonate in CH_2Cl_2 . Acid **65** was submitted without purification to the esterification with diol **67** which was obtained by reduction of **66** with sodium borohydride. Crude crown ether **63** was obtained in 45% yield (*Scheme 5.6*).



Scheme 5.6 Synthesis of crown ether-derived dialdehyde **63** (cf. *Scheme 5.5*). Reagents and conditions: a) DMAP, DCC, DMF, r.t., 14 h; b) TFA, CH₂Cl₂, r.t., 20 min; c) NaBH₄, MeOH, r.t., 1 h; d) DMAP, DCC, DMF, r.t., 14 h.

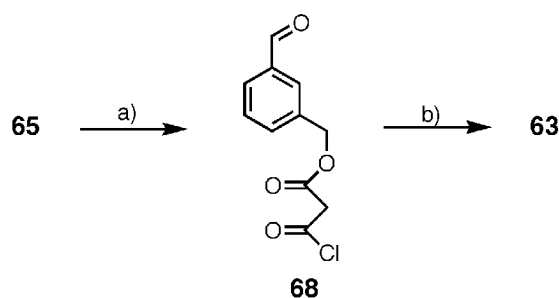
Its purification is pivotal for a high-yielding macrocyclization [424] with dipyrromethane **54** (*Scheme 5.5*), but it revealed to be very difficult. All employed purification methods (chromatography on SiO₂, recrystallization from various solvents (hexane, hexane/toluene (1 : 1), ethanol/water (1 : 1)), precipitation from chloroform or dichloromethane by addition of hexane, and reverse phase chromatography led to unsatisfactory results [424]

The major problem was the separation of ester **63** from the unreacted acid (**65**), and different protocols were tested to drive the esterification to completion (*Table 5.1*). Unfortunately, these attempts did not lead to a breakthrough.

Table 5.1 Reaction conditions for the synthesis of **63** (*Scheme 5.7*)

| Entry | 67 | 65 | DCC | DMAP | Yield of crude of reaction % |
|-------|-----------|-----------|---------|---------|------------------------------|
| 1 | 1 eq. | 3 eq. | 3 eq. | 0.3 eq. | 42% |
| 2 | 1 eq. | 2.5 eq. | 2.5 eq. | 0.3 eq. | 45% |
| 3 | 1 eq. | 2 eq. | 2 eq. | 0.3 eq. | 35% |
| 4 | 1 eq. | 3 eq. | 2.5 eq. | 0.3 eq. | 40% |

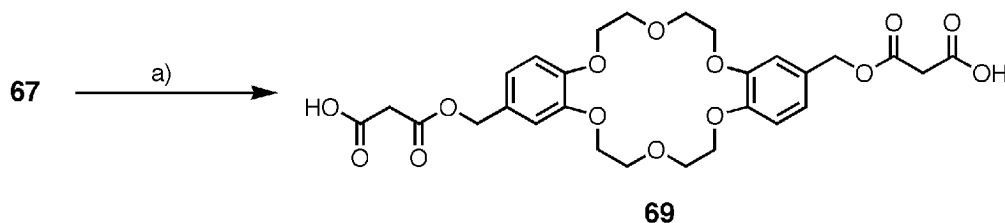
At the same time, another synthetic route was investigated (*Scheme 5.7*). Acid **65** was reacted with oxalyl chloride in dry CH_2Cl_2 to form the corresponding acid chloride, **68**, which reacted with crown ether-derived diol **67** in CH_2Cl_2 in the presence of Et_3N . However, this yielded a complex mixture in which **63** could be identified neither by mass spectrometry nor by NMR spectroscopy.



| Attempts | 65 (eq) | $(\text{COCl})_2$ eq. | T °C |
|----------|----------------|-----------------------|--------|
| 1 | 1 | 20 | r.t. |
| 2 | 1 | 20 | reflux |
| 3 | 1 | 100 | r.t. |
| 4 | 1 | 100 | reflux |

Scheme 5.7 Synthesis of dibenzo[18]crown-6 derivative **63**. Reagents and conditions: a) $(\text{COCl})_2$, CH_2Cl_2 , 40 °C, 14 h; b) **67**, Et_3N , THF, DCC, DMAP, r.t., 14 h.

Since the esterification between porphyrin-derived diol **56** and *tert*-butyl hydrogen malonate (**57**) (*Scheme 5.3*) successfully worked in the presence of DCC and DMAP, it was envisaged to react dibenzo[18]crown-6-derived diol **67** with *Meldrum's* acid to yield crown ether **69** bearing two carboxy groups [417, 418] (*Scheme 5.9*).



Scheme 5.8 Synthesis of crown ether-derived diacid **69**. Reagents and conditions: a) *Meldrum's* acid, THF, reflux, 3 h.

Although diacid **69** was identified by mass spectrometry, it could not be obtained as a pure compound.

5.2 Conclusion

The remarkable photochemical behavior of fullerene-porphyrin dyad **45** and triad **46** (*Figure 5.1*) inspired design and synthesis of the sophisticated C₆₀-bisporphyrin conjugate **47** (*Figure 5.2*) and of [60]fullerene-porphyrin-crown ether conjugate **61** (*Scheme 5.5*). Although various synthetic efforts did not afford the desired compounds, we are confident that the chemistry herein explored will be of interest and utility for further explorations into the synthesis of conjugates combining fullerenes with other functional entities such as porphyrins and crown ethers.

6 Experimental Part

6.1 General Instrumentation

Column chromatography. Adsorption chromatography columns were packed with Fluka silica gel 60 (SiO₂; 230-400 mesh, particle size 0.040-0.063 mm). Flash column chromatography was run at a maximum head pressure of 0.2 bar.

Thin layer chromatography (TLC). Macherey Nagel Alugram SIL G/UV₂₃₄; layer thickness 0.2 mm. Visualization by UV light (254 or 366 nm).

IR spectra (cm⁻¹). Perkin-Elmer Spektrum BX II. Selected absorption bands are reported by wavenumber (cm⁻¹) and their relative intensities are described as *s* (strong), *m* (medium), or *w* (weak).

NMR spectra. Bruker AMX 500, or Varian Gemini-300 spectrometers at 25 °C. Chemical shifts are reported in ppm downfield from tetramethylsilane using the residual solvent signals as an internal reference (CHCl₃, δ_H 7.26). Coupling constants (*J*) are given in Hz. The resonance multiplicity is described as *s* (singlet), *d* (doublet), *t* (triplet), *q* (quartet), *dd* (doublet of doublet), and *m* (multiplet). All spectra were recorded at 25 °C.

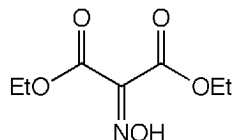
Mass spectra. HR-FT-ICR-MALDI mass spectra were performed by the MS-service at the *Laboratorium für Organische Chemie* of *ETH Zürich*. The spectra were measured on an *Ion Spec Ultima FT-ICR* instrument using 2,5-dihydroxybenzoic acid (DHB) as matrix.

Melting points. Büchi Smp 20 apparatus. All melting points were measured in open capillaries and are reported uncorrected.

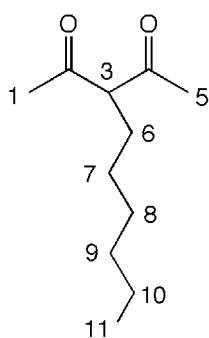
6.1.1 Materials

Reagents and solvents were purchased reagent-grade from *Fluka*, *Aldrich*, *ABCR*, *Acros* or *J. T. Baker* and used without further purification. Moisture-sensitive reactions were run under argon (Ar) in oven-dried (180 °C) glassware. Evaporation and concentration under reduced pressure were done below 50 °C at water aspirator pressure, and compounds were dried at 10⁻² Torr. Column chromatography was performed using distilled technical grade solvents.

6.1.2 Experimental Procedures

Diethyl 2-Hydroximinomalonate (49) [407]

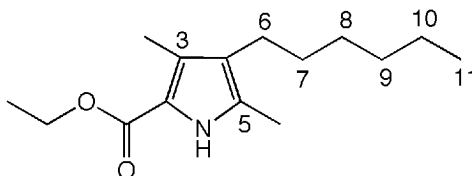
In a 250-mL round-bottomed flask, an aq. solution of NaNO_2 (95 g, 1.38 mol) was added portionwise under stirring to a solution of diethylmalonate (80 g, 0.5 mol) in CH_3COOH (86 mL). Evolution of gas had to stop before a new portion of aq. NaNO_2 was added. After the addition was complete, the mixture was separated into two layers. Et_2O (50 mL) was added to the organic layer, and the resulting solution was neutralized with aq. NaHCO_3 and washed with H_2O (3×50 mL). The organic phase was concentrated under reduced pressure affording a colorless oil. Purification by distillation yielded **49** (57 g, 60%). Colorless oil. B.p.₁₂ 175 °C (Lit. [407]: 172 °C). $^1\text{H-NMR}$ (300 MHz, CDCl_3): 4.25 (*q*, $J = 7.1$, 4 H, CH_2CH_3); 1.25 (*t*, $J = 7.1$, 6 H, CH_2CH_3). $^{13}\text{C-NMR}$ (75 MHz, CDCl_3): 156.15, 143.55, 62.12, 13.85.

3-Hexylpentane-2,4-dione (50) [425]

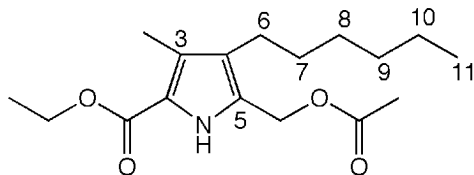
In a dry 250-mL round-bottomed flask, 1-iodohexane (10 g, 50 mmol), pentane-2,4-dione (7.1 g, 70.0 mmol) and K_2CO_3 (10 g, 70 mmol) in dry acetone (50 mL) was refluxed under nitrogen for 24 h. Filtration of the reaction mixture and purification by distillation yielded **50** (5.1 g, 55%). Yellow oil. B.p.₁₆ 120-123 °C (Lit. [425]: 123-124 °C). $^1\text{H-NMR}$ (300 MHz,

CDCl₃): 3.56-3.81 (*m*, 1 H, H-C(3)); 2.15 (*s*, 6 H, H-C(1), H-C(5)); 1.77-1.85 (*m*, 2 H, H-C(6)); 1.20-1.32 (*m*, 8 H, H-C(7), H-C(8), H-C(9), H-C(10)); 0.85 (*t*, *J* = 8.1, 3 H, H-C(11)).
¹³C-NMR (75 MHz, CDCl₃): 207.13, 76.47, 31.88, 29.92, 27.77 (× 2), 25.26, 22.69, 14.13.

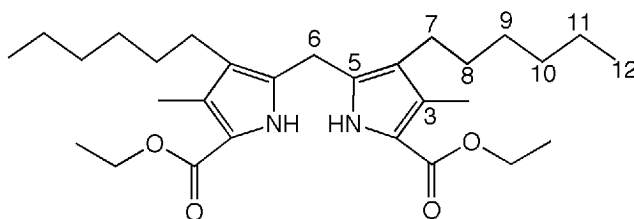
Ethyl 4-Hexyl-3,5-dimethylpyrrole-2-carboxylate (51) [408]



In a 100-mL three-necked flask equipped with a mechanical stirrer, dropping funnel, thermometer, and gas exit, **50** (5 g, 27 mmol) was dissolved in CH₃COOH (15 mL). The resulting solution was heated and at 80 °C, a mixture of anhydrous CH₃COONa (7 g, 86 mmol) and Zn dust (5.6 g, 86.0 mmol) was added under vigorous stirring. At 95 °C, a solution of **49** (5.1 g, 27.0 mmol) in a mixture of CH₃COOH (7 mL) and water (3 mL) was added over a period of 50 min and the temperature was maintained between 95 and 105 °C. After heating to 100-105 °C for an additional 20 min, the reaction mixture was added to 30 mL of boiling 95% ethanol. Two recrystallizations (95% EtOH) yielded pure **51** (3.4 g, 50%). White solid. M.p. 62-64 °C (EtOH) (Lit. [426]: 61-62 °C (EtOH)). ¹H-NMR (300 MHz, CDCl₃): 8.56 (*s*, 1 H, NH); 4.28 (*q*, *J* = 7.2, 2 H, OCH₂CH₃); 2.33 (*t*, *J* = 7.2, 2 H, H-C(6)); 2.26 (*s*, 3 H, CH₃-C(3)); 2.19 (*s*, 3 H, CH₃-C(5)); 1.28-1.42 (*m*, 11 H, H-C(7), H-C(8), H-C(9), H-C(10), H-C(11)); 0.88 (*t*, *J* = 7.2, 3 H, OCH₂CH₃). ¹³C-NMR (75 MHz, CDCl₃): 162.47, 129.96, 125.67, 119.90 (× 2), 59.73, 31.61, 28.92, 28.15, 23.15, 22.54, 14.60 (× 2), 11.31, 10.69.

Ethyl 5-Acetoxymethyl-3-methyl-4-hexylpyrrole-2-carboxylate (52) [409]

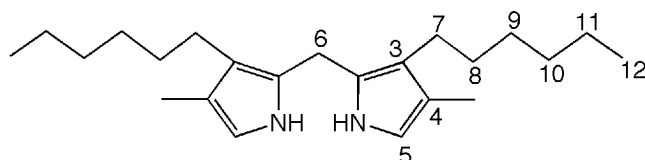
To a vigorously stirred solution of **51** (3 g, 12 mmol) in glacial CH_3COOH (90 mL), $\text{Pb}(\text{OAc})_4$ (5.3 g, 12 mmol) was added at 25 °C. After 2 h, the solvent was evaporated *in vacuo* and the residue poured into water (200 mL). The precipitate was separated and washed with water (70 mL). Recrystallization (MeOH) yielded **52** (2.9 g, 77%). Pink solid. M.p.: 134-137 °C (MeOH) (Lit. [427]: 131-132 °C). $^1\text{H-NMR}$ (300 MHz, CDCl_3): 8.95 (*s*, 1 H, NH); 5.01 (*s*, 2 H, $\text{CH}_2\text{-C}(5)$); 4.30 (*q*, $J = 7.2$, 2 H, OCH_2CH_3); 2.42 (*t*, $J = 7.2$, 2 H, H-C(6)); 2.26 (*s*, 3 H, $\text{CH}_3\text{-C}(3)$); 2.06 (*s*, 3 H, $\text{CH}_3\text{-C}(5)$); 1.28-1.42 (*m*, 11 H, H-C(7), H-C(8), H-C(9), H-C(10), H-C(11)); 0.88 (*t*, $J = 7.2$, 3 H, OCH_2CH_3). $^{13}\text{C-NMR}$ (75 MHz, CDCl_3): 171.12, 162.20, 127.43, 124.53, 121.95, 118.58, 59.67, 57.46, 31.61, 28.62 ($\times 2$), 23.46, 22.54, 20.56, 14.60 ($\times 2$), 10.23.

Diethyl 2,2'-Methylenedi(3-hexyl-4-methylpyrrole-2-carboxylate) (53) [409]

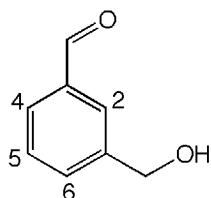
To a 250-mL round-bottomed flask, **52** (5 g, 16 mmol) in a mixture of EtOH (100 mL) and HCl_{conc} (3 mL) was added. The mixture was heated to reflux for 1 h. After cooling to 25 °C, the product crystallized. Filtration and washing with EtOH (200 mL) yielded **53** (3 g, 40%). White solid. M.p. 195-197 °C (EtOH) (Lit. [427]: 196-198 °C (EtOH)). $^1\text{H-NMR}$ (300 MHz, CDCl_3): 8.63 (*s*, 2 H, NH); 4.26 (*q*, $J = 7.2$, 4 H, OCH_2CH_3); 3.84 (*s*, 2 H, H-C(6)); 2.35 (*t*, $J = 7.2$, 4 H, H-C(7), H-C(7')); 2.26 (*s*, 6 H, $\text{CH}_3\text{-C}(3)$, $\text{CH}_3\text{-C}(3')$); 1.27-1.37 (*m*, 22 H, H-C(8), H-C(8), H-C(9), H-C(9'), H-C(10), H-C(10'), H-C(11), H-C(11')), H-

C(12), H-C(12')); 0.87 (*t*, $J = 7.2$, 6 H, OCH₂CH₃). ¹³C-NMR (75 MHz, CDCl₃): 162.00, 129.51, 128.18, 126.50, 114.58, 59.50, 31.61, 28.92 (× 2), 24.84, 23.43, 22.54, 14.09 (× 2), 10.50.

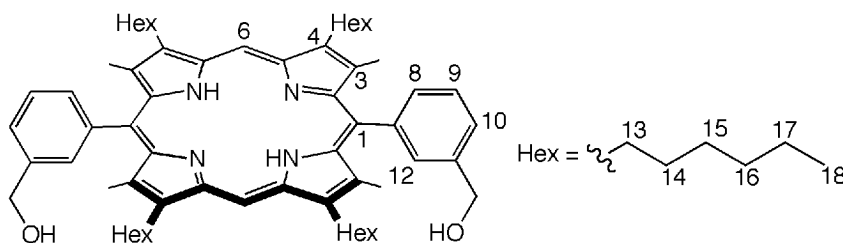
2,2'-Methylenedi(3-hexyl-4-methylpyrrole) (**54**) [410]



To refluxing EtOH (50 mL), **53** (3 g, 6.2 mmol) and 10% NaOH (13 mL) was added, and the solution heated under reflux for 5 h. The solvent was removed *in vacuo* affording a pink residue. To this residue, water (30 mL) was added and the resulting suspension was extracted with CH₂Cl₂ (3 × 30 mL) to remove the residual diester. The aqueous phase was cooled to 0 °C and neutralized with CH₃COOH to give a white precipitate which was extracted with Et₂O (3 × 20 mL). Removal of Et₂O *in vacuo* gave the crude diacid which was dissolved in the dark under Ar in HOCH₂CH₂NH₂ (16 mL) and refluxed for 6 h. The resulting dark brown solution was poured into an ice-water mixture (35 mL) and extracted with CH₂Cl₂ (3 × 30 mL). The combined organic phases were concentrated *in vacuo*. FC (SiO₂, argon, darkness, CH₂Cl₂) yielded **54** (1.5 g, 70%). Brown solid. M.p. 131-133 °C (Lit: [427]: 132-136 °C). ¹H-NMR (300 MHz, CDCl₃): 7.32 (*s*, 2 H, NH); 6.35 (*s*, 2 H, H-C(5), H-C(5')); 3.82 (*s*, 2 H, H-C(6)); 2.44 (*t*, $J = 9.9$, 4 H, H-C(7), H-C(7')); 2.07 (*s*, 6 H, H₃C-C(4), H₃C-C(4')); 1.33-1.48 (*m*, 16 H, H-C(8), H-C(8'), H-C(9), H-C(9'), H-C(10), H-C(10'), H-C(11), H-C(11')); 0.93 (*t*, $J = 9.6$, 6 H, H-C(12), H-C(12')). ¹³C-NMR (75 MHz, CDCl₃): 131.86, 124.83, 121.57, 114.42, 31.61, 28.92, 28.15, 22.84 (× 2), 22.46, 14.09, 10.87.

3-Hydroxymethylbenzaldehyde (**55**) [383, 411, 428]

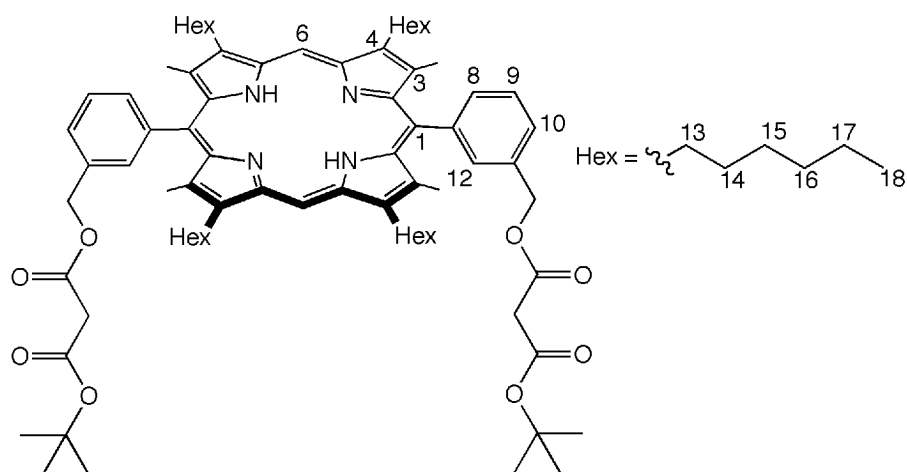
To a solution of isophthalaldehyde (5 g, 36 mmol) in EtOH (100 mL), NaBH₄ (0.36 g, 9.1 mmol) was added at r.t. The mixture was stirred for 1 h, quenched with water and extracted (CH₂Cl₂). The organic layer was dried (MgSO₄) and evaporated *in vacuo*. FC (SiO₂, CH₂Cl₂/AcOEt 8:2) yielded **55** (2.6 g, 52%). Pale yellow oil. ¹H-NMR (300 MHz, CDCl₃): 9.92 (*s*, 1 H, CHO); 7.81 (*s*, 1 H, H-C(2)); 7.72 (*d*, *J* = 7.5, 1 H, H-C(6)); 7.57 (*d*, *J* = 7.5, 1 H, H-C(4)); 7.46 (*t*, *J* = 7.5, 1 H, H-C(5)); 4.70 (*s*, 2 H, ArCH₂). ¹³C-NMR (75 MHz, CDCl₃): 192.29, 140.27, 134.10, 133.32, 131.86, 131.51, 126.13, 19.52.

5,15-Bis[3-(hydroxymethyl)phenyl]-2,8,12,18-tetrahexyl-3,7,13,17-tetramethylporphyrin (**56**) [406]

To a 250-mL round-bottomed flask charged with a solution of **54** (1.5 g, 4.4 mmol) and **55** (603 mg, 4.4 mmol) in acetonitrile (100 mL), a solution of trichloroacetic acid (214 mg, 1.3 mmol) in acetonitrile (20 mL) was added. The mixture was stirred 14 h at r.t. under nitrogen. A solution of *p*-chloranil (4.32 g, 17.6 mmol) in THF (80 mL) was added, and the mixture was stirred for 6 h. After evaporation of the solvent, the residue was dissolved in CH₂Cl₂ and neutralized by addition of Et₃N (pH = 8). The solvent was evaporated *in vacuo*, and the residue was passed through a short plug of SiO₂, (CH₂Cl₂) to remove the oxidant and then with CH₂Cl₂/AcOEt 9.5:0.5 to recover the desired product together with its regioisomer. FC (SiO₂, CH₂Cl₂/AcOEt 9:1) yielded **56** (1.6 g, 40%). Purple solid. M.p.: > 300 °C. IR (neat):

3300s, 1600m, 1584w, 1470m, 1360m, 1256w, 1206w, 1145w, 1023w, 998m, 978s, 805s, 721s, 689w. $^1\text{H-NMR}$ (300 MHz, CDCl_3): 10.3 (s, 2 H, H-C(6)); 8.02-8.08 (m, 4 H, H-C(8), H-C(12)); 7.72-7.82 (m, 4 H, H-C(9), H-C(10)); 4.98 (s, 4 H, ArCH_2O); 3.98 (t, $J = 7.2$, 8 H, H-C(13)); 2.49 (s, 12 H, $\text{CH}_3\text{-C}(3)$); 2.06-2.24 (m, 8 H, H-C(14)); 1.69-1.79 (m, 8 H, H-C(15)); 1.27-1.53 (m, 16 H, H-C(16), H-C(17)); 0.88 (t, $J = 7.2$, 12 H, H-C(18)); -2.33 (s, 2 H, NH). $^{13}\text{C-NMR}$ (75 MHz, CDCl_3): 159.53, 148.20, 146.53, 144.47, 137.42, 130.33, 129.43 ($\times 2$), 127.99 ($\times 2$), 127.77, 127.68, 127.53, 122.33 ($\times 2$), 99.03, 97.26, 65.71, 32.03, 31.61, 29.51, 28.92, 27.93, 26.70, 24.67, 22.99, 22.54, 14.09, 13.45, 11.43, 10.39 ($\times 2$). HR-MALDI-MS: 915.3385 (M^+ , $\text{C}_{62}\text{H}_{82}\text{N}_4\text{O}_2^+$, calc: 915.3401).

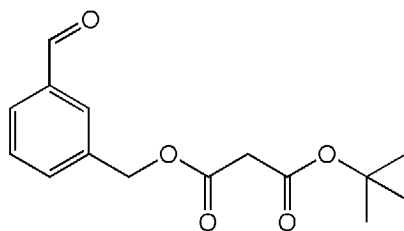
5,15-Bis(3-[(3-tert-butoxy-3-oxopropanoyl)oxy]methyl)phenyl)-2,8,12,18-tetrahexyl-3,7,13,17-tetramethylporphyrin (48)



To a dry DMF solution (9 mL) containing **56** (1 g, 1.09 mmol), DMAP (0.027 g, 0.18 mmol), and *tert*-butylmalonate **57** (0.52 g, 3.27 mmol), DCC (0.67 g, 3.27 mmol) was added at 0 °C. The reaction mixture was stirred 14 h at r.t., filtered to remove a white precipitate (*N,N'*-dicyclohexylurea), and the solvent evaporated *in vacuo*. The residue was dissolved in $\text{CH}_2\text{Cl}_2/\text{AcOEt}$ (1:1), washed with 0.1% aq. TFA, with H_2O , and dried over MgSO_4 . The solvents were evaporated *in vacuo*. FC (SiO_2 , $\text{CH}_2\text{Cl}_2/\text{AcOEt}$ 95:5) yielded **48** (0.92 g, 70%). Brown solid. M.p.: > 300 °C. IR (neat): 3296s, 2928m, 2870m, 1725s, 1586m, 1522m, 1456w, 1378m, 1255s, 1227s, 1206s, 1175w, 1094s, 1022s, 867w, 805s, 750w, 727w, 689w. $^1\text{H NMR}$ (300 MHz, CDCl_3): 10.25 (s, 2 H, H-C(6)); 8.04-8.09 (m, 4 H, H-C(8), H-

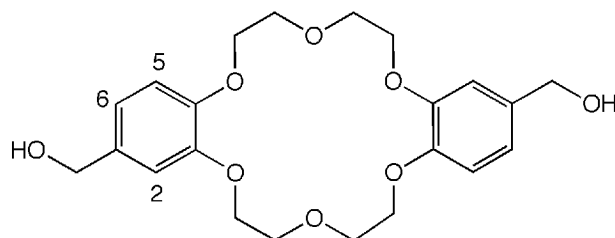
C(12)); 7.72-7.82 (*m*, 4 H, H-C(9), H-C(10)); 5.47 (*s*, 4 H, ArCH₂O); 3.98 (*t*, *J* = 7.2, 8 H, CH₂C₅H₁₁); 3.40 (*s*, 4 H, COCH₂CO); 2.47 (*s*, 12 H, H-C(3)); 2.16-2.21 (*m*, 8 H, CH₂CH₂C₄H₉); 1.69-1.76 (*m*, 8 H, (CH₂)₂CH₂C₃H₇); 1.33-1.53 (*m*, 16 H, (CH₂)₃(CH₂)₂CH₃); 0.91 (*t*, *J* = 7.2, 12 H, (CH₂)₅CH₃); -2.42 (*s*, 2 H, NH). ¹³C-NMR (75 MHz, CDCl₃): 166.28, 166.00, 148.20, 144.48 (× 2), 140.79, 140.08, 139.31, 138.05, 131.28, 130.62, 129.43, 129.16, 127.98, 127.10, 126.88, 125.84, 115.36, 100.00, 99.03, 81.40, 67.58, 46.83, 32.03, 31.61, 29.51, 28.92, 27.90, 27.89, 26.70, 24.67, 22.99, 22.54, 14.09, 14.05, 12.42, 10.39. HR-MALDI-MS: 1199.6432 (*M*⁺, C₇₆H₁₀₂N₄O₈⁺, calc: 1199.6450).

tert-Butyl (3-Formylphenyl)methyl Malonate (**64**)



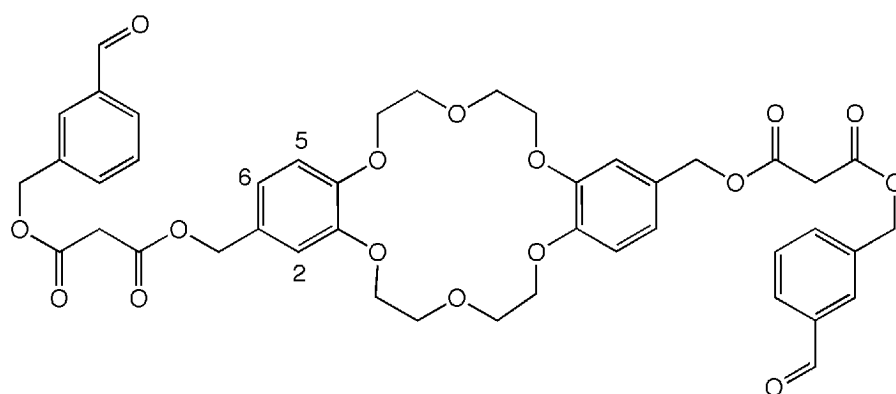
To a 100-mL round-bottomed flask charged with a solution of **55** (1.0 g, 7.3 mmol), DMAP (0.085 g, 0.7 mmol) and *tert*-butyl malonate (1.74 g, 10.9 mmol) in dry DMF (35 mL), DCC (2.2 g, 10.9 mmol) was added at 0 °C. The reaction mixture was stirred at r.t. for 14 h. The mixture was filtered to remove a white precipitate (*N,N'*-dicyclohexylurea), and the solvent was evaporated *in vacuo*. Colorless oil. FC (SiO₂, CH₂Cl₂/AcOEt 7:3) yielded **64** (1.81 g, 89 %). IR (neat): 2984*m*, 2733*w*, 1732*s*, 1609*m*, 1583*m*, 1448*m*, 1371*s*, 1333*s*, 1300*s*, 1279*s*, 1147*s*, 1032*s*, 894*w*, 850*w*, 794*m*, 750*m*, 694*m*. ¹H-NMR (300 MHz, CDCl₃): 10.01 (*s*, 1 H, CHO); 7.53-7.87 (*m*, 4H, ArH); 5.24 (*s*, 2 H, ArCH₂); 3.35 (*s*, 2 H, COCH₂CO); 1.45 (*s*, 9 H, C(CH₃)₃). ¹³C-NMR (75 MHz, CD₃OD): 194.35; 166.28 (× 2), 137.78 (× 2), 130.68, 129.77, 127.96 (× 2), 81.40, 66.57, 46.83, 27.90.

6,7,9,10,17,18,20,21-Octahydrodibenzo[b,k][1,4,7,10,13,16]hexaoxacyclooctadecin-2,13-diyl dimethanol (**67**) [383]



NaBH₄ (0.82 g, 21 mmol) was added to a suspension of **66** (1.1 g, 2.6 mmol) in MeOH (300 mL) at 0 °C. After stirring for 1h at r.t., the mixture was partitioned between H₂O and AcOEt and the organic layer was separated, dried (MgSO₄), and evaporated *in vacuo* to give **67** (1 g, 85 %). White solid. M.p. 167-169 °C (Lit. [383]: 166-169 °C). ¹H-NMR (300 MHz, CD₃OD): 3.95-3.97 (m, 8 H, ArOCH₂CH₂); 4.18-4.20 (m, 8 H, ArOCH₂CH₂); 4.51 (s, 4 H, ArCH₂); 6.87-6.96 (m, 6 H, ArH). ¹³C-NMR (75 MHz, CD₃OD): 150.23, 149.58, 137.01, 121.19, 114.3 (× 2), 71.12 (× 2), 70.01, 69.91, 65.35.

1,1'-Bis[(3-formylphenyl)methyl] 3,3'-[(6,7,9,10,17,18,20,21-Octahydrodibenzo[b,k][1,4,7,10,13,16]hexaoxacyclooctadecin-2,13-diyl)dimethylene] Bis(malonate) (**63**)

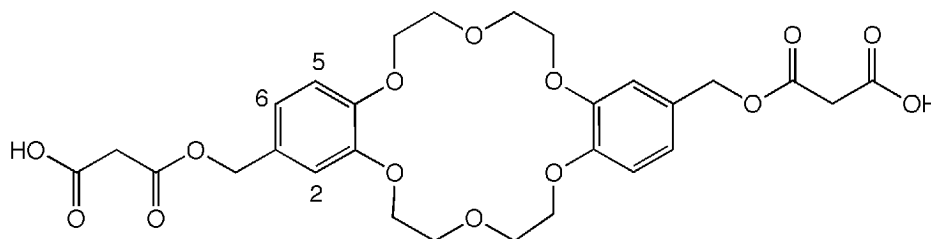


To a 100-mL round-bottomed flask charged with a solution of **64** (0.5 g, 1.8 mmol) in CH₂Cl₂ (25 mL), was added TFA (0.2 g, 1.8 mmol). After stirring at r.t. for 1 h, the mixture was washed with water (3 × 50 mL), the organic phase was dried (MgSO₄), and the solvent

evaporated *in vacuo*. The residue was immediately used in the subsequent esterification reaction without additional purification.

To a dry solution of the alcohol residue **65**, **66** (0.19 g, 0.45 mmol), and DMAP (0.015 g, 0.13 mmol) in DMF (5 mL), was added DCC (0.278 g, 1.35 mmol) at 0 °C. The reaction mixture was stirred at r.t. for 14 h. The mixture was filtered to remove a white precipitate (*N,N*-dicyclohexylurea), and the solvent evaporated *in vacuo*. Purifications of the residue (chromatography on SiO₂, recrystallization from hexane, hexane/toluene 1 : 1, ethanol/water 1 : 1, precipitation from chloroform and from dichloromethane upon addition of hexane) did not lead to the pure product.

3,3'-[(6,7,9,10,17,18,20,21-Octahydrodibenzo[b,k] [1,4,7,10,13,16]hexaoxacyclooctadecin-2,13-diyl)dimethylene] Bis(malonate) (69)



A solution of **67** (100 mg, 0.24 mmol) and *Meldrum's acid* (83 mg, 0.58 mmol) in THF (50 ml) was heated to reflux for 3 h. The solvent was evaporated *in vacuo*. Purifications of the residue (chromatography on SiO₂, recrystallization from ethanol/water 1:1) did not lead to the pure product.

6.2 *Langmuir and Langmuir-Blodgett Films*

6.2.1 General Instrumentation

Langmuir films. Data were collected with a *NIMA* (611D/2B/1PTFE/WIN/CAB) system (*Nima Instruments*, Coventry, England) using a symmetrical compression *Teflon* trough and hydrophilic barriers. The whole setup was in a *Plexiglas* enclosure resting on a vibration-free table (*MOD-1* plus active vibration isolation systems, *Hacyonics GmbH*, Göttingen, Germany). Surface pressures were measured by means of a platinum Wilhelmy plate.

Surface Potential Measurements. KSV-SPOT 1 (*KSV Instruments*, Helsinki, Finland).

Langmuir–Blodgett layers. Glass slides from *Marienfeld* (microscope slides $76 \times 26 \times 1$ mm). The glass substrates were cleaned with a 10% soap solution in hot ultrapure water and then rinsed 10 times with ultrapure water. All treatments were done in an ultrasonic bath. *Water subphase*. The ultrapure water ($\rho = 18 \text{ M}\Omega$) was purified through a *Milli-Q Plus A10* system (*Millipore Co*).

Brewster Angle Microscope. The BAM images were recorded with a *MiniBAM Plus* or *BAM-2-Plus* setup from *Nanofilm Technology GmbH* (Göttingen, Germany). The illumination source (laser diode, $\lambda = 660 \text{ nm}$) was operated at an angle of incidence $\theta = 52\text{--}54^\circ$. The images were recorded with a CCD (charge coupled device) camera at a resolution $< 20 \mu\text{m}$.

UV-VIS spectra. *Varian Cary 5* spectrophotometer. All spectra of LB layers were recorded immediately after the transfer over the wavelength range 350–650 nm.

Grazing-Incidence X-ray Analysis. Spectrometer equipped with a Ni- β filter, a programmable divergence slit ($1/32^\circ$), a parallel-plate collimator, a flat Ge monochromator, and a proportional Xe detector. All measurements were recorded immediately after the transfer of the *Langmuir* layers onto the solid support.

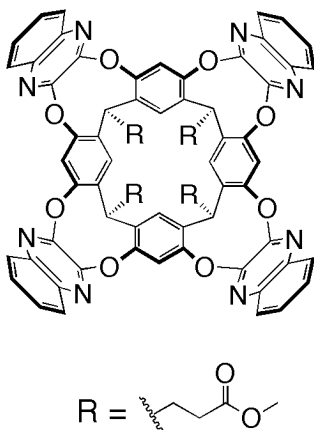
6.2.2 Experimental Procedures

Spreading solutions were prepared by dissolving the analytes in CHCl_3 (analysis grade from *Acros*) or toluene (analysis grade from *J.T. Baker*), according to equation 1.1 (*Section 1.3.2, Chapter 1*). For a typical experiment, 25 μL of fresh solution were spread on the aqueous subphase with a microsyringe and the monolayers were compressed with a speed of $20 \text{ cm}^2/\text{min}$. All measurements were repeated three times to ensure reproducibility.

BAM investigations were performed by disposing a black glass plate at the bottom of the trough to avoid stray light. Subsequently, the solutions of the analytes were spread and the layers were observed over the whole duration of the experiments. In each experiment the black glass plate was positioned in different parts of the trough to monitor the layer in different points.

Stearic acid

A spreading solution was prepared by dissolving stearic acid (4.1 mg, 0.0145 mmol) in CHCl_3 (5 ml). The fresh solution (25 μL) was spread on the water subphase, and the film was left for 30 min to equilibrate before compression started.

Resorcin[4]arene-based cavitand 11

A spreading solution was prepared by dissolving **11** (22 mg, 0.0016 mmol) in CHCl_3 (1 ml). The fresh solution (25 μL) was spread on the water subphase, and the film was left for 30 min to equilibrate before compression started. The solution of cavitand **11** was also spread on water subphases containing TFA, AgNO_3 , FeCl_3 , CuSO_4 , KCl , and $\text{Zn}(\text{OAc})_2$.

Spreading of **11** on a water subphase containing TFA

The subphases at pH = 3, 2, and 1 were prepared by adding TFA to ultra pure water (550 mL) and the pH was determined with 691 pHmeter from *Metrohm AG* (Herisau, Switzerland).

pH = 3: TFA (79 mg, 0.55 mmol)

pH = 2: TFA (0.79 g, 5.5 mmol)

pH = 1: TFA (7.9 g, 55 mmol)

After stirring at r.t. for 1 h, the resulting acidic solutions were added to the *Langmuir* trough. The fresh solution of **11** (25 μL) was spread on the acidic subphases, and the film was left for 40 min to equilibrate before compression started.

Spreading of **11** on water subphases containing AgNO₃, FeCl₃, CuSO₄, and KCl

The subphases were prepared by adding the metal salts to the ultra pure water (550 mL) in concentrations that were 10, 50, and 100 times higher than that of the cavitand solution ((Mⁿ⁺) : (**11**) = 10 : 1, 50 : 1, and 100 : 1). After stirring at r.t. for 1 h, the resulting solutions containing the metal salts were added to the *Langmuir* trough. The fresh solution of **11** (25 µL) was spread on the metal salt-containing subphases, and the film was left for 40 min to equilibrate before compression started. The quantities of metal salts used for the preparation of the subphases are shown below.

(Ag⁺) : (**11**) = 10 : 1 → Ag⁺: 2.7 mg, 0.016 mmol

(Ag⁺) : (**11**) = 50 : 1 → Ag⁺: 13.6 mg, 0.08 mmol

(Ag⁺) : (**11**) = 100 : 1 → Ag⁺: 27 mg, 0.16 mmol

(Fe³⁺) : (**11**) = 10 : 1 → Fe³⁺: 2.6 mg, 0.016 mmol

(Fe³⁺) : (**11**) = 50 : 1 → Fe³⁺: 13 mg, 0.08 mmol

(Fe³⁺) : (**11**) = 100 : 1 → Fe³⁺: 26 mg, 0.16 mmol

(Cu²⁺) : (**11**) = 10 : 1 → Cu²⁺: 2.5 mg, 0.016 mmol

(Cu²⁺) : (**11**) = 50 : 1 → Cu²⁺: 12.7 mg, 0.08 mmol

(Cu²⁺) : (**11**) = 100 : 1 → Cu²⁺: 25 mg, 0.16 mmol

(K⁺) : (**11**) = 10 : 1 → K⁺: 1.2 mg, 0.016 mmol

(K⁺) : (**11**) = 50 : 1 → K⁺: 6 mg, 0.08 mmol

(K⁺) : (**11**) = 100 : 1 → K⁺: 12 mg, 0.16 mmol

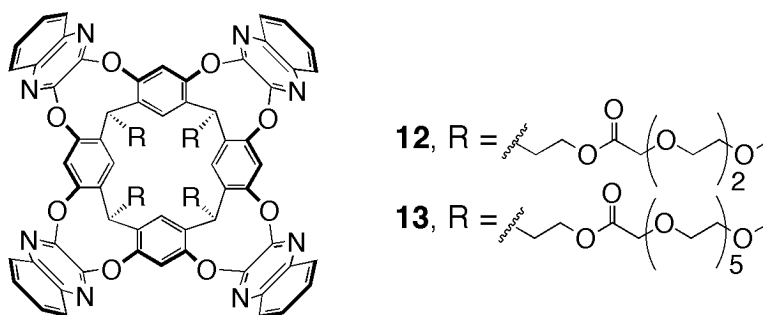
Spreading of **11** on a water subphase containing Zn(OAc)₂

The subphase was prepared by adding Zn(OAc)₂ to ultra pure water (550 mL). The concentration of zinc ions is 5000 times higher than the concentration of cavitand in the spreading solution ((Zn(II)) : (**11**) = 5000 : 1).

(Zn(II)) : (**11**) = 5000 : 1 → Zn(II): 2 g, 8 mmol.

After stirring at r.t. for 1 h, the resulting Zn(II)-containing solution was added to the *Langmuir* trough. In a first experiment, 25 μL of a fresh solution of **11** were spread on the Zn(II)-containing subphase and the film was left 40 min to equilibrate before compression started. In a second experiment, a fresh solution of **11** (25 μL) was spread on the Zn(II)-containing subphase and the film was left 10 min to equilibrate before compression started. Then, a fresh solution of Zn(OAc)₂ (5.13 mg, 0.023 mmol) in a mixture of CHCl₃/MeOH (2.8 mL : 0.4 mL) was added and the layers were left to equilibrate for an additional 30 min before compression started.

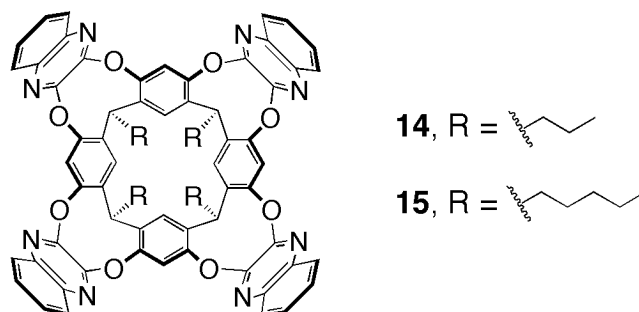
Resorcin[4]arene-based cavitands 12 and 13



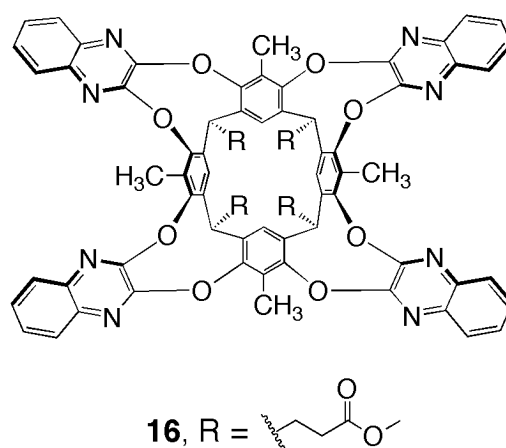
Spreading solutions were prepared by dissolving different quantities of **12** (3.98 mg, 0.001 mmol; 2.57 mg, 0.00137 mmol; 1.92 mg, 0.00194 mmol) in CHCl₃ (1 mL).

Spreading solutions of **13** had the same concentrations as **12**. They were prepared by dissolving **13** (4.6 mg, 0.001 mmol; 3.3 mg, 0.00137 mmol; 2.6 mg, 0.00194 mmol) in CHCl₃ (1 mL).

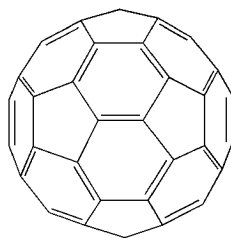
The fresh solutions of **12** or **13** (25 μL) were spread on pure water subphases and the films were left for 30 min to equilibrate before compression started.

Resorcin[4]arene-based cavitands 14 and 15

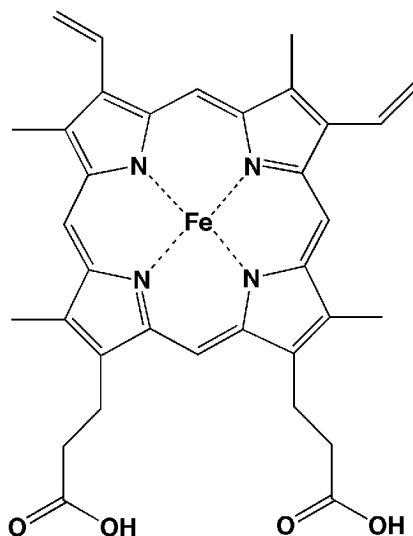
Spreading solutions of **14** and **15** were prepared by dissolving each **14** (9.7 mg, 0.008 mmol) and **15** (10.6 mg, 0.008 mmol) in CHCl_3 (5 mL). Analogously to the previous experiment, fresh solutions of **14** or **15** were spread on pure water subphases and the films were left for 30 min to equilibrate before compression started.

Resorcin[4]arene-based cavitand 16

A spreading solution was prepared by dissolving **16** (1.05 mg, 0.00073 mmol) in CHCl_3 (5 mL). The fresh solution of **16** (25 μL) was spread on a pure water subphase, and the film was left for 30 min to equilibrate before compression started.

Pristine C₆₀

A spreading solution was prepared by dissolving C₆₀ (0.48 mg, 6.9×10^{-4} mmol) in toluene (3 mL). The fresh solution of C₆₀ was spread on a pure water subphase, and the film was left 40 min to equilibrate before compression started

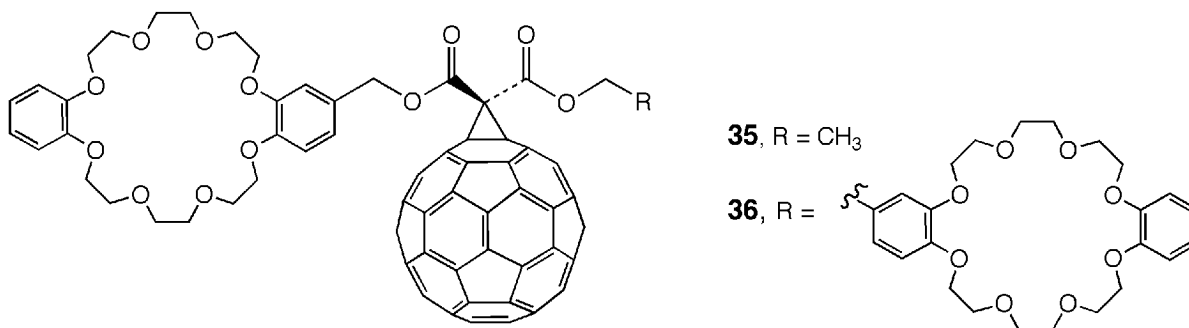
Hemin

The subphase was prepared by dissolving CdCl₂ (36.7 mg, 0.2 mmol) in ultrapure water (1000 mL).

A *Langmuir* monolayer of hemin was prepared by spreading 25 μ L of a fresh solution of hemin (0.024 mg, 3.72×10^{-5} mmol) in DMF (3 ml).

For the preparation of the mixed film (hemin/ODA 1 : 2), solutions of hemin in DMF and of ODA (0.02 mg, 7.44×10^{-5} mmol) in CHCl₃ (3 mL) were spread onto the above-mentioned subphase and the films were then left for 40 min to equilibrate before compression started.

[60]Fullerene-crown ether conjugates **35** and **36**



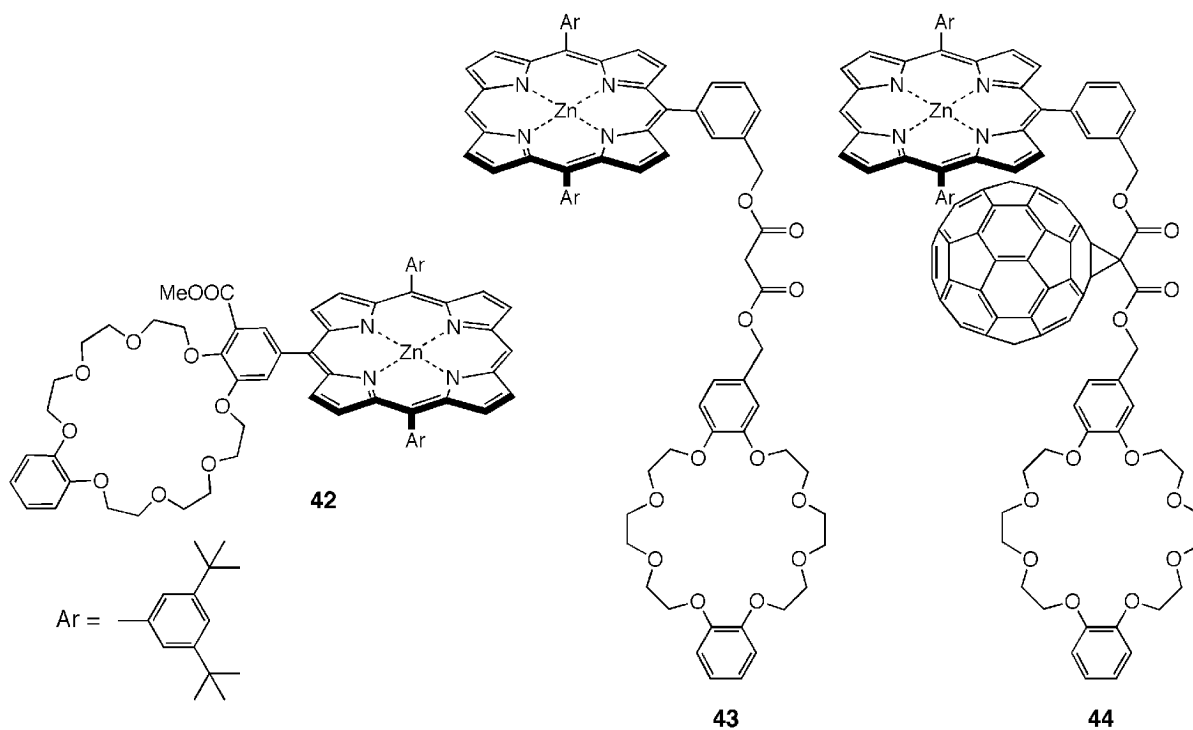
Spreading solutions of **35** and **36** were prepared by dissolving each **35** (4.6 mg, 0.0035 mmol) and **36** (6.1 mg, 0.0035 mmol) in CHCl₃ (5 mL). The fresh solutions were spread on a pure water subphase, and the films were left for 40 min to equilibrate before compression started.

Compression/expansion cycles were performed by compressing the monolayers up to 35 mN m⁻¹. The monolayers were left at this pressure for 5 min before the expansion started.

The spreading behavior of both conjugates was studied on 1M aq. LiCl, NaCl, KCl, CsCl, and CaCl₂ subphases.

The subphases were prepared by adding metal chlorides to ultrapure water (550 mL) and the resulting solutions were stirred at r.t. for 1 h. The quantity of metal chloride added in each experiment are reported in the following table:

| LiCl | NaCl | KCl | CsCl | CaCl ₂ |
|--------|--------|------|--------|-------------------|
| 23.3 g | 32.1 g | 41 g | 92.6 g | 61 g |

Porphyrin derivatives **42** – **44**

Spreading solutions of **42**, **43**, and **44** were prepared by dissolving each **42** (1.76 mg, 0.0014 mmol), **43** (1.96 mg, 0.0014 mmol), and **44** (2.97 mg, 0.0014 mmol) in CHCl_3 (2 mL), respectively. The fresh solutions were spread on a pure water subphase and left for 30 min to equilibrate before compression started. Compression/expansion cycles were performed by first compressing the monolayers up to 40 mN m^{-1} (**42**), 25 mN m^{-1} (**43**), or 30 mN m^{-1} (**44**). The monolayers were left at these pressures for 5 min before the expansion started.

All monolayers (**42**, **43**, and **44**) were studied on 1M aq. KCl and CsCl subphases.

LB layers were obtained by transfer of the *Langmuir* films onto glass slides. Transfers were performed at surface pressures of 20 mN m^{-1} (**42**) and 15 mN m^{-1} (**43**, **44**) and at a dipping speed (V_{dip}) of 7 mm/min. In all cases, the transfer started during the upstroke movement and the transfer ratios were 0.5 ± 0.1 for the first deposition but rapidly decreased to zero for subsequent depositions. In the cases of **42** and **43**, Z-type multilayered films were formed, whereas Y-type multilayers were obtained for **44**.

Immediately after the transfer of one LB layer, **43** and **44** were analyzed by *grazing-incidence X-ray diffraction* to measure the thickness and the quality (roughness) of the

monolayer. The UV-VIS absorption spectra were also measured immediately after the transfer of one/several layers.

7 Literature

1. F. Schreiber, *Prog. Surf. Sci.* **2000**, *65*, 151-256. Structure and Growth of Self-Assembling Monolayers.
2. A. Ulman, *An Introduction to Ultrathin Organic Films from Langmuir-Blodgett to Self-Assembly*, Academic Press, San Diego, **1991**.
3. J. S. Lindsey, *New J. Chem.* **1991**, *15*, 153-180. Self-Assembly in Synthetic Routes to Molecular Devices. Biological Principles and Chemical Perspectives: A Review.
4. L. Stryer, *Biochemistry*, 4th Revised Edition, W. H. Freeman, New York, **1996**.
5. G. M. Whitesides, J. P. Mathias, C. T. Seto, *Science* **1991**, *254*, 1312-1319. Molecular Self-Assembly and Nanochemistry: A Chemical Strategy for the Synthesis of Nanostructures.
6. H. Fraenkel-Conrat, R. C. Williams, *Proc. Natl. Acad. Sci. USA* **1955**, *41*, 690-698. Reconstitution of Active Tobacco Mosaic Virus from Its Inactive Protein and Nucleic Acid Components.
7. C. D. Bain, E. B. Troughton, Y. T. Tao, J. Evall, G. M. Whitesides, R. G. Nuzzo, *J. Am. Chem. Soc.* **1989**, *111*, 321-335. Formation of Monolayer Films by the Spontaneous Assembly of Organic Thiols from Solution onto Gold.
8. G. M. Whitesides, P. E. Laibinis, *Langmuir* **1990**, *6*, 87-96. Wet Chemical Approaches to the Characterization of Organic Surfaces: Self-Assembled Monolayers, Wetting, and the Physical-Organic Chemistry of the Solid-Liquid Interface.
9. R. G. Nuzzo, D. L. Allara, *J. Am. Chem. Soc.* **1983**, *105*, 4481-4483. Adsorption of Bifunctional Organic Disulfid on Gold Surfaces.
10. R. G. Nuzzo, L. H. Dubois, D. L. Allara, *J. Am. Chem. Soc.* **1990**, *112*, 558-569. Fundamental Studies of Microscopic Wetting on Organic Surfaces. 1. Formation and Structural Characterization of Self-Consistent Series of Polyfunctional Organic Monolayers.
11. L. H. Dubois, R. G. Nuzzo, *Annu. Rev. Phys. Chem.* **1992**, *43*, 437-463. Synthesis, Structure and Properties of Model Organic Surfaces.
12. D. J. Cram, S. Karbach, H.-E. Kim, C. B. Knobler, E. F. Maverick, J. L. Ericson, R. C. Hegelson, *J. Am. Chem. Soc.* **1988**, *110*, 2229-2237. Host-Guest Complexation. 46. Cavitands as Open Molecular Vessels from Solvates.

13. E. Dalcanale, P. Soncini, G. Bacchilega, F. Ugozzoli, *J. Chem. Soc., Chem. Commun.* **1989**, 500-502. Selective Complexation of Neutral Molecules in Organic Solvents. Host-Guest Complexes and Cavities between Cavitands and Aromatic Compounds.
14. P. Soncini, S. Bonsignore, E. Dalcanale, F. Ugozzoli, *J. Org. Chem.* **1992**, *57*, 4608-4612. Cavitands as Versatile Molecular Receptors.
15. T. Haino, D. M. Rudkevich, A. Shivanyuk, K. Rissanen, J. Rebek, *Chem. Eur. J.* **2000**, *6*, 3797-3805. Induced-Fit Molecular Recognition with Water-Soluble Cavitands.
16. D. M. Rudkevich, J. Rebek Jr., *Eur. J. Org. Chem.* **1999**, 1991-2005. Deepening Cavitands.
17. M. Vincenti, E. Dalcanale, P. Soncini, G. Guglielmetti, *J. Am. Chem. Soc.* **1990**, *112*, 445-447. Host-Guest Complexation in the Gas Phase by Desorption Chemical Ionization Mass Spectrometry.
18. M. Vincenti, E. Pelizzetti, E. Dalcanale, P. Soncini, *Pure Appl. Chem.* **1993**, *65*, 1507-1512. Molecular Recognition in the Gas-Phase.
19. M. Vincenti, E. Dalcanale, *J. Chem. Soc., Perkin Trans. 2* **1995**, 1069-1076. Host-Guest Complexation in the Gas-Phase. Investigation of the Mechanism of Interaction between Cavitands and Neutral Guest Molecules.
20. O. D. Fox, M. G. B. Drew, P. D. Beer, *Angew. Chem.* **2000**, *112*, 139-144; *Angew. Chem. Int. Ed.* **2000**, *39*, 135-140. Resorcarene-Based Nanoarchitectures: Metal-Directed Assembly of a Molecular Loop and Tetrahedron.
21. F. Fochi, P. Jacopozzi, E. Wegelius, K. Rissanen, P. Cozzini, E. Marastoni, E. Fiscaro, P. Manini, R. Fokkens, E. Dalcanale, *J. Am. Chem. Soc.* **2001**, *123*, 7539-7552. Self-Assembly and Anion Encapsulation Properties of Cavitand-Based Coordination Cages.
22. L. Pirondini, F. Bertolini, B. Cantadori, F. Ugozzoli, C. Massera, E. Dalcanale, *Proc. Natl. Acad. Sci. USA* **2002**, *99*, 4911-4915. Supramolecular Chemistry and Self-Assembly Special Feature: Design and Self-Assembly of Wide and Robust Coordination Cages.
23. E. Menozzi, R. Pinalli, E. A. Speets, B. J. Ravoo, E. Dalcanale, D. N. Reinhoudt, *Chem. Eur. J.* **2004**, *10*, 2199-2206. Surface-Confined Single Molecules: Assembly and Disassembly of Nanosize Coordination Cages on Gold (111).
24. J. Janata, *Principle of Chemical Sensors*, Plenum Press, New York, **1989**.

-
25. D. K. Shenoy, E. B. Feresenbert, R. Pinalli, E. Dalcanale, *Langmuir* **2003**, *19*, 10454-10456. Effect of Thin Film Processing on Cavitand Selectivity.
 26. E. B. Feresenbert, E. Dalcanale, C. Dulcey, D. K. Shenoy, *Sens. Actuators B* **2004**, *97*, 211-220. Optical Sensing of the Selective Interaction of Aromatic Vapors with Cavitands.
 27. D. J. Cram, J. M. Cram, *Container Molecules and Their Guests*. Monographs in Supramolecular Chemistry, J. F. Stoddart (Ed.), The Royal Society of Chemistry, Cambridge, **1994**.
 28. A. W. Adamson, *Physical Chemistry of Surfaces*, Wiley, Chichester, UK, **1993**.
 29. C. D. Bain, G. M. Whitesides, *J. Am. Chem. Soc.* **1988**, *110*, 3665-3666. Correlations Between Wettability and a Structure in Monolayers of Alkanethiols Adsorbed on Gold.
 30. Y. Yamakoshi, R. R. Schlittler, J. K. Gimzewski, F. Diederich, *J. Mat. Chem.* **2001**, *11*, 2895-2897. Synthesis of Molecular-Gripper-Type Dynamic Receptors and STM-Imaging of Self-Assembled Monolayers on Gold.
 31. S.-G. Liu, C. Martineau, J.-M. Raimundo, J. Roncali, L. Echegoyen, *Chem. Commun.* **2001**, 913-914. Formation and Electrochemical Desorption of Stable and Electroactive Self-Assembled Monolayers (SAMs) of Oligothiophene-Fulleropyrrolidine Dyads.
 32. H. Imahori, H. Norieda, H. Yamada, Y. Nishimura, I. Yamazaki, Y. Sakata, S. Fukuzumi, *J. Am. Chem. Soc.* **2001**, *123*, 100-110. Light-Harvesting and Photocurrent Generation by Cold Electrodes Modified with Mixed Self-Assembled Monolayers of Boron-Dipyrrin and Ferrocene-Porphyrin-Fullerene Triad.
 33. H. Imahori, T. Azuma, A. Ajavakom, H. Norieda, H. Yamada, Y. Sakata, *J. Phys. Chem. B* **1999**, *103*, 7233-7237. An Investigation of Photocurrent Generation by Gold Electrodes Modified with Self-Assembled Monolayers of C₆₀.
 34. X. Shi, W. B. Caldwell, K. Chen, C. A. Mirkin, *J. Am. Chem. Soc.* **1994**, *116*, 11598-11599. A Well-Defined Surface-Confinable Fullerene: Monolayer Self-Assembly on Au(111).
 35. N. Martin, L. Sanchez, B. Illescas, I. Perez, *Chem. Rev.* **1998**, *98*, 2527-2548. C₆₀-Based Electroactive Organofullerenes.
 36. D. M. Guldi, M. Prato, *Acc. Chem. Res.* **2000**, *33*, 695-703. Excited-State Properties of C₆₀ Fullerene Derivatives.
 37. D. Gust, T. A. Moore, A. L. Moore, *Acc. Chem. Res.* **2001**, *34*, 40-48. Mimicking Photosynthetic Solar Energy Transduction.

38. D. M. Guldi, *Chem. Soc. Rev.* **2002**, *1*, 22-36. Fullerene-Porphyrin Architectures; Photosynthetic Antenna and Reaction Center Models.
39. H. Imahori, Y. Sakata, *Eur. J. Org. Chem.* **1999**, 2445-2457. Fullerenes as Novel Acceptors in Photosynthetic Electron Transfer.
40. H. Yamada, H. Imahori, S. Fukuzumi, *J. Mater. Chem.* **2002**, *12*, 2034-2040. Photocurrent Generation Using Gold Electrodes Modified with Self-Assembled Monolayers of a Fullerene-Porphyrin Dyad.
41. O. Enger, F. Nuesch, M. Fibbioli, L. Echegoyen, E. Pretsch, F. Diederich, *J. Mater. Chem.* **2000**, *10*, 2231-2233. Photocurrent Generation at a Fullerene Self-Assembled Monolayer-Modified Gold Electrode Cast with a Polyurethane Membrane.
42. M. Fibbioli, K. Bandyopadhyay, S.-G. Liu, L. Echegoyen, O. Enger, F. Diederich, P. Bühlmann, E. Pretsch, *Chem. Commun.* **2000**, 339-340. Redox-Active Self-Assembled Monolayers as Novel Solid Contacts for Ion-Selective Electrodes.
43. M. Fibbioli, K. Bandyopadhyay, S.-G. Liu, L. Echegoyen, O. Enger, F. Diederich, D. Gingery, P. Bühlmann, H. Persson, U. W. Suter, E. Pretsch, *Chem. Mater.* **2002**, *14*, 1721-1729. Redox Active Self-Assembled Monolayers for Solid-Contact Polymeric Membrane Ion-Selective Electrodes.
44. W. B. Caldwell, K. Chen, C. A. Mirkin, S. J. Babinec, *Langmuir* **1993**, *9*, 1945-1947. Self-Assembled Monolayer Films of C₆₀ on Cysteamine-Modified Gold.
45. V. T. Hoang, L. M. Rogers, F. D'Souza, *Electrochem. Commun.* **2001**, *4*, 50-53. Synthesis and Formation of Monolayer Self-Assembly of Thiol Appended Fullerenes and Fullerene-Ferrocene Dyads on Gold Electrode.
46. T. Gu, K. Whitesell, M. A. Fox, *J. Org. Chem.* **2004**, *69*, 4075-4080. Electrochemical Charging of a Fullerene-Functionalized Self-Assembled on Au(111).
47. F. Arias, L. A. Godinez, S. R. Wilson, A. E. Kaifer, L. Echegoyen, *J. Am. Chem. Soc.* **1996**, *118*, 6086-6087. Interfacial Hydrogen Bonding. Self-Assembly of a Monolayer of a Fullerene-Crown Ether Derivative on Gold Surfaces Derivatized with an Ammonium-Terminated Alkanethiolate.
48. R. M. Izatt, K. Pawlak, J. S. Bradshaw, R. L. Bruening, *Chem. Rev.* **1991**, *91*, 1721-2085. Thermodynamic and Kinetic Data for Macrocyclic Interaction with Cations and Anions.
49. W. Koh, D. Dubois, W. Kutner, M. T. Jones, K. M. Kadish, *J. Phys. Chem.* **1993**, *97*, 6871-6879. Electrosynthesis and Electrodeposition of Fullerene C₆₀ⁿ⁺ (n = 0, 1, 2, or 3)

- Films: Electrochemical Quartz Crystal Microbalance Study in Acetonitrile Solutions of Alkali-Metal, Alkaline-Earth-Metal, and Tetra-*n*-butylammonium Cations.
50. C. E. D. Chidsey, C. R. Bertozzi, T. M. Putvinski, A. M. Majsce, *J. Am. Chem. Soc.* **1990**, *112*, 4301-4306. Coadsorption of Ferrocene-Terminated and Unsubstituted Alkanethiols on Gold: Electroactive Self-Assembled Monolayers.
 51. S. B. Sachs, S. P. Dudek, R. P. Hsung, L. R. Sita, J. F. Smalley, M. D. Newton, S. W. Feldberg, C. E. D. Chidsey, *J. Am. Chem. Soc.* **1997**, *119*, 10563-10564. Rates of Interfacial Electron Transfer through π -Conjugated Spacers.
 52. W. B. Caldwell, D. J. Campbell, K. Chen, B. R. Herr, C. A. Mirkin, A. Malik, M. K. Durbin, P. Dutta, K. G. Huang, *J. Am. Chem. Soc.* **1995**, *117*, 6071-6082. A Highly Ordered Self-Assembled Monolayer Film of an Azobenzenealkanethiol on Au(111): Electrochemical Properties and Structural Characterization by Synchrotron in-Plane X-Ray Diffraction, Atomic Force Microscopy, and Surface-Enhanced Raman Spectroscopy.
 53. D. J. Campbell, B. R. Herr, J. C. Hulteen, R. P. Van Duyne, C. A. Mirkin, *J. Am. Chem. Soc.* **1996**, *118*, 10211-10219. Ion-Gated Electron Transfer in Self-Assembled Monolayer Films.
 54. J. Zak, H. Yuan, M. Ho, L. K. Woo, M. D. Porter, *Langmuir* **1993**, *9*, 2772-2774. Thiol-Derivatized Metalloporphyrins: Monomolecular Films for the Electrocatalytic Reduction of Dioxygen at Gold Electrodes.
 55. J. E. Hutchinson, T. A. Postlethwaite, R. W. Murray, *Langmuir* **1993**, *9*, 3277-3283. Molecular Films of Thiol-Derivatized Tetraphenylporphyrins on Gold: Film Formation and Electrocatalytic Dioxygen Reduction.
 56. H. Imahori, H. Norieda, S. Ozawa, K. Ushida, H. Yamada, T. Azuma, K. Tamaki, Y. Sakata, *Langmuir* **1998**, *14*, 5335-5338. Chain Length Effect on Photocurrent from Polymethylene-Linked Porphyrins in Self-Assembled Monolayers.
 57. H. Imahori, Y. Sakata, *Adv. Mater.* **1997**, *9*, 537-546. Donor-Linked Fullerenes: Photoinduced Electron Transfer and Its Potential Application.
 58. H. Imahori, K. Hagiwara, M. Aoki, T. Akiyama, S. Taniguchi, T. Okada, M. Shirakawa, Y. Sakata, *J. Am. Chem. Soc.* **1996**, *118*, 11771-11782. Linkage and Solvent Dependence of Photoinduced Electron Transfer in Zincporphyrin-C₆₀ Dyads.
 59. C. A. Mirkin, W. B. Caldwell, *Tetrahedron* **1996**, *52*, 5113-5130. Thin Film, Fullerene-Based Materials.

-
60. K. Uosaki, T. Kondo, X. Q. Zhang, M. Yanagida, *J. Am. Chem. Soc.* **1997**, *119*, 8367-8368. Very Efficient Visible-Light-Induced Uphill Electron Transfer at a Self-Assembled Monolayer with a Porphyrin-Ferrocene-Thiol Linked Molecule.
 61. J. A. J. Brunink, C. Di Natale, F. Bungaro, F. A. M. Davide, A. D'Amico, R. Paolesse, T. Boschi, M. Faccio, G. Ferri, *Anal. Chim. Acta* **1996**, *325*, 53-64. The Application of Metalloporphyrins as Coating Material for Quartz Microbalance-Based Chemical Sensors.
 62. C. Di Natale, A. Macagnano, F. Davide, A. D'Amico, R. Paolesse, T. Boschi, M. Faccio, G. Ferri, *Sens. Actuators B* **1995**, *44*, 521-526. An Electronic Nose for Food Analysis.
 63. R. H. Felton, *The Porphyrins*, vol. VII, D. Dolphin (Ed.), Academic Press, New York, **1978**.
 64. R. Pinalli, M. Suman, E. Dalcanale, *Eur. J. Org. Chem* **2004**, 451-462. Cavitands at Work: From Molecular Recognition to Supramolecular Sensors.
 65. R. Paolesse, C. Di Natale, A. Macagnano, F. Davide, T. Boschi, A. D'Amico, *Sens. Actuators B* **1998**, *47*, 70-76. Self-Assembled Monolayers of Mercaptoporphyrins as Sensing Material for Quartz Crystal Microbalance Chemical Sensors
 66. T. A. Postlethwaite, J. E. Hutchinson, K. W. Hathcock, R. W. Murray, *Langmuir* **1995**, *11*, 4109-4116. Optical, Electrochemical, and Electrocatalytic Properties of Self-Assembled Thiol Derivatized Porphyrins on Transparent Gold Films.
 67. D. G. Wu, D. Cahen, P. Graf, R. Naaman, A. Nitzan, D. Shvarts, *Chem. Eur. J.* **2001**, *7*, 1743-1749. Direct Detection of Low-Concentration NO in Physiological Solutions by a New GaAs-Based Sensor.
 68. G. Ashkenasy, D. Cahen, M. Cohen, A. Shanzer, V. Ayelet, *Acc. Chem. Res.* **2002**, *35*, 121-128. Molecular Engineering of Semiconductor Surfaces and Devices.
 69. D. G. Wu, G. Ashkenasy, D. Shvarts, R. V. Ussyshkin, R. Naaman, A. Shanzer, D. Cahen, *Angew. Chem.* **2000**, *112*, 4670-4674; *Angew. Chem. Int. Ed.* **2000**, *39*, 4496-4500. Novel NO Biosensor Based on the Surface Derivatization of GaAs by "Hinged" Iron Porphyrins.
 70. G. L. J. Gaines, *Thin Solid Films* **1983**, *99*, ix-xiii. On the History of Langmuir-Blodgett Films.
 71. B. Franklin, *Philos. Trans. Royal Society London* **1774**, *64*, 445-460. Of the Stilling of Waves by Means of Oil.
 72. A. Pockels, *Nature* **1891**, *43*, 437-439. Surface Tension.

-
73. I. Langmuir, *J. Am. Chem. Soc.* **1932**, *54*, 2798-2832. Vapor Pressures, Evaporation, Condensation and Adsorption.
 74. I. Langmuir, *J. Am. Chem. Soc.* **1917**, *39*, 1848-1906. The Constitution and Fundamental Properties of Solids and Liquids. II. Liquids.
 75. I. Langmuir, *J. Chem. Phys.* **1933**, *1*, 756-776. Oil Lenses on Water and the Nature of Monomolecular Expanded Films.
 76. K. B. Blodgett, *J. Am. Chem. Soc.* **1935**, *57*, 1007-1022. Films Built by Depositing Successive Monomolecular Layers on a Solid Surface.
 77. K. B. Blodgett, *J. Phys. Chem.* **1937**, *41*, 975-984. Properties of Built-Up Films of Barium Stearate.
 78. K. B. Blodgett, I. Langmuir, *Phys. Rev.* **1937**, *51*, 964-982. Built-Up Films of Barium Stearate and Their Optical Properties.
 79. H. Möhwald, *Ann. Rev. Phys. Chem.* **1990**, *41*, 441-476. Phospholipid and Phospholipid-Protein Monolayers at the Air-Water Interface.
 80. H. M. McConnell, *Ann. Rev. Phys. Chem.* **1991**, *42*, 171-195. Structures and Transitions in Lipid Monolayers at the Air-Water Interface.
 81. S. Rivière, S. Hénon, J. Meunier, D. K. Schwartz, M.-W. Tsao, C. M. Knobler, *J. Chem. Phys.* **1994**, *101*, 10045-10051. Textures and Phase Transitions in Langmuir Monolayers of Fatty Acids. A Comparative Brewster Angle Microscope and Polarized Fluorescence Microscope Study.
 82. C. M. Knobler, R. C. Desai, *Ann. Rev. Phys. Chem.* **1992**, *43*, 207-236. Phase Transitions in Monolayers.
 83. R. Seoane, J. Miñones, O. Conde, J. Miñones Jr., M. Casas, E. Iribarnegaray, *J. Phys. Chem. B* **2000**, *104*, 7735-7744. Thermodynamic and Brewster Angle Microscopy Studies of Fatty Acid/Cholesterol Mixtures at the Air-Water Interface.
 84. A. Datta, M. K. Sanyal, A. Dhanabalan, S. S. Major, *J. Phys. Chem. B* **1997**, *101*, 9280-9286. Formation of Highly Condensed Ferric Stearate Monolayers at the Air-Water Interface.
 85. M.-J. Hwang, K. Kim, *Langmuir* **1999**, *15*, 3563-3569. Poly(ethylenimine) as a Subphase Stabilizer of Stearic Acid Monolayers at the Air-Water Interface: Surface Pressure–Area Isotherm and Infrared Spectroscopy Study.
 86. S. Siegel, D. Hönig, D. Vollhardt, D. Möbius, *J. Phys. Chem.* **1992**, *96*, 8157-8160. Direct Observation of Three-Dimensional Transformation of Insoluble Monolayers.

87. C. McFate, D. Ward, J. Olmsted, *Langmuir* **1993**, *9*, 1036-1039. Organized Collapse of Fatty Acid Monolayers.
88. K. S. Birdi, D. T. Vu, *Langmuir* **1994**, *10*, 623-625. Structures of Collapsed Lipid Monolayers Investigated as Langmuir–Blodgett Films by Atomic Force Microscopy.
89. I. Langmuir, *Trans. Faraday Soc.* **1920**, *15*, 62-74. The Mechanism of the Surface Phenomenon of Flotation.
90. I. Langmuir, *J. Chem. Phys.* **1933**, *1*, 3-12. An Extension of the Phase Rule for Adsorption under Equilibrium and Non-Equilibrium Conditions.
91. J. A. Zasadzinski, R. Viswanathan, L. Madsen, J. Garnaes, D. K. Schwartz, *Science* **1994**, *263*, 1726-1733. Langmuir–Blodgett Films.
92. G. G. Roberts, *Langmuir–Blodgett Films*, Plenum Press, New York, **1990**.
93. M. C. Petty, *Langmuir–Blodgett Film: An Introduction*, Cambridge University Press, Cambridge, **1996**.
94. G. L. J. Gaines, *Insoluble Monolayers at Liquid-Gas Interfaces*, Interscience Publisher, **1966**.
95. M. R. Buhaenko, J. W. Goodwin, R. M. Richardson, M. F. Daniel, *Thin Solid Films* **1985**, *134*, 217-226. The Influence of Shear Viscosity of Spread Monolayers on the Langmuir–Blodgett Process.
96. B. R. Malcolm, *Thin Solid Films* **1985**, *134*, 201-208. Studies of the Flow of Molecular Monolayers During Compression and the Effect of a Plateau in the Pressure–Area Curve.
97. E. P. Honig, J. H. T. Hengest, D. J. den Engelson, *J. Colloid Interface Sci.* **1973**, *45*, 92-102. Langmuir–Blodgett Deposition Ratios.
98. D. K. Schwartz, *Surf. Sci. Rep.* **1997**, *27*, 241-334. Langmuir–Blodgett Film Structure.
99. W. M. Reichert, C. J. Bruckner, J. Joseph, *Thin Solid Films* **1987**, *152*, 345-376. Langmuir–Blodgett Films and Black Lipid Membranes in Biospecific Surface-Selective Sensors.
100. J. Anzai, S. Lee, T. Osa, *Bull. Chem. Soc. Jpn.* **1989**, *62*, 3018-3020. Reactive Langmuir–Blodgett Membrane for Biosensor Applications. Use of Succinimidyl Behenoate–Based Membranes as Support for Covalently Immobilizing Alpha-Chymotrypsin.
101. Y. Okahata, T. Tsuruta, K. Ijio, K. Ariga, *Langmuir* **1988**, *4*, 1373-1375. Langmuir–Blodgett Films of an Enzyme-Lipid Complex for Sensor Membranes.

102. A. Arya, U. J. Krull, M. Thompson, H. E. Wong, *Anal. Chim. Acta* **1985**, *173*, 331-336. Langmuir–Blodgett Deposition of Lipid Films on Hydrogel as a Basis for Biosensor Development.
103. M. Sriyudthsak, H. Yamagishi, T. Moriizumi, *Thin Solid Films* **1988**, *160*, 463-469. Enzyme-Immobilized Langmuir–Blodgett Film for a Biosensor.
104. D. G. Zhu, M. C. Petty, H. Ancelin, J. Yarwood, *Thin Solid Films* **1989**, *176*, 151-156. On the Formation of Langmuir–Blodgett Films Containing Enzymes.
105. S. Y. Lee, J. Anzai, T. Osa, *Sens. Actuators B* **1993**, *12*, 153-158. Enzyme-Modified Langmuir–Blodgett Membranes in Glucose Electrodes Based on Avidin-Biotin Interaction.
106. M. Aizawa, M. Matsuzawa, H. Shinohara, *Thin Solid Films* **1988**, *160*, 477-481. An Optical Chemical Sensor Using a Fluorophor- Embedded Langmuir–Blodgett Film.
107. J. Anzai, J. Hashimoto, T. Osa, T. Matsuo, *Anal. Sci.* **1988**, *4*, 247-250. Penicillin Sensors Based on an Ion-Sensitive Field-Effect Transistor Coated with Stearic-Acid Langmuir–Blodgett Membrane.
108. R. Singhal, A. Gambhir, M. K. Pandey, S. Annapoorni, B. D. Malhorta, *Biosens. Bioelect.* **2002**, *17*, 697-703. Immobilization of Urease on Poly(*N*-vinyl carbazole)/Stearic Acid Langmuir–Blodgett Films for Application to Urea Biosensor.
109. R. Singhal, W. Takashima, K. Kaneto, S. B. Samanta, S. Annapoorni, B. D. Malhorta, *Sens. Actuators B* **2002**, *86*, 42-48. Langmuir–Blodgett of Poly(3-dodecyl thiophene) for Application to Glucose Biosensor.
110. S. Hénon, J. Meunier, *Rev. Sci. Instrum.* **1990**, *62*, 936-939. Microscope at the Brewster Angle: Direct Observation of First-Order Phase Transitions in Monolayers.
111. D. Hönig, D. Möbius, *J. Phys. Chem.* **1991**, *95*, 4590-4592. Direct Visualization of Monolayers at the Air-Water Interface by Brewster Angle Microscopy.
112. J. Meunier, *Colloids Surf. A* **2000**, *171*, 33-40. Why a Brewster Angle Microscope?
113. D. Vollhardt, *Adv. Colloid Interface Sci.* **1996**, *64*, 143-171. Morphology and Phase Behavior of Monolayers.
114. D. Hönig, D. Möbius, *Thin Solid Films* **1992**, *210-211*, 64-68. Reflectometry at the Brewster Angle and Brewster Angle Microscopy at the Air-Water Interface.
115. S. Hénon, J. Meunier, *J. Chem. Phys.* **1993**, *98*, 9148-9154. Phase Transition in Gibbs Films: Star Textural Defects in Tilted Mesophases.

-
116. R. Albalat, J. Claret, J. Ignés-Mullol, F. Sagues, C. Moran, L. Perez, P. Clapes, A. Pinazo, *Langmuir* **2003**, *19*, 10878-10884. Langmuir Monolayers of Diacyl Glycerol Aminoacid-Based Surfactants. Effect of the Substitution Pattern of the Glycerol Backbone.
117. A. Vaes, M. Van der Auwerker, F. C. De Schryver, B. Laguitton, A. Jonas, P. Henderson, H. Ringsdorf, *Langmuir* **1998**, *14*, 5250-5254. Y-Type Langmuir–Blodgett Films of 2,3-Bis((2-hydroxyethyl)oxy)-6,7,10,11-tetrakis(pentyloxy)triphenylene: An X-ray Reflection Study.
118. D. Felder, J. L. Gallani, D. Guillon, B. Heinrich, J. F. Nicoud, J. F. Nierengarten, *Angew. Chem.* **2000**, *112*, 207-210; *Angew. Chem. Int. Ed.* **2000**, *39*, 201-204. Investigations of Thin Films with Amphiphilic Dendrimers Bearing Peripheral Fullerene Subunits.
119. J. F. Nierengarten, J. F. Eckert, Y. Rio, M. D. Carreon, J. L. Gallani, D. Guillon, *J. Am. Chem. Soc.* **2001**, *123*, 9743-9748. Amphiphilic Diblock Dendrimers: Synthesis and Incorporation in Langmuir and Langmuir–Blodgett Films.
120. P. Datta, *Curr. Sci.* **2000**, *78*, 1478-1483. Grazing Incidence X-Ray Diffraction.
121. J. L. Gallani, D. Felder, D. Guillon, B. Heinrich, J. F. Nierengarten, *Langmuir* **2002**, *18*, 2908-2913. Micelle Formation in Langmuir Films of C₆₀ Derivatives.
122. J. O. Jeppensen, J. Perkins, J. Becher, J. F. Stoddart, *Angew. Chem.* **2001**, *113*, 1256-1261; *Angew. Chem. Int. Ed.* **2001**, *40*, 1216-1221. Slow Shuttling in an Amphiphilic Bistable [2]Rotaxane Incorporating a Tetrathiafulvalene Unit.
123. V. Balzani, A. Credi, F. M. Raymo, J. F. Stoddart, *Angew. Chem.* **2000**, *112*, 3484-3530; *Angew. Chem. Int. Ed.* **2000**, *39*, 3348-3391. Artificial Molecular Machines.
124. J. P. Sauvage, *Science* **2001**, *291*, 2105-2106. A Light-Driven Linear Motor at the Molecular Level.
125. M. J. Blanco, M. C. Jiménez, J. C. Chembron, V. Heitz, M. Linke, J. P. Sauvage, *Chem. Soc. Rev.* **1999**, *28*, 293-305. Rotaxanes as New Architectures for Photoinduced Electron Transfer and Molecular Motions.
126. R. Jäger, F. Vögtle, *Angew. Chem.* **1997**, *109*, 966-980; *Angew. Chem. Int. Ed.* **1997**, *36*, 930-944. A New Synthetic Strategy Towards Molecules with Mechanical Bonds: Nonionic Template Synthesis of Amide-Linked Catenanes and Rotaxanes.

-
127. A. M. Brouwer, C. Frochot, F. G. Gatti, D. A. Leigh, L. Mottier, F. Paolucci, S. Roffia, G. W. H. Wurpel, *Science* **2001**, *291*, 2124-2128. Photoinduction of Fast, Reversible Translation Motion in a Hydrogen-Bonded Molecular Shuttle.
128. V. Bermudez, N. Capron, T. Gase, F. G. Gatti, F. Kajzar, D. A. Leigh, F. Zerbetto, S. Zhang, *Nature* **2000**, *406*, 608-611. Influencing Intramolecular Motion with an Alternating Electric Field.
129. A. Casnati, A. Pochini, R. Ungaro, C. Bocchi, F. Ugozzoli, R. J. M. Egberink, H. Struijk, R. Lutgenberg, F. de Jong, D. N. Reinhoudt, *Chem. Eur. J.* **1996**, *2*, 436-445. 1,3-Alternate Calix[4]arene-crown-5 Conformers: New Synthetic Ionophores with Better K^+/Na^+ Selectivity than Valinomycin.
130. J. R. Moran, S. Karbach, D. J. Cram, *J. Am. Chem. Soc.* **1982**, *104*, 5826-5828. Cavitands: Synthetic Molecular Vessels.
131. D. J. Cram, *Science* **1983**, *219*, 1177-1183. Cavitands: Organic Hosts with Enforced Cavities.
132. J. R. Moran, J. L. Ericson, E. Dalcanale, J. A. Bryant, C. B. Knobler, D. J. Cram, *J. Am. Chem. Soc.* **1991**, *113*, 5707-5714. Vases and Kites as Cavitands.
133. L. M. Tunstad, J. A. Tucker, E. Dalcanale, J. Weiser, J. A. Bryant, J. C. Sherman, R. C. Hegelson, C. B. Knobler, D. J. Cram, *J. Org. Chem.* **1989**, *54*, 1305-1312. Host-Guest Complexation. 48. Octol Building Blocks for Cavitands and Carcerands.
134. D. J. Cram, H.-J. Choi, J. A. Bryant, C. B. Knobler, *J. Am. Chem. Soc.* **1992**, *114*, 7748-7765. Solvophobic and Entropic Driving Forces for Forming Velcralexes, which Are Four-Fold, Lock-Key Dimers in Organica Media.
135. M. E. Tanner, C. B. Knobler, D. J. Cram, *J. Org. Chem.* **1992**, *57*, 40-46. Host-Guest Complexation. 60. Rigidly Hollow Hosts that Encapsulate Small Molecules.
136. A. G. S. Högberg, *J. Am. Chem. Soc.* **1980**, *102*, 6046-6050. Cyclooligomeric Phenol-Aldehyde Condensation Products. 2. Stereoselective Synthesis and DNMR Study of Two 1,8,15,22-Tetraphenyl[14]metacyclophan-3,5,10,12,17,19,24,26-octols.
137. A. G. S. Högberg, *J. Org. Chem.* **1980**, *45*, 4498-4500. Two Stereoisomeric Macrocyclic Resorcinol-Acetaldehyde Condensation Product.
138. H. Erdtman, S. Högberg, S. Abrahamsson, B. Nilsson, *Tetrahedron Lett.* **1968**, *9*, 1679-1682. Cyclooligomeric Phenol-Aldehyde Condensation Products I.
139. F. Weinelt, H.-J. Schneider, *J. Org. Chem.* **1991**, *56*, 5527-5535. Mechanism of Macrocyclic Genesis. The Condensation of Resorcinol with Aldehydes.
-

-
140. P. Timmerman, W. Verboom, D. N. Reinhoudt, *Tetrahedron* **1996**, *52*, 2663-2704. Resorcinarenes.
141. A. G. S. Högberg, *J. Am. Chem. Soc.* **1980**, *102*, 6046-6050. Stereoselective Synthesis and DNMR Study of Two 1,8,15,22-Tetraphenyl[1₄]metacyclophan-3,5,10,12,17,24,26-octols.
142. L. Abis, E. Dalcanale, A. Duvosel, S. Spera, *J. Org. Chem.* **1988**, *53*, 5475-5479. Structurally New Macrocycles from the Resorcinol Aldehyde Condensation. Configurational and Conformational Analyses by Means of Dynamic NMR, NOE, and T1 Experiments.
143. L. Pirondini, D. Bonifazi, E. Menozzi, E. Wegelius, K. Rissanen, C. Massera, E. Dalcanale, *Eur. J. Org. Chem.* **2001**, 2311-2320. Synthesis and Coordination Chemistry of Lower Rim Cavitand Ligands.
144. F. Hof, S. L. Craig, C. Nuckolls, J. Rebek, *Angew. Chem.* **2002**, *114*, 1556-1576; *Angew. Chem. Int. Ed.* **2002**, *41*, 1488-1508. Molecular Encapsulation.
145. A. R. Renslo, F. C. Tucci, D. M. Rudkevich, J. Rebek, *J. Am. Chem. Soc.* **2000**, *122*, 4573-4582. Synthesis and Assembly of Self-Complementary Cavitands.
146. V. A. Azov, B. Jaun, F. Diederich, *Helv. Chim. Acta* **2004**, *87*, 449-462. NMR Investigations into the Vase-Kite Conformational Switching of Resorcin[4]arene Cavitands.
147. P. J. Skinner, A. G. Cheetham, A. Beeby, V. Gramlich, F. Diederich, *Helv. Chim. Acta* **2001**, *84*, 2146-2153. Conformational Switching of Resorcin[4]arene Cavitands by Protonation.
148. D. J. Cram, K. D. Stewart, I. Goldberg, K. N. Trueblood, *J. Am. Chem. Soc.* **1985**, *107*, 2574-2575. Complementary Solutes Enter Nonpolar Preorganized Cavities in Lipophilic Noncomplementary Media.
149. J. A. Tucker, C. B. Knobler, K. N. Trueblood, D. J. Cram, *J. Am. Chem. Soc.* **1989**, *111*, 3688-3699. Host-Guest Complexation. 49. Cavitands Containing Two Binding Cavities.
150. F. L. Dickert, U. P. A. Baumler, H. Stathopoulos, *Anal. Chem.* **1997**, *69*, 1000-1005. Mass-Sensitive Solvent Vapor Detection with Calix[4]resorcinarenes: Tuning Sensitivity and Predicting Sensor Effects.
151. M. Vincenti, C. Minero, E. Pelizzetti, A. Secchi, E. Dalcanale, *Pure Appl. Chem.* **1995**, *67*, 1075-1084. Host-Guest Chemistry in the Gas-Phase and at the Gas-Solid Interface - Fundamental Aspects and Practical Applications.
-

-
152. B. H. Huisman, D. M. Rudkevich, F. vanVeggel, D. N. Reinhoudt, *J. Am. Chem. Soc.* **1996**, *118*, 3523-3524. Self-Assembled Monolayers of Carceplexes on Gold.
153. H. Schönherr, G. J. Vancso, B. H. Huisman, F. vanVeggel, D. N. Reinhoudt, *Langmuir* **1997**, *13*, 1567-1570. An Atomic Force Microscopy Study of Self-Assembled Monolayers of Calix[4]resorcinarene Adsorbates on Au(111).
154. B. H. Huisman, D. M. Rudkevich, A. Ferran, W. Verboom, F. van Veggel, D. N. Reinhoudt, *Eur. J. Org. Chem.* **2000**, 269-274. Synthesis of (Hemi)Carceplex Adsorbates for Self-Assembly on Gold.
155. S. Flink, F. van Veggel, D. N. Reinhoudt, *Adv. Mat.* **2000**, *12*, 1315-1328. Sensor Functionalities in Self-Assembled Monolayers.
156. E. U. T. Vanvelzen, J. F. J. Engbersen, D. N. Reinhoudt, *J. Am. Chem. Soc.* **1994**, *116*, 3597-3598. Self-Assembled Monolayers of Receptor Adsorbates on Gold - Preparation and Characterization.
157. E. U. T. Vanvelzen, J. F. J. Engbersen, P. J. Delange, J. W. G. Mahy, D. N. Reinhoudt, *J. Am. Chem. Soc.* **1995**, *117*, 6853-6862. Self-Assembled Monolayers of Resorcin[4]arene Tetrasulfides on Gold.
158. A. R. Far, D. M. Rudkevich, T. Haino, J. Rebek, *Org. Lett.* **2000**, *2*, 3465-3468. A Polymer-Bound Cavitand.
159. J. K. Gimzewski, C. Joachim, *Science* **1999**, *283*, 1683-1688. Nanoscale Science of Single Molecules Using Local Probes.
160. J. K. Gimzewski, C. Joachim, R. R. Schlittler, V. Langlais, H. Tang, I. Johannsen, *Science* **1998**, *281*, 531-533. Rotation of a Single Molecule within a Supramolecular Bearing.
161. T. A. Jung, R. R. Schlittler, J. K. Gimzewski, H. Tang, C. Joachim, *Science* **1996**, *271*, 181-184. Controlled Room-Temperature Positioning of Individual Molecules: Molecular Flexure and Motion.
162. M. T. Cuberes, R. R. Schlittler, J. K. Gimzewski, *Appl. Phys. Lett.* **1996**, *69*, 3016-3018. Room-Temperature Repositioning of Individual C₆₀ Molecules at Cu Steps: Operation of a Molecular Counting Device.
163. A. K. Hassan, A. V. Nabok, A. K. Ray, F. Davis, C. J. M. Stirling, *Thin Solid Films* **1998**, *327-329*, 686-689. Complexation of Metal Ions with Langmuir-Blodgett Films of Novel Calixarene Azo-Derivatives.

-
164. A. K. Hassan, A. V. Nabok, A. K. Ray, A. Lucke, K. Smith, C. J. M. Stirling, F. Davis, *Mater. Sci. Eng. C* **1999**, *8-9*, 251-255. Thin Films of Calix-4-resorcinarene Deposited by Spin Coating and Langmuir–Blodgett Techniques: Determination of Film Parameters by Surface Plasmon Resonance.
165. A. K. Hassan, A. K. Ray, A. V. Nabok, S. Panigrahi, *IEE Proc. Sci. Meas. Technol.* **2000**, *147*, 137-140. Surface Plasmon Resonance Studies on Spin Coated Films of Azobenzene Substituted Calix-4-resorcinarene Molecules.
166. H. G. Liu, X. S. Feng, L. J. Zhang, G. L. Ji, D. J. Qian, Y. I. Lee, K. Z. Yang, *Mater. Sci. Eng. C* **2003**, *23*, 585-592. Influences of Hydrophilic and Hydrophobic Substituents on the Organization of Supramolecular Assemblies of Porphyrin Derivatives Formed at the Air-Water Interface.
167. P. Shahgaldian, A. W. Coleman, *Langmuir* **2001**, *17*, 6851-6854. Anion and Cation Interactions with *p*-Dodecanoylcalix[4]arene Monolayers at the Air-Water Interface.
168. A. Van der Heyden, J. B. Regnouf-de-Vains, P. Warszynski, J. O. Dalbavie, A. Zywockinski, E. Rogalska, *Langmuir* **2002**, *18*, 8854-8861. Probing Inter- and Intramolecular Interactions of Six New *p*-*tert*-Butylcalix[4]arene-Based Bipyridyl Podands with Langmuir Monolayers.
169. F. Liu, G.-Y. Lu, W.-J. He, M.-H. Liu, L.-G. Zhu, H.-M. Wu, *New J. Chem.* **2002**, *26*, 601-606. Molecular Recognition of Nucleotides by a Calix[4]arene Derivative with Two Alkyl Guanidinium Groups at the Air-Water Interface.
170. F. Liu, G. Y. Lu, W. J. He, M. H. Liu, L. G. Zhu, *Thin Solid Films* **2002**, *414*, 72-77. Supramolecular Interaction of Diamino Calix[4]arene Derivative with Nucleotides at the Air-Water Interface.
171. A. V. Nabok, N. V. Lavrik, Z. I. Kazantseva, B. A. Nesterenko, L. N. Markovskiy, V. I. Kalchenko, A. N. Shivaniuk, *Thin Solid Films* **1995**, *259*, 244-247. Complexing Properties of Calix[4]resorcinolarene LB Films.
172. K. Kurihara, K. Ohto, Y. Tanaka, Y. Aoyama, T. Kunitake, *J. Am. Chem. Soc.* **1991**, *113*, 444-450. Molecular Recognition of Sugars by Monolayers of Resorcinol-Dodecanal Cyclotetramer.
173. P. Prus, M. Pietraszkiewicz, R. Bilewicz, *Mater. Sci. Eng. C* **2001**, *18*, 157-159. Calix[4]resorcinarene: Molecular Recognition in Langmuir Films.
174. Spartan SGI version 5.1.3 open GL, Wavefunction Inc., Irvine, **1998**.

-
175. V. A. Azov, P. Skinner, Y. Yamakoshi, P. Seiler, V. Gramlich, F. Diederich, *Helv. Chim. Acta* **2003**, *86*, 3648-3669. Functionalized and Partially or Differentially Bridged Resorcin[4]arene Cavitanes: Synthesis and Solid-State Structures.
176. N. Vila-Romeu, M. Nieto-Suarez, P. Dynarowicz-Latka, I. Prieto, *J. Phys. Chem. B* **2002**, *106*, 9820-9824. Mixed Langmuir Monolayers of Gramicidin A and Ethyl Palmitate: Pressure–Area Isotherms and Brewster Angle Microscopy.
177. W. J. He, D. Vollhardt, R. Rudert, L. G. Zhu, J. B. Li, *Langmuir* **2003**, *19*, 385-392. Phase Transition and Domain Morphology in Langmuir Monolayers of a Calix[4]arene Derivative Containing no Alkyl Chain.
178. E. Loste, E. Diaz-Marti, A. Zarbakhsh, F. C. Meldrum, *Langmuir* **2003**, *19*, 2830-2837. Study of Calcium Carbonate Precipitation under a Series of Fatty Acid Langmuir Monolayers Using Brewster Angle Microscopy.
179. Z. Khattari, E. Hatta, P. Heinig, P. Steffen, T. M. Fischer, R. Bruinsma, *Phys. Rev. E* **2002**, *65*, 041603(1)-041603(11). Cavitation of Langmuir Monolayers.
180. D. Vollhardt, *Adv. Colloid Interface Sci.* **1999**, *79*, 19-57. Phase Transition in Adsorption Layers at the Air-Water Interface.
181. D. Vollhardt, V. B. Fainerman, *J. Phys. Chem. B* **2002**, *106*, 345-351. Kinetics of Two-Dimensional Phase Transition of Langmuir Monolayers.
182. V. B. Fainerman, D. Vollhardt, *J. Phys. Chem. B* **1999**, *103*, 145-150. Equations of State for Langmuir Monolayers with Two-Dimensional Phase Transitions.
183. V. B. Fainerman, D. Vollhardt, *J. Phys. Chem. B* **2003**, *107*, 3098-3100. Equation of State for Monolayers under Consideration of the Two-Dimensional Compressibility in the Condensed State.
184. V. B. Fainerman, D. Vollhardt, V. Melzer, *J. Chem. Phys.* **1997**, *107*, 243-251. Kinetics of Two-Dimensional Phase Transition of Amphiphilic Monolayers at the Air-Water Interface.
185. E. Ruckenstein, *Colloids Surf. A* **2001**, *183-185*, 423-427. Nonconventional First Order Transitions in Insoluble Monolayers of Surfactants.
186. X. H. Bu, H. Liu, M. Du, K. M. C. Wong, V. W. W. Yam, *Inorg. Chim. Acta* **2002**, *333*, 32-40. Coordinative Versatility of 2,3-Bis(2-pyridyl)-5,8-dimethoxyquinoxaline (L) to Different Metal Ions: Syntheses, Crystal Structures and Properties of $[\text{Cu}(\text{I})\text{L}]_2^{2+}$ and $[\text{ML}]^{2+}$ (M = Cu(II), Ni(II), Zn(II) and Co(II)).

187. F. Al-Ali, C. Déjugnat, G. Etemad-Moghadam, I. Rico-Lattes, *J. Coll. Interf. Sci.* **2004**, 273, 512-516. Langmuir Films of (α -Amino)phosphorus Amphiphiles on Various Ion-Containing Subphases.
188. A. E. Martell, R. D. Hancock, *Metal Complexes in Aqueous Solutions*, Plenum Press, **1996**.
189. F. A. Cotton, G. Wilkinson, P. L. Gaus, *Basic Inorganic Chemistry*, John Wiley & Sons, **1987**.
190. V. A. Azov, F. Diederich, Y. Lill, B. Hecht, *Helv. Chim. Acta* **2003**, 86, 2149-2155. Synthesis and Conformational Switching of Partially and Differentially Bridged Resorcin[4]arenes Bearing Fluorescent Dye Labels.
191. Z. Xu, N. B. Holland, R. E. Marchant, *Langmuir* **2001**, 17, 377-383. Conformations of Short-Chain Poly(ethylene oxide) Lipopolymers at the Air-Water Interface: A Combined Film Balance and Surface Tension Study.
192. P. G. de Gennes, *Macromolecules* **1980**, 13, 1069-1075. Conformations of Polymers Attached to an Interface.
193. T. R. Baekmark, G. Elender, D. D. Lasic, E. Sackmann, *Langmuir* **1995**, 11, 3975-3987. Conformational Transitions of Mixed Monolayers of Phospholipids and Poly(ethylene oxide) Lipopolymers and Interaction Forces with Solid-Surfaces.
194. P. G. de Gennes, *Adv. Colloid Interface Sci.* **1987**, 27, 189-209. Polymers at an Interface: A Simplified View.
195. A. Malzert, F. Boury, P. Saulnier, J. P. Benoit, J. E. Proust, *Langmuir* **2001**, 17, 7837-7841. Interfacial Properties of a PEG2000-PLA50 Diblock Copolymer at the Air-Water Interface.
196. A. Berman, M. Cohen, O. Regev, *Langmuir* **2002**, 18, 5681-5686. Catanionic Vesicle-PEG-Lipid System: Langmuir Film and Phase Diagram Study.
197. V. Tsukanova, C. Salesse, *Macromolecules* **2003**, 36, 7227-7235. High-Pressure Transition of a Poly(ethylene glycol)-Grafted Phospholipid Monolayer at the Air-Water Interface.
198. A. Napoli, N. Tirelli, E. Wehrli, J. A. Hubbell, *Langmuir* **2002**, 18, 8324-8329. Lyotropic Behavior in Water of Amphiphilic ABA Triblock Copolymers Based on Poly(propylene sulfide) and Poly(ethylene glycol).

-
199. J. Majewsky, T. L. Kuhl, M. C. Gerstenberg, J. N. Israelachvili, G. S. Smith, *J. Phys. Chem. B* **1997**, *101*, 3122-3129. Structure of Phospholipid Monolayers Containing Poly(ethylene glycol) Lipids at the Air-Water Interface.
200. M. Kawaguchi, M. Tohyama, Y. Mutoh, A. Takahashi, *Langmuir* **1998**, *4*, 407-410. Ellipsometry Study of Polymer Monolayers Spread at the Air-Water Interface. 1. Thickness of Monolayers.
201. A. Malzert, F. Boury, P. Saulnier, J. P. Benoit, J. E. Proust, *Langmuir* **2000**, *16*, 1861-1867. Interfacial Properties of Mixed Polyethylene Glycol/Poly(D,L-lactide-co-glycolide) Films Spread at the Air-Water Interface.
202. C. Barentin, P. Muller, J. F. Joanny, *Macromolecules* **1998**, *31*, 2198-2211. Polymer Brushes Formed by End-Capped Poly(ethylen oxide) (PEO) at the Air-Water Interface.
203. F. Lagugné-Labarthe, T. Yu, W. R. Barger, D. K. Shenoy, E. Dalcanale, Y. R. Shen, *Chem. Phys. Lett.* **2003**, *381*, 322-328. Orientation of Cavitands at the Air-Water and Air-Solid Interfaces Studied by Second Harmonic Generation.
204. R. C. Hughes, A. J. Ricco, M. A. Butler, S. J. Martin, *Science* **1991**, *254*, 74-80. Chemical Microsensors.
205. R. Baum, *Chem. Eng. News* **1994**, *72*, 29. C₆₀ Used to Produce Silicon-Carbide.
206. Y. Xiao, Z. Yao, D. Jin, *J. Phys. Chem.* **1994**, *98*, 5557-5558. High-Resolution Electron Microscopy and Electron Diffraction Study on the C₆₀ Langmuir-Blodgett Films.
207. M. Matsumoto, H. Tachibana, R. Azumi, M. Tanaka, T. Nakamura, *Langmuir* **1995**, *11*, 660-665. Langmuir-Blodgett Film of Amphiphilic C₆₀ Carboxylic Acid.
208. C. Jehoulet, Y. S. Obeng, Y. T. Kim, F. M. Zhou, A. J. Bard, *J. Am. Chem. Soc.* **1992**, *114*, 4237-4247. Electrochemistry and Langmuir Trough Studies of C₆₀ and C₇₀ Films.
209. Y. S. Obeng, A. J. Bard, *J. Am. Chem. Soc.* **1991**, *113*, 6279-9280. Langmuir Films of C₆₀ at the Air-Water Interface.
210. C. T. Ewins, B. Stewart, *Thin Solid Films* **1996**, *284-285*, 49-52. Langmuir-Blodgett Films Containing C₆₀ and Cadmium Sulphide.
211. H. M. Patel, J. M. Didymus, K. K. W. Wong, A. Hirsch, A. Skiebe, I. Lamparth, S. Mann, *Chem. Commun.* **1996**, 611-612. Fullerenes: Interaction of Divalent Metal Ions with Langmuir Monolayers and Multilayers of Mono-Substituted C₆₀-Malonic Acid.
212. T. Nakamura, H. Tachibana, M. Yumura, M. Matsumoto, R. Azumi, M. Tanaka, Y. Kawabata, *Langmuir* **1992**, *8*, 4-6. Formation of Langmuir-Blodgett Films of a Fullerene.
-

-
213. J. Milliken, D. D. Dominguez, H. H. Nelson, W. R. Barger, *Chem. Mater.* **1992**, *4*, 252-254. Incorporation of C₆₀ in Langmuir–Blodgett Films.
214. C. Ewins, B. Stewart, *J. Chem. Soc., Faraday Trans.* **1994**, *90*, 969-972. Formation and Structure of Langmuir–Blodgett Films of C₆₀ and Arachidic Acid.
215. S. S. Shiratori, M. Shimizu, K. Ikezaki, *Thin Solid Films* **1998**, *327-329*, 655-658. Molecular Sifter Using Space Controlled Langmuir–Blodgett Films by Fullerene Molecules.
216. F. Diederich, J. Effing, U. Jonas, L. Jullien, T. Plesnivy, H. Ringsdorf, C. Thilgen, D. Weinstein, *Angew. Chem.* **1992**, 1683-1686; *Angew. Chem. Int. Ed.* **1992**, *31*, 1599-1602. C₆₀ and C₇₀ in a Basket? - Investigations of Multilayers from Azacrown Compounds and Fullerenes.
217. L. Dei, P. LoNostro, G. Capuzzi, P. Baglioni, *Langmuir* **1998**, *14*, 4143-4147. Langmuir Films of *p*-tert Butylcalix[8]arene. Conformations at the Air-Water Interface and Complexation of Fullerene C₆₀.
218. P. LoNostro, A. Casnati, L. Bossoletti, L. Dei, P. Baglioni, *Coll. Surf. A* **1996**, *116*, 203-209. Complexation Properties of Calixarenes in Langmuir Films at the Air-Water Interface.
219. R. M. Fleming, A. P. Ramirez, M. J. Rosseinsky, D. W. Murphy, R. C. Haddon, S. M. Zahurak, A. V. Makhija, *Nature* **1991**, *352*, 701-703. Preparation and Structure of the Alkali-Metal Fulleride A₄C₆₀.
220. U. Jonas, F. Cardullo, P. Belik, F. Diederich, A. Gügel, E. Harth, A. Herrmann, L. Isaacs, K. Müllen, H. Ringsdorf, C. Thilgen, P. Uhlmann, A. Vasella, C. A. A. Waldruff, M. Walter, *Chem. Eur. J.* **1995**, *1*, 243-251. Synthesis of a [60]Fullerene Cryptate and Systematic Langmuir–Blodgett and Thin Film Investigations of Amphiphilic Fullerene Derivatives.
221. H. W. Kroto, J. R. Heath, S. C. O'Brien, R. F. Curl, R. E. Smalley, *Nature (London)* **1985**, *318*, 162-163. C₆₀: Buckminsterfullerene.
222. W. Krätschmer, L. D. Lamb, K. Fostiropoulos, D. R. Huffman, *Nature (London)* **1990**, *347*, 354-358. Solid C₆₀: A New Form of Carbon.
223. R. C. Haddon, *Acc. Chem. Res.* **1988**, *21*, 243-249. π -Electrons in 3 Dimensions.
224. R. C. Haddon, *Acc. Chem. Res.* **1992**, *25*, 127-133. Electronic Structure, Conductivity, and Superconductivity of Alkali Metal Doped C₆₀.

-
225. W. Krätschmer, K. Fostiropoulos, D. R. Huffman, *Chem. Phys. Lett.* **1990**, *170*, 167-170. The Infrared and Ultraviolet Absorption Spectra of Laboratory-Produced Carbon Dust: Evidence for the Presence of the C₆₀ Molecules.
226. R. Taylor, J. P. Hare, A. K. Abdul-Sada, H. W. Kroto, *J. Chem. Soc., Chem. Commun.* **1990**, 1423-1425. Isolation, Separation, and Characterization of the Fullerenes C₆₀ and C₇₀: The Third Form of Carbon.
227. H. Ajie, M. M. Alvarez, S. J. Anz, R. D. Beck, F. Diederich, K. Fostiropoulos, D. R. Huffman, W. Krätschmer, Y. Rubin, K. E. Schriver, D. Sensharma, R. L. Whetten, *J. Phys. Chem.* **1990**, *94*, 8630-8633. Characterization of the Soluble All-Carbon Molecules C₆₀ and C₇₀.
228. J. M. Hawkins, A. Meyer, T. A. Lewis, S. Loren, F. J. Hollander, *Science* **1991**, *252*, 312-313. Crystal Structure of Osmylated C₆₀: Confirmation of the Soccer Ball Framework.
229. H.-B. Bürgi, E. Blanc, D. Schwarzenbach, S. Liu, Y. Lu, M. M. Kappes, J. A. Ibers, *Angew. Chem.* **1992**, *104*, 667-669; *Angew. Chem. Int. Ed.* **1992**, *31*, 640-643. The Structure of C₆₀. Orientational Disorder in the Low-Temperature Modifications of C₆₀.
230. S. Liu, Y. Lu, M. M. Kappes, J. A. Ibers, *Science* **1991**, *254*, 408-410. Structure of C₆₀ Molecule: X-Ray Crystal Structure Determination of a Twin at 110 K.
231. W. I. F. David, R. M. Ibberson, J. C. Matthewman, K. Prassides, T. J. S. Dennis, J. P. Hare, H. W. Kroto, R. Taylor, D. R. M. Walton, *Nature (London)* **1991**, *353*, 147-149. Crystal Structure and Bonding of Ordered C₆₀.
232. A. L. Balch, J. W. Lee, B. C. Noll, M. M. Olmstead, *J. Chem. Soc., Chem. Commun.* **1993**, 56-58. Disorder in a Crystalline Form of Buckminsterfullerene - C₆₀·4C₆H₆.
233. J. D. Crane, P. B. Hitchcock, H. W. Kroto, R. Taylor, D. R. M. Walton, *J. Chem. Soc., Chem. Commun.* **1992**, 1764-1765. Preparation and Characterization of C₆₀(Ferrocene)₂.
234. C. S. Yannoni, P. P. Bernier, D. S. Bethune, G. Meijer, J. R. Salem, *J. Am. Chem. Soc.* **1991**, *113*, 3190-3192. NMR Determination of the Bond Lengths in C₆₀.
235. K. Hedberg, L. Hedberg, D. S. Bethune, C. A. Brown, H. C. Dorn, R. D. Johnson, M. De Vries, *Science* **1991**, *254*, 410-412. Bond Lengths in Free Molecules of Buckminsterfullerene C₆₀ from Gas-Phase Electron Diffraction.
236. R. C. Haddon, L. E. Brus, K. Raghavachari, *Chem. Phys. Lett.* **1986**, *125*, 459-464. Electronic Structure and Bonding of Icosahedral C₆₀.
-

-
237. M. Bühl, A. Hirsch, *Chem. Rev.* **2001**, *101*, 1153-1183. Spherical Aromaticity of Fullerenes.
238. P. W. Fowler, J. Woolrich, *Chem. Phys. Lett.* **1986**, *127*, 78-83. π -Systems in Three Dimensions.
239. L. Echegoyen, L. E. Echegoyen, *Acc. Chem. Res.* **1998**, *31*, 593-601. Electrochemistry of Fullerenes and Their Derivatives.
240. R. E. Haufler, J. Conceicao, L. P. F. Chibante, Y. Chai, N. E. Byrne, S. Flanagan, M. M. Haley, S. C. O'Brien, C. Pam, Z. Xiao, W. E. Billups, M. A. Ciufolini, R. H. Hauge, J. L. Margrave, L. J. Wilson, R. F. Curl, R. E. Smalley, *J. Phys. Chem.* **1994**, *94*, 8634-8636. Efficient Production of C₆₀ (Buckminsterfullerene), C₆₀H₃₆, and the Solvated Bucky Ion.
241. P.-M. Allemand, A. Koch, F. Wudl, Y. Rubin, F. Diederich, M. M. Alvarez, S. J. Anz, R. L. Whetten, *J. Am. Chem. Soc.* **1991**, *113*, 1050-1051. Two Different Fullerenes Have the Same Cyclic Voltammetry.
242. D. Dubois, K. M. Kadish, S. Flanagan, R. E. Haufler, L. P. F. Chibante, L. J. Wilson, *J. Am. Chem. Soc.* **1991**, *113*, 4364-4366. Spectroelectrochemical Study of the C₆₀ and C₇₀ Fullerenes and their Monoanions, Dianions, Trianions, and Tetraanions.
243. D. Dubois, K. M. Kadish, S. Flanagan, L. J. Wilson, *J. Am. Chem. Soc.* **1991**, *113*, 7773-7774. Electrochemical Detection of Fulleronium and Highly Reduced Fulleride (C₆₀⁵⁻) Ions in Solution.
244. D. Dubois, G. Moninot, W. Kutner, M. Jones, K. M. Kadish, *J. Phys. Chem.* **1992**, *96*, 7137-7145. Electroreduction of Buckminsterfullerene, C₆₀, in Aprotic Solvents: Solvent, Supporting Electrolyte, and Temperature Effects.
245. Q. Xie, E. Perez-Cordero, L. Echegoyen, *J. Am. Chem. Soc.* **1992**, *114*, 3978-3980. Electrochemical Detection of C₆₀⁶⁻ and C₇₀⁶⁻: Enhanced Stability of Fullerides in Solution.
246. Y. Ohsawa, T. Saji, *J. Chem. Soc., Chem. Commun.* **1992**, 781-782. Electrochemical Detection of C₆₀⁶⁻ at Low Temperature.
247. S. H. Yang, C. L. Pettiette, J. Conceicao, O. Cheshnovsky, R. E. Smalley, *Chem. Phys. Lett.* **1987**, *139*, 233-238. UPS of Buckminsterfullerene and Other Large Clusters of Carbon.

-
248. Y.-P. Sun, G. E. Lawson, J. E. Riggs, B. Ma, N. X. Wang, D. K. Moton, *J. Phys. Chem. A* **1998**, *101*, 5626-5632. Photophysical and Nonlinear Optical Properties of [60]Fullerene Derivatives.
249. B. Ma, C. E. Bunker, R. Guduru, X. F. Zhang, Y.-P. Sun, *J. Phys. Chem. A* **1997**, *101*, 5626-5632. Quantitative Spectroscopies Studies of the Photoexcited State Properties of Methano and Pyrrolidino [60]Fullerene Derivatives.
250. B. Ma, Y.-P. Sun, *J. Chem. Soc., Perkin Trans. 2* **1996**, 2157-2162. Fluorescence Spectra and Quantum Yields of [60]Fullerene and [70]Fullerene under Different Solvent Conditions. A Quantitative Examination using a Near-Infrared-Sensitive Emission Spectrometer.
251. F. Cardullo, P. Seiler, L. Isaacs, J. F. Nierengarten, R. F. Haldimann, F. Diederich, T. Mordasini Denti, W. Thiel, C. Boudon, J. P. Gisselbrecht, M. Gross, *Helv. Chim. Acta* **1997**, *80*, 343-371. Bis- Through Tetrakis-Adducts of C₆₀ by Reversible Tether-Directed Remote Functionalization and Systematic Investigation of the Changes in Fullerene Properties as a Function of Degree, Pattern, and Nature of Functionalization.
252. A. Curioni, P. Giannozzi, J. Hutter, W. Andreoni, *J. Phys. Chem.* **1995**, *99*, 4008-4014. C₆₁H₂ in Molecular and Solid Phases: Density-Functional Approach to Structural and Electronic Properties.
253. N. Armaroli, F. Diederich, C. O. Dietrich Buchecker, L. Falmigni, G. Marconi, J.-F. Nierengarten, J.-P. Sauvage, *Chem. Eur. J.* **1998**, *4*, 406-416. A Copper(II)-Complexed Rotaxane with Two Fullerene Stoppers: Synthesis, Electrochemistry, and Photoinduced Processes.
254. L. Isaacs, F. Diederich, *Helv. Chim. Acta* **1993**, *76*, 2454-2464. Structures and Chemistry of Methanofullerenes - a Versatile Route into *N*-[(Methanofullerene)Carbonyl]-Substituted Amino-Acids.
255. A. F. Hebard, M. J. Rosseinsky, R. C. Haddon, D. W. Murphy, S. H. Glarum, T. T. M. Palstra, A. P. Ramirez, A. R. Kortan, *Nature (London)* **1991**, *350*, 600-601. Superconductivity at 18 K in Potassium-Doped C₆₀.
256. M. J. Rosseinsky, A. P. Ramirez, S. H. Glarum, D. W. Murphy, R. C. Haddon, A. F. Hebard, T. T. M. Palstra, A. R. Kortan, S. M. Zahurak, A. V. Makhija, *Phys. Rev. Lett.* **1991**, *66*, 2830-2832. Superconductivity at 28 K in RBXC₆₀.
-

-
257. X. K. Wang, T. G. Zhang, W. P. Lin, Z. L. Sheng, G. K. Wong, M. M. Kappes, R. P. H. Chang, J. B. Ketterson, *Appl. Phys. Lett.* **1992**, *60*, 810-812. Large 2nd-Harmonic Response of C₆₀ Thin Films.
258. C. Jehoulet, A. J. Bard, F. Wudl, *J. Am. Chem. Soc.* **1991**, *113*, 5456-5457. Electrochemical Reduction and Oxidation of C₆₀ Films.
259. L. O. S. Bulhoes, Y. S. Obeng, A. J. Bard, *Chem. Mater.* **1993**, *5*, 110-114. Langmuir–Blodgett and Electrochemical Studies of Fullerene Films.
260. M. Prato, *Top. Curr. Chem.* **1999**, *199*, 173-187. Fullerene Materials.
261. R. C. Haddon, A. S. Perel, R. C. Morris, T. T. M. Palstra, A. F. Hebard, R. M. Fleming, *Appl. Phys. Lett.* **1995**, *67*, 121-123. C₆₀ Thin Film Transistor.
262. G. Williams, C. Pearson, M. R. Bryce, M. C. Petty, *Thin Solid Films* **1992**, *209*, 150-152. Langmuir–Blodgett Films of C₆₀.
263. L. Giovanelli, G. Le Lay, *Appl. Surf. Sci.* **2000**, *162*, 513-518. A Chemical and Morphological Study of Fullerene Derivatives Langmuir–Blodgett Films.
264. R. Back, R. Lennox, *J. Phys. Chem.* **1992**, *96*, 8149-8152. C₆₀ and C₇₀ at the Air-Water Interface.
265. N. C. Maliszewskyj, P. A. Heiney, D. R. Jones, R. M. Strongin, M. A. Cichy, A. B. Smith III, *Langmuir* **1993**, *9*, 1439-1441. Langmuir Films of C₆₀, C₆₀O, C₆₂H₂.
266. R. Castillo, S. Ramos, J. Ruiz-Garcia, *Physica A* **1997**, 105-113. Brewster Angle Microscopy of Fullerene Monolayers.
267. P. Wang, Y. Maruyama, R. M. Metzger, *Langmuir* **1996**, *12*, 3932-3937. Superconductivity of C₆₀ Langmuir–Blodgett Films Doped with Potassium: Low-Field Signal and Electron Spin Resonance Study.
268. Y. Tomioka, M. Ishibashi, H. Kajiyama, Y. Taniguchi, *Langmuir* **1993**, *9*, 32-35. Preparation and Structural Characterization of Fullerene C₆₀ Langmuir Film.
269. P. Wang, M. Shamsuzzoha, X.-L. Wu, W.-J. Lee, R. M. Metzger, *J. Phys. Chem.* **1992**, *96*, 9025-9028. Order and Disorder in C₆₀ Langmuir–Blodgett Films: Direct Imaging by Scanning Tunneling Microscopy and High-Resolution Transmission Electron Microscopy.
270. P. A. Heiney, J. E. Fischer, A. R. Mcghee, W. A. Romanow, A. M. Denenstein, J. P. McCauley, A. B. Smith, D. Cox, *Phys. Rev. Lett.* **1991**, *66*, 2911-2914. Orientational Ordering Transition in Solid C₆₀.

-
271. T. Kawai, S. Scheib, M. P. Cava, R. M. Metzger, *Langmuir* **1997**, *13*, 5627-5633. Langmuir–Blodgett Films of a Thermally Labile 1:1 Adduct of C₆₀ Fullerene and 8-(9-Anthryl)-7-Oxaoctanoic Acid.
272. K. Oh-ishi, J. Okamura, T. Ishi-i, M. Sano, S. Shinkai, *Langmuir* **1999**, *15*, 2224-2226. Large Monolayer Domain Formed by C₆₀-Azobenzene Derivative.
273. Y. Nakamura, M. Taki, A. Asami, S. Inokuma, K. Hiratani, K. Taguchi, M. Higuchi, J. Nishimura, *Bull. Chem. Soc. Jpn.* **2000**, *73*, 1615-1619. Langmuir Films of Amphiphilic [60]Fullerene Derivatives.
274. D. Felder, M. G. Nava, M. D. Carreon, J. F. Eckert, M. Luccisano, C. Schall, P. Masson, J. L. Gallani, B. Heinrich, D. Guillon, J. F. Nierengarten, *Helv. Chim. Acta* **2002**, *85*, 288-319. Synthesis of Amphiphilic Fullerene Derivatives and Their Incorporation in Langmuir and Langmuir–Blodgett Films.
275. P. Wang, R. M. Metzger, B. Chen, *Thin Solid Films* **1998**, *327-329*, 96-99. Stable Monolayers of Fullerene Derivatives.
276. C. J. Hawker, P. M. Saville, J. W. White, *J. Org. Chem.* **1994**, *59*, 3503-3505. The Synthesis and Characterization of a Self-Assembling Amphiphilic Fullerene.
277. D. M. Guldi, Y. Tian, J. H. Fendler, H. Hungerbühler, K. D. Asmus, *J. Phys. Chem.* **1995**, *99*, 17673-17676. Stable Monolayers and Langmuir–Blodgett Films of Functionalized Fullerenes.
278. F. Diederich, U. Jonas, V. Gramlich, A. Herrmann, H. Ringsdorf, C. Thilgen, *Helv. Chim. Acta* **1993**, *76*, 2445-2453. Synthesis of a Fullerene Derivative of Benzo[18]crown-6 by Diels-Alder Reaction: Complexation Ability, Amphiphilic Properties, and X-Ray Crystal Structure of a Dimethoxy-1,9-(methanol[1,2]benzenomethano)fullerene[60] Benzene Clathrate.
279. S. Wang, R. M. Leblanc, F. Arias, L. Echegoyen, *Langmuir* **1997**, *13*, 1672-1676. Surface and Optical Properties of Langmuir and LB Films of a Crown-Ether C₆₀ Derivative.
280. M. Maggini, L. Pasimeni, M. Prato, G. Scorrano, L. Valli, *Langmuir* **1994**, *10*, 4164-4166. Incorporation of an Acyl Group in Fulleropyrrolidines: Effects on Langmuir Monolayers.
281. M. Maggini, A. Karisson, L. Pasimeni, G. Scorrano, M. Prato, L. Valli, *Tetrahedron Lett.* **1994**, *35*, 2985-2988. Synthesis of *N*-Acylated Fulleropyrrolidines: New Materials for the Preparation of Langmuir–Blodgett Films Containing Fullerenes.
-

-
282. C. Bingel, *Chem. Ber.* **1993**, *126*, 1957-1959. Cyclopropanierung von Fullerenen.
283. C. Bingel, H. Schiffer, *Liebigs Ann. Chem.* **1995**, 1551-1553. Biscyclopropanation of C₇₀.
284. F. Cardullo, F. Diederich, L. Echegoyen, T. Habicher, N. Jayaraman, R. M. Leblanc, J. F. Stoddart, S. P. Wang, *Langmuir* **1998**, *14*, 1955-1959. Stable Langmuir and Langmuir–Blodgett Films of Fullerene-Glycodendron Conjugates.
285. J. F. Nierengarten, C. Schall, J. F. Nicoud, B. Heinrich, D. Guillon, *Tetrahedron Lett.* **1998**, *39*, 5747-5750. Amphiphilic Cyclic Fullerene Bisadducts: Synthesis and Langmuir Films at the Air-Water Interface.
286. S. Zhang, Y. Rio, F. Cardinali, C. Bourgogne, J. L. Gallani, J. F. Nierengarten, *J. Org. Chem.* **2003**, *68*, 9787-9797. Amphiphilic Diblock Dendrimers with a Fullerene Core.
287. C. J. Pedersen, *J. Am. Chem. Soc.* **1967**, *89*, 7017-7036. Cyclic Polyethers and Their Complexes with Metal Salts.
288. C. J. Pedersen, H. K. Frensdorff, *Angew. Chem.* **1972**, *84*, 16-25; *Angew. Chem. Int. Ed.* **1972**, *11*, 16-25. Macrocyclic Polyethers and Their Complexes.
289. G. W. Gokel, *Crown Ether and Cryptands*. Monographs in Supramolecular Chemistry, J. F. Stoddart (Ed.), The Royal Society of Chemistry, London, **1991**.
290. B. Dietrich, P. Viout, J. M. Lehn, *Macrocyclic Chemistry: Aspects of Organic and Inorganic Supramolecular Chemistry*, VCH, Weinheim, Germany, **1993**.
291. I. K. Lednev, M. C. Petty, *Adv. Mater.* **1996**, *8*, 615-630. Langmuir Monolayers and Langmuir–Blodgett Multilayers Containing Macrocyclic Ionophores.
292. I. K. Lednev, M. C. Petty, *J. Phys. Chem.* **1994**, *98*, 9601-9605. Langmuir–Blodgett Films of Chromoionophores Containing a Crown Ether Ring: Complex Formation with Ag⁺ Cations in Water.
293. S. Iqbal, F. J. B. Kremer, J. A. Preece, H. Ringsdorf, M. Steinbeck, J. F. Stoddart, J. Shen, N. D. Tinker, *J. Mat. Chem.* **1997**, *7*, 1147-1154. Detecting a Transition-Metal Amine at Tailored Surfaces.
294. Z. Q. Yao, P. Liu, R. Z. Yan, L. Y. Liu, X. H. Liu, W. C. Wang, *Thin Solid Films* **1992**, *210*, 208-210. Studies on Nonlinear Optical Properties of Langmuir–Blodgett Films Formed from Azobenzocrown Ether Derivatives.
295. H. Matsumura, T. Watanabe, K. Furusawa, S. Inokuma, T. Kuwamura, *Bull. Chem. Soc. Jpn.* **1987**, *60*, 2747-2750. Electrical Double-Layer Formed on the Monolayer of Crown-Ether Compounds.

-
296. I. K. Lednev, M. C. Petty, *Langmuir* **1994**, *10*, 4185-4189. Aggregate Formation in Langmuir–Blodgett Films of an Amphiphilic Benzothiazolium Styryl Chromoionophore.
297. P. A. Heiney, M. R. Stetzer, Y. Mindyuk, E. DiMasi, A. R. McGhie, H. Liu, A. B. Smith III, *J. Phys. Chem. B* **1999**, *103*, 6206-6214. Langmuir Films of Amphiphilic Crown Ethers.
298. H. J. Zhang, Z. Lin, J. Shen, X. Y. Tang, *Thin Solid Films* **1992**, *210-211*, 628-630. Langmuir–Blodgett Films of Crown Ether Containing Biphenyl Mesogenic Groups.
299. H. Sasaki, A. Ueno, J. Anzai, T. Osa, *Bull. Chem. Soc. Jpn.* **1986**, *59*, 1953-1956. Benzo15-Crown-5 Linked Spirobenzopyran. 1. Photocontrol of Cation-Binding Ability and Photoinduced Membrane-Potential Changes.
300. I. K. Lednev, M. C. Petty, *J. Phys. Chem.* **1995**, *99*, 4176-4180. Complex Formations of an Amphiphilic Benzothiazolium Styryl Chromoionophore with Metal Cations in a Monolayers at the Air-Water Interface.
301. S. Y. Zaitsev, M. Belohradsky, J. Zavada, D. Möbius, *Thin Solid Films* **1994**, *248*, 78-82. Ionic Selectivity of the Surface-Active Derivatives of Crown-Ethers in Monolayers.
302. R. Plehnert, J. A. Schröter, C. Tschierske, *Langmuir* **1998**, *14*, 5245-5249. Selective Cationic Binding at the Air-Water Interface by Thin Films of Rigid Amphiphiles Bearing Laterally Attached Crown Ether Moieties.
303. D. A. Leigh, A. E. Moody, F. A. Wade, T. A. King, D. West, G. S. Bahra, *Langmuir* **1995**, *11*, 2334-2336. Second Harmonic Generation from Langmuir–Blodgett Films of Fullerene Aza-Crown Ethers and Their Potassium Ion Complexes.
304. I. K. Lednev, M. C. Petty, *Adv. Mater. Opt. Electron.* **1995**, *5*, 137-143. Ion-Selective Langmuir–Blodgett Films of a Chromoionophore.
305. I. K. Lednev, M. C. Petty, *Adv. Mater. Opt. Electron.* **1994**, *4*, 225-232. Langmuir–Blodgett Films of a Benzothiazolium Dye Containing a Crown Ether Ring.
306. L. M. Goldenberg, G. Williams, M. R. Bryce, A. P. Monkman, M. C. Petty, A. Hirsch, A. Soi, *J. Chem. Soc., Chem. Commun.* **1993**, 1310-1312. Electrochemical Studies on Langmuir–Blodgett Films of 1-*tert*-Butyl-1,9-Dihydrofullerene[60].
307. Y. Takeda, H. Yano, *Bull. Chem. Soc. Jpn.* **1980**, *53*, 1720-1722. A Conductance Study of the Complexation Reaction of Dibenzo[24]crown-8 with Alkali Metal Ions in Propylene Carbonate and Methanol.
308. M. Hiraoka, *Crown Compounds: Their Characteristics and Applications*, Elsevier Science Publishers, Amsterdam, **1982**.
-

-
309. H. K. Frensdorff, *J. Am. Chem. Soc.* **1971**, *93*, 600-606. Stability Constants of Cyclic Polyether Complexes with Univalent Cations.
310. E. D. Glendening, D. Feller, M. A. Thompson, *J. Am. Chem. Soc.* **1994**, *116*, 10657-10669. An *ab initio* Investigation of the Structure and Alkali Metal Cation Selectivity of 18-Crown-6.
311. R. M. Izatt, J. S. Bradshaw, S. A. Nielsen, J. D. Lamb, J. J. Christensen, *Chem. Rev.* **1985**, *85*, 271-339. Thermodynamic and Kinetic Data for Cation Macrocycle Interaction.
312. E. Bakker, M. Willer, M. Lerchl, K. Seller, E. Pretsch, *Anal. Chem.* **1994**, *66*, 516-521. Determination of Complex Formation Constants of Neutral Cation-Selective Ionophores in Solvent Polymeric Membranes.
313. J. J. Christensen, D. J. Eatough, R. M. Izatt, *Chem. Rev.* **1974**, *74*, 352-384. The Synthesis and Ion Binding of Synthetic Multidentate Macrocyclic Compounds.
314. R. M. Izatt, J. J. Christensen, *Synthetic Multidentate Macrocyclic Compounds*, Academic Press, New York, **1978**.
315. M. Y. Okamura, G. Feher, N. Nelson, *Photosynthesis*, Academic Press, New York, **1982**.
316. F. Rabanal, B. R. Gibney, W. F. Degrado, C. C. Moser, P. L. Dutton, *Inorg. Chim. Acta* **1996**, *243*, 213-218. Engineering Photosynthesis: Synthetic Redox Proteins.
317. R. Jones, R. H. Tredgold, A. Hoofar, *Thin Solid Films* **1985**, *123*, 307-314. Effects of Thickness on Surface Potential and Surface Conductivity in Non-Insulating Langmuir-Blodgett Multilayers of Porphyrins.
318. R. B. Beswick, C. W. Pitt, *Chem. Phys. Lett.* **1988**, *143*, 589-592. Oxygen Detection Using Phosphorescent Langmuir-Blodgett Films of a Metalloporphyrin.
319. E. Karmann, J. P. Meyer, D. Schlettwein, N. I. Jaeger, M. Anderson, A. Schmidt, N. Armstrong, *Mol. Cryst. Liq. Cryst. A* **1996**, *283*, 283-291. Photoelectrochemical Effects and (Photo)conductivity of "N-Type" Phthalocyanines.
320. D. Beljonne, G. E. O'Keefe, P. J. Hamer, R. H. Friend, H. L. Anderson, J. L. Bredas, *J. Chem. Phys.* **1997**, *106*, 9439-9460. Investigation of the Linear and Nonlinear Optical Response of Edge-Linked Conjugated Zinc Porphyrin Oligomers by Optical Spectroscopy and Configuration Interaction Techniques.
321. J. J. Piet, J. M. Warman, H. L. Anderson, *Chem. Phys. Lett.* **1997**, *266*, 70-74. Photo-Induced Charge Separation on Conjugated Porphyrin Chains.

-
322. C. L. Honeybourne, *J. Phys. Chem. Solids* **1987**, *48*, 109-141. Solid Thin-Films of Extended π -Systems: Deposition, Characterization and Application.
323. H. Möhwald, A. Miller, W. Stich, W. Knoll, A. Ruau-del-Teixier, T. Lehmann, J.-H. Furhop, *Thin Solid Films* **1986**, *141*, 261-275. Intermolecular Interactions in Monolayers of Porphyrins.
324. M. Ringuet, J. Gagnon, R. M. Leblanc, *Langmuir* **1986**, *2*, 700-704. Monolayer Studies of a New Surfactant Carboxyporphyrin.
325. S. Y. Luk, R. Mayers, J. O. Williams, *J. Chem. Soc., Chem. Commun.* **1987**, 215-216. Langmuir–Blodgett Films of Porphyrins Containing a Metal-Metal Sigma Bond.
326. M. Fujihira, K. Nishiyama, H. Yamada, *Thin Solid Films* **1985**, *132*, 77-82. Photoelectrochemical Responses of Optically Transparent Electrodes Modified with Langmuir–Blodgett Films Consisting of Surfactant Derivatives of Electron Donor, Acceptor and Sensitizer Molecules.
327. M. R. Moore, *Historical Introduction to Porphyrins and Porphyrins*, in *Biosynthesis of Heme and Chlorophylls*, H. A. Dailey (Ed.), McGraw-Hill, New York, **1990**, p. 1-41.
328. H. A. Dailey, *Biosynthesis of Heme and Chlorophylls*, McGraw-Hill, New York, **1990**.
329. T. Arai, K. Kobata, H. Mihara, T. Fujimoto, N. Nishino, *Bull. Chem. Soc. Jpn.* **1995**, *68*, 1989-1998. A Membrane-Protein Model Polypeptides with 4-Alpha-Helix Bundle Structure on 5,10,15,20-Tetrakis[2-(carboxymethoxy)phenyl]porphyrin.
330. T. Arai, N. Takei, N. Nishino, T. Fujimoto, *J. Chem. Soc., Chem. Commun.* **1996**, 2133-2134. Solvent-Dependent Chiral Assembling of Two Zinc Porphyrins in a Zinc-Free-Base-Zinc Trimeric Porphyrin Array.
331. G. R. Geier, T. Sasaki, *Tetrahedron Lett.* **1997**, *38*, 3821-3824. The Design, Synthesis, and Characterization of a Porphyrin-Peptide Conjugate.
332. D. Voet, J. G. Voet, *Biochemistry*, Wiley Interscience, New York, **1990**.
333. J. Deisenhofer, J. R. Norris, *The Photosynthetic Reaction Center*, Academic Press, San Diego, **1993**.
334. M. Gouterman, *Optical Spectra and Electronic Structure*, in *The Porphyrins*, D. Dolphin (Ed.), Academic Press, New York, **1978**, p. 1-165.
335. H. L. Anderson, *Chem. Commun.* **1999**, 2323-2330. Building Molecular Wires from the Colours of Life: Conjugated Porphyrin Oligomers.
-

-
336. D. Kuciauskas, A. P. Liddell, S. Lin, T. E. Johnson, S. J. Weghorn, J. L. Lindsey, A. L. Moore, T. A. Moore, D. Gust, *J. Am. Chem. Soc.* **1999**, *121*, 8604-8614. An Artificial Photosynthetic Antenna-Reaction Center Complex.
337. M. R. Wasielewski, *Chem. Rev.* **1992**, *92*, 435-461. Photoinduced Electron Transfer in Supramolecular Systems for Artificial Photosynthesis.
338. K. Kato, H. Araki, K. Shinbo, F. Kaneko, C. M. Dooling, T. H. Richardson, *Jpn. J. Appl. Phys.* **2002**, *41*, 2779-2783. Evaluation of Structure and Gas Response in Porphyrin Langmuir–Blodgett Films by Attenuated Total Reflection Measurements.
339. M. Anikin, N. V. Tkachenko, H. Lemmetyinen, *Langmuir* **1997**, *13*, 3002-3008. Arrangement of a Hydrophobically Shielded Porphyrin, 5,10,15,20-Tetrakis(3,5-di-*tert*-butylphenyl)porphyrin, in Octadecylamine Langmuir–Blodgett Multilayers.
340. K. Aramata, M. Kamachi, M. Takahashi, A. Yamagishi, *Langmuir* **1997**, *13*, 5161-5167. Orientation of Porphyrin Moieties in Langmuir–Blodgett Films of Tetraphenylporphyrin Vinyl Monomers and Their Polymers.
341. R. Azumi, M. Matsumoto, S. Kuroda, M. J. Crossley, *Langmuir* **1995**, *11*, 4495-4498. Orientation Control of Functional Molecules in Langmuir–Blodgett Films Caused by a Trigger Molecule: Infrared Spectroscopic Study on the Orientation of *n*-Alkane, Trigger Molecule.
342. A. Tronin, J. Strzalka, X. Chen, P. L. Dutton, J. K. Blasie, *Langmuir* **2000**, *16*, 9878-9886. Determination of the Porphyrin Orientation Distribution in Langmuir Monolayers by Polarized Epifluorescence.
343. C. Y. Liu, H. L. Pan, M. A. Fox, A. J. Bard, *Science* **1993**, *261*, 897-899. High-Density Nanosecond Charge Trapping in Thin Films of the Photoconductor ZnODEP.
344. J. H. Fendler, F. C. Meldrum, *Adv. Mater.* **1995**, *7*, 607-632. The Colloid-Chemical Approach to Nanostructured Materials.
345. A. E. Alexander, *J. Chem. Soc.* **1937**, 1813-1816. Monolayers of Porphyrins and Related Compounds.
346. J. A. Bergeron, G. L. Gaines Jr., W. D. Bellamy, *J. Colloid Interface Sci.* **1967**, *25*, 97-106. Monolayers of Porphyrin Esters: Spectral Disturbances and Molecular Interactions.
347. H. A. Dick, J. R. Bolton, G. Picard, G. Munger, R. M. Leblanc, *Langmuir* **1988**, *4*, 133-136. Fluorescence Lifetime of 5-(4-Carboxyphenyl)-10,15,20-Tritolylporphyrin in a Mixed Langmuir–Blodgett Film with Dioleoylphosphatidylcholine. A Proposed Standard.

-
348. J. M. Kroon, E. J. R. Sudholter, A. Schenning, R. J. M. Nolte, *Langmuir* **1995**, *11*, 214-220. Self-Organization of Amphiphilic Porphyrins at the Air-Water Interface.
349. H. Chou, C. T. Chen, K. F. Stork, P. W. Bohn, K. S. Suslick, *J. Phys. Chem* **1994**, *98*, 383-385. Langmuir–Blodgett Films of Amphiphilic Push-Pull Porphyrins.
350. R. Paolesse, L. Valli, C. Goletti, C. Di Natale, A. Froiia, A. Macagnano, G. Bussetti, P. Chiaradia, A. D'Amico, *Mater. Sci. Eng. C* **2002**, *22*, 219-225. Langmuir–Blodgett Films of a Modified Tetraphenylporphyrin.
351. R. Azumi, M. Matsumoto, S. Kuroda, L. G. King, M. J. Crossley, *Langmuir* **1995**, *11*, 4056-4060. Orientation Change of Dimer-Type Porphyrin in Langmuir–Blodgett Films Caused by a Trigger Molecule.
352. G. A. Schick, I. C. Schreiman, R. W. Wagner, J. S. Lindsey, D. F. Bocian, *J. Am. Chem. Soc.* **1989**, *111*, 1344-1350. Spectroscopic Characterization of Porphyrin Monolayer Assemblies.
353. R. F. Khairutdinov, N. Serpone, *J. Phys. Chem. B* **1999**, *103*, 761-769. Photoluminescence and Transient Spectroscopy of Free Base Porphyrin Aggregates.
354. R. Azumi, M. Matsumoto, Y. Kawabata, S. Kuroda, M. Sugi, L. G. King, M. J. Crossley, *J. Phys. Chem.* **1993**, *97*, 12862-12869. Orientation Change of Porphyrin in Langmuir–Blodgett Films Caused by a Trigger Molecule.
355. J. Jin, L. S. Li, X. Q. Wang, Y. Li, Y. J. Zhang, X. Chen, Y. Z. Li, T. J. Li, *Langmuir* **1999**, *15*, 6969-6974. Steady-State Spectroscopic and Photovoltage Studies of Hemin and Hemin/*n*-Octadecylamine Langmuir–Blodgett Films.
356. D. M. Guldi, I. Zilbermann, G. A. Anderson, K. Kordatos, M. Prato, R. Tafuro, L. Valli, *J. Mater. Chem.* **2004**, *14*, 303-309. Langmuir–Blodgett and Layer-by-Layer Films of Photoactive Fullerene-Porphyrin Dyads.
357. D. Bonifazi, *ETH Dissertation No. 15599*, From Solution to Surfaces: Synthesis, Physical Properties, and Materials Application of Novel Fullerene and Porphyrin Derivatives, **2004**.
358. A. Ruaudel-Teixier, A. Barraud, B. Belbeoch, M. Roulliay, *Thin Solid Films* **1983**, *99*, 33-40. Langmuir–Blodgett Films of Pure Porphyrins.
359. E. Sartori, M. P. Fontana, M. Costa, E. Dalcanale, V. Paganuzzi, *Thin Solid Films* **1996**, *284-285*, Langmuir–Blodgett Films of Mesogenic Porphyrin Derivatives.

-
360. P. Facci, M. P. Fontana, E. Dalcanale, M. Costa, T. Sacchelli, *Langmuir* **2000**, *16*, 7726-7730. Molecular Reorganization in Langmuir–Blodgett Films of Mesogenic Zn-Porphyrin Octaesters.
361. M. I. Viseu, A. M. Gonçalves da Silva, P. Antunes, S. M. B. Costa, *Langmuir* **2002**, *18*, 5772-5781. Organization of Cationic Porphyrins in Mixed Langmuir–Blodgett Films. An Absorption and Steady-State Fluorescence Study.
362. T. Martynski, A. Biadasz, D. Bauman, *Z. Naturforsch.* **2003**, *58a*, 97-102. Molecular Organization in Langmuir Films of Dichroic Azo Dye Liquid Crystal Mixtures. II. Surface Potential Measurements.
363. D. J. Qian, C. Nakamura, J. Miyake, *Thin Solid Films* **2001**, *397*, 266-275. Spectroscopic Studies of the Multiporphyrin Arrays at the Air-Water Interface and in Langmuir-Blodgett Films.
364. M. Kasha, H. R. Rawls, M. Ashraf El-Bayoumi, *Pure Appl. Chem.* **1965**, 371-392. The Exciton Model in Molecular Spectroscopy.
365. M. Kasha, *Radiat. Res.* **1963**, *20*, 55-70. Energy Transfer Mechanisms and Molecular Exciton Model for Molecular Aggregates.
366. M. Kasha, *Molecular Excitons in Small Aggregates*, in *Spectroscopy of the Excited State*, B. Di Bartolo (Ed.), Plenum Press, New York, **1976**, p. 337-363.
367. V. Czikkely, H. D. Försterling, H. Kuhn, *Chem. Phys. Lett.* **1970**, *6*, 11-14. Light Absorption and Structure of Aggregates of Dye Molecules.
368. V. Czikkely, H. D. Försterling, H. Kuhn, *Chem. Phys. Lett.* **1970**, *6*, 207-210. Extended Dipole Model for Aggregates of Dye Molecule.
369. K. Ikegami, C. Mingotaud, M. Lan, *Thin Solid Films* **2001**, *393*, 193-198. Intramolecular Charge Transfer in Merocyanine Dye Molecules Enhanced by Formation of J-Aggregates.
370. K. Ikegami, C. Mingotaud, M. Lan, *J. Phys. Chem. B* **1999**, *103*, 11261-11268. J-Aggregates in Langmuir-Blodgett Films of a Merocyanine Dye without Metallic Cations: Using FT-IR to Observe Changes in the Electronic Structures of the Molecules upon Aggregation.
371. D. J. Qian, C. Nakamura, J. Miyake, *Langmuir* **2000**, *16*, 9615-9619. Multiporphyrin Array from Interfacial Metal-Mediated Assembly and Its Langmuir-Blodgett Films.

-
372. D. J. Qian, H.-G. Liu, J. Jiang, *Colloids Surf. A* **2000**, *163*, 191-197. Monolayers and Langmuir–Blodgett Films of (Phthalocyaninato)(tetra-4-pyridylporphyrinato)cerium Double-Decker Heterocomplex.
373. B. N. Choudhury, A. C. Weedon, J. R. Bolton, *Langmuir* **1998**, *14*, 6192-6198. Effects of Molecular Organization on Photophysical Behavior. 1. Steady-State Fluorescence and Fluorescence Quantum Yield Studies of Langmuir–Blodgett Monolayers of Some Surfactant Porphyrins.
374. M. Gouterman, D. Holten, E. Lieberman, *Chem. Phys.* **1977**, *25*, 139-153. Porphyrins XXXV. Exciton Coupling in μ -Oxo Scandium Dimers.
375. J. Bardwell, J. R. Bolton, *Photochem. Photobiol.* **1984**, *39*, 735-746. Monolayer Studies of 5-(4-Carboxyphenyl)-10,15,20-Tritolyl-Porphyrin. 1. Optical Studies of Films at the Air-Water Interface and of Films Transferred onto Solid Substrates.
376. J. A. Bardwell, J. R. Bolton, *Photochem. Photobiol.* **1984**, *40*, 319-327. Monolayer Studies of 5-(4-Carboxyphenyl)-10,15,20-Tritolyl-Porphyrin. 2. Photovoltaic Study of Multilayer Sandwich Cells.
377. N. V. Tkachenko, C. Guenther, H. Imahori, K. Tamaki, Y. Sakata, S. Fukuzumi, H. Lemmetyinen, *Chem. Phys. Lett.* **2000**, *326*, 344-350. Near Infra-Red Emission of Charge-Transfer Complexes of Porphyrin-Fullerene Films.
378. H. Imahori, N. V. Tkachenko, V. Vehmanen, K. Tamaki, H. Lemmetyinen, Y. Sakata, S. Fukuzumi, *J. Phys. Chem. A* **2001**, *105*, 1750-1756. An Extremely Small Reorganization Energy of Electron Transfer in Porphyrin-Fullerene Dyad.
379. T. J. Kesti, N. V. Tkachenko, V. Vehmanen, H. Yamada, H. Imahori, S. Fukuzumi, H. Lemmetyinen, *J. Am. Chem. Soc.* **2002**, *124*, 8067-8077. Exciplex Intermediates in Photoinduced Electron Transfer of Porphyrin-Fullerene Dyads.
380. H. Imahori, *Org. Biomol. Chem.* **2004**, *2*, 1425-1433. Porphyrin-Fullerene Linked Systems as Artificial Photosynthetic Mimics.
381. N. V. Tkachenko, V. Vehmanen, J. P. Nikkanen, H. Yamada, H. Imahori, S. Fukuzumi, H. Lemmetyinen, *Chem. Phys. Lett.* **2002**, *366*, 245-252. Porphyrin-Fullerene Dyad with a Long Linker: Formation of Charge Transfer Conformer in Langmuir–Blodgett Film.
382. N. V. Tkachenko, E. Vuorimaa, T. Kesti, A. S. Alekseev, A. Y. Tauber, P. H. Hynninen, H. Lemmetyinen, *J. Phys. Chem. B* **2000**, *104*, 6371-6379. Vectorial Photoinduced Electron Transfer in Phytychlorin-[60]Fullerene Langmuir–Blodgett Films.
-

383. J. P. Bourgeois, *ETH Dissertation No. 13956*, Regioselective Synthesis of *trans*-1 Fullerene-C₆₀ Bis-Adducts Directed by Crown Ether and Tetraphenyl Porphyrin Tethers, **2000**.
384. M. M. Olmstead, D. A. Costa, K. Maitra, B. C. Noll, S. L. Phillips, P. M. Van Calcar, A. L. Balch, *J. Am. Chem. Soc.* **1999**, *121*, 7090-7097. Interaction of Curved and Flat Molecular Surfaces. The Structures of Crystalline Compounds Composed of Fullerene (C₆₀, C₆₀O, C₇₀, and C₁₂₀O) and Metal Octaethylporphyrin Units.
385. P. D. W. Boyd, M. C. Hodgson, C. E. F. Rickard, A. G. Oliver, L. Chaker, P. J. Brothers, R. D. Bolskar, F. S. Tham, C. A. Reed, *J. Am. Chem. Soc.* **1999**, *121*, 10487-10495. Selective Supramolecular Porphyrin-Fullerene Interactions.
386. N. Armaroli, G. Marconi, L. Echegoyen, J. P. Bourgeois, F. Diederich, *Chem. Eur. J.* **2000**, *6*, 1629-1645. Charge-Transfer Interactions in Face-to-Face Porphyrin-Fullerene Systems: Solvent-Dependent Luminescence in the Infrared Spectral Region.
387. N. V. Tkachenko, L. Rantala, A. Y. Tauber, J. Helaja, P. H. Hynninen, H. Lemmetyinen, *J. Am. Chem. Soc.* **1999**, *121*, 9378-9387. Photoinduced Electron Transfer in Phytochlorin-[60]Fullerene Dyads.
388. J. M. Olson, *Photochem. Photobiol.* **1998**, *67*, 61-75. Chlorophyll Organization and Function in Green Photosynthetic Bacteria.
389. G. McDermott, S. M. Prince, A. A. Freer, A. M. Hawthornthwaitelawless, M. Z. Papiz, R. J. Cogdell, N. W. Isaacs, *Nature* **1995**, *374*, 517-521. Crystal-Structure of an Integral Membrane Light-Harvesting Complex from Photosynthetic Bacteria.
390. P. Jordan, P. Fromme, H. T. Witt, O. Klukas, W. Saenger, N. Krauss, *Nature* **2001**, *411*, 909-917. Three-Dimensional Structure of Cyanobacterial Photosystem I at 2.5 Angstrom Resolution.
391. A. Zouni, H. T. Witt, J. Kern, P. Fromme, N. Krauss, W. Saenger, P. Orth, *Nature* **2001**, *409*, 739-743. Crystal Structure of Photosystem II from *Synechococcus Elongatus* at 3.8 Angstrom Resolution.
392. A. M. Braun, M.-T. Maurette, O. E., *Photochemical Technology*, John Wiley & Sons Ltd., New York, **1991**.
393. G. J. Kavarnos, *Fundamentals of Photoinduced Electron Transfer*, VCH Publishers, Inc., New York, **1993**.
394. D. Gust, T. A. Moore, A. L. Moore, *Acc. Chem. Res.* **1993**, *26*, 198-205. Molecular Mimicry of Photosynthetic Energy and Electron Transfer.

395. M. R. Wasielewski, *Chem. Rev.* **1992**, *92*, 453-461. Photoinduced Electron Transfer in Supramolecular Systems for Artificial Photosynthesis.
396. T. Asaki, M. Ohkohchi, R. Matsusaka, N. Mataga, R. P. Zhang, A. Osuka, Y. Maruyama, *J. Am. Chem. Soc.* **1993**, *115*, 5665-5674. Intramolecular Photoinduced Charge Separation and Charge Recombination of the Product Ion Pair States of a Series of Fixed-Distance Dyads of Porphyrins and Quinones: Energy Gap and Temperature Dependences of the Rate Constants.
397. D. Bonifazi, F. Diederich, *Chem. Commun.* **2002**, 2178-2179. Strong Intramolecular Chromophore Interactions in Novel Bis([60]fullerene)-Oligoporphyrin Nanoarrays.
398. H. Imahori, K. Tamaki, H. Yamada, K. Yamada, Y. Sakata, Y. Nishimura, I. Yamazaki, M. Fujitsuka, O. Ito, *Carbon* **2000**, *38*, 1599-1605. Photosynthetic Electron Transfer Using Fullerenes as Novel Acceptors.
399. H. Imahori, Y. Sakata, *Chem. Lett.* **1996**, 199-200. Synthesis of Closely Spaced Porphyrin-Fullerene.
400. S. Higashida, H. Imahori, T. Kaneda, Y. Sakata, *Chem. Lett.* **1998**, 605-606. Synthesis and Photophysical Behaviour Of Porphyrins with Two C₆₀ Units.
401. P. A. Liddel, D. Kuciauskas, J. P. Sumida, B. Nash, D. Nguyen, A. L. Moore, T. A. Moore, *J. Am. Chem. Soc.* **1997**, *119*, 1400-1405. Photoinduced Charge Separation and Charge Recombination to a Triplet State in a Carotene-Porphyrin-Fullerene Triad.
402. H. Imahori, K. Hagiwara, T. Akiyama, S. Taniguchi, T. Okada, Y. Sakata, *Chem. Lett.* **1995**, 265-266. Synthesis and Photophysical Property of Porphyrin-Linked Fullerene.
403. P. Cheng, S. R. Wilson, D. I. Schuster, *Chem. Commun.* **1999**, 89-90. A Novel Parachute-Shaped C₆₀-Porphyrin Dyad.
404. P. A. Liddel, J. P. Sumida, A. N. Macpherson, L. Noss, G. R. Seely, K. N. Clark, A. L. Moore, T. A. Moore, D. Gust, *Photochem. Photobiol.* **1994**, *60*, 537-541. Preparation and Photophysical Studies of Porphyrin-C₆₀ Dyads.
405. D. Kuciauskas, S. Lin, G. R. Seely, A. L. Moore, T. A. Moore, T. Gust, T. Drovetskaya, C. A. Reed, D. W. Boyd, *J. phys. Chem.* **1996**, *100*, 15926-15932. Energy and Photoinduced Electron Transfer in Porphyrin-Fullerene Dyads.
406. K. Tashiro, T. Aida, J. Y. Zheng, K. Kinbara, K. Saigo, S. Sakamoto, K. Yamaguchi, *J. Am. Chem. Soc.* **1999**, *121*, 9477-9478. A Cyclic Dimer of Metalloporphyrin Forms a Highly Stable Inclusion Complex with C₆₀.

407. M. V. Cherchez, *Bull. Chem. Soc. Jpn.* **1930**, *47*, 1279-1281. Préparation de l'Isonitrosomalonnate d'Ethyle.
408. G. G. Kleinspehn, *J. Am. Chem. Soc.* **1955**, *77*, 1546-1548. A Novel Route to Certain 2-Pyrrolocarboxylic Ester and Nitriles.
409. A. W. Johnson, I. T. Kay, E. Markham, R. Price, K. B. Shaw, *J. Chem. Soc.* **1959**, 3416-3424. Colouring Matters Derived from Pyrroles. Part II. Improved Synthesis of Some Dipyrrromethenes and Porphyrins.
410. H. Aissaoui, S. Ghirlanda, C. Gmür, W. D. Woggon, *J. Mol. Cat. A* **1996**, *113*, 393-402. The Synthesis of a New Active-Site Analogue of Cytochrome P450 Carrying Substrate Recognition Sites and Athiolate Ligand.
411. D. Tanner, O. Wennerström, *Acta Chem. Scand.* **1983**, *37*, 693-698. Cyclophanetriene for Wittig Reaction and Titanium-Mediated Reductive Coupling.
412. A. K. Burrell, D. L. Officier, P. G. Plieger, D. C. W. Reid, *Chem. Rev.* **2001**, *101*, 2751-2796. Synthetic Routes to Multiporphyrin Arrays.
413. G. R. Geier III, B. J. Littler, J. S. Lindsey, *J. Chem. Soc. Perkin Trans. 2* **2001**, 701-711. Investigation of Porphyrin-Forming Reactions. Part 3. The Origin of Scrambling in Dipyrrromethane + Aldehyde Condensation Yielding *trans*-A₂B₂-Tetraarylporphyrins.
414. X. Feng, M. O. Senge, *J. Chem. Soc. Perkin Trans. 1* **2001**, 1030-1038. An Efficient Synthesis of Highly Functionalized Asymmetric Porphyrins with Organolithium Reagents.
415. B. J. Littler, Y. Ciringh, J. S. Lindsey, *J. Org. Chem.* **1999**, *64*, 2864-2872. Investigations of Conditions Giving Minimal Scrambling in the Synthesis of *trans*-Porphyrins from Dipyrrromethanes and Aldehydes.
416. J. S. Manga, D. S. Lawrence, *Tetrahedron Lett.* **1989**, *30*, 6989-6992. High Yield Synthesis of 5,15-Diarylporphyrins.
417. B. C. Chen, *Heterocycles* **1991**, *32*, 529-597. Meldrum's Acid in Organic Synthesis.
418. D. Felder, M. D. Carreon, J. L. Gallani, D. Guillon, J. F. Nierengarten, C. Thierry, R. Deschenaux, *Helv. Chim. Acta* **2001**, *84*, 1119-1132. Amphiphilic Fullerene-Cholesterol Derivatives: Synthesis and Preparation of Langmuir and Langmuir-Blodgett Films.
419. J. P. Bourgeois, L. Echegoyen, M. Fibbioli, E. Pretsch, F. Diederich, *Angew. Chem.* **1998**, *110*, 2203-2207; *Angew. Chem. Int. Ed.* **1998**, *37*, 2118-2121. Regioselective Synthesis of *trans*-1 Fullerene Bis-Adducts Directed by a Crown Ether Tether: Alkali Metal Cation Modulated Redox Properties of Fullerene-Crown Ether Conjugates.

420. C. H. Lee, J. L. Lindsey, *Tetrahedron* **1994**, *50*, 11424-11440. One-Flask Synthesis of Meso-Substituted Dipyrromethanes and Their Application in the Synthesis of Trans-Substituted Porphyrin Building Blocks.
421. G. R. Geier III, J. L. Lindsey, *J. Org. Chem.* **1999**, *64*, 1596-1603. N-Confused Tetraphenylporphyrin and Tetraphenylsapphyrin Formation in One-Flask Syntheses of Tetraphenylporphyrin.
422. F. Y. Li, K. Yang, J. S. Tyhonas, K. A. MacCrum, J. L. Lindsey, *Tetrahedron* **1997**, *53*, 12339-12360. Beneficial Effect of Salts on Acid-Catalyzed Condensation Leading to Porphyrin Formation.
423. B. Jiang, S. W. Yang, D. C. Arbini, W. E. Jones Jr., *Chem. Commun.* **1998**, 213-214. Synthesis of Soluble Conjugated Metalloporphyrin Polymers with Tunable Electronic Properties.
424. A. Osuka, F. Kobayashi, Y. Maruyama, *Bull. Chem. Soc. Jpn.* **1991**, *64*, 1213-1225. Synthesis of Strapped, Dimeric, and Trimeric Porphyrins Based on Intramolecular Macrocyclization Reactions.
425. M. Ringuet, D. Girard, C. Chapados, *Can. J. Chem.* **1991**, *69*, 1070-1079. Vibrational and Electronic Spectra of New Liposoluble Metalloporphyrins in a Nonpolar Noncoordinating Solvent.
426. S. F. MacDonald, A. Markovac, *Can. J. Chem.* **1965**, *43*, 3247-3252. Higher Homologues from Pyrroles and Dipyrromethenes.
427. M. V. Berezin, A. S. Semeikin, A. I. V'yugin, *Russ. J. Phys. Chem.* **1996**, *70*, 1265-1268. Thermochemistry of Solution of Linear Pyrroles.
428. V. P. Baillargeon, J. K. Stille, *J. Am. Chem. Soc.* **1986**, *108*, 452-461. Palladium-Catalyzed Formylation of Organic Halides with Carbon Monoxide and Tin Hydride.

Curriculum Vitae

- 1972 Born on May 21, in Rome, Italy
- 1977-1982 Primary School at “*Scuola Elementare Glenn Doman*”, Rome, Italy.
- 1982-1985 Secondary School at “*Scuola Media Eur*”, Rome, Italy.
- 1985-1990 High School at “*Liceo Scientifico E. Majorana*”, Rome, Italy.
- 1990-1999 Chemistry studies at the University “*La Sapienza*” of Rome.
Diploma Thesis under the supervision of *Prof. Dr. L. Mandolini* and *Dr. G. Mancini*. Degree in Chemistry with *honoris* (110 *cum laude*).
- 1999 Research in the group of *Dr. G. Mancini*.
- 2000-2004 Ph.D Thesis in organic chemistry at the *Swiss Federal Institute of Technology* (ETH) Zürich, under the direction of *Prof. Dr. F. Diederich*.
- 2001-2004 Teaching assistant in the Praktikum “*Organische Chemie*” for undergraduate students at ETH, Zürich.

Zürich, September 2004

Federica Marotti